Understanding Protein Folding Mechanisms of Chaperone Proteins Using Cryo-EM

by

Stephanie Gates

A dissertation submitted in partial fulfillment
of the requirements for the degree of
Doctor of Philosophy
(Chemical Biology)
in the University of Michigan
2017

Doctoral Committee:

Associate Professor Daniel R. Southworth, Chair
Professor Ari Gafni
Professor Janet Smith
Professor Duxin Sun

Stephanie N. Gates
sngates@umich.edu

ORCID iD: 0000-0002-4312-2900

© Stephanie N Gates 2017

DEDICATION

This thesis is dedicated to my parents, Patricia and John Gates, for always pushing me to follow my dreams and encouraging my excitement about science from a young age.

ACKNOWLEDGMENTS

Many friends and family have been central to my ability to complete my Ph.D research.

First, I would like to thank my wonderful mentor, Dan Southworth, who has taught me many things about scientific thinking and effective ways to communicate science. I have appreciated our entire journey, as he learned to be a mentor and I learned to be an independent scientist. I would also like to thank my committee for their continued support and helpful guidance along the way.

I would like to thank my parents for always supporting and believing in me. My sister, Denise Harkess, has been a great role model, and she has always been there to lean on when I doubted myself. My brothers, Thomas and Brian Gates, constantly push me to think outside the box with our many philosophical debates, or just silly rants. My in-laws, Robin, Larry and Allen Yokom and Kenny Harkess, are so supportive of me and always brighten my day.

The members of the Southworth lab have been immensely supportive and helpful throughout my graduate experience. Specifically, Eric Tse has been a great resource for learning biochemistry and data processing, as well as a great friend that has helped me push through some very difficult challenges in the lab. Both Eric Tse and Alex Rizo read through my thesis chapters and help me get through the thesis writing process. Min Su, the LSI EM Facility director, trained me to do cryo-EM and helped me troubleshoot many technical issues throughout the years.

The 2012 Chemical Biology Cohort has been an incredible support system during my graduate career. We have helped each other prepare for talks, enjoyed many beers to celebrate successes, and complained about the many struggles we have encountered. This experience was much more manageable having such great friends to share it with.

I would like to thank my incredible professors from Millikin University, Dr. George Bennett, Dr. Paris Barnes, Dr. Clarence Josefson, Dr. Anne Rammelsberg, and Dr. Jeffrey Hughes, who inspired me and excited me about a career in science

Dr. Kirsten Daykin, a fellow Millikin Alum and recent Ph.D graduate, is my favorite lab partner, and our many fun times spent in the research labs at Millikin led to my future in science. Kirsten has been a great friend and it was fun to experience graduate school with her, even though we were in different states.

Dr. Lauren Rodenbarger, another Millikin Alum, has helped guide me through the final stretch with many helpful tips about writing a thesis, and guidance in the postdoc application process.

Most of all, I would like to thank my husband, co-author, and 24-hour collaborator, Adam Yokom for his constant love and support. We made it through many 12-hour alternating shifts on the microscope, months of frustration and anticipation processing the data, and hundreds of cups of coffee and beer writing our papers and theses. Adam pushes me every day to be a better

scientist, and I look forward to many years of arguing over the right way to interpret data and finding more exciting questions to ask in the process.

TABLE OF CONTENTS

Dedication ii
Acknowledgments iii
List of Figures viii
List of Tables xi
List of Abbreviations xii
Abstract xiv
CHAPTER 1 - INTRODUCTION
1.1 Protein folding and quality control is regulated by chaperone proteins 1
1.2 Hsp104 yeast disaggregase 4
1.3 Get3 is a redox regulated holdase 10
1.4 Hsp90 foldase is a drug target for many diseases 14
1.5 The importance of cryo-EM as a structural biology tool 19
1.6 References 27
CHAPTER 2 – SPIRAL ARCHITECTURE OF THE HSP104 DISAGGREGASE REVEALS THE BASIS FOR POLYPEPTIDE TRANSLOCATION
2.1 – Abstract 38
2.2 – Introduction 39
2.3 – The Hsp104 hexamer adopts an asymmetric spiral architecture 42
2.4 – The Hsp104:AMPPNP hexamer adopts an asymmetric spiral architecture 45
2.5 – Heteromeric NBD1-NBD2 interaction defines the hexamer seam 50
2.6 – Arrangement of the MD and NTD highlight critical functions 54
2.7 – Spiral staircase of pore loops defines the substrate path 57
2.8 – Discussion 59
2.9 – Materials and Methods 63
2.10 – References 67
CHAPTER 3 – RATCHET-LIKE POLYPEPTIDE TRANSLOCATION MECHANISM OF THE AAA+ DISAGGREGASE HSP104
3.1 – Abstract 72
3.2 – Introduction 73
3.3 – Forming a Stable Substrate-Bound Hsp104 Complex for Cryo-EM 74
3.4 – Initial 2D and 3D analysis of substrate-bound Hsp104 76
3.5 – Tyr Pore-Loop Contacts Along Substrate 79
3.6 – Ratchet-Like States of Protomers 82
3.7 – Coordinated Nucleotide Pockets 85
3.8 – Allosteric Control by the MD 89
3.9 – NBD1-Driven Rearrangement Engages Substrate 94
3.10 – Discussion 97
3.11 – Materials and Methods 100

3.12 – References 109
CHAPTER 4 – THE PROTEIN TARGETING FACTOR GET3 MOONLIGHTS AS ATP-INDEPENDENT CHAPERONE UNDER OXIDATIVE STRESS CONDITIONS
4.1 – Abstract 114
4.2 – Introduction 115
4.3 – Get3 – A redox-regulated chaperone in eukaryotes 117
4.4 – Mechanism of Get3's activation process 120
4.5 – Activation of Get3's chaperone function is a fully reversible process *in vitro* 122
4.6 – The minimal unit of chaperone-active Get3 is the oxidized tetramer 123
4.7 – Oxidative activation of Get3 causes massive structural rearrangements 130
4.8 – Dissecting the two Get3 functions *in vivo* 135
4.9 – Get3 co-localizes with unfolding proteins during oxidative stress *in vivo* 140
4.10 – Substrate binds Get3 tetramer in hydrophobic pocket 141
4.11 – Discussion 144
4.12 – Materials and Methods 146
4.13 – References 151
CHAPTER 5 – HSP90 CO-CHAPERONE, FKBP51, REGULATES TAU STABILIZATION
5.1 – Abstract 155
5.2 – Introduction 155
5.3 – Hsp90 conformational states are prominent by Size Exclusion Chromatography 158
5.4 – Negative Stain EM analysis of Hsp90:FKBP51:AMPPNP 159
5.5 – Cryo-EM of Hsp90:FKBP51:AMPPNP 161
5.6 – p23 Stabilizes the Hsp90:FKBP51 complex 163
5.7 – Discussion 165
5.8 – Materials and Methods 166
5.9 – References 170
CHAPTER 6 – DISCUSSION AND FUTURE DIRECTIONS
6.1 Hsp104 Disaggregase 173
6.2 Hsp104 Future Directions 175
6.3 Get3 is a redox holdase 178
6.4 Get3 Future Directions 179
6.5 Hsp90:FKBP51 complex 181
6.6 Hsp90 Future Directions 182
6.7 References 183

LIST OF FIGURES

Figure 1-1. Protein folding pathway energy landscape 2
Figure 1-2. Chaperone protein network. 3
Figure 1-3. Hsp104 disaggregase function. 5
Figure 1-4. AAA+ machines are involved in many cellular processes. 6
Figure 1-5. Cryo-EM structures of Hsp104 and ClpB. 8
Figure 1-6. ClpB crystal structure colored by domain. 9
Figure 1-7. Hsp33 and Get3 conserved cysteines. 12
Figure 1-8. Get3 TA-binding protein membrane insertion. 13
Figure 1-9. Hsp90 hydrolysis and structural rearrangement cycle 16
Figure 1-10. Cryo-EM sample preparation and reconstruction workflow. 20
Figure 1-11. Setup of microscope lenses. 21
Figure 1-12. 2D images projected into a 3D model. 22
Figure 1-13. CCD vs. Direct Detectors DQE. 26
Figure 2-1. 2D Cryo-EM analysis of Hsp104:AMPPNP. 42
Figure 2-2. Resolution of Hsp104:AMPPNP Final Model and 2D verification. 43
Figure 2-3. Spiral architecture and three-tiered domain arrangement of the Hsp104:AMPPNP hexamer complex by cryo-EM. 45
Figure 2-4. Atomic model of Hsp104:AMPPNP. 47
Figure 2-5. Protomer arrangement of Hsp104. 48
Figure 2-6. Difference maps of nucleotide pockets. 49
Figure 2-7. Basis for protomer spiral and NBD1:NBD2 AAA+ interaction at the hexamer seam. 51
Figure 2-8. Conformational differences in the AAA+ domains of the individual protomers. 52
Figure 2-9. Expanded view of the model and amp showing the NBD1-NBD2 interaction from inside the channel. 53
Figure 2-10. Distinct arrangements of the NTD, MD, and CTD in the hexamer. 55
Figure 2-11. Density for CTD between protomers. 56
Figure 2-12. MD makes contact with neighboring NBD1. 57
Figure 2-13. Two-turn spiral arrangement of the substrate-binding Tyr pore loops around the channel. 59
Figure 3-1. Substrate-bound Hsp104:casein closed complex. 75
Figure 3-2. Forming a Stable Substrate-Bound Hsp104 Complex for Cryo-EM. 76
Figure 3-3. Analysis and cryo-EM processing of the Hsp104:casein complex. 77
Figure 3-4. 3D classification scheme for the Hsp104:casein dataset. 78
Figure 3-5. High-resolution of AAA+ domains and substrate. 79
Figure 3-6. Structural basis for substrate binding in the axial channel. 79
Figure 3-7. Tyrosine pore loops form a spiral of contacts around substrate. 81

Figure 3-8. High-resolution extended state shows different mobile protomer conformation. 83
Figure 3-9. Hsp104:casein extended-state conformation advances substrate contacts. 84
Figure 3-10. Conformational differences and pore-loop substrate contacts in the closed and extended states. 85
Figure 3-11. Arrangement of the nucleotide pockets in the closed and extended states. 86
Figure 3-12. Extended-state activation of the nucleotide pockets is coupled to translocation. 87
Figure 3-13. 2D and 3D analysis of Hsp104:ADP model. 89
Figure 3-14. Large rotation of MD coiled-coil with hydrolysis. 90
Figure 3-15. Mutations of MD-NBD1 salt bridges. 91
Figure 3-16. MD and NTD Classification of closed, casein bound data. 93
Figure 3-17. 3D Classification protocol for sorting closed and open particles. 94
Figure 3-18. Nucleotide-state and NBD function in the open-closed conformations and model for the disaggregation cycle. 95
Figure 3-19. Hsp104:ATP adopts the same open conformation as AMPPNP and ADP. 96
Figure 3-20. Mutant casein binding experiments. 97
Figure 3-21. Hsp104 translocation mechanism involves processive and non-processive modes. 98
Figure 3-22. Comparison of the channel in the open and closed state. 99
Figure 4-1. ROS-mediated activation of Get3 as ATP-independent chaperone. 117
Figure 4-2. Get3 functions as chaperone when oxidized. 118
Figure 4-3. Get3 chaperone activity with Cu^{2+}. 119
Figure 4-4. ATPase activity of $Get3_{ox}$ and $Get3_{red}$. 120
Figure 4-5. Oxidation of Get3 causes zinc release. 121
Figure 4-6. Activation of Get3's chaperone function is a fully reversible process. 123
Figure 4-7. Far-UV Circular Dichroism and ATPase activity of $Get3_{ox}$. 124
Figure 4-8. Chaperone-active $Get3_{ox}$ forms distinct oligomeric species. 125
Figure 4-9. SEC-MALS reveals $Get3_{ox}$ is a tetramer. 126
Figure 4-10. Negative-stain EM particles and 2D class averages of $Get3_{ox}$. 127
Figure 4-11. 2D and 3D negative stain EM analysis of $Get3_{ox}$ and $Get3_{red}$. 128
Figure 4-12. $Get3_{ox}$ 3D reconstruction scheme. 129
Figure 4-13. Final 3D model of the $Get3_{ox}$ tetramer, filtered to 19 Å. 130
Figure 4-14. 3D model of $Get3_{ox}$ tetramer with dimer crystal structure docked in. 130
Figure 4-15. Oxidative stress mediated disulfide bond formation and conformational rearrangements of Get3. 131
Figure 4-16. Get3 peptides and MS spectra. 132
Figure 4-17. Deuteration levels of $Get3_{ox}$ and $Get3_{red}$ peptides. 133
Figure 4-18. Get3 undergoes massive conformational rearrangements upon oxidation. 134
Figure 4-19. Get3I193D has chaperone activity independent of TA protein targeting. 136
Figure 4-20. Cell viability assays of WT and mutant Get3. 137
Figure 4-21. Localization of Sed5, TA-binding protein. 138
Figure 4-22. Get3 accumulates at deposition sites of mistargeted Sed5 under stress conditions. 140

Figure 4-23. SEC-MALS reveals 4:1 stoichiometry of Get3:luciferase. 142
Figure 4-24. Negative Stain EM of Get3:luciferase complex shows extra density in hydrophobic pocket. 143
Figure 4-25. Get3-Moonlighting as ATP-independent chaperone under oxidative stress conditions. 144
Figure 5-1. SEC-MALS of Hsp90 establishes elution shift from Open to Closed state. 158
Figure 5-2. Negative stain electron miscroscopy (EM) evaluation of Hsp90:AMPPNP and Hsp90:FKBPP51:AMPPNP. 160
Figure 5-3. Negative stain 3D EM model of Hsp90:FKBP51:AMPPPNP docked with Hsp90 and FKBP51. 161
Figure 5-4. Representative cryo-EM micrograph and single particles of Hsp90:FKBP51:AMPPNP complex. 162
Figure 5-5. Cryo-EM 2D reference-free class averages. 162
Figure 5-6. Hsp90:FKBP51:p23:AMPPNP can be purified by SEC. 164

LIST OF TABLES

Table 1. Data collection, processing and model parameters for all reconstructions and atomic models. 100
Table 2. Cross-correlation analysis and particle distributions for the open and closed hexamer states following 3D classification. 105

LIST OF ABBREVIATIONS

3D- Three dimensional
AAA+ - ATPases Associated with diverse cellular Activities
AD- Alzheimer's disease
ADP- adenosine diphosphate
AMPPNP- Adenylyl-imidodiphosphate
AR- androgen receptor
ATP- Adenosine triphosphate
CCD- Charged Coupled Device
Cdc37- cell division cycle control protein 37
CHIP- C-terminus of Hsc70 Interacting Protein
CTD- C-terminal domain
CTF- contrast transfer function
Cyp40- cyclophilin 40
DDD- Direct Electron Detector Devices
DQE- detective quantum efficiency
EM- electron microscopy
ER- Endoplasmic Reticulum
FEG- Field Emission Gun
FKBP- FK506-binding protein
FRET- Fluorescence Resonance Energy Transfer
FSC- Fourier Shell Correlation
GET- Guided entry of Tail anchored proteins
GR- glucocorticoid receptor
HOP- Hsp70-Hsp90 Orgranizing Protein
HSP- Heat Shock Protein
MD- Middle Domain
MT- microtubule
NBD- Nucleotide Binding Domain
NEF- Nucleotide Exchange Factor
NFTs- neurofibrillary tangles
NMR- nuclear magnetic resonance spectroscopy
NTD- N-terminal domain
PP5- protein phosphatase 5
PR- progesterone receptor
SAXS- small angle x-ray scattering

TA- tail-anchored proteins
TEM- Transmission electron microscope
TPR- tetratricopeptide repeat
UPS- Ubiquitin Proteasome System
VPP- Volta phase plate
ZPP- Zernike phase plate

ABSTRACT

Chaperone proteins are central to protein quality control and cell signaling. Three major classes of chaperones include foldases, holdases and disaggregases. Foldases aid proteins in folding to their native state, as well as prevent them from misfolding, a process that is regulated by ATP hydrolysis. Holdases are ATP-independent chaperones that respond to cellular stress, such as heat shock and oxidation, and protect proteins from aggregation. Disaggregases rescue aggregated proteins, resolubilize them and hand them off to foldases to be refolded. Together, these three classes of chaperones regulate many cellular processes and maintain proteostasis. In this study, three chaperones were characterized using electron microscopy: Hsp104 (disaggregase), Get3 (holdase), and FKBP51 (foldase).

Hsp104 is a double ring AAA+ protein that is active as a hexamer and is capable of pulling apart amorphous aggregates and amyloid fibrils. AAA+ proteins have conserved ATP hydrolysis pockets and conserved translocation mechanism to thread polymers through the central channel. Previous structural work of Hsp104 and other AAA+ proteins has been limited to low resolution due to the dynamic nature of the hexamer. In this study, we have determined three high-resolution structures of Hsp104. First, an open, asymmetric spiral conformation of Hsp104:AMPPNP to 5.6Å, which revealed a large hexamer seam with a unique hetero-AAA+ interaction between the Nucleotide Binding Domain (NBD) 1 and 2. Next we determined two structures of Hsp104 bound to substrate in the presence of ATPγS; the closed (4.0Å) and extended (4.1Å) states. The critical substrate binding tyrosine loops are arranged in a two-turn spiral around the substrate, showing direct interactions between the tyrosine and polypeptide

chain. The closed state has only five of six protomers engaged, whereas in the extended state all six protomers are engaged with a translocation step of 6-7Å between states. From our structures, we propose a processive rotary translocation mechanism between the closed and extended states, with a non-processive step from the open to closed states upon substrate binding. These structures give insight into the translocation of the highly conserved AAA+ class of proteins.

In another study, the holdase activity of Get3 was investigated. Get3 is important for ATP-dependent Tail Anchored-binding protein membrane insertion in yeast. We established that upon oxidative stress, Get3 undergoes a structural rearrangement from a reduced, ATP-dependent dimer, to an oxidized, ATP-independent tetramer with a general chaperone function. Using negative stain-EM we further characterized the Get3ox tetramer to determine that it has a 'W' shape, revealing a hydrophobic patch to bind substrates. Lastly, we studied the interaction between Hsp90 and its cochaperone, FKBP51, an immunophilin that is upregulated in cancer and Alzheimers disease. We determined that Hsp90 binds FKBP51 in its closed, ATP-bound state, a complex that is stabilized by another cochaperone, p23. Negative stain EM establishes the contacts between Hsp90 and FKBP51, which could be used as potential drug targets with improved specificity from Hsp90 inhibitors. We have determined the structures of three different chaperone classes, showing the very dynamic nature of molecular chaperones and elucidating functional mechanisms of these chaperones. Overall this thesis work has made advancements in all three areas studied, utilizing structure determination to correlate with function.

CHAPTER 1

INTRODUCTION

1.1 Protein folding and quality control is regulated by chaperone proteins

Protein folding and quality control is important for all cellular processes. Due to the high frequency of protein folding events that occur in the crowded cellular environment, a set of proteins, termed 'molecular chaperones', is essential for guiding proteins down the proper folding pathway to their low energy, native states (Fig. 1-1). In the central dogma of biology, DNA is transcribed to RNA, which is translated into a string of amino acids to form the polypeptide chain. The polypeptide chain folds into a native 3-dimensional (3D) conformation for proper function.

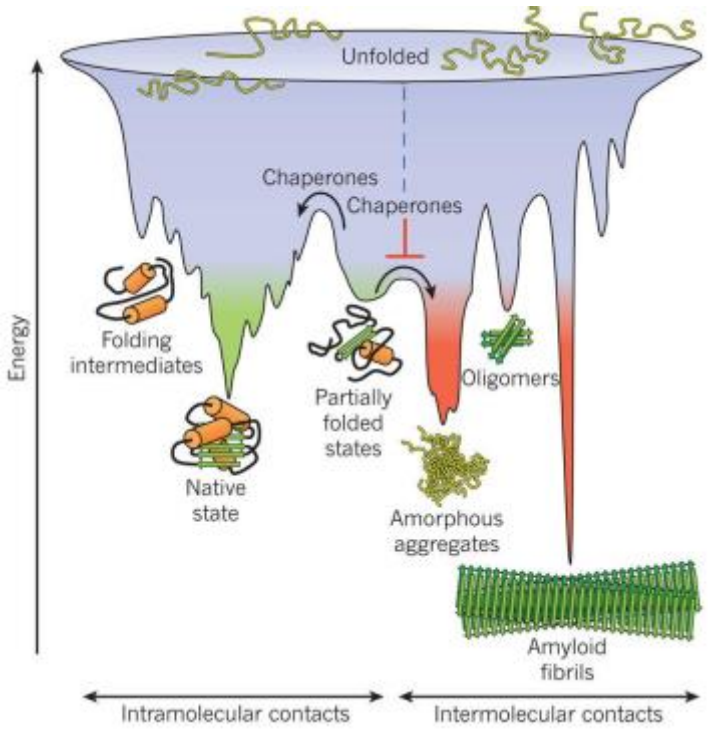

Figure 1-1. Protein folding pathway energy landscape (Hartl, Bracher, and Hayer-Hartl 2011). High energy unfolded polypeptide chains (yellow) fold into lower energy folding intermediates with the assistance of chaperones, resulting in the stable and folded Native state. Proteins can misfold into low energy toxic amorphous aggregates, oligomers and amyloid fibrils, therefore chaperones are necessary to prevent misfolding.

In the protein folding network, there are a wide range of chaperones for each step of the folding pathway (Fig. 1-2). General molecular chaperones, such as Heat Shock Proteins (Hsps) Hsp70 and Hsp90, bind to client proteins in non-native and intermediate structural states to aid in folding proteins into the native state as they cycle adenosine triphosphate (ATP) and conformational states (Fig. 1-2A,B) (Wegele, Müller, and Buchner 2004). Hsp70 binds nascent polypeptides in the early stages of the folding pathway whereas Hsp90 binds clients in later stages of folding to activate hormone receptors or other signaling proteins (Fig. 1-2A,B) (Pearl and Prodromou 2006). 'Foldases' are a class of chaperones that make direct structural modifications to proteins, such as isomerization of prolyl peptide bonds or formation and isomerization of disulfide bonds (Nagradova 2007). Chaperones and foldases work together to properly fold client proteins.

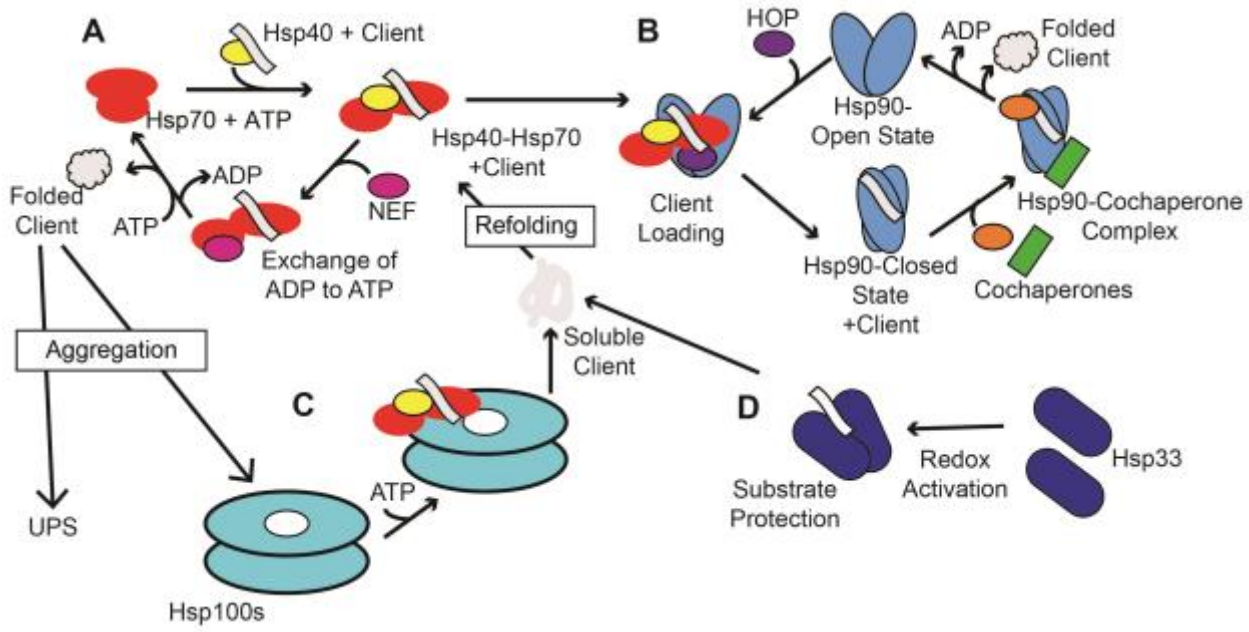

Figure 1-2. Chaperone protein network. The chaperone network involves the interplay between many classes of chaperones for proper folding and degradation of client proteins. (A) Hsp40 (yellow) delivers nascent polypeptides to Hsp70 (red). Nucleotide Exchange Factors (NEF, pink) allow Hsp70 to exchange adenosine diphosphate (ADP) to adenosine triphosphate (ATP), causing the conformational change of Hsp70 and release of the folded protein. (B) Hsp70 and Hsp40 hand client proteins to Hsp90 (light blue) with the assistance of Hsp70-Hsp90 Orgranizing Protein (HOP, purple). Hsp90 cycles between an Open State and Closed State with client binding, ATP hydrolysis, and association of Cochaperones (orange and green). When proteins aggregate, they are either targeted to the Ubiquitin Proteasome System (UPS) for degradation, or (C) Disaggregases such as the Hsp100 family (cyan) to be resolubilized and refolded by the Hsp70 system. (D) Under redox stress, Holdase chaperones, such as Hsp33, undergo conformational changes to bind and protect substrates. Following stress, these substrates are handed off to the Hsp70 system for refolding.

Under cellular stress conditions, such as heat shock or oxidation, many chaperones are upregulated and protect proteins from aggregation. Expression of a special class of chaperones is induced during cell stress, termed ‘holdases’, which undergo conformational changes to expose hydrophobic binding pockets to protect proteins from aggregation in an ATP-independent manner (Fig. 1-2D). Holdases often remain bound to substrates until cellular conditions improve, and the proteins can be handed off and refolded by the ATP-dependent foldases (Fig. 1-2D). Another class of chaperones termed ‘unfoldases’ or ‘disaggregases’, are essential to unfold and

resolubilize aggregates to alleviate any toxicity which may otherwise result (Fig. 1-2C). Often substrates resolubilized by disaggregases are handed off to foldases in order to return to their native folded state (Fig. 1-2C). Misregulation of these chaperone pathways is implicated in a variety of diseases, including neurodegenerative diseases and cancer. This thesis explores the structure and function of three classes of chaperones: Disaggregases (Hsp104), Holdases (Get3), Foldases (FKBP51).

1.2 Hsp104 yeast disaggregase

Hsp100 Chaperones

To maintain proteostasis, cells have a special set of chaperones, namely the Hsp100s, that can rescue aggregated proteins to alleviate cellular toxicity. Hsp100s collaborate with Hsp70 and Hsp40 for substrate recruitment, and are important for refolding substrates following disaggregation. Within the Hsp100 chaperones there are unfoldases and disaggregases (Doyle and Wickner 2009; Saibil 2013). *E. coli* ClpA and ClpX are unfoldases that associate with the ClpP protease for protein degradation, a process similar to proteasomal degradation (Hoskins et al. 2002). Importantly, ClpA and ClpX rely on the Hsp70/DnaK system for substrate recognition rather than the ubiquitin signaling marker used by the proteasome (Zavilgelsky et al. 2002). These unfoldases can have one or two highly conserved Nucleotide Binding Domains (NBDs), making them a part of the ATPases Associated with diverse cellular Activities (AAA+) protein class. These NBDs form a hexamer ring complex that associates with the ClpP protease to feed polypeptide chains into the proteolytic channel for degradation (Olivares et al. 2014).

Hsp100 disaggregases pull apart aggregates independent of a protease. This class of proteins includes *E. coli* ClpB and *S. cerevisiae* Hsp104, which share ~45% sequence identity and are thought to be structurally similar. Hsp104 and ClpB are considered type II AAA+

proteins because they contain two independently conserved AAA+ domains (Iyer et al. 2004). Hsp104 and ClpB are catalytically active as hexamers and translocate amorphous aggregates and amyloid fibers through their central channel, powered by ATP hydrolysis, to resolubilize the proteins (Fig. 1-3) (Olivares, Baker, and Sauer 2016; Sweeny and Shorter 2016). This process is highly regulated by Hsp70 and Hsp40, which are also implicated in refolding proteins following disaggregation (Glover and Lindquist 1998; Mogk, Kummer, and Bukau 2015). The mechanism of polypeptide unfolding has remained elusive, despite significant investigation into substrate recognition and hydrolysis. The lack of structural data of these protein complexes has limited our understanding of this mechanism.

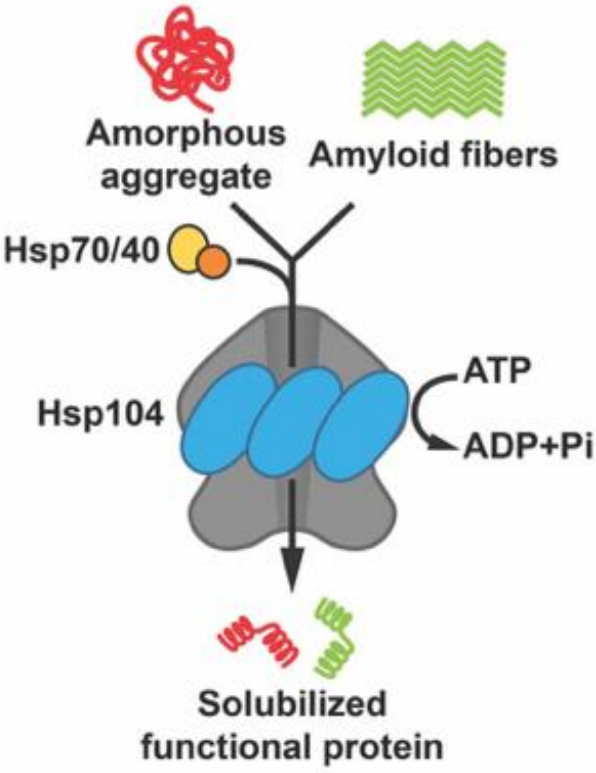

Figure 1-3. Hsp104 disaggregase function (Mack and Shorter 2016). Hsp70 and Hsp40 deliver amorphous aggregates and amyloid fibers to the Hsp104 hexamer. ATP hydrolysis drives polypeptide threading through the central channel, resolubilizing the protein to be refolded by Hsp70 and Hsp40.

AAA+ proteins have many functional roles

AAA+ proteins have very conserved NBDs and translocation functions, yet they are found across a wide variety of species and systems. For example, ClpXP is an Hsp100 chaperone involved in disaggregation, the proteasome is a protease involved in degradation, p97 is involved in disassembly and ER export, and MCM DNA helicase is important for separating DNA strands for other processes (Fig. 1-4) (Snider, Thibault, and Houry 2008). AAA+ proteins use the energy from ATP hydrolysis to translocate proteins or DNA through their central channel (Olivares, Baker, and Sauer 2016). Central to this translocation mechanism are the critical substrate-binding Tyr or Phe pore loops of the NBDs (Weibezahn et al. 2004; Lum et al. 2004; Tessarz, Mogk, and Bukau 2008). Mechanistic studies of these proteins have revealed a complex ATP hydrolysis cycle, therefore making structural determination of the intact hexamers very important.

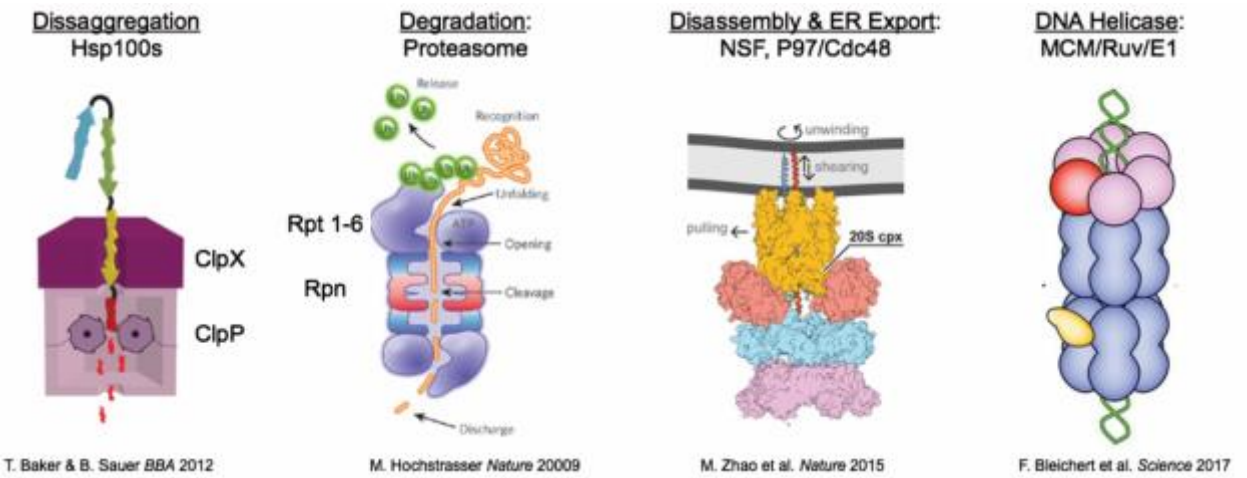

Figure 1-4. AAA+ machines are involved in many cellular processes . ClpXP is a member of the Hsp100 class of AAA+ unfoldases (Baker and Sauer 2012). The proteasome has a AAA+ ring (Rpt 1-6) to thread polypeptides through the protease (Hochstrasser 2009). NSF and p97/Cdc48 are AAA+ proteins involved in disassembly and Endoplasmic Reticulum (ER) export (Zhao et al, 2015). MCM/Ruv/E1 are DNA helicases with AAA+ domains that thread DNA through the central channel (Bleichert et al, 2017).

AAA+ proteins have conserved structure

The AAA+ domains have been well characterized by X-ray crystallography and NMR (Chang, Lee, and Tsai 2017; Erzberger and Berger 2006; Wendler et al. 2012). All AAA+ proteins have conserved ATP hydrolysis residues within the nucleotide binding domains (NBDs), with a Rossmann fold domain with a β-sheet and a C-terminal alpha helical domain making up the nucleotide pocket (Saffert, Enenkel, and Wendler 2017, 1). Each NBD contains residues associated with hydrolysis, including the Walker A and B, sensor-1 and sensor-2, as well as trans-Arginine finger that interacts directly with the γ-phosphate of ATP (Walker et al. 1982; Karata et al. 1999; Neuwald et al. 1999). Proper hexamer formation is critical for the trans Arg-finger position into the neighboring NBD. Models for ATPase activity vary within the field, with some support for a stochastic hydrolysis mechanism (Cordova et al. 2014; Shin et al. 2009; Olivares, Baker, and Sauer 2016) as well as some support for a highly coordinated firing of nucleotide pockets. There is also evidence that hydrolysis rates vary between AAA+ domains, because ClpX has only four active hydrolysis pockets, and the NBD1 of Hsp104 hydrolyzes faster than the NBD2 (Martin, Baker, and Sauer 2005; Hattendorf and Lindquist 2002). These differences may be important for the diverse functions of AAA+ proteins.

Hsp104 regulation of yeast homeostasis

In yeast, Hsp104 is critical for the protein stress response, whereas the deletion of Hsp104 reduces yeast survival rates and increases protein aggregation (cite). In both heat and oxidative stress Hsp104 is found to be critical for survival (Sanchez et al. 1992). Another important role of Hsp104 is prion propagation, which helps carry on non-genomic traits from mother to daughter cells during fission (Shorter and Lindquist 2006). Hsp104 fragments prions

into smaller species for efficient transfer to daughter cells. Although incredibly important in bacteria and yeast, Hsp104 is not conserved in higher eukaryotes.

Hsp104 structure

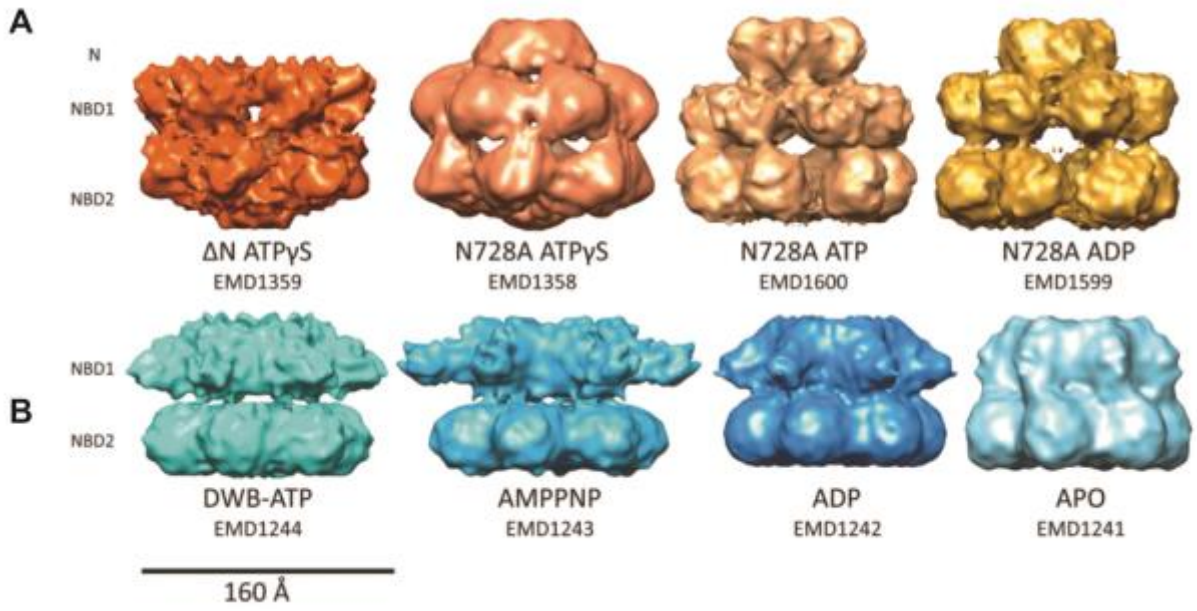

Figure 1-5. Cryo-EM structures of Hsp104 (A) and ClpB (B) (Wendler et al. 2007; S. Lee, Choi, and Tsai 2007). Previous cryo-EM structures of Hsp104 (A) and ClpB (B) demonstrate the three tier architecture, with the NTD, NBD1 and NBD2 making up the three tiers.

Structural information was lacking when we began this project, with no crystal structures of Hsp104, and only low-resolution electron microscopy (EM) reconstructions (Fig. 1-5). What we gain from these structures is the overall symmetric three-tiered structure of the hexamer (Fig 1-5). Due to the high sequence identity between Hsp104 and ClpB, the bacterial homolog, the ClpB crystal structure (pdb 1qvr)(S. Lee et al. 2003) provides great insight into the domain architecture of an Hsp104 monomer (Fig. 1-6). The NTD (pink) has been implicated in substrate binding and recognition (Rosenzweig et al. 2015; Doyle, Hoskins, and Wickner 2012). The two NBDs (blue) are the conserved AAA+ domains, important for ATP binding and hydrolysis. Inserted into the NBD1 (green) is the Middle Domain (MD), a coiled-coil important for Hsp70

binding and allosteric control of ATP hydrolysis (Kedzierska et al. 2003; Seyffer et al. 2012; J. Lee et al. 2013; Desantis et al. 2014). The CTD (orange) is important for hexamer formation, but is not found on ClpB (Mackay et al. 2008).

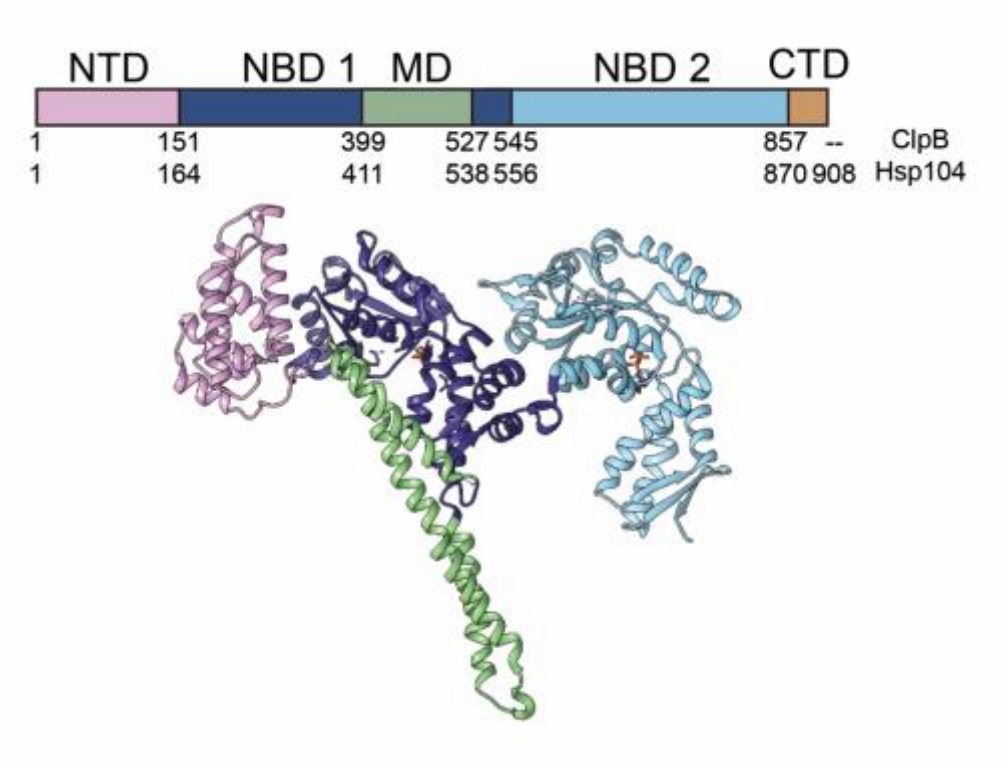

Figure 1-6. ClpB crystal structure colored by domain (S. Lee et al. 2003). N-terminal Domain (NTD) (pink), NBD1 (dark blue), NBD2 (light blue), Middle Domain (MD) (green), and C-terminal domain (CTD) (orange).

Hsp104 as a potential therapeutic

Work from the Linquist and Shorter labs has shown that potentiated variants of Hsp104 can resolubilize human disease amyloids, such as alpha-synuclein and FUS, in yeast model systems (Jackrel et al. 2014; Shorter and Lindquist 2006). This is an incredible attribute because these amyloids are found in the brains of neurodegenerative disease patients, and is an exciting avenue for potential protein therapeutics to combat neurodegenerative disease (Fatima et al. 2017). Mutational analysis of the regulatory MD has shown marked hyperactivation of the Hsp104, uncoupling disaggregase function from the canonical Hsp70/Hsp40 regulation system

(Jackrel et al. 2014). The Hsp104 MD structure is controversial, considering past structures were at too low a resolution to accurately localize this domain, making it difficult to understand the mechanism of potentiation through single point mutations (S. Lee et al. 2003; Wendler and Saibil 2010). Overall, structural analysis of the Hsp104 hexamer is needed to improve the possibility of Hsp104 as a protein therapeutic.

1.3 Get3 is a redox regulated holdase

The holdase class of chaperones are ATP-independent and include Hsp40/DnaJ (Rüdiger, Schneider-Mergener, and Bukau 2001), Hsp33 (Graf et al. 2004) and small heat shock proteins (sHsps) (G. J. Lee et al. 1997) that bind to unfolded substrates via hydrophobic interactions, but are unable to refold them to their native state (Rüdiger, Schneider-Mergener, and Bukau 2001; Haslbeck 2002; Linke et al. 2003; Hoffmann et al. 2004; Stromer et al. 2004). In most cases, holdases hand substrates off to foldases, such as Hsp70/DnaK, for refolding (G. J. Lee and Vierling 2000; Mogk, Schlieker, et al. 2003; Mogk, Deuerling, et al. 2003; Hoffmann et al. 2004). During cell stress holdases will remain bound to the unfolded substrate until proper folding conditions return (Hoffmann et al. 2004). It's been shown that holdases usually undergo structural rearrangements to attain high-affinity substrate binding conformations, a switch that is triggered by cell stress conditions. For example, Hsp33 is a redox triggered holdase, and sHsps can be triggered by heat stress (Winter and Jakob 2004).

Oxidative stress

Oxidative stress has been shown to be particularly harmful to cells, and is implicated in a variety of diseases, such as neurodegenerative diseases, cancer, and apoptosis (Chung et al. 2001; Kyselová et al. 2002; Ueda et al. 2002; Calabrese et al. 2003). Accumulation of reactive oxygen species (ROS) leads to damage to many cellular macromolecules, such as DNA,

membranes and proteins (Halliwell 1991). Oxidation can also lead to depletion of ATP, making the ATP-dependent heat shock response less effective in protecting cells. In order to rescue cells from the toxic effects of oxidative stress, it is important to have ATP-independent holdase chaperones that can protect proteins from aggregation until the cell can return to normal conditions.

Redox regulated chaperones, Hsp33

Hsp33 has been identified as a redox sensitive holdase chaperone that protects cells against oxidative stress (Jakob et al. 1999). Activation of Hsp33 holdase activity involves forming two intramolecular disulfide bonds, connecting Cys 232 with Cys 234 and Cys 265 with Cys 268 (Barbirz, Jakob, and Glocker 2000), releasing zinc and forming a dimer (Jakob et al. 1999; Graumann et al. 2001) (Fig. 1-7A). During this massive rearrangement following oxidation, the C-terminus redox switch domain loses its structure and unfolds (Graf et al. 2004). Unfolding the C-terminal domain exposes a hydrophobic substrate binding site, increasing exposure of hydrophobic surfaces for efficient substrate binding (Raman et al. 2001). Once activated by disulfide bond formation and zinc release, Hsp33 prevents oxidative stress mediated protein aggregation, thereby increasing bacterial oxidative stress resistance (Jakob et al. 1999).

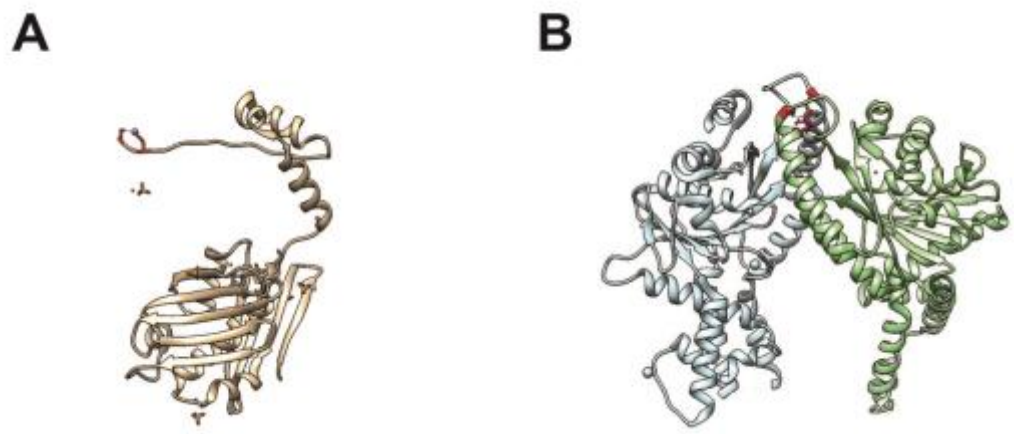

Figure 1-7. Hsp33 and Get3 conserved cysteines. (A) Hsp33 crystal structure, with Cys 232 and Cys 234 indicated in red, coordinating a zinc ion (Vijayalakshmi et al. 2001). (B) Get3 dimer crystal structure, with Cys 285 and Cys 288 indicated in red, coordinating a zinc ion (Hu et al. 2009).

Get3 TA-protein insertion function

Get3 is another chaperone that has highly conserved cysteines, reminiscent of the Hsp33 cysteines involved in disulfide bonds. As seen in the crystal structure, Get3 is a dimer, with the four conserved cysteines (C285/C288) arranged at the dimerization point, coordinating a zinc ion (Fig. 1-7B). Get3 is well characterized as a yeast ATPase central to the Guided Entry of Tail-anchored proteins (GET) pathway, which is required for proper insertion of tail-anchored proteins into the endoplasmic reticulum membrane (Favaloro et al. 2008; Schuldiner et al. 2008; Stefanovic and Hegde 2007). Cytosolic Get3 dimer undergoes significant conformational changes induced by substrate binding and ATP hydrolysis (Suloway, Rome, and Clemons 2012). Tail-anchored (TA) proteins are a class of transmembrane proteins that are inserted into the membrane post-translationally. Consequently, as TA proteins are translated a lot of hydrophobic residues are exposed in the cytosol which, if not properly inserted into the hydrophobic core of the lipid bilayer, could aggregate and be toxic to the cell (Denic, Dötsch, and Sinning 2013). The Get3 dimer binds ATP and the TA proteins following translation, causing the dimer

to transition into the closed state (Fig. 1-8). Get3 shuttles the TA proteins to the membrane by associating with Get1/2 membrane proteins and hydrolyzes ATP to release the protein for proper insertion (Fig 1-8) (Denic, Dötsch, and Sinning 2013).

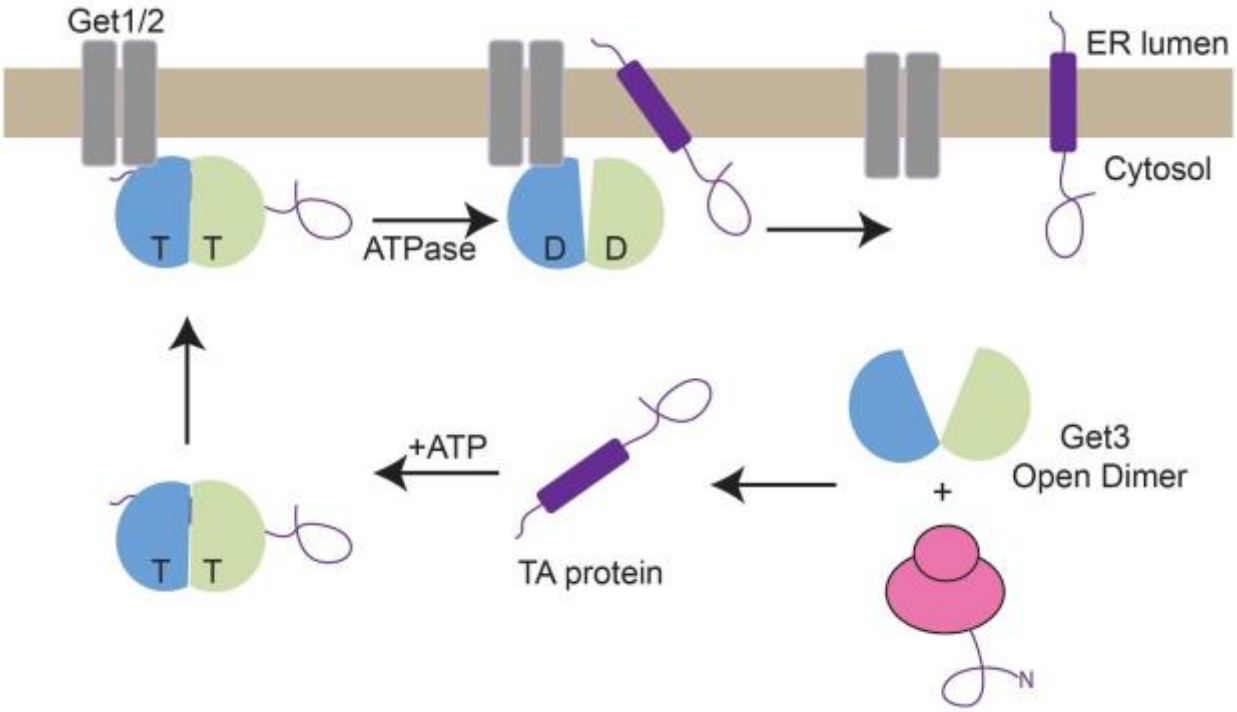

Figure 1-8. Get3 TA-binding protein membrane insertion. The Open Get3 Dimer (blue/green) binds to TA proteins (purple) and ATP (T) to transition into the Closed Get3 Dimer. Get3 shuttles the TA proteins to the membrane, associates with Get1/2 transmembrane proteins (grey) and hydrolyzes ATP the ADP (D) for TA protein release and membrane insertion.

Get3 as a potential holdase chaperone

Deletion of the GET3 gene in yeast displays a few phenotypes: copper, H_2O_2, heat sensitivity and the inability to grow on iron–limiting media (Schuldiner et al. 2008; Shen et al. 2003). These phenotypes suggest the Get3 may have another function other than just TA-protein insertion. Despite Get3 being structurally different from Hsp33 (Fig. 1-7), the conserved cysteines at the dimerization domain suggest that Get3 could have a similar redox control as Hsp33. It was discovered in the Jakob lab that upon oxidative stress, Get3 becomes an ATP-independent

general chaperone, no longer involved in membrane insertion (Powis et al. 2013). Because Hsp33 is known to undergo large structural rearrangements upon oxidation to expose hydrophobic residues, it is important to explore the potential conformational changes Get3 undergoes to activate its holdase chaperone function under oxidative stress conditions.

1.4 Hsp90 is a drug target for many diseases

Hsp90 is central to protein quality control, interacting directly with client substrates and promoting ATP hydrolysis-dependent folding. Additionally, Hsp90 is involved in coordinating protein 'triage' decisions that trigger ubiquitination and proteasome-directed degradation with other Heat Shock Protein (HSP) family members (Cook and Petrucelli 2013). Hsp90 clients include protein kinases and transcription factors, such as JAKs and p53, which are important for proper signal transduction in cells (Gronemeyer, Gustafsson, and Laudet 2004). Client binding is tightly regulated by other chaperones, termed co-chaperones, which facilitate proper client loading and refolding (Zuehlke and Johnson 2010).

Hsp90 Structural rearrangement in the hydrolysis cycle

Hsp90 is a homodimer comprised of three major domains: an N-terminal nucleotide binding domain (NTD), a middle domain (MD) important for client recognition and ATP hydrolysis, and the C-terminal dimerization domain (CTD). The CTD also contains the "MEEVD" sequence which binds the tetratricopeptide repeat (TPR) domains of co-chaperone proteins (Pearl and Prodromou 2006; Taipale, Jarosz, and Lindquist 2010; Young, Obermann, and Hartl 1998). Extensive structural studies of Hsp90 have revealed many different conformational states dependent on the hydrolysis and client binding cycle (Fig 1-9). The crystal structure of the nucleotide-free *E. coli* Hsp90, HtpG, demonstrates the open 'V' conformation with the NTDs rotated away from each other (Shiau et al. 2006) (Fig 1-9, state 1). By Small

Angle X-ray Scattering (SAXS) and cryo-EM, a more extended apo open state was also established (Bron et al. 2008; Krukenberg et al. 2008) (Fig. 1-9, state 1).

Upon ATP binding, as seen by SAXS with the non-hydrolyzable ATP analog, Adenylyl-imidodiphosphate (AMPPNP), we see the NTDs rotate toward each other in a left handed helical twist to form a secondary dimerization contact, establishing the closed state (Krukenberg et al. 2008) (Fig. 1-9, state 2). This conformation is also seen in the crystal structure of yeast Hsp82 bound to AMPPNP and p23 co-chaperone, with p23 bound between the NTDs (Ali et al. 2006) (Fig. 1-9, state 2b). The secondary NTD dimerization localizes the critical arginine of the MD in proximity to activate the nucleotide pocket, exposing the large hydrophobic region of the MD to bind clients. Also seen in the closed state is a rotation of the NTD lid that swings around to fold over the nucleotide binding site (Chadli et al. 2000; Prodromou et al. 2000). Following hydrolysis, Hsp90 assumes the adenosine diphosphate (ADP) compact dimer conformation, with a large buried surface area (Shiau et al. 2006; Southworth and Agard 2008) (Fig. 1-9, state 3). Using negative stain EM, the Agard lab confirmed that Hsp90 exists in the three states: extended apo (Fig. 1-9, state 1), closed ATP (Fig. 1-9, state 2) and compact ADP (Fig. 1-9, state 3), but the equilibrium of the states differs by species (Southworth and Agard 2008). Release of ADP allows Hsp90 to resume the apo conformation to begin the cycle again.

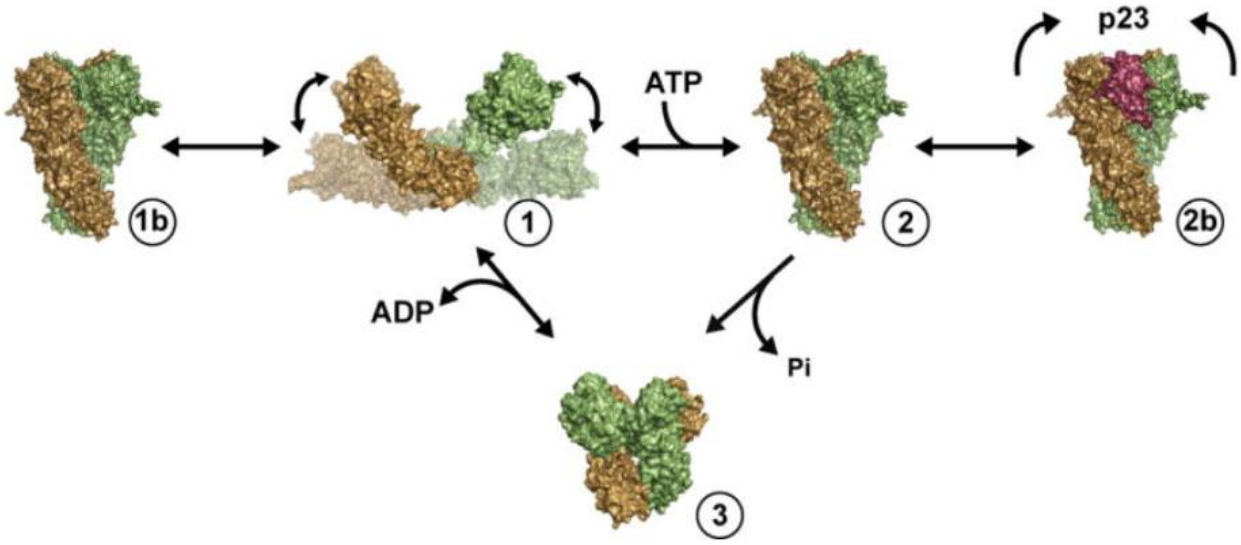

Figure 1-9. Hsp90 hydrolysis and structural rearrangement cycle (Southworth and Agard 2008). During ATP hydrolysis, the Hsp90 dimer cycles between three main states: extended apo (1), closed ATP bound (2), and compact ADP bound (3). It's also been identified that Hsp90 can exist in a closed apo (1b) and closed ATP bound with p23 at the NTD dimerization contact (2b).

The Hsp90 hydrolysis cycle is highly regulated by substrate binding and co-chaperone interactions (Csermely et al. 1993; Kirschke et al. 2014; Lavery et al. 2014). Co-chaperones, such as Hsp70/Hsp40 and Hsp70-Hsp90 Orgranizing Protein (HOP), assist with client loading. P23 acts as a hydrolysis regulator by slowing hydrolysis and stabilizing the closed, ATP-bound state (Ali et al. 2006). Other co-chaperones, such as TPR-domain proteins protein phosphatase 5 (PP5) and FK506 Binding Protein 51 (FKBP51), bind Hsp90 directly to alter client binding and hydrolysis. More structural studies of these co-chaperone interactions are important to better understand where co-chaperones fit into this hydrolysis cycle.

Hsp90 clients are implicated in many disease states

Hsp90 regulates many clients that control essential cellular processes, such as growth, differentiation, division, movement and death (Prodromou et al. 1999). Hsp90 clients include many oncogenic proteins, such as p53, Raf-1 and ErbB2, and its upregulation in cancer makes it a prime drug target (Workman 2004). Hsp90 protects mutated and misregulated oncogenic

proteins, preventing their degradation. Therefore, inhibition of Hsp90 ATP hydrolysis recruits ubiquitin ligases for proteasomal degradation of clients, and downregulation of the oncogenic client proteins (Harris, Shiau, and Agard 2004; Scheufler et al. 2000). Prominent Hsp90 inhibitors, geldanamycin and radicicol, have severe toxicity due to targeting Hsp90 in normal cells as well as cancerous cells(Roe et al. 1999; Sidera and Patsavoudi 2014; Jhaveri et al. 2012; Trendowski 2015).

An important Hsp90 client is tau, a protein that is highly expressed in neuronal axons that binds β-tubulin to promote microtubule (MT) polymerization and stability (Weingarten et al. 1975). Tau exists in an equilibrium between phosphorylated, cytosolic forms and dephosphorylated MT-bound states. Mutations and other covalent modifications are involved in tau hyperphosphorylation and misfolding, which induces oligomerization into filaments and neurofibrillary tangles (NFTs) (Grundke-Iqbal et al. 1986; Cao and Konsolaki 2011). The presence of filaments and NFTs are hallmarks of neurodegenerative tauopathies such as Alzheimer's disease (AD) and dementia. Inhibitors of Hsp90 increase C-terminus of Hsc70 Interacting Protein (CHIP) mediated ubiquitin ligase proteasomal degradation, decreasing levels of phosphorylated tau (Dickey et al. 2006, 2007). The Hsp90:tau structure was determined by SAXS and nuclear magnetic resonance spectroscopy (NMR), revealing Hsp90 in the open extended state, with the tau binding site mapped onto the NTD and MD, an interaction dependent on the conformational changes of Hsp90 associated with ATP hydrolysis (Karagöz et al. 2014). Addressing this direct interaction between Hsp90 and tau is a good therapueutic target for neurodegenerative diseases.

Hsp90 co-chaperones alter malignancy and neurodegeneration, making the Hsp90-cochaperone complexes good targets for drug design specifically to avoid cytotoxicity

(Workman et al. 2007; Moulick et al. 2011; Lindberg et al. 2015; Rodina et al. 2016; Yi and Regan 2008). Hsp90 co-chaperones include p23, cell division cycle control protein (Cdc37), FKBP51 and FKBP52 immunophilins, CHIP E3 ubiquitin ligase, PP5 phosphatase and cyclophilin 40 (Cyp40) (Allan and Ratajczak 2011). FKBP51 is an immunophilin containing three TPR domains, as well as FK1 and FK2 peptidyl-prolyl isomerase domains that promote client protein folding as well as bind the immunosuppressant FK506 (Craft and Sawyers 1998). FKBP51 expression increases with age and AD (Blair et al. 2013), and its regulation of Hsp90 tau-binding protects neurotoxic tau from degradation.

Hsp90 regulates many steroid hormone receptors, such as the glucocorticoid (GR), androgen (AR) and progesterone (PR) receptors, all of which act as ligand-regulated transcription factors to modulate transcription of target genes (Gronemeyer, Gustafsson, and Laudet 2004; Ratajczak, Cluning, and Ward 2015). Hsp90 minimally requires HOP, Hsp70, Hsp40 and p23 to bind the GR (Smith 2004; Smith and Toft 2008). The Hsp90:FKBP51 complex causes a decrease in GR hormone-binding by stabilizing an inactive GR conformation (Denny et al. 2000; Reynolds et al. 1999; Scammell et al. 2001). Conversely, FKBP51 facilitates hormone-binding competence of the AR in a Hsp90:FKBP51:p23:AR complex, increasing the AR transcriptional response (Ni et al. 2010). Higher expression levels of FKBP51 lead to high levels of the androgen-liganded receptor, which is implicated in prostate cancer (Periyasamy et al. 2010). This Hsp90 co-chaperone interaction is a great drug target specific to neurodegenerative diseases and receptor signaling diseases, making is an important structural target.

1.5 The importance of cryo-EM as a structural biology tool

Single particle electron microscopy

Electron microscopy (EM) is a structural biology technique used to determine structures of proteins and protein complexes. Single particle EM involves collecting 2D images of protein particles on carbon (negative stain) or in vitreous ice (cryo) in random orientations. Using computational methods, the individual particles are sorted into classes based on orientation parameters, and can be used to generate a 3D model. In recent years many technological advances, such as direct electron detectors and autoloaders, have revolutionized the capabilities of cryo-EM, allowing for high resolution structures (< 3Å) of a wide variety of protein complexes and sizes (Nogales and Scheres 2015). Electron microscopy is the main technique used in the studies discussed in this thesis, therefore this section is a brief overview of this technique.

Negative stain EM

There are two primary methods of EM: negative stain and cryo-EM. To prepare negative stain samples, protein is applied onto a carbon substrate over a copper support grid. The sample is dried and fixed in a heavy metal stain, such as uranyl formate (Ohi et al. 2004). Negative stain EM results in high contrast images because the background signal comes from the scattering of the heavy metal stain, while the protein signal is from the absence of stain. This leads to lower resolution reconstructions because the protein is indirectly imaged, additionally the resolution is limited to the dry stain granules (~15-20Å in size). Negative stain can also lead to flattening of the particles because samples are dehydrated during the staining process. Particles lying flat on the grid could also result in preferential orientation of particles, limiting the number of views and

subsequent 3D reconstructions efforts. Negative stain is a great technique for obtaining low resolution initial models and general domain architecture of difficult to study proteins.

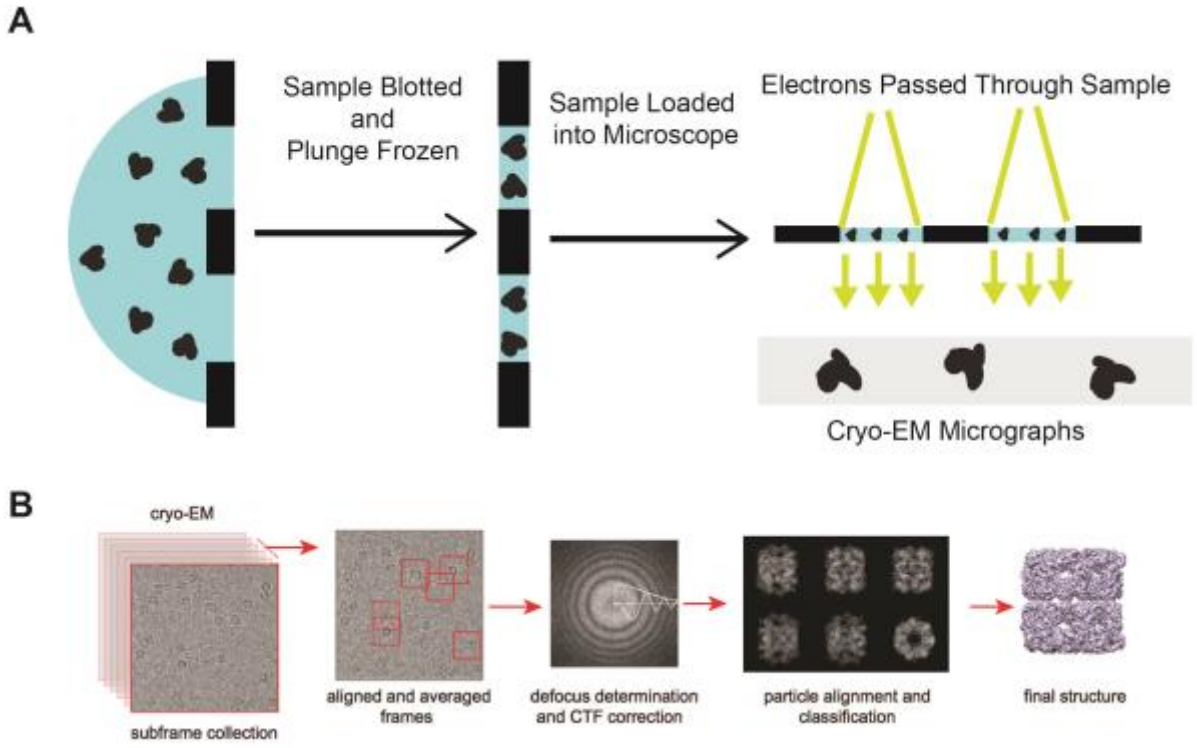

Figure 1-10. Cryo-EM sample preparation and reconstruction workflow. (A) Sample is applied to a holy carbon grid, so when it is blotted the particles are in a thin layer of buffer in each hole, and it is quickly plunged into liquid ethane. In the microscope, electrons are passed through this layer of ice to get an image of the particles**.** (B) Subframe images are collected, aligned, contrast transfer function (CTF) corrected, and particles are picked and aligned and classified in 2D and 3D (Carroni and Saibil 2016).

Cryo-EM

In cryo-EM, small amount of aqueous sample is applied to a holy carbon EM grid, excess sample is blotted away and the remaining sample is rapidly plunge-frozen in liquid ethane at temperatures near -180 degrees (Lepault, Booy, and Dubochet 1983) (Fig. 1-10A). Protein molecules are frozen in a thin layer of vitreous ice, the random 3D orientations are maintained in a hydrated state (Fig 1-10A). Cryo-EM samples are more susceptible to radiation damage than negative stain samples, and therefore must be imaged at lower electron doses (Stark, Zemlin, and

Boettcher 1996). Low dose conditions lead to lower contrast of the particles, therefore more particles are necessary to boost this signal-to-noise via particle averaging analysis. Cryo-EM has the potential for high resolution structure determination because protein is imaged directly.

Image acquisition

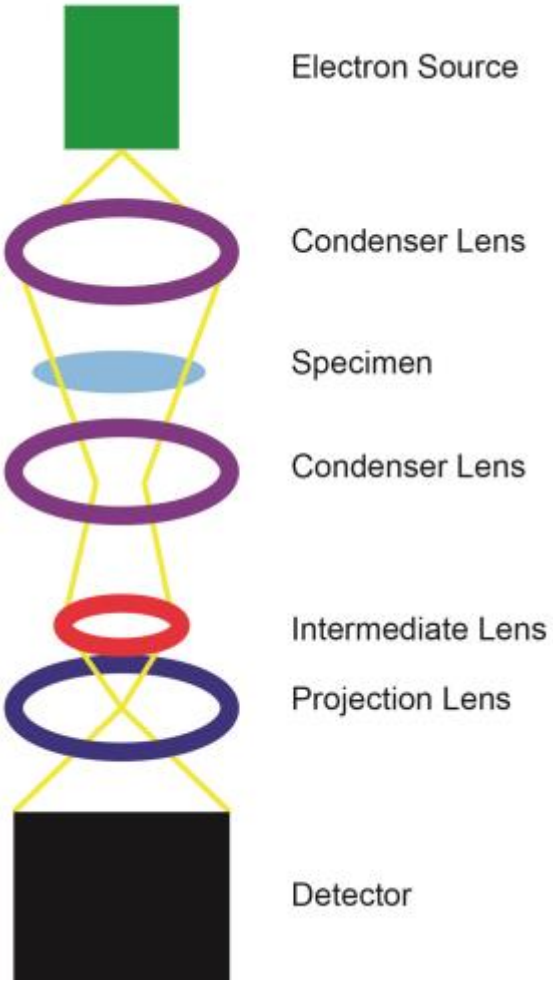

Figure 1-11. Setup of microscope lenses. In a transmission electron microscope, the electron beam (green) is projected through a series of lenses: condenser lens (purple), intermediate lens (red), and projection lens (blue). The sample specimen is located between the two consenser lenses. The final image of the electron scattering of the sample is collected by the detector (black).

Transmission electron microscopes (TEM) use Field Emission Guns (FEGs) as an electron source. FEGs are usually made out of tungsten or lanthanum hexaboride. The microscope relies on multiple electromagnetic lenses (Fig. 1-11). Electrons are first emitted

through the condenser lens to focus them onto the sample specimen, at which point they scatter depending on how they interact with the ice and the particles. Next, the electrons are sent through the objective lens, intermediate lens, and projector lens to form and magnify the image. Finally, the electrons are projected into the image chamber, where the signal is received by a detector (Frank 2006). Images can be recorded on film or Charged Coupled Device (CCD), but more recently Direct Electron Detector Devices (DDDs) were developed and result in higher resolution data. The advancement of this technology will be discussed more below.

The quality of images can be affected by a few types of lens aberrations: chromatic aberration, spherical aberration, and astigmatism (Frank 2006). Chromatic aberration can occur when electrons of differing energy are bent according to their energy level when they go through the objective lens. Spherical aberration occurs when electrons are deflected in differing rates depending on their proximity to the center of the specimen. Astigmatism occurs when the electromagnetic lenses don't have cylindrical symmetry. There are a variety of apertures and stigmators within the microscope that are important for proper alignment of the beam for data collection (Frank 2006). Having a parallel beam is important for high-quality data, and FEI has developed the Titan Krios, a 300kV Transmission Electron Microscope (TEM) equipped with an autoloader, with a third condenser lens that is meant to ensure that the beam remains parallel for ideal imaging conditions.

Single Particle Analysis

The images that are obtained from TEM will contain single particles which are distinct from the background signal. In order to get meaningful information out of these single particles, they are all individually selected and a stack of extracted particles is generated. This stack of particles is then submitted to reference free 2D classification in order to boost signal-to-noise by

aligning particles in the same orientation and averaging the information. In the reference free approach, projections of the experimental particles are used as the initial references and particles are sorted and aligned to them using cross correlation criteria. This occurs iteratively, generating new references with each round of classification to improve alignments (Ohi et al. 2004). Many different EM software packages do a good job of generating 2D reference free class averages, including Relion (Scheres 2012), Spider (Frank et al. 1996) and ISAC (Yang et al. 2012).

In 3D refinement, angular projection matching of particles against the initial model is used to assign Euler angles to single particles (Fig. 1-12). This process is also iterative, generating a new model each round based on the experimental data and improvement of angular assignment (Frank 2006). Refinement occurs with the data randomly split into half maps, and concludes when the two half maps converge into the final 3D model (Frank 2006; Scheres 2012). Resolution of the 3D map is determined as an average of all the local resolution, which can be variable depending on the flexibility of each domain. The Fourier Shell Correlation (FSC) is determined by the cross correlation of the two half maps in Fourier space at each spatial frequency, and the gold standard cutoff(0.143) is used to calculate final resolution (Penczek 2010).

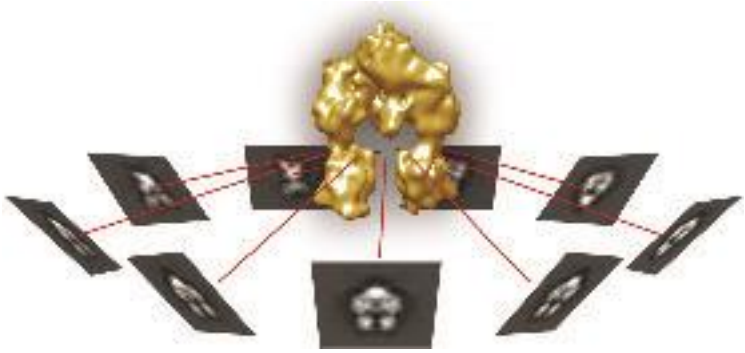

Figure 1-12. 2D images projected into a 3D model (Skiniotis and Southworth 2016). 2D particles are assigned orientation parameters, therefore the particles represent different views of the protein in 3D space.

3D classification programs increase sorting capability

In any EM particle dataset, there can be heterogeneity in conformation states, especially with highly dynamic protein complexes. In an effort to address this issue, many EM programs have established 3D classification protocols to effectively sort particles between conformational states. With the development of programs like Relion Class3D (Scheres 2012) and CryoSparc (Punjani et al. 2017), it is getting easier and faster to effectively sort particles into distinct classes of different conformations, and potentially solve more than one structure from a single dataset. This is incredibly beneficial, considering many proteins are dynamic and exist in multiple conformations *in vivo*. This will allow EM to provide more relevant structural information than was possible in the past.

The Resolution Revolution

Recent advances in EM technology, such as direct detectors and autoloaders, have allowed for a 'resolution revolution', allowing us to obtain high resolution structures of classically difficult to work with proteins. Before direct detectors were developed, EM images were collected either on film or with CCD cameras. CCDs receive the electron signal on a thin layer of phosphor scintillator that convert signals from electrons to photons to generate a representative image (Wu, Armache, and Cheng 2016). Although this is pretty effective for EM data acquisition, it results in lower resolution data because of data lost in the conversion. In the past five years, direct electron detectors were developed to address this problem.

Direct electron detectors devices can record micrographs by directly integrating charges generated by an incident electron on the camera sensor, rather than converting the electron signal to a light signal as in CCD cameras. This improvement produces a much smaller point-spread function (PSF), or the charge generated by a single electron event distribution region. Reducing

the PSF has vastly improved the Detective Quantum Efficiency (DQE), which is a measurement of the signal-to-noise performance as a function of spatial frequency (Fig. 1-13). This overall led to an increase in signal-to-noise, resulting in higher resolution data. Another advantage of DDDs is the high frame rate that enables the recording of cryo-EM data as dose-fractionated image stacks rather than a single image (Brilot et al. 2012). Drift correction software, such as Driftcorr, Motioncor, and Unblur, have been developed to align subframes, which addresses the issue of stage or beam-induced motion, recovering high-resolution signal that is distorted by that motion and overall improves image quality (Li et al. 2013; Bai et al. 2013; Campbell et al. 2012). Dose weighting can also be used to dampen the contribution of later frames in which radiation damage has accumulated, but still allowing for a higher total electron dose for early processing steps (Li et al. 2013; Grant and Grigorieff 2015). These advances boost signal-to-noise while excluding high-frequency noise caused by radiation damage. People often throw out the first few frames due to charging effects because the most movement occurs in the first few frames. With all of these advancements, we are able to get the higher resolution information out of our TEM images.

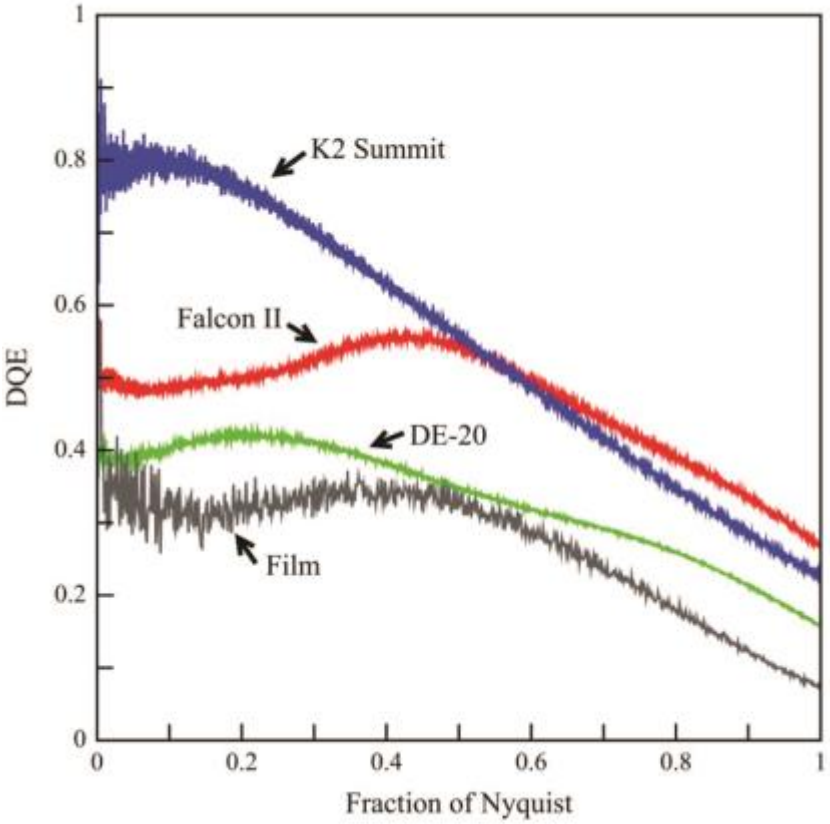

Figure 1-13. Direct Detectors have improved detective quantum efficiency (DQE) (McMullan et al. 2014). Measured DQE as a function of spatial frequency for the direct detectors DE-20 (green), Falcon II (red) and K2 Summit (blue). The corresponding DQE of photographic film from is shown in black.

Chaperones are good cryo-EM targets

Chaperone proteins are intrinsically dynamic, making them difficult structural targets for X-ray crystallography. With the development of effective 3D classification methods it has become much more attainable to study chaperone protein structure with EM (Verba et al. 2016). The technological advancements of the EM field have also presented opportunities to work on projects that have escaped the grasp of crystallography and NMR, due to sample size and heterogeneity. As the technology continues to advance, more of these challenging proteins are becoming possible to study, answering increasingly interesting scientific questions.

1.6 References

Ali, Maruf M. U., S. Mark Roe, Cara K. Vaughan, Phillipe Meyer, Barry Panaretou, Peter W. Piper, Chrisostomos Prodromou, and Laurence H. Pearl. 2006. "Crystal Structure of an Hsp90-Nucleotide-P23/Sba1 Closed Chaperone Complex." *Nature* 440 (7087): 1013–17. doi:10.1038/nature04716.

Allan, Rudi Kenneth, and Thomas Ratajczak. 2011. "Versatile TPR Domains Accommodate Different Modes of Target Protein Recognition and Function." *Cell Stress & Chaperones* 16 (4): 353–67. doi:10.1007/s12192-010-0248-0.

Bai, Xiao-Chen, Israel S. Fernandez, Greg McMullan, and Sjors H. W. Scheres. 2013. "Ribosome Structures to Near-Atomic Resolution from Thirty Thousand Cryo-EM Particles." *ELife* 2 (February): e00461. doi:10.7554/eLife.00461.

Baker, Tania A., and Robert T. Sauer. 2012. "ClpXP, an ATP-Powered Unfolding and Protein-Degradation Machine." *Biochimica Et Biophysica Acta* 1823 (1): 15–28. doi:10.1016/j.bbamcr.2011.06.007.

Barbirz, S., U. Jakob, and M. O. Glocker. 2000. "Mass Spectrometry Unravels Disulfide Bond Formation as the Mechanism That Activates a Molecular Chaperone." *The Journal of Biological Chemistry* 275 (25): 18759–66. doi:10.1074/jbc.M001089200.

Blair, Laura J., Bryce A. Nordhues, Shannon E. Hill, K. Matthew Scaglione, John C. O'Leary, Sarah N. Fontaine, Leonid Breydo, et al. 2013. "Accelerated Neurodegeneration through Chaperone-Mediated Oligomerization of Tau." *The Journal of Clinical Investigation* 123 (10): 4158–69. doi:10.1172/JCI69003.

Bleichert, Franziska, Michael R. Botchan, and James M. Berger. 2017. "Mechanisms for Initiating Cellular DNA Replication." *Science (New York, N.Y.)* 355 (6327). doi:10.1126/science.aah6317.

Brilot, Axel F., James Z. Chen, Anchi Cheng, Junhua Pan, Stephen C. Harrison, Clinton S. Potter, Bridget Carragher, Richard Henderson, and Nikolaus Grigorieff. 2012. "Beam-Induced Motion of Vitrified Specimen on Holey Carbon Film." *Journal of Structural Biology* 177 (3): 630–37. doi:10.1016/j.jsb.2012.02.003.

Bron, Patrick, Emmanuel Giudice, Jean-Paul Rolland, Rubén M. Buey, Pascale Barbier, J. Fernando Díaz, Vincent Peyrot, Daniel Thomas, and Cyrille Garnier. 2008. "Apo-Hsp90 Coexists in Two Open Conformational States in Solution." *Biology of the Cell* 100 (7): 413–25. doi:10.1042/BC20070149.

Calabrese, V., G. Scapagnini, C. Colombrita, A. Ravagna, G. Pennisi, A. M. Giuffrida Stella, F. Galli, and D. A. Butterfield. 2003. "Redox Regulation of Heat Shock Protein Expression in Aging and Neurodegenerative Disorders Associated with Oxidative Stress: A Nutritional Approach." *Amino Acids* 25 (3–4): 437–44. doi:10.1007/s00726-003-0048-2.

Campbell, Melody G., Anchi Cheng, Axel F. Brilot, Arne Moeller, Dmitry Lyumkis, David Veesler, Junhua Pan, et al. 2012. "Movies of Ice-Embedded Particles Enhance Resolution in Electron Cryo-Microscopy." *Structure (London, England: 1993)* 20 (11): 1823–28. doi:10.1016/j.str.2012.08.026.

Cao, Weihuan, and Mary Konsolaki. 2011. "FKBP Immunophilins and Alzheimer's Disease: A Chaperoned Affair." *Journal of Biosciences* 36 (3): 493–98.

Carroni, Marta, and Helen R. Saibil. 2016. "Cryo Electron Microscopy to Determine the Structure of Macromolecular Complexes." *Methods (San Diego, Calif.)* 95 (February): 78–85. doi:10.1016/j.ymeth.2015.11.023.

Chadli, A., I. Bouhouche, W. Sullivan, B. Stensgard, N. McMahon, M. G. Catelli, and D. O. Toft. 2000. "Dimerization and N-Terminal Domain Proximity Underlie the Function of the Molecular Chaperone Heat Shock Protein 90." *Proceedings of the National Academy of Sciences of the United States of America* 97 (23): 12524–29. doi:10.1073/pnas.220430297.

Chang, Chiung-Wen, Sukyeong Lee, and Francis T. F. Tsai. 2017. "Structural Elements Regulating AAA+ Protein Quality Control Machines." *Frontiers in Molecular Biosciences* 4 (May). doi:10.3389/fmolb.2017.00027.

Chung, H. Y., H. J. Kim, J. W. Kim, and B. P. Yu. 2001. "The Inflammation Hypothesis of Aging: Molecular Modulation by Calorie Restriction." *Annals of the New York Academy of Sciences* 928 (April): 327–35.

Cook, Casey, and Leonard Petrucelli. 2013. "Tau Triage Decisions Mediated by the Chaperone Network." *Journal of Alzheimer's Disease: JAD* 33 Suppl 1: S145-151. doi:10.3233/JAD-2012-129008.

Cordova, Juan Carlos, Adrian O. Olivares, Yongdae Shin, Benjamin M. Stinson, Stephane Calmat, Karl R. Schmitz, Marie-Eve Aubin-Tam, Tania A. Baker, Matthew J. Lang, and Robert T. Sauer. 2014. "Stochastic but Highly Coordinated Protein Unfolding and Translocation by the ClpXP Proteolytic Machine." *Cell* 158 (3): 647–58. doi:10.1016/j.cell.2014.05.043.

Craft, N., and C. L. Sawyers. 1998. "Mechanistic Concepts in Androgen-Dependence of Prostate Cancer." *Cancer Metastasis Reviews* 17 (4): 421–27.

Csermely, P., J. Kajtár, M. Hollósi, G. Jalsovszky, S. Holly, C. R. Kahn, P. Gergely, C. Söti, K. Mihály, and J. Somogyi. 1993. "ATP Induces a Conformational Change of the 90-KDa Heat Shock Protein (Hsp90)." *The Journal of Biological Chemistry* 268 (3): 1901–7.

Denic, Vladimir, Volker Dötsch, and Irmgard Sinning. 2013. "Endoplasmic Reticulum Targeting and Insertion of Tail-Anchored Membrane Proteins by the GET Pathway." *Cold Spring Harbor Perspectives in Biology* 5 (8): a013334. doi:10.1101/cshperspect.a013334.

Denny, W. B., D. L. Valentine, P. D. Reynolds, D. F. Smith, and J. G. Scammell. 2000. "Squirrel Monkey Immunophilin FKBP51 Is a Potent Inhibitor of Glucocorticoid Receptor Binding." *Endocrinology* 141 (11): 4107–13. doi:10.1210/endo.141.11.7785.

Desantis, Morgan E., Elizabeth A. Sweeny, David Snead, Eunice H. Leung, Michelle S. Go, Kushol Gupta, Petra Wendler, and James Shorter. 2014. "Conserved Distal Loop Residues in the Hsp104 and ClpB Middle Domain Contact Nucleotide-Binding Domain 2 and Enable Hsp70-Dependent Protein Disaggregation." *The Journal of Biological Chemistry* 289 (2): 848–67. doi:10.1074/jbc.M113.520759.

Dickey, Chad A., Judith Dunmore, Bingwei Lu, Ji-Wu Wang, Wing C. Lee, Adeela Kamal, Francis Burrows, Christopher Eckman, Michael Hutton, and Leonard Petrucelli. 2006. "HSP Induction Mediates Selective Clearance of Tau Phosphorylated at Proline-Directed Ser/Thr Sites but Not KXGS (MARK) Sites." *FASEB Journal: Official Publication of the Federation of American Societies for Experimental Biology* 20 (6): 753–55. doi:10.1096/fj.05-5343fje.

Dickey, Chad A., Adeela Kamal, Karen Lundgren, Natalia Klosak, Rachel M. Bailey, Judith Dunmore, Peter Ash, et al. 2007. "The High-Affinity HSP90-CHIP Complex Recognizes and Selectively Degrades Phosphorylated Tau Client Proteins." *The Journal of Clinical Investigation* 117 (3): 648–58. doi:10.1172/JCI29715.

Doyle, Shannon M., Joel R. Hoskins, and Sue Wickner. 2012. "DnaK Chaperone-Dependent Disaggregation by Caseinolytic Peptidase B (ClpB) Mutants Reveals Functional Overlap in the N-Terminal Domain and Nucleotide-Binding Domain-1 Pore Tyrosine." *The Journal of Biological Chemistry* 287 (34): 28470–79. doi:10.1074/jbc.M112.383091.

Doyle, Shannon M., and Sue Wickner. 2009. "Hsp104 and ClpB: Protein Disaggregating Machines." *Trends in Biochemical Sciences* 34 (1): 40–48. doi:10.1016/j.tibs.2008.09.010.

Erzberger, Jan P., and James M. Berger. 2006. "Evolutionary Relationships and Structural Mechanisms of AAA+ Proteins." *Annual Review of Biophysics and Biomolecular Structure* 35: 93–114. doi:10.1146/annurev.biophys.35.040405.101933.

Fatima, Munazza Tamkeen, Zeyaul Islam, Ejaj Ahmad, and Parveen Salahuddin. 2017. "Emerging Targets and Latest Proteomics Based Therapeutic Approaches in Neurodegenerative Diseases." *Current Protein & Peptide Science*, July. doi:10.2174/1389203718666170731114757.

Favaloro, Vincenzo, Milan Spasic, Blanche Schwappach, and Bernhard Dobberstein. 2008. "Distinct Targeting Pathways for the Membrane Insertion of Tail-Anchored (TA) Proteins." *Journal of Cell Science* 121 (11): 1832–40. doi:10.1242/jcs.020321.

Frank, Joachim. 2006. *Three-Dimensional Electron Microscopy of Macromolecular Assemblies: Visualization of Biological Molecules in Their Native State*. Oxford University Press.

Glover, J. R., and S. Lindquist. 1998. "Hsp104, Hsp70, and Hsp40: A Novel Chaperone System That Rescues Previously Aggregated Proteins." *Cell* 94 (1): 73–82.

Graf, Paul C. F., Maria Martinez-Yamout, Stephen VanHaerents, Hauke Lilie, H. Jane Dyson, and Ursula Jakob. 2004. "Activation of the Redox-Regulated Chaperone Hsp33 by Domain Unfolding." *The Journal of Biological Chemistry* 279 (19): 20529–38. doi:10.1074/jbc.M401764200.

Grant, Timothy, and Nikolaus Grigorieff. 2015. "Measuring the Optimal Exposure for Single Particle Cryo-EM Using a 2.6 Å Reconstruction of Rotavirus VP6." *ELife* 4 (May): e06980. doi:10.7554/eLife.06980.

Graumann, J., H. Lilie, X. Tang, K. A. Tucker, J. H. Hoffmann, J. Vijayalakshmi, M. Saper, J. C. Bardwell, and U. Jakob. 2001. "Activation of the Redox-Regulated Molecular Chaperone Hsp33--a Two-Step Mechanism." *Structure (London, England: 1993)* 9 (5): 377–87.

Gronemeyer, Hinrich, Jan-Ake Gustafsson, and Vincent Laudet. 2004. "Principles for Modulation of the Nuclear Receptor Superfamily." *Nature Reviews. Drug Discovery* 3 (11): 950–64. doi:10.1038/nrd1551.

Grundke-Iqbal, I., K. Iqbal, M. Quinlan, Y. C. Tung, M. S. Zaidi, and H. M. Wisniewski. 1986. "Microtubule-Associated Protein Tau. A Component of Alzheimer Paired Helical Filaments." *The Journal of Biological Chemistry* 261 (13): 6084–89.

Halliwell, Barry. 1991. "Reactive Oxygen Species in Living Systems: Source, Biochemistry, and Role in Human Disease." *The American Journal of Medicine* 91 (3): S14–22. doi:10.1016/0002-9343(91)90279-7.

Harris, Seth F., Andrew K. Shiau, and David A. Agard. 2004. "The Crystal Structure of the Carboxy-Terminal Dimerization Domain of HtpG, the Escherichia Coli Hsp90, Reveals a Potential Substrate Binding Site." *Structure (London, England: 1993)* 12 (6): 1087–97. doi:10.1016/j.str.2004.03.020.

Hartl, F. Ulrich, Andreas Bracher, and Manajit Hayer-Hartl. 2011. "Molecular Chaperones in Protein Folding and Proteostasis." *Nature* 475 (7356): 324–32. doi:10.1038/nature10317.

Haslbeck, M. 2002. “SHsps and Their Role in the Chaperone Network.” *Cellular and Molecular Life Sciences: CMLS* 59 (10): 1649–57.
Hattendorf, Douglas A., and Susan L. Lindquist. 2002. “Cooperative Kinetics of Both Hsp104 ATPase Domains and Interdomain Communication Revealed by AAA Sensor-1 Mutants.” *The EMBO Journal* 21 (1–2): 12–21. doi:10.1093/emboj/21.1.12.
Hochstrasser, Mark. 2009. “Origin and Function of Ubiquitin-like Proteins.” *Nature* 458 (7237): 422–29. doi:10.1038/nature07958.
Hoffmann, Jörg H., Katrin Linke, Paul C. F. Graf, Hauke Lilie, and Ursula Jakob. 2004. “Identification of a Redox-Regulated Chaperone Network.” *The EMBO Journal* 23 (1): 160–68. doi:10.1038/sj.emboj.7600016.
Hoskins, Joel R., Katsuhiko Yanagihara, Kiyoshi Mizuuchi, and Sue Wickner. 2002. “ClpAP and ClpXP Degrade Proteins with Tags Located in the Interior of the Primary Sequence.” *Proceedings of the National Academy of Sciences of the United States of America* 99 (17): 11037–42. doi:10.1073/pnas.172378899.
Hu, Junbin, Jingzhi Li, Xinguo Qian, Vlad Denic, and Bingdong Sha. 2009. “The Crystal Structures of Yeast Get3 Suggest a Mechanism for Tail-Anchored Protein Membrane Insertion.” *PloS One* 4 (11): e8061. doi:10.1371/journal.pone.0008061.
Iyer, Lakshminarayan M., Detlef D. Leipe, Eugene V. Koonin, and L. Aravind. 2004. “Evolutionary History and Higher Order Classification of AAA+ ATPases.” *Journal of Structural Biology* 146 (1–2): 11–31. doi:10.1016/j.jsb.2003.10.010.
Jackrel, Meredith E., Morgan E. DeSantis, Bryan A. Martinez, Laura M. Castellano, Rachel M. Stewart, Kim A. Caldwell, Guy A. Caldwell, and James Shorter. 2014. “Potentiated Hsp104 Variants Antagonize Diverse Proteotoxic Misfolding Events.” *Cell* 156 (1–2): 170–82. doi:10.1016/j.cell.2013.11.047.
Jakob, U., W. Muse, M. Eser, and J. C. Bardwell. 1999. “Chaperone Activity with a Redox Switch.” *Cell* 96 (3): 341–52.
Jhaveri, Komal, Tony Taldone, Shanu Modi, and Gabriela Chiosis. 2012. “Advances in the Clinical Development of Heat Shock Protein 90 (Hsp90) Inhibitors in Cancers.” *Biochimica Et Biophysica Acta* 1823 (3): 742–55. doi:10.1016/j.bbamcr.2011.10.008.
Karagöz, G. Elif, Afonso M. S. Duarte, Elias Akoury, Hans Ippel, Jacek Biernat, Tania Morán Luengo, Martina Radli, et al. 2014. “Hsp90-Tau Complex Reveals Molecular Basis for Specificity in Chaperone Action.” *Cell* 156 (5): 963–74. doi:10.1016/j.cell.2014.01.037.
Karata, K., T. Inagawa, A. J. Wilkinson, T. Tatsuta, and T. Ogura. 1999. “Dissecting the Role of a Conserved Motif (the Second Region of Homology) in the AAA Family of ATPases. Site-Directed Mutagenesis of the ATP-Dependent Protease FtsH.” *The Journal of Biological Chemistry* 274 (37): 26225–32.
Kedzierska, Sabina, Vladimir Akoev, Micheal E. Barnett, and Michal Zolkiewski. 2003. “Structure and Function of the Middle Domain of ClpB from Escherichia Coli.” *Biochemistry* 42 (48): 14242–48. doi:10.1021/bi035573d.
Kirschke, Elaine, Devrishi Goswami, Daniel Southworth, Patrick R. Griffin, and David A. Agard. 2014. “Glucocorticoid Receptor Function Regulated by Coordinated Action of the Hsp90 and Hsp70 Chaperone Cycles.” *Cell* 157 (7): 1685–97. doi:10.1016/j.cell.2014.04.038.
Krukenberg, K.A., F. Förster, L.M. Rice, A. Sali, and D.A. Agard. 2008. “A Novel Conformation of E. Coli Hsp90 in Solution: Insights into the Conformational Dynamics

of Hsp90." *Structure (London, England : 1993)* 16 (5): 755–65. doi:10.1016/j.str.2008.01.021.
Kyselová, P., M. Zourek, Z. Rusavý, L. Trefil, and J. Racek. 2002. "Hyperinsulinemia and Oxidative Stress." *Physiological Research* 51 (6): 591–95.
Lavery, Laura A., James R. Partridge, Theresa A. Ramelot, Daniel Elnatan, Michael A. Kennedy, and David A. Agard. 2014. "Structural Asymmetry in the Closed State of Mitochondrial Hsp90 (TRAP1) Supports a Two-Step ATP Hydrolysis Mechanism." *Molecular Cell* 53 (2): 330–43. doi:10.1016/j.molcel.2013.12.023.
Lee, G. J., A. M. Roseman, H. R. Saibil, and E. Vierling. 1997. "A Small Heat Shock Protein Stably Binds Heat-Denatured Model Substrates and Can Maintain a Substrate in a Folding-Competent State." *The EMBO Journal* 16 (3): 659–71. doi:10.1093/emboj/16.3.659.
Lee, G. J., and E. Vierling. 2000. "A Small Heat Shock Protein Cooperates with Heat Shock Protein 70 Systems to Reactivate a Heat-Denatured Protein." *Plant Physiology* 122 (1): 189–98.
Lee, Jungsoon, Ji-Hyun Kim, Amadeo B. Biter, Bernhard Sielaff, Sukyeong Lee, and Francis T. F. Tsai. 2013. "Heat Shock Protein (Hsp) 70 Is an Activator of the Hsp104 Motor." *Proceedings of the National Academy of Sciences of the United States of America* 110 (21): 8513–18. doi:10.1073/pnas.1217988110.
Lee, Sukyeong, Jae-Mun Choi, and Francis T. F. Tsai. 2007. "Visualizing the ATPase Cycle in a Protein Disaggregating Machine: Structural Basis for Substrate Binding by ClpB." *Molecular Cell* 25 (2): 261–71. doi:10.1016/j.molcel.2007.01.002.
Lee, Sukyeong, Mathew E. Sowa, Yo-hei Watanabe, Paul B. Sigler, Wah Chiu, Masasuke Yoshida, and Francis T. F. Tsai. 2003. "The Structure of ClpB: A Molecular Chaperone That Rescues Proteins from an Aggregated State." *Cell* 115 (2): 229–40.
Lepault, J., F. P. Booy, and J. Dubochet. 1983. "Electron Microscopy of Frozen Biological Suspensions." *Journal of Microscopy* 129 (Pt 1): 89–102.
Li, Xueming, Paul Mooney, Shawn Zheng, Christopher R. Booth, Michael B. Braunfeld, Sander Gubbens, David A. Agard, and Yifan Cheng. 2013. "Electron Counting and Beam-Induced Motion Correction Enable near-Atomic-Resolution Single-Particle Cryo-EM." *Nature Methods* 10 (6): 584–90. doi:10.1038/nmeth.2472.
Lindberg, Iris, James Shorter, R. Luke Wiseman, Fabrizio Chiti, Chad A. Dickey, and Pamela J. McLean. 2015. "Chaperones in Neurodegeneration." *The Journal of Neuroscience: The Official Journal of the Society for Neuroscience* 35 (41): 13853–59. doi:10.1523/JNEUROSCI.2600-15.2015.
Linke, Katrin, Tobias Wolfram, Johanna Bussemer, and Ursula Jakob. 2003. "The Roles of the Two Zinc Binding Sites in DnaJ." *The Journal of Biological Chemistry* 278 (45): 44457–66. doi:10.1074/jbc.M307491200.
Lum, Ronnie, Johnny M. Tkach, Elizabeth Vierling, and John R. Glover. 2004. "Evidence for an Unfolding/Threading Mechanism for Protein Disaggregation by Saccharomyces Cerevisiae Hsp104." *The Journal of Biological Chemistry* 279 (28): 29139–46. doi:10.1074/jbc.M403777200.
Mack, Korrie L., and James Shorter. 2016. "Engineering and Evolution of Molecular Chaperones and Protein Disaggregases with Enhanced Activity." *Frontiers in Molecular Biosciences* 3 (March). doi:10.3389/fmolb.2016.00008.

Mackay, Ryder G., Christopher W. Helsen, Johnny M. Tkach, and John R. Glover. 2008. "The C-Terminal Extension of Saccharomyces Cerevisiae Hsp104 Plays a Role in Oligomer Assembly." *Biochemistry* 47 (7): 1918–27. doi:10.1021/bi701714s.

Martin, Andreas, Tania A. Baker, and Robert T. Sauer. 2005. "Rebuilt AAA + Motors Reveal Operating Principles for ATP-Fuelled Machines." *Nature* 437 (7062): 1115–20. doi:10.1038/nature04031.

McMullan, G., A. R. Faruqi, D. Clare, and R. Henderson. 2014. "Comparison of Optimal Performance at 300keV of Three Direct Electron Detectors for Use in Low Dose Electron Microscopy." *Ultramicroscopy* 147 (December): 156–63. doi:10.1016/j.ultramic.2014.08.002.

Mogk, Axel, Elke Deuerling, Sonja Vorderwülbecke, Elizabeth Vierling, and Bernd Bukau. 2003. "Small Heat Shock Proteins, ClpB and the DnaK System Form a Functional Triade in Reversing Protein Aggregation." *Molecular Microbiology* 50 (2): 585–95.

Mogk, Axel, Eva Kummer, and Bernd Bukau. 2015. "Cooperation of Hsp70 and Hsp100 Chaperone Machines in Protein Disaggregation." *Frontiers in Molecular Biosciences* 2: 22. doi:10.3389/fmolb.2015.00022.

Mogk, Axel, Christian Schlieker, Kenneth L. Friedrich, Hans-Joachim Schönfeld, Elizabeth Vierling, and Bernd Bukau. 2003. "Refolding of Substrates Bound to Small Hsps Relies on a Disaggregation Reaction Mediated Most Efficiently by ClpB/DnaK." *The Journal of Biological Chemistry* 278 (33): 31033–42. doi:10.1074/jbc.M303587200.

Moulick, Kamalika, James H. Ahn, Hongliang Zong, Anna Rodina, Leandro Cerchietti, Erica M. Gomes DaGama, Eloisi Caldas-Lopes, et al. 2011. "Affinity-Based Proteomics Reveal Cancer-Specific Networks Coordinated by Hsp90." *Nature Chemical Biology* 7 (11): 818–26. doi:10.1038/nchembio.670.

Nagradova, Natalya. 2007. "Enzymes Catalyzing Protein Folding and Their Cellular Functions." *Current Protein & Peptide Science* 8 (3): 273–82.

Neuwald, A. F., L. Aravind, J. L. Spouge, and E. V. Koonin. 1999. "AAA+: A Class of Chaperone-like ATPases Associated with the Assembly, Operation, and Disassembly of Protein Complexes." *Genome Research* 9 (1): 27–43.

Ni, Li, Chun-Song Yang, Daniel Gioeli, Henry Frierson, David O. Toft, and Bryce M. Paschal. 2010. "FKBP51 Promotes Assembly of the Hsp90 Chaperone Complex and Regulates Androgen Receptor Signaling in Prostate Cancer Cells." *Molecular and Cellular Biology* 30 (5): 1243–53. doi:10.1128/MCB.01891-08.

Nogales, Eva, and Sjors H.W. Scheres. 2015. "Cryo-EM: A Unique Tool for the Visualization of Macromolecular Complexity." *Molecular Cell* 58 (4): 677–89. doi:10.1016/j.molcel.2015.02.019.

Ohi, Melanie, Ying Li, Yifan Cheng, and Thomas Walz. 2004. "Negative Staining and Image Classification - Powerful Tools in Modern Electron Microscopy." *Biological Procedures Online* 6: 23–34. doi:10.1251/bpo70.

Olivares, Adrian O., Tania A. Baker, and Robert T. Sauer. 2016. "Mechanistic Insights into Bacterial AAA+ Proteases and Protein-Remodelling Machines." *Nature Reviews. Microbiology* 14 (1): 33–44. doi:10.1038/nrmicro.2015.4.

Olivares, Adrian O., Andrew R. Nager, Ohad Iosefson, Robert T. Sauer, and Tania A. Baker. 2014. "Mechanochemical Basis of Protein Degradation by a Double-Ring AAA+ Machine." *Nature Structural & Molecular Biology* 21 (10): 871–75. doi:10.1038/nsmb.2885.

Pearl, Laurence H., and Chrisostomos Prodromou. 2006. “Structure and Mechanism of the Hsp90 Molecular Chaperone Machinery.” *Annual Review of Biochemistry* 75: 271–94. doi:10.1146/annurev.biochem.75.103004.142738.

Penczek, Pawel A. 2010. “Resolution Measures in Molecular Electron Microscopy.” *Methods in Enzymology* 482: 73–100. doi:10.1016/S0076-6879(10)82003-8.

Periyasamy, S., T. Hinds, L. Shemshedini, W. Shou, and E. R. Sanchez. 2010. “FKBP51 and Cyp40 Are Positive Regulators of Androgen-Dependent Prostate Cancer Cell Growth and the Targets of FK506 and Cyclosporin A.” *Oncogene* 29 (11): 1691–1701. doi:10.1038/onc.2009.458.

Powis, Katie, Bianca Schrul, Heather Tienson, Irina Gostimskaya, Michal Breker, Stephen High, Maya Schuldiner, Ursula Jakob, and Blanche Schwappach. 2013. “Get3 Is a Holdase Chaperone and Moves to Deposition Sites for Aggregated Proteins When Membrane Targeting Is Blocked.” *Journal of Cell Science* 126 (Pt 2): 473–83. doi:10.1242/jcs.112151.

Prodromou, C., B. Panaretou, S. Chohan, G. Siligardi, R. O’Brien, J. E. Ladbury, S. M. Roe, P. W. Piper, and L. H. Pearl. 2000. “The ATPase Cycle of Hsp90 Drives a Molecular ‘Clamp’ via Transient Dimerization of the N-Terminal Domains.” *The EMBO Journal* 19 (16): 4383–92. doi:10.1093/emboj/19.16.4383.

Prodromou, C., G. Siligardi, R. O’Brien, D. N. Woolfson, L. Regan, B. Panaretou, J. E. Ladbury, P. W. Piper, and L. H. Pearl. 1999. “Regulation of Hsp90 ATPase Activity by Tetratricopeptide Repeat (TPR)-Domain Co-Chaperones.” *The EMBO Journal* 18 (3): 754–62. doi:10.1093/emboj/18.3.754.

Punjani, Ali, John L. Rubinstein, David J. Fleet, and Marcus A. Brubaker. 2017. “CryoSPARC: Algorithms for Rapid Unsupervised Cryo-EM Structure Determination.” *Nature Methods* 14 (3): 290–96. doi:10.1038/nmeth.4169.

Raman, B., L. V. Siva Kumar, T. Ramakrishna, and C. Mohan Rao. 2001. “Redox-Regulated Chaperone Function and Conformational Changes of Escherichia Coli Hsp33.” *FEBS Letters* 489 (1): 19–24.

Ratajczak, Thomas, Carmel Cluning, and Bryan K Ward. 2015. “Steroid Receptor-Associated Immunophilins: A Gateway to Steroid Signalling.” *The Clinical Biochemist Reviews* 36 (2): 31–52.

Reynolds, P. D., Y. Ruan, D. F. Smith, and J. G. Scammell. 1999. “Glucocorticoid Resistance in the Squirrel Monkey Is Associated with Overexpression of the Immunophilin FKBP51.” *The Journal of Clinical Endocrinology and Metabolism* 84 (2): 663–69. doi:10.1210/jcem.84.2.5429.

Rodina, Anna, Tai Wang, Pengrong Yan, Erica DaGama Gomes, Mark P. S. Dunphy, Nagavarakishore Pillarsetty, John Koren, et al. 2016. “The Epichaperome Is an Integrated Chaperome Network That Facilitates Tumour Survival.” *Nature* 538 (7625): 397–401. doi:10.1038/nature19807.

Roe, S. M., C. Prodromou, R. O’Brien, J. E. Ladbury, P. W. Piper, and L. H. Pearl. 1999. “Structural Basis for Inhibition of the Hsp90 Molecular Chaperone by the Antitumor Antibiotics Radicicol and Geldanamycin.” *Journal of Medicinal Chemistry* 42 (2): 260–66. doi:10.1021/jm980403y.

Rosenzweig, Rina, Patrick Farber, Algirdas Velyvis, Enrico Rennella, Michael P. Latham, and Lewis E. Kay. 2015. “ClpB N-Terminal Domain Plays a Regulatory Role in Protein

Disaggregation." *Proceedings of the National Academy of Sciences of the United States of America* 112 (50): E6872-6881. doi:10.1073/pnas.1512783112.
Rüdiger, S., J. Schneider-Mergener, and B. Bukau. 2001. "Its Substrate Specificity Characterizes the DnaJ Co-Chaperone as a Scanning Factor for the DnaK Chaperone." *The EMBO Journal* 20 (5): 1042–50. doi:10.1093/emboj/20.5.1042.
Saffert, Paul, Cordula Enenkel, and Petra Wendler. 2017. "Structure and Function of P97 and Pex1/6 Type II AAA+ Complexes." *Frontiers in Molecular Biosciences* 4 (May). doi:10.3389/fmolb.2017.00033.
Saibil, Helen. 2013. "Chaperone Machines for Protein Folding, Unfolding and Disaggregation." *Nature Reviews. Molecular Cell Biology* 14 (10): 630–42. doi:10.1038/nrm3658.
Sanchez, Y., J. Taulien, K. A. Borkovich, and S. Lindquist. 1992. "Hsp104 Is Required for Tolerance to Many Forms of Stress." *The EMBO Journal* 11 (6): 2357–64.
Scammell, J. G., W. B. Denny, D. L. Valentine, and D. F. Smith. 2001. "Overexpression of the FK506-Binding Immunophilin FKBP51 Is the Common Cause of Glucocorticoid Resistance in Three New World Primates." *General and Comparative Endocrinology* 124 (2): 152–65. doi:10.1006/gcen.2001.7696.
Scheres, Sjors H. W. 2012. "RELION: Implementation of a Bayesian Approach to Cryo-EM Structure Determination." *Journal of Structural Biology* 180 (3): 519–30. doi:10.1016/j.jsb.2012.09.006.
Scheufler, C., A. Brinker, G. Bourenkov, S. Pegoraro, L. Moroder, H. Bartunik, F. U. Hartl, and I. Moarefi. 2000. "Structure of TPR Domain-Peptide Complexes: Critical Elements in the Assembly of the Hsp70-Hsp90 Multichaperone Machine." *Cell* 101 (2): 199–210. doi:10.1016/S0092-8674(00)80830-2.
Schuldiner, Maya, Jutta Metz, Volker Schmid, Vladimir Denic, Magdalena Rakwalska, Hans Dieter Schmitt, Blanche Schwappach, and Jonathan S. Weissman. 2008. "The GET Complex Mediates Insertion of Tail-Anchored Proteins into the ER Membrane." *Cell* 134 (4): 634–45. doi:10.1016/j.cell.2008.06.025.
Seyffer, Fabian, Eva Kummer, Yuki Oguchi, Juliane Winkler, Mohit Kumar, Regina Zahn, Victor Sourjik, Bernd Bukau, and Axel Mogk. 2012. "Hsp70 Proteins Bind Hsp100 Regulatory M Domains to Activate AAA+ Disaggregase at Aggregate Surfaces." *Nature Structural & Molecular Biology* 19 (12): 1347–55. doi:10.1038/nsmb.2442.
Shen, Jian, Ching-Mei Hsu, Bae-Kwang Kang, Barry P. Rosen, and Hiranmoy Bhattacharjee. 2003. "The Saccharomyces Cerevisiae Arr4p Is Involved in Metal and Heat Tolerance." *Biometals: An International Journal on the Role of Metal Ions in Biology, Biochemistry, and Medicine* 16 (3): 369–78.
Shiau, Andrew K., Seth F. Harris, Daniel R. Southworth, and David A. Agard. 2006. "Structural Analysis of E. Coli Hsp90 Reveals Dramatic Nucleotide-Dependent Conformational Rearrangements." *Cell* 127 (2): 329–40. doi:10.1016/j.cell.2006.09.027.
Shin, Yongdae, Joseph H. Davis, Ricardo R. Brau, Andreas Martin, Jon A. Kenniston, Tania A. Baker, Robert T. Sauer, and Matthew J. Lang. 2009. "Single-Molecule Denaturation and Degradation of Proteins by the AAA+ ClpXP Protease." *Proceedings of the National Academy of Sciences of the United States of America* 106 (46): 19340–45. doi:10.1073/pnas.0910484106.
Shorter, James, and Susan Lindquist. 2006. "Destruction or Potentiation of Different Prions Catalyzed by Similar Hsp104 Remodeling Activities." *Molecular Cell* 23 (3): 425–38. doi:10.1016/j.molcel.2006.05.042.

Sidera, Katerina, and Evangelia Patsavoudi. 2014. “HSP90 Inhibitors: Current Development and Potential in Cancer Therapy.” *Recent Patents on Anti-Cancer Drug Discovery* 9 (1): 1–20.

Skiniotis, Georgios, and Daniel R. Southworth. 2016. “Single-Particle Cryo-Electron Microscopy of Macromolecular Complexes.” *Microscopy (Oxford, England)* 65 (1): 9–22. doi:10.1093/jmicro/dfv366.

Smith, David F. 2004. “Tetratricopeptide Repeat Cochaperones in Steroid Receptor Complexes.” *Cell Stress & Chaperones* 9 (2): 109–21.

Smith, David F., and David O. Toft. 2008. “Minireview: The Intersection of Steroid Receptors with Molecular Chaperones: Observations and Questions.” *Molecular Endocrinology (Baltimore, Md.)* 22 (10): 2229–40. doi:10.1210/me.2008-0089.

Snider, Jamie, Guillaume Thibault, and Walid A. Houry. 2008. “The AAA+ Superfamily of Functionally Diverse Proteins.” *Genome Biology* 9 (4): 216. doi:10.1186/gb-2008-9-4-216.

Southworth, Daniel R., and David A. Agard. 2008. “Species-Dependent Ensembles of Conserved Conformational States Define the Hsp90 Chaperone ATPase Cycle.” *Molecular Cell* 32 (5): 631–40. doi:10.1016/j.molcel.2008.10.024.

Stark, Holger, Friedrich Zemlin, and Christoph Boettcher. 1996. “Electron Radiation Damage to Protein Crystals of Bacteriorhodopsin at Different Temperatures.” *Ultramicroscopy* 63 (2): 75–79. doi:10.1016/0304-3991(96)00045-9.

Stefanovic, Sandra, and Ramanujan S. Hegde. 2007. “Identification of a Targeting Factor for Posttranslational Membrane Protein Insertion into the ER.” *Cell* 128 (6): 1147–59. doi:10.1016/j.cell.2007.01.036.

Stromer, Thusnelda, Elke Fischer, Klaus Richter, Martin Haslbeck, and Johannes Buchner. 2004. “Analysis of the Regulation of the Molecular Chaperone Hsp26 by Temperature-Induced Dissociation: The N-Terminal Domail Is Important for Oligomer Assembly and the Binding of Unfolding Proteins.” *The Journal of Biological Chemistry* 279 (12): 11222–28. doi:10.1074/jbc.M310149200.

Suloway, Christian J. M., Michael E. Rome, and William M. Clemons. 2012. “Tail-Anchor Targeting by a Get3 Tetramer: The Structure of an Archaeal Homologue.” *The EMBO Journal* 31 (3): 707–19. doi:10.1038/emboj.2011.433.

Sweeny, Elizabeth A., and James Shorter. 2016. “Mechanistic and Structural Insights into the Prion-Disaggregase Activity of Hsp104.” *Journal of Molecular Biology* 428 (9 Pt B): 1870–85. doi:10.1016/j.jmb.2015.11.016.

Taipale, Mikko, Daniel F. Jarosz, and Susan Lindquist. 2010. “HSP90 at the Hub of Protein Homeostasis: Emerging Mechanistic Insights.” *Nature Reviews. Molecular Cell Biology* 11 (7): 515–28. doi:10.1038/nrm2918.

Tessarz, Peter, Axel Mogk, and Bernd Bukau. 2008. “Substrate Threading through the Central Pore of the Hsp104 Chaperone as a Common Mechanism for Protein Disaggregation and Prion Propagation.” *Molecular Microbiology* 68 (1): 87–97. doi:10.1111/j.1365-2958.2008.06135.x.

Trendowski, Matthew. 2015. “PU-H71: An Improvement on Nature’s Solutions to Oncogenic Hsp90 Addiction.” *Pharmacological Research* 99 (September): 202–16. doi:10.1016/j.phrs.2015.06.007.

Ueda, Shugo, Hiroshi Masutani, Hajime Nakamura, Toru Tanaka, Masaya Ueno, and Junji Yodoi. 2002. "Redox Control of Cell Death." *Antioxidants & Redox Signaling* 4 (3): 405–14. doi:10.1089/15230860260196209.

Verba, Kliment A., Ray Yu-Ruei Wang, Akihiko Arakawa, Yanxin Liu, Mikako Shirouzu, Shigeyuki Yokoyama, and David A. Agard. 2016. "Atomic Structure of Hsp90-Cdc37-Cdk4 Reveals That Hsp90 Traps and Stabilizes an Unfolded Kinase." *Science (New York, N.Y.)* 352 (6293): 1542–47. doi:10.1126/science.aaf5023.

Vijayalakshmi, J., M. K. Mukhergee, J. Graumann, U. Jakob, and M. A. Saper. 2001. "The 2.2 A Crystal Structure of Hsp33: A Heat Shock Protein with Redox-Regulated Chaperone Activity." *Structure (London, England: 1993)* 9 (5): 367–75.

Walker, J. E., M. Saraste, M. J. Runswick, and N. J. Gay. 1982. "Distantly Related Sequences in the Alpha- and Beta-Subunits of ATP Synthase, Myosin, Kinases and Other ATP-Requiring Enzymes and a Common Nucleotide Binding Fold." *The EMBO Journal* 1 (8): 945–51.

Wegele, H., L. Müller, and J. Buchner. 2004. "Hsp70 and Hsp90--a Relay Team for Protein Folding." *Reviews of Physiology, Biochemistry and Pharmacology* 151: 1–44. doi:10.1007/s10254-003-0021-1.

Weibezahn, Jimena, Peter Tessarz, Christian Schlieker, Regina Zahn, Zeljka Maglica, Sukyeong Lee, Hanswalter Zentgraf, et al. 2004. "Thermotolerance Requires Refolding of Aggregated Proteins by Substrate Translocation through the Central Pore of ClpB." *Cell* 119 (5): 653–65. doi:10.1016/j.cell.2004.11.027.

Weingarten, M. D., A. H. Lockwood, S. Y. Hwo, and M. W. Kirschner. 1975. "A Protein Factor Essential for Microtubule Assembly." *Proceedings of the National Academy of Sciences of the United States of America* 72 (5): 1858–62.

Wendler, Petra, Susanne Ciniawsky, Malte Kock, and Sebastian Kube. 2012. "Structure and Function of the AAA+ Nucleotide Binding Pocket." *Biochimica et Biophysica Acta (BBA) - Molecular Cell Research*, AAA ATPases: structure and function, 1823 (1): 2–14. doi:10.1016/j.bbamcr.2011.06.014.

Wendler, Petra, and Helen R. Saibil. 2010. "Cryo Electron Microscopy Structures of Hsp100 Proteins: Crowbars in or Out?" *Biochemistry and Cell Biology = Biochimie Et Biologie Cellulaire* 88 (1): 89–96. doi:10.1139/o09-164.

Wendler, Petra, James Shorter, Celia Plisson, Anil G. Cashikar, Susan Lindquist, and Helen R. Saibil. 2007. "Atypical AAA+ Subunit Packing Creates an Expanded Cavity for Disaggregation by the Protein-Remodeling Factor Hsp104." *Cell* 131 (7): 1366–77. doi:10.1016/j.cell.2007.10.047.

Winter, Jeannette, and Ursula Jakob. 2004. "Beyond Transcription--New Mechanisms for the Regulation of Molecular Chaperones." *Critical Reviews in Biochemistry and Molecular Biology* 39 (5–6): 297–317. doi:10.1080/10409230490900658.

Workman, Paul. 2004. "Combinatorial Attack on Multistep Oncogenesis by Inhibiting the Hsp90 Molecular Chaperone." *Cancer Letters* 206 (2): 149–57. doi:10.1016/j.canlet.2003.08.032.

Workman, Paul, Francis Burrows, Len Neckers, and Neal Rosen. 2007. "Drugging the Cancer Chaperone HSP90: Combinatorial Therapeutic Exploitation of Oncogene Addiction and Tumor Stress." *Annals of the New York Academy of Sciences* 1113 (October): 202–16. doi:10.1196/annals.1391.012.

Yang, Zhengfan, Jia Fang, Johnathan Chittuluru, Francisco J. Asturias, and Pawel A. Penczek. 2012. "Iterative Stable Alignment and Clustering of 2D Transmission Electron Microscope Images." *Structure (London, England: 1993)* 20 (2): 237–47. doi:10.1016/j.str.2011.12.007.

Yi, Fang, and Lynne Regan. 2008. "A Novel Class of Small Molecule Inhibitors of Hsp90." *ACS Chemical Biology* 3 (10): 645–54. doi:10.1021/cb800162x.

Young, J. C., W. M. Obermann, and F. U. Hartl. 1998. "Specific Binding of Tetratricopeptide Repeat Proteins to the C-Terminal 12-KDa Domain of Hsp90." *The Journal of Biological Chemistry* 273 (29): 18007–10.

Zavilgelsky, G. B., V. Yu Kotova, M. M. Mazhul', and I. V. Manukhov. 2002. "Role of Hsp70 (DnaK-DnaJ-GrpE) and Hsp100 (ClpA and ClpB) Chaperones in Refolding and Increased Thermal Stability of Bacterial Luciferases in Escherichia Coli Cells." *Biochemistry. Biokhimiia* 67 (9): 986–92.

Zhao, Minglei, Shenping Wu, Qiangjun Zhou, Sandro Vivona, Daniel J. Cipriano, Yifan Cheng, and Axel T. Brunger. 2015. "Mechanistic Insights into the Recycling Machine of the SNARE Complex." *Nature* 518 (7537): 61–67. doi:10.1038/nature14148.

Zuehlke, Abbey, and Jill L. Johnson. 2010. "Hsp90 and Co-Chaperones Twist the Functions of Diverse Client Proteins." *Biopolymers* 93 (3): 211–17. doi:10.1002/bip.21292.

CHAPTER 2

SPIRAL ARCHITECTURE OF THE HSP104 DISAGGREGASE REVEALS THE BASIS FOR POLYPEPTIDE TRANSLOCATION

This chapter is published:
AL Yokom, SN Gates, ME Jackrel, KL Mack, M Su, J Shorter, and DR Southworth. Spiral architecture of the Hsp104 disaggregase reveals the basis for polypeptide translocation. *Nat Struct Mol Biol* **23**, 830-837 (2016).[1]

2.1 Abstract

Hsp104 is a conserved member of AAA+ protein disaggregases that promotes survival during cellular stress. Hsp104 remodels amyloids, supporting prion propagation, and disassembles toxic oligomers connected to neurodegenerative diseases. A definitive structural mechanism of its disaggregase activity, however, has remained elusive. We have determined the ATP-state cryo-EM structure of wildtype *Saccharomyces cerevisiae* Hsp104, revealing a near-helical hexamer architecture that coordinates the mechanical power of the twelve AAA+ domains for disaggregation. An unprecedented heteromeric AAA+ interaction defines an asymmetric seam in an apparent catalytic arrangement that aligns the domains in a two-turn spiral. N-terminal domains form a broad channel entrance for substrate engagement and Hsp70 interaction. Middle-domain helices bridge adjacent protomers across the nucleotide pocket, explaining roles in ATP hydrolysis and protein disaggregation. Remarkably, substrate-binding pore loops line the channel

[1] My contribution to this chapter was cryo-EM sample preparation, data collection and analysis. Contributions by Adam Yokom (Dan Southworth lab, University of Michigan) and the Jim Shorter lab (University of Pennsylvania), including ME Jackrel and KL Mack, are indicated within the text.

in a spiral arrangement likely optimized for substrate transfer across the AAA+ domains, establishing a continuous path for polypeptide translocation.

2.2 Introduction

Heat shock protein (Hsp) 104, found in yeast, is a member of the Hsp100 class of molecular chaperones that contain highly conserved AAA+ (ATPases Associated with diverse cellular Activities) domains and serve essential roles in thermotolerance and protein quality control (Sanchez and Lindquist 1990; Parsell et al. 1994; Mogk, Kummer, and Bukau 2015). Hsp104 and its bacterial homolog, ClpB, form large hexameric-ring structures that cooperate with the Hsp70 system to unfold and rescue aggregated protein states by active translocation of polypeptide substrates through a central channel (Glover and Lindquist 1998; Weibezahn et al. 2004; Lum et al. 2004). In addition to solubilizing stress-induced disordered aggregates (Weibezahn et al. 2004; Lum et al. 2004; Motohashi et al. 1999), Hsp104 recognizes and remodels cross-β structures of amyloid fibrils, such as those found in Sup35 prions, which enables Hsp104 to control prion inheritance in yeast (Shorter and Lindquist 2004; Chernoff et al. 1995; Moriyama, Edskes, and Wickner 2000). This function in prion disaggregation is enhanced in Hsp104 compared to ClpB, and studies have identified potentiated Hsp104 variants that reduce the toxicity of proteins linked to neurodegenerative diseases including TDP-43, FUS and α-synuclein (Lo Bianco et al. 2008; Jackrel et al. 2014; Cushman-Nick, Bonini, and Shorter 2013). Despite fundamental roles in protein quality control and promising therapeutic activity in rescuing amyloidogenic states (Jackrel and Shorter 2014), how Hsp104 and its family members function as powerful molecular motors to solubilize proteins is not fully understood.

Hsp104 and ClpB contain a mobile N-terminal domain (NTD), implicated in substrate engagement (Rosenzweig et al. 2015; Doyle, Hoskins, and Wickner 2012), two evolutionarily

distinct AAA+ nucleotide binding domains (NBD1 and NBD2) that bind substrates and power translocation, and a middle domain (MD) that is required for disaggregation and interaction with Hsp70 (Kedzierska et al. 2003; Rosenzweig et al. 2013; Seyffer et al. 2012; J. Lee et al. 2013; Desantis et al. 2014). Hsp104 also contains a C-terminal domain (CTD) not found in ClpB that is required for hexamerization (Mackay et al. 2008). The crystal structure of ClpB (S. Lee et al. 2003) from a thermophilic eubacterium (*Thermus thermophilus*) identified the conserved type II AAA+ domain architecture wherein the NBDs are comprised of large and small subdomains that form the ATP binding pocket and contain the respective Walker A and B motifs and 'sensor' residues required for ATP hydrolysis. The MD, located within the small subdomain of NBD1, forms an ~85 Å-long flexible coiled-coil that is proposed to adopt a number of conformations in the hexamer during the hydrolysis cycle (S. Lee et al. 2003; S. Lee, Choi, and Tsai 2007; Wendler et al. 2007; Carroni et al. 2014; Sweeny et al. 2015).

Polypeptide translocation between NBD1 and NBD2 is controlled via allosterically driven ATP hydrolysis events (Hattendorf and Lindquist 2002; Wendler et al. 2009) and, for Hsp104, cooperativity between protomers is required for disaggregation of highly stable amyloids (DeSantis et al. 2012). Substrate binding is favored in the ATP-bound state (Bösl, Grimminger, and Walter 2005), and involves direct interaction with highly conserved tyrosine residues in flexible NBD "pore loops" (Weibezahn et al. 2004; Lum et al. 2004; Tessarz, Mogk, and Bukau 2008) that are proposed to line the axial channel and operate by hydrolysis-driven substrate hand-off cycles. How this occurs across the 100 Å-long channel and between the two distinct AAA+ domains remains unknown. A number of cryo-EM models at modest resolutions between 11 and 20 Å of Hsp104 mutants (Wendler et al. 2007, 2009; S. Lee et al. 2010) and ClpB (S. Lee et al. 2003; S. Lee, Choi, and Tsai 2007) have been described and propose various

structural arrangements but generally show a symmetric hexamer with three distinct rings comprised of the NTD, NBD1, and NBD2. Structural studies have also identified different nucleotide states that involve changes in the pore diameter and conformation of the domains (S. Lee, Choi, and Tsai 2007; Sweeny et al. 2015; Wendler et al. 2009). The oligomeric state, however, is dynamic, requiring presence of nucleotide for stability (Parsell, Kowal, and Lindquist 1994) and the protomers exchange rapidly during the hydrolysis cycle (DeSantis et al. 2012; Aguado et al. 2015; Werbeck, Schlee, and Reinstein 2008); consequently, the high resolution architecture of the hexameric, active complex has remained out of reach.

Here we set out to elucidate the structural mechanism of the Hsp104 disaggregase. We have determined the cryo-EM structure of wild-type Hsp104 from yeast (*Saccharomyces cerevisiae*) bound to AMPPNP (a nonhydrolyzable ATP analog) at 5.6 Å resolution. The structure reveals a helical-like arrangment involving a 10-Å rise between protomers that results in a seam where the first protomer is offset by more than 40 Å from the sixth. This offset brings NBD1 from one protomer into contact with NBD2 in the adjacent protomer, forming a heteromeric AAA+ interaction at the seam. Well-defined density corresponding to the conserved Tyr pore loops presents a spiral of substrate-binding surfaces along the axial channel. Remarkably, the protomer offset optimally positions the NBD1 and NBD2 pore loops at the seam for coordinated transfer of substrates across the AAA+ domains.

2.3 The Hsp104 hexamer adopts an asymmetric spiral architecture

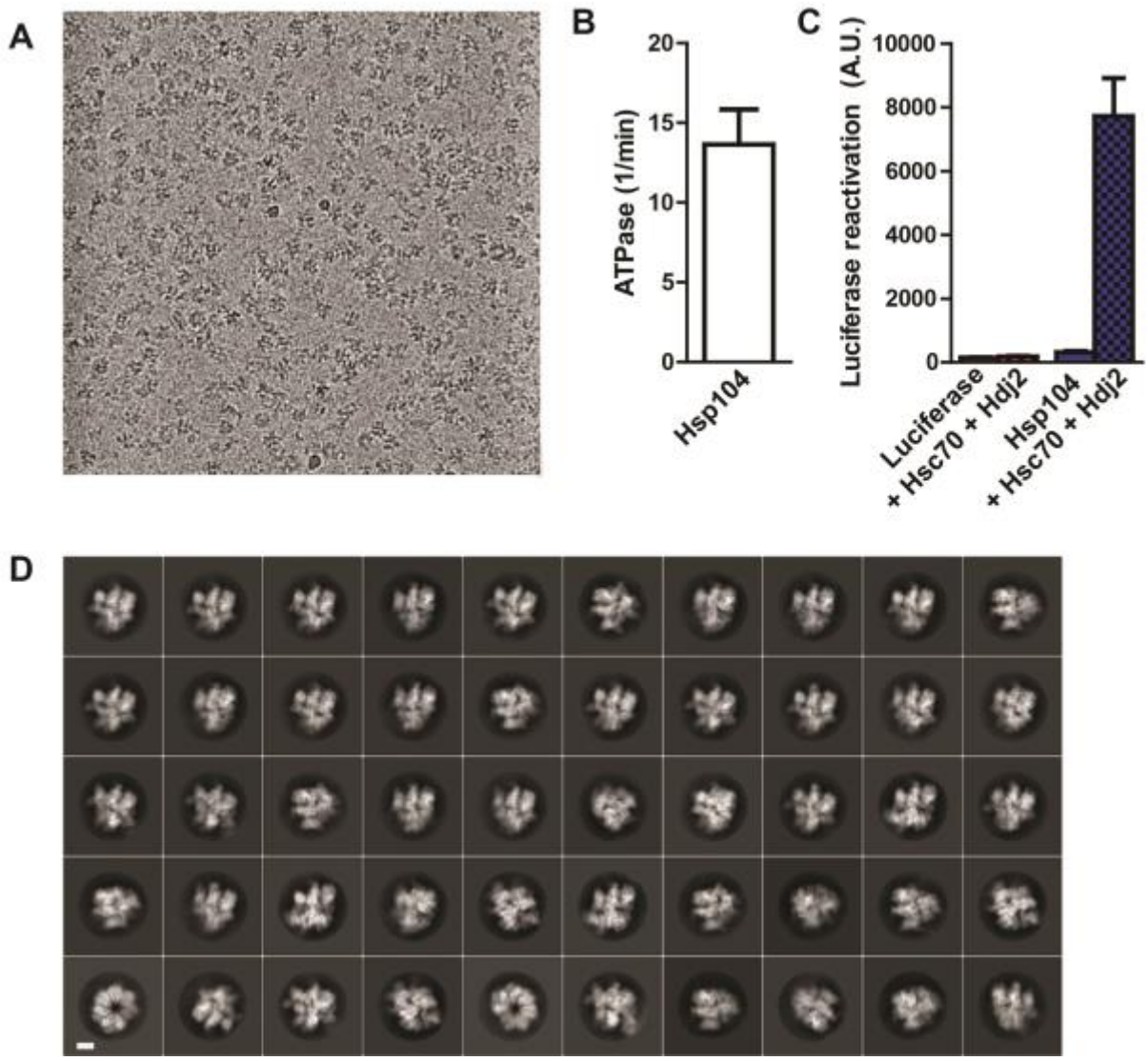

Figure 2-1. 2D Cryo-EM analysis of Hsp104:AMPPNP. (A) Representative cryo-EM micrograph of Hsp104 hexamers. Scale bar equals 50 Å (B) Purified Hsp104 hexamer is active for ATPase function, measured as the release of inorganic phosphate over 5 minutes. Value represents mean ± SEM (n = 3). (C) Purified Hsp104 is active for luciferase disaggregation. Recovered luciferase luminescence determined following incubations with Hsp104 plus (checkered bars) or minus (clear bars) equimolar Hsc70 and Hdj2. Values represent means ± SEM (n = 3). (D) 2D reference free class averages of Hsp104. The top 50 populated views are shown. The cryo-EM figures were created by Adam Yokom (Southworth lab, University of Michigan), the ATPase assay and Luciferase reactivation assays were performed by the Shorter lab (University of Pennsylvania).

We determined the cryo-EM structure of the intact, wild-type Hsp104 complex in the presence of AMP-PNP to mimic the substrate-binding ATP state (Shorter and Lindquist 2004). Purified Hsp104 was functionally active in ATPase and disaggregase assays (Fig. 2-1B). Cryo-EM images of Hsp104-AMP-PNP show homogeneous oligomeric complexes (Fig. 2-1A) and reference-free 2D classification reveals a variety of distinct views with well-resolved structural features (Fig. 2-1C). These 2D averages reveal clear top-view ring shapes and side-view projections with three layers that show a striking asymmetry and unique protomer arrangement that is different from what has been described previously (Fig. 2-1C) (Wendler et al. 2007, 2009).

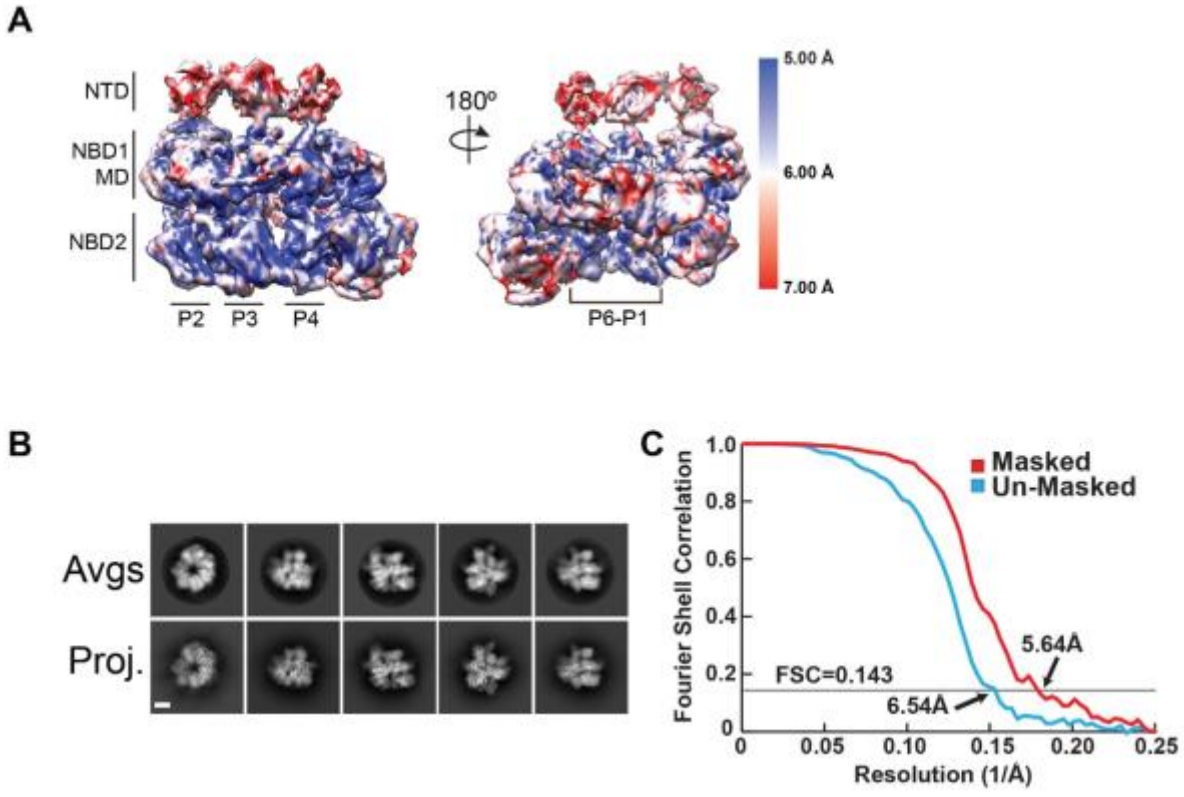

Figure 2-2. Resolution of Hsp104:AMPPNP Final Model and 2D verification. (A) Local resolution of the 3D reconstruction determined by ResMap and shown from 5 Å (blue) to 7 Å (red). (B) Comparison of reference free class averages and 2D projections of the final 3D reconstruction. Scale bar equals 50 Å. (C) Gold standard FSC curve for the un-masked and masked reconstructions of the final model estimated from the FSC=0.143 criterion to be 6.54 Å

and 5.64 Å, respectively. The cryo-EM figures were created by Adam Yokom (Southworth lab, University of Michigan).

The final cryo-EM reconstruction following 3D refinement with no imposed symmetry was achieved at indicated resolutions of 6.5 Å and 5.6 Å for the un-masked and masked maps, respectively (Fig. 2-2A,C). The final map is comprised of 85% of the single particle data following sorting by 2D classification. No additional conformations or oligomeric states were identified by 3D classification, thus the final map represents the predominant form of Hsp104 in the dataset. 2D projections of the 3D map match the reference-free averages, confirming the overall asymmetric architecture (Fig 2-2B).

2.4 The Hsp104:AMPPNP hexamer adopts an asymmetric spiral architecture

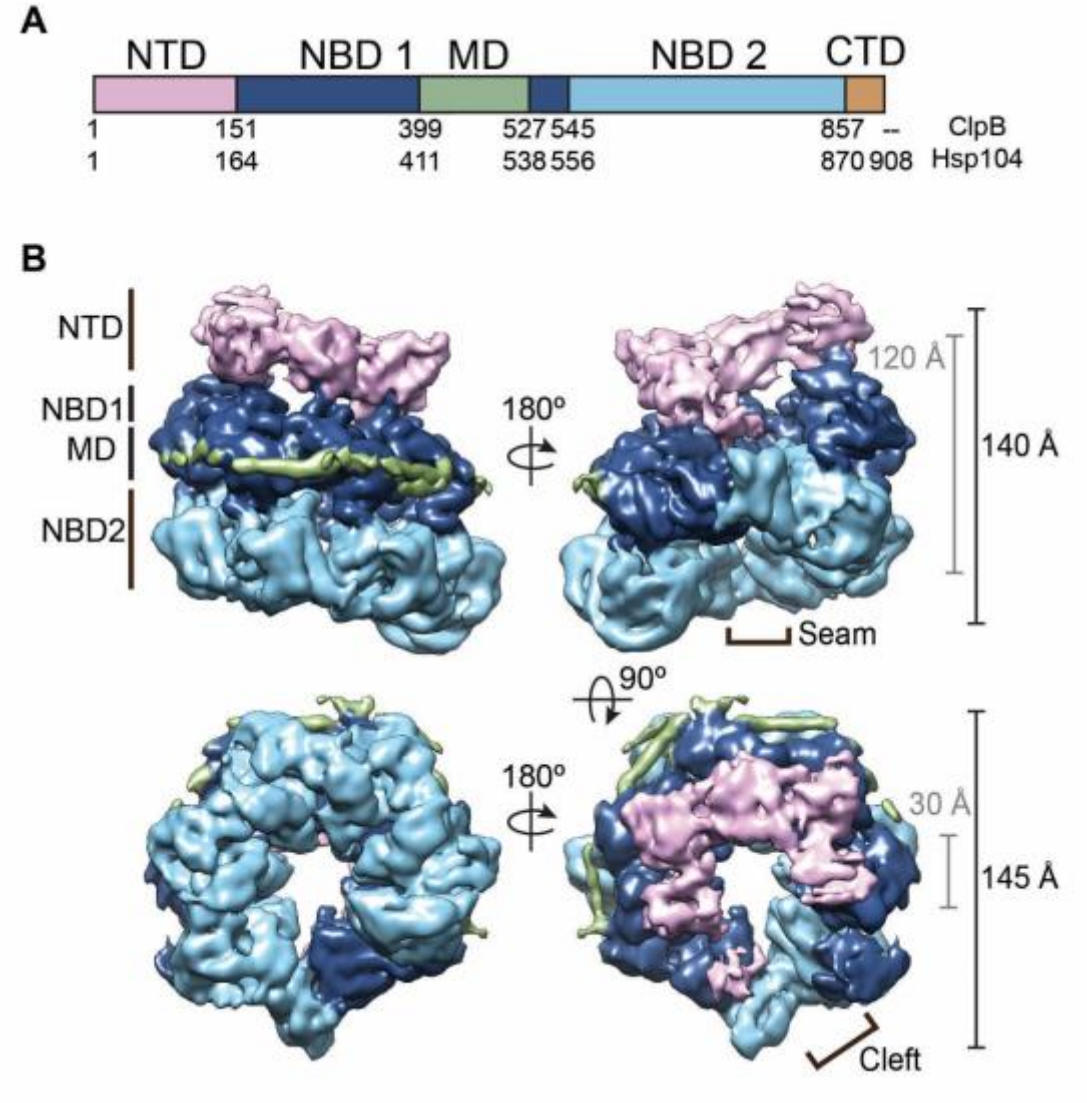

Fig 2-3. Spiral architecture and three-tiered domain arrangement of the Hsp104:AMPPNP hexamer complex by cryo-EM. (A) Schematic showing individual domains and corresponding residue numbers for *T. thermophilus* ClpB and *S. cerevisiae* Hsp104. (B) Views of the final, sharpened 3D density map (4σ) of Hsp104 showing spiral, three-tier architecture. The domains are colored as in (A), based on the atomic model. Approximate dimensions of the channel (grey) and exterior (black) are shown, and the hexamer "seam" and channel "cleft" are indicated. The cryo-EM figures were created by Adam Yokom (Southworth lab, University of Michigan).

The 3D reconstruction reveals Hsp104:AMPPNP is a ring-shaped hexamer with three distinct domain-layers that correspond to the NTD, NBD1-MD and NBD2, consistent with other studies (Fig. 2-3B) (Wendler et al. 2007, 2009; S. Lee et al. 2010). In striking contrast to

previous models, the protomers are arranged in a helical spiral and the NBD rings connect together to form a distinct asymmetric seam. The NBD1 and NBD2 show the highest resolution density, at approximately 5 Å, while the NTDs as well as regions at the hexamer seam are more flexible and at ~6-7 Å resolution (Fig. 2-2A). Density for the MD coiled-coil is partly resolved on one face of the hexamer where it wraps around the outside of the hexamer adjacent to the NBD1s (Fig. 2-3B). The central channel is approximately 25-30 Å in diameter, but opens to form a wide cleft at the hexamer seam due to the spiral offset of the adjacent protomers.

The crystal structure from *Thermus thermophilus* ClpB (S. Lee et al. 2003) (PDB: 1QVR), which has ~45% sequence identity with Hsp104, was used for initial fitting and to determine a homology model for Hsp104. Helices are designated as they are for the ClpB structure (Fig. 2-4A) The reconstruction was docked by rigid body fitting of the domains followed by flexible fitting to achieve an atomic model with the highest correlation to the map, at 0.92. The protomers are designated 1 through 6, with protomer 1 (P1) in the highest position in the side-view orientation, and proceeding counterclockwise when viewed from the NTD-face (Fig. 2-5A). The NBDs fit well, with a cross-correlation value of 0.94, and identify the conserved AAA+ subdomain architecture with α- helical and β-sheet regions that are well resolved for each of the protomers (Fig. 2-4B).

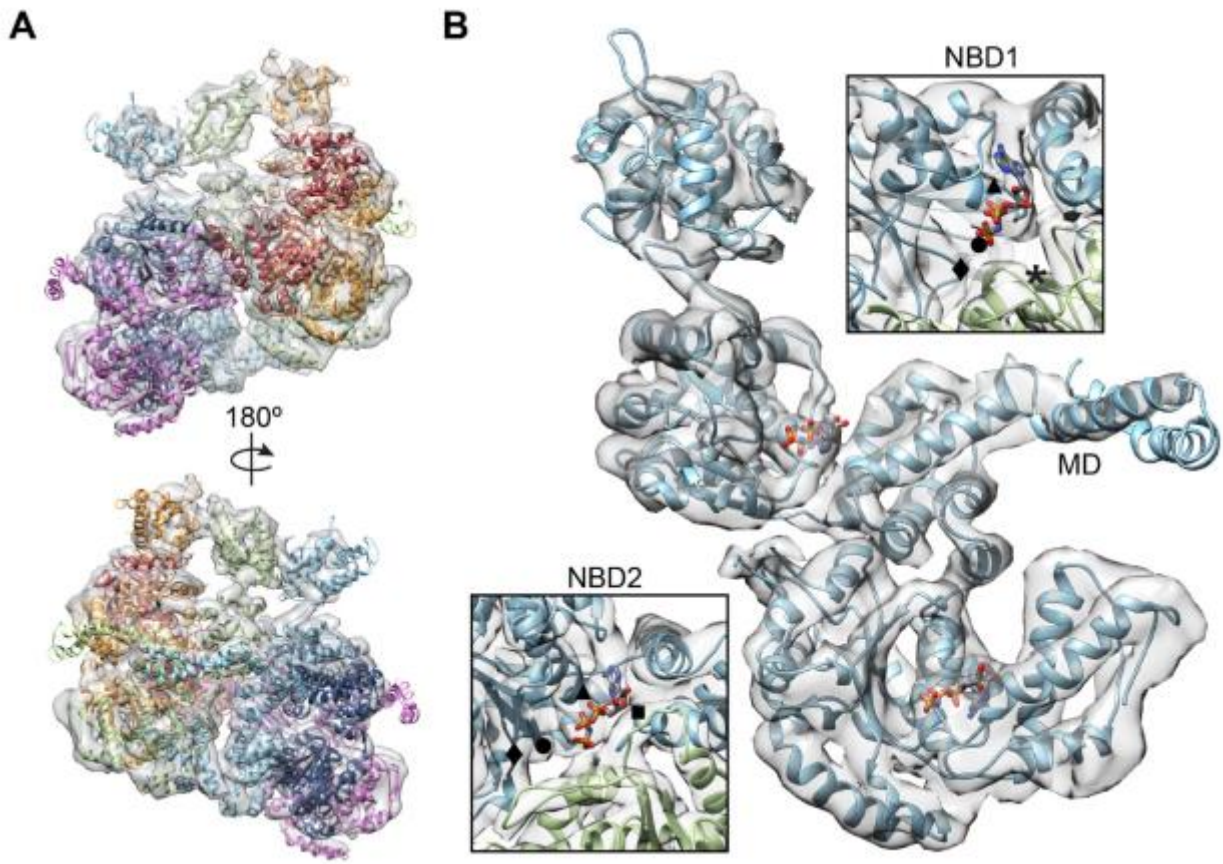

Figure 2-4. Atomic model of Hsp104:AMPPNP. (A) Side views of the Hsp104 hexamer molecular model determined by flexibly fitting the homology model based on the ClpB structure (PDB: 1QVR) (S. Lee et al. 2003). (B) Molecular model of a segmented protomer (P4) showing bound nucleotides and well-resolved density for the NBD1 and NBD2 AAA+ domains. Enlarged views of the nucleotide pockets are shown with indicated positions for Walker A (triangle) and B (diamond), Sensor 1 (circle) and 2 (square) and arginine finger (asterisk) residues. The cryo-EM figures were created by Adam Yokom (Southworth lab, University of Michigan).

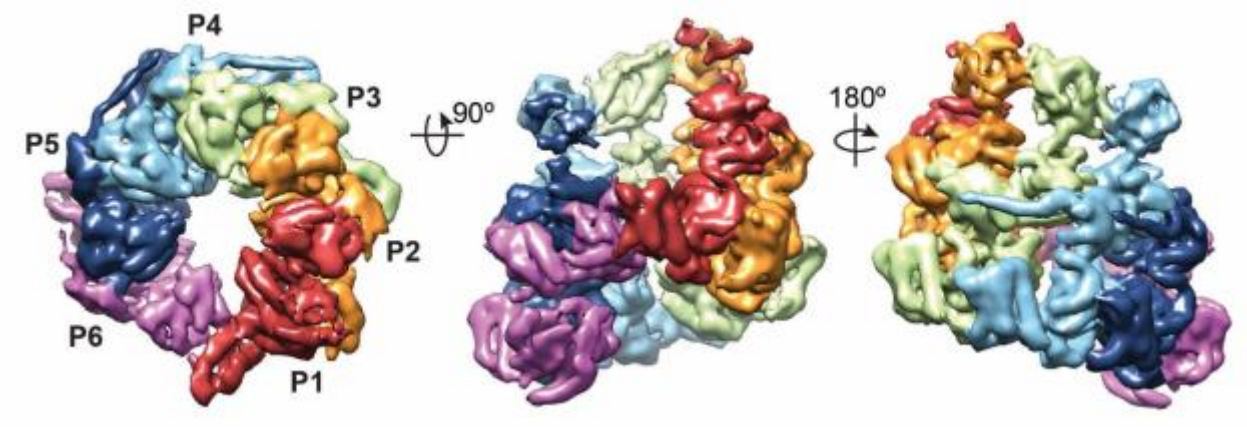

Figure 2-5. Protomer arrangement of Hsp104. Top-view, showing NBD1 density and protomer labels, and side views of the sharpened map (5σ) with each protomer colored based on the molecular model. The cryo-EM figures were created by Adam Yokom (Southworth lab, University of Michigan).

Difference map analysis between the final map and a nucleotide free model indicate nucleotide is present in the majority NBDs, with clear density observed in 9 sites, reduced density in two sites, indicating partial occupancy or flexibility, and no density at one site (Fig. 2-6). The NBD1s show a canonical AAA+ arrangement, including expected positions for the Walker A (K218), Walker B (E285), and sensor-1 (T317) residues. Putative arginine finger residues R334 and R333 (Wendler et al. 2007) are within 7 and 10 Å, respectively, of the nucleotide pocket of the adjacent protomer, indicating a catalytically active arrangement. The NBD2s are similarly well defined showing conserved interprotomer interactions and positions for the Walker A (K620), Walker B (E687), sensor-1 (N728) and sensor-2 (R826) residues, and the proposed arginine (Fig. 2-4B). Protomers P1 and P6 that make up the unusual hexamer seam are in a different conformation and are discussed in further detail below.

Density corresponding to the MD coiled-coil that is partly resolved for P3-P6 was docked with residues 409-467 that correspond to helix L1 and part of helix L2 that connect to the NBD1 large subdomain (Fig. 2-4B). Density for the C-terminal-half of the extended, 85 Å helix L2 as well as helix L3 and helix L4, which includes Hsp70 interaction sites (Rosenzweig et al. 2013)

could not be clearly identified, indicating this portion of the MD remains flexible. The NTDs form globular lobes of density that interact and follow the helical arrangement of the NBDs, forming a broad entrance to the channel (Fig 2-3B,2-5). Despite the NTD flexibility, the NTD-NBD1 linkers are well defined, enabling unambiguous connection to the corresponding protomer. NTD structures could be modeled for protomers P2-P4 (Fig. 2-4A), which exhibit the best-resolved features, and the cross correlation of the fit was determined to be 0.91. Further details of the MD and NTD conformations are discussed below.

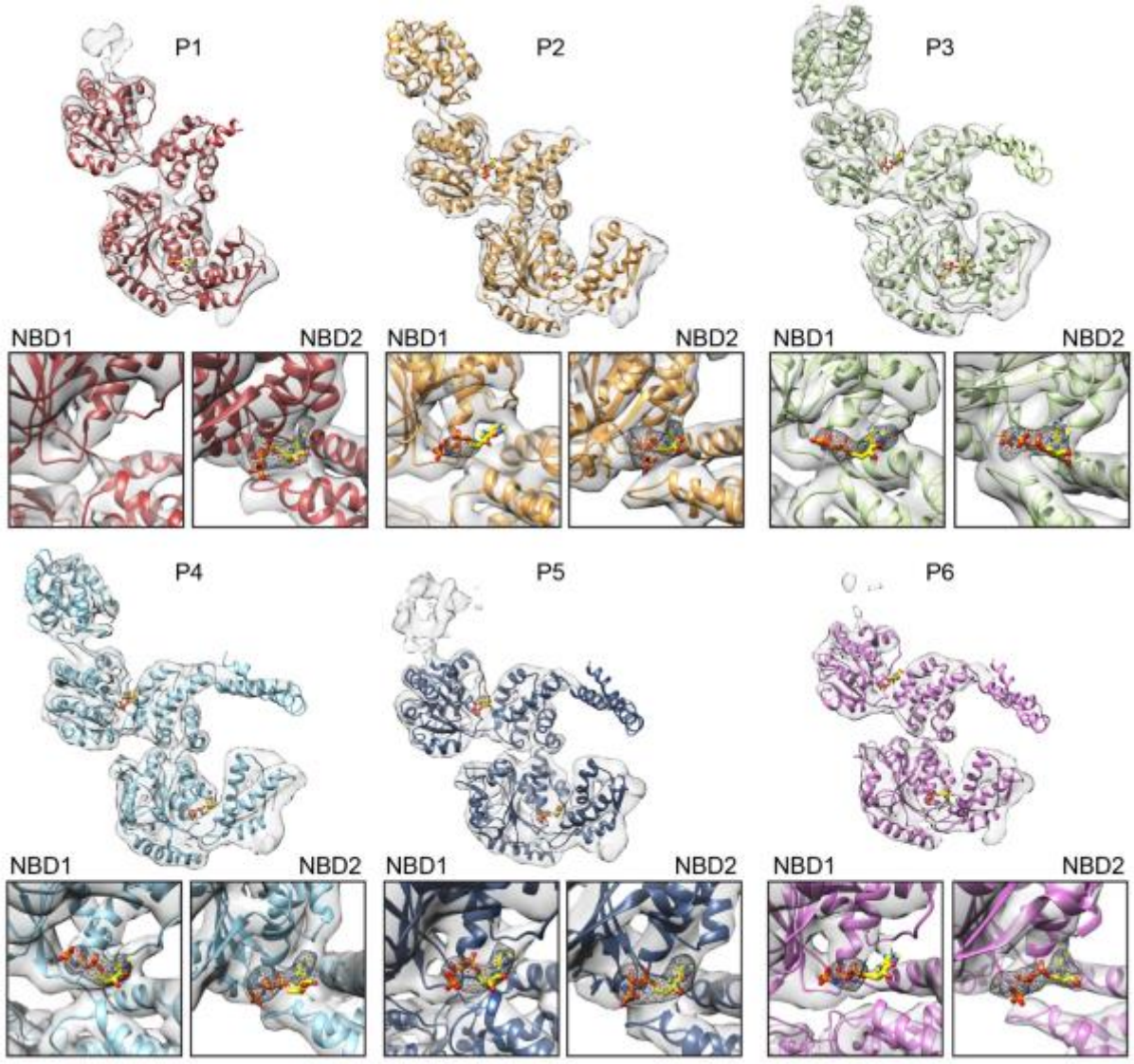

Figure 2-6. Difference maps of nucleotide pockets. Hsp104 molecular models for each protomer in the asymmetric hexamer with the segmented density shown at 5σ. Below are

enlarged views of the nucleotide pockets with difference maps, generated by subtracting a model with no nucleotide from the cryo-EM map, shown as mesh to visualize density for bound nucleotide. AMPPNP is shown as sticks where density is observed in the pocket for the difference maps. The cryo-EM figures were created by Adam Yokom (Southworth lab, University of Michigan).

2.5 Heteromeric NBD1-NBD2 interaction defines the hexamer seam

The most striking structural feature of the Hsp104 hexamer is the helical-like arrangement of the protomers. While canonical AAA+ interactions are generally maintained around the hexamer, each protomer is tilted slightly, resulting in an approximate 7-fold helical symmetry. Going from P1 to P6, the protomers each rise nearly 10 Å and rotate 53°, on average (Fig. 2-7A). The individual protomers vary in conformation and position around the hexamer, indicating the complex is indeed asymmetric (Fig. 2-8). When the NBD1s are superimposed, continuous conformational changes are observed from P1-P6 (Fig. 2-8A), while the greatest protomer differences are between P1 and P6 at the hexamer seam (Fig. 2-8B). The conformational changes primarily involve rotations of the NBD1 and NBD2 small subdomains, which move inward relative to the channel axis by approximately 10° and 20°, respectively, resulting in a more compact P1 protomer compared to P6.

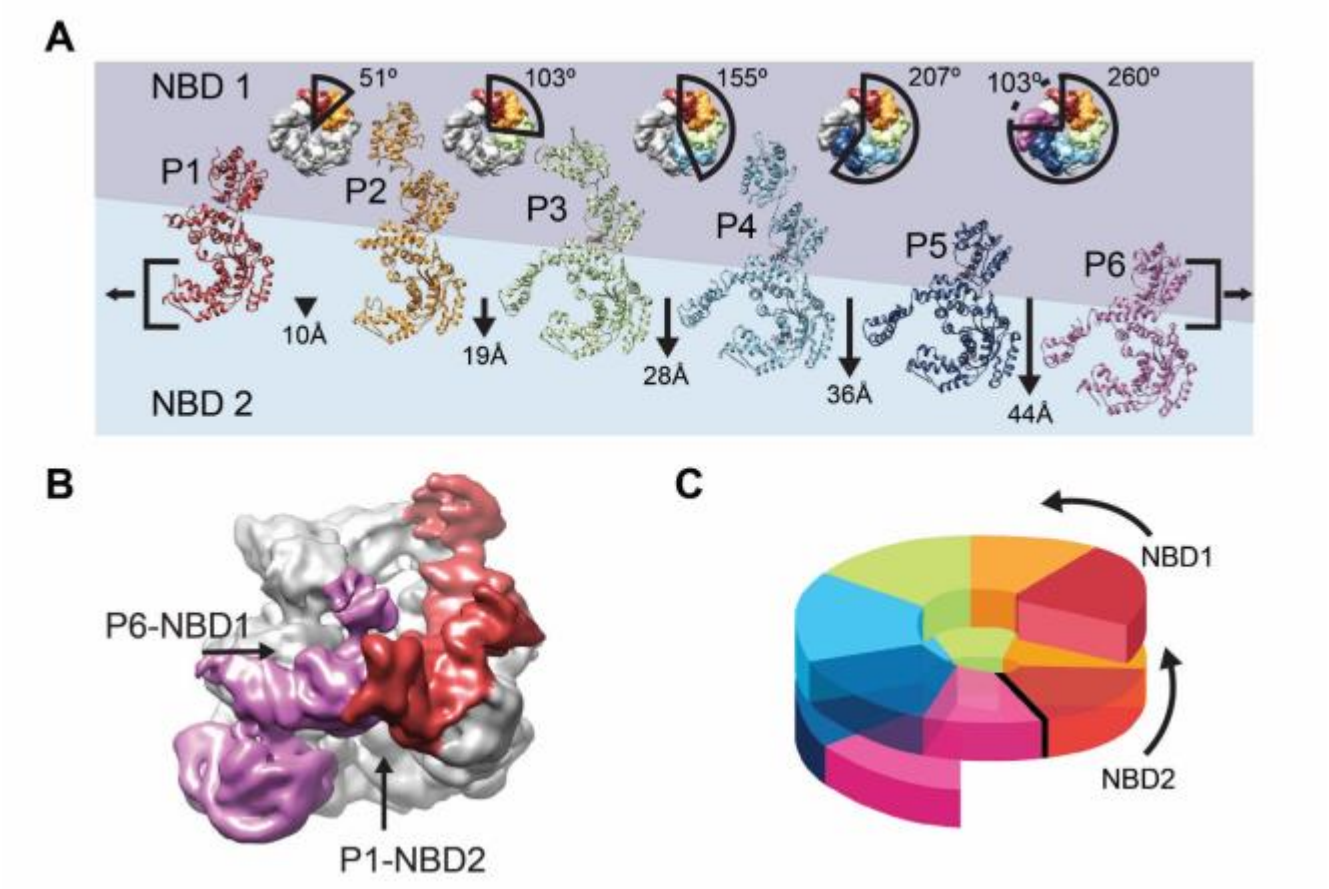

Figure 2-7. Basis for the protomer spiral and NBD1:NBD2 AAA+ interaction at the hexamer seam. (A) Protomer positions shown in top views and individually unrolled from the hexamer with the indicated rotation and translation shift relative to P1. Brackets indicate alignment of NBD1 and NBD2 AAA+ domains for P6 and P1, respectively. (B) Low-pass filtered map colored for P1 (red) and P6 (magenta), highlighting the P6-NBD1–P1-NBD2 interaction. (C) Cartoon model showing the NBD1 and NBD2 AAA+ domains connect and form a two-turn spiral. The cryo-EM figures were created by Adam Yokom (Southworth lab, University of Michigan).

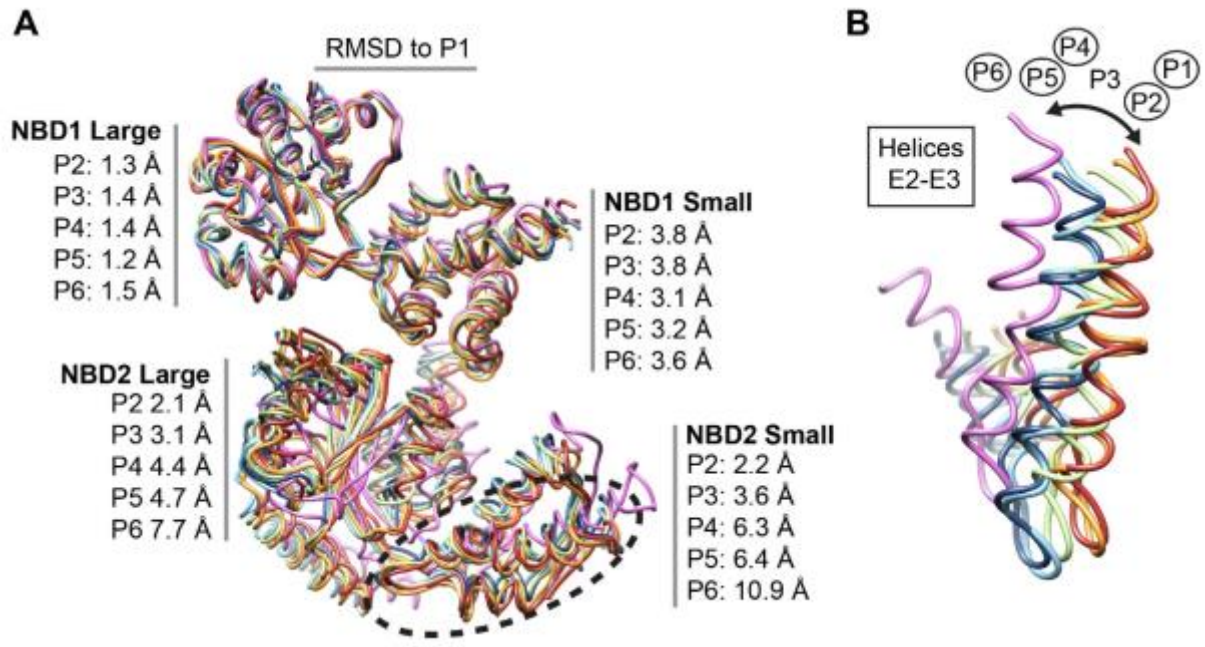

Figure 2-8. Conformational differences in the AAA+ domains of the individual protomers. (A) Overlay of the backbone trace for the protomer NBDs following alignment to the P1 NBD1 large subdomain. RMSD values compared to P1 are shown and identify increasing differences from P2 to P6. (B) Enlarged view of circled region of (A) showing helices E2 and E3 for the 6 aligned protomers, highlighting conformational changes for P1 to P6. The cryo-EM figures were created by Adam Yokom (Southworth lab, University of Michigan).

The helical shift of the protomers results in a 44 Å-offset between P1 and P6, yet these protomers interact together, covering a 100° rotation around the channel axis to complete the hexamer ring (Fig. 2-7A). Remarkably, this large offset positions the P6-NBD1 adjacent the P1-NBD2, resulting in an in an NBD1-NBD2 interaction that connects the AAA+ domains in a two-turn spiral (Fig. 2-7C). Although at a slightly lower resolution compared to other protomers, density is well defined in this region and reveals interactions that are mediated by the B3 and B6 connecting loops from the P6-NBD1 and helices E2 and E3 from the P1-NBD2 (Fig. 2-9). Density corresponding to the P1-CTD also contacts the P6 NBD1, towards the outside of the channel, potentially stabilizing the interaction.

Despite the unusual NBD1-NBD2 interaction, density is present that corresponds to bound nucleotide for the P1-NBD2, indicating a potentially active, catalytic site (Fig. 2-9). While

the inter-protomer AAA+ interaction is different compared to the more canonical interfaces at the other sites, putative arginine finger residues R334 and R333 in the P6-NBD1 are localized approximately 10-12 Å away from the P1-NBD2 nucleotide pocket. Interestingly, another highly conserved arginine residue, R307 in P6, is within 5 Å of the P1-NBD2 pocket. Thus, either a small conformational change that repositions R334 or R333 or activation by R307 could support ATP hydrolysis. In contrast, density is not observed in the P1-NBD1 pocket, indicating nucleotide is not present (Fig. 2-9).

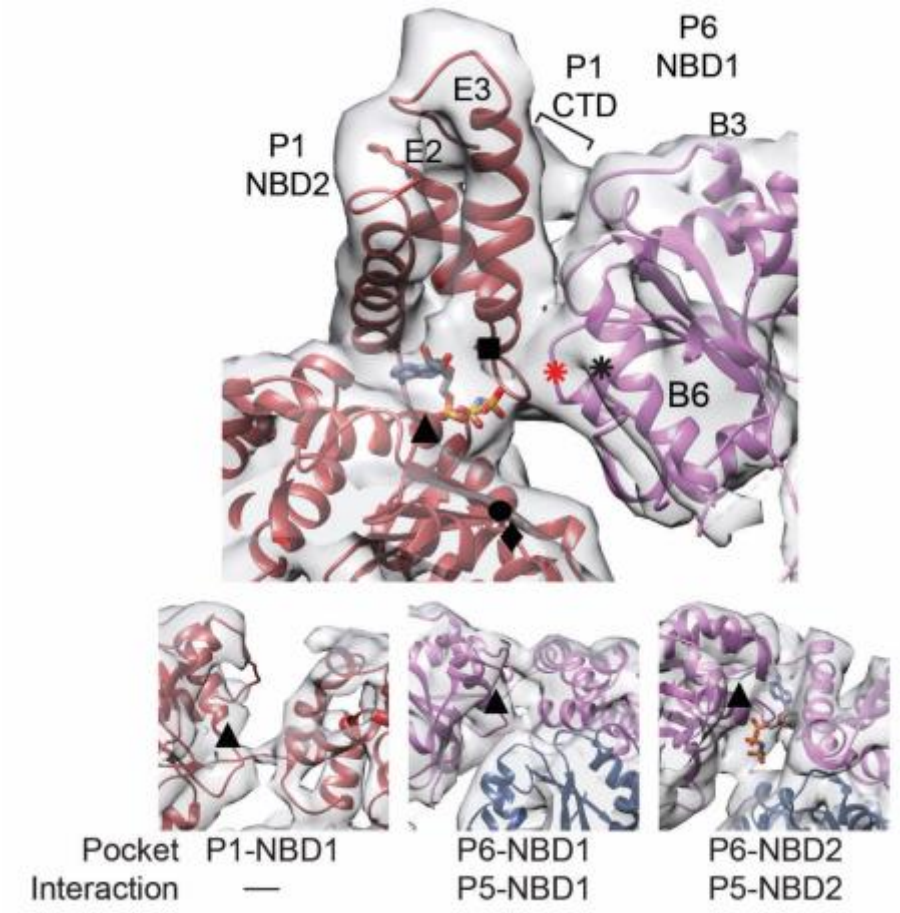

Figure 2-9. Expanded view of the model and map showing the NBD1–NBD2 interaction from inside the channel. Interface regions are indicated: B3 and B6 helices (NBD1 large subdomain), E2 and E3 helices (NBD2 small subdomain) and the P1 CTD. Positions for the Walker A (triangle) and B (diamond), Sensor 1 (circle) and 2 (square) and putative arginine finger R333, R334 (asterisk) and R307 (red asterisk) residues are indicated. Sub-panels show nucleotide pockets for the P1-NBD1, P6-NBD1 and P6-NBD2 with Walker A residues (triangle)

indicated. Nucleotide is shown for sites where density is observed in the pocket. The cryo-EM figures were created by Adam Yokom (Southworth lab, University of Michigan).

However, because of the protomer offset, P1-NBD1 is not supported by an adjacent AAA+ domain from P6, thus the nucleotide pocket is likely destabilized and inactive. Despite the adjacent P5-NBD1 in an apparent canonical orientation, density in the P6-NBD1 pocket appears weak relative to the other protomers, indicating partial occupancy or flexibility. Finally, density for nucleotide is observed for the P6-NBD2; this site is supported by the adjacent P5-NBD2, which is in a similar arrangement to the other protomers. Overall, comparison of the AAA+ domains for protomers 1 and 6 reveals a mix of nucleotide states and an asymmetric structural organization with distinct interactions relative to the rest of the hexamer that potentially support unique functions during disaggregation.

2.6 Arrangement of the MD and NTD highlight critical functions

The conserved NTDs bind hydrophobic regions of substrates and are proposed to direct polypeptides to the NBD pore loops as well as enhance cooperative substrate binding required for amyloid disaggregation (Rosenzweig et al. 2015; Sweeny et al. 2015). In our Hsp104 map the P1-P5 NTDs surround the axial channel, forming a C-shaped entrance that is approximately 35 Å in diameter (Fig. 2-10A). The opening widens substantially to approximately 50 Å moving towards the P6 NTD at the hexamer seam, creating a large cleft that opens along the side of the hexamer. Although the P6-NTD is more flexible and less well resolved, interactions between the adjacent P5-NTD as well as an unusual interaction with P1-NBD2 are identified when viewed at a reduced threshold for the density (Fig. 2-10A). Because of the NTD separation, the P1-NBD1 largely defines an equatorial channel entrance. Based on the arrangement in the other protomers, the P1-MD would extend across the cleft towards the P6-NTD, however density was not sufficiently resolved for localization. Based on modeling the P2-P4 NTDs, only the P3 NTD

appears to be positioned with its hydrophobic substrate-binding cleft (Rosenzweig et al. 2015) facing towards the channel, while the P2 and P4 NTDs each adopt different orientations (Fig. 2-10B). Thus, while the NTDs interact to form a defined ring at the channel entrance, the interfaces are variable and multiple conformations are adopted around the hexamer, which could enable binding to heterogeneous protein aggregate surfaces.

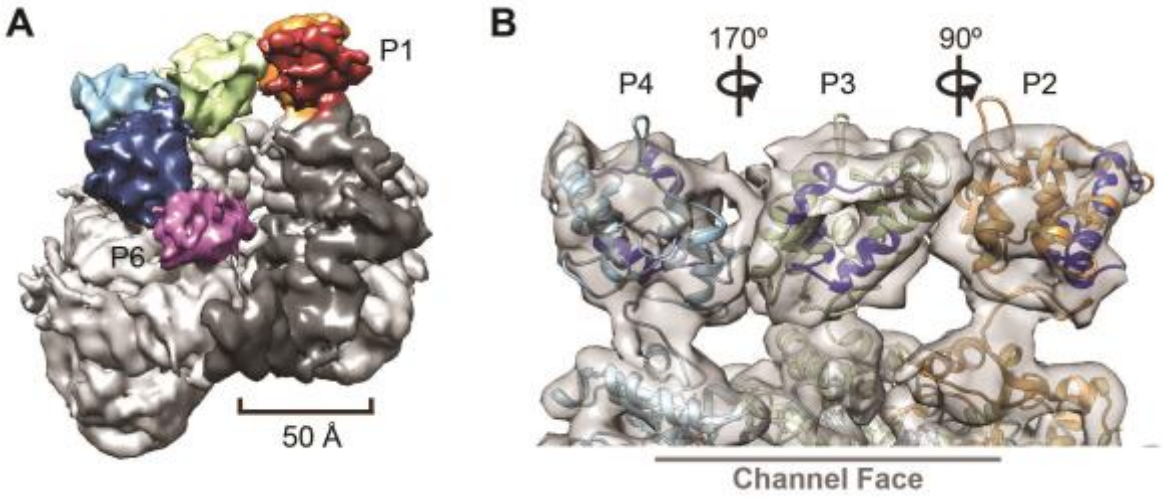

Figure 2-10. Distinct arrangements of the NTD, MD and CTD in the hexamer. (A) 3D map in a tilted orientation showing the NTDs, colored by protomer, interacting around the channel entrance and the 50 Å-wide cleft defined by the P1 and P6 NTDs and P1 AAA+ (dark grey). (B) Enlarged view of the modeled P2-P4 NTDs showing different orientations around the NBD1 connecting linker. Rotations are relative to P3, and hydrophobic substrate binding sites (Rosenzweig et al. 2015) are indicated (blue). The cryo-EM figures were created by Adam Yokom (Southworth lab, University of Michigan).

Conversely, the channel exit on the opposite face of the hexamer is largely defined by the NBD2, however an additional lobe of density is observed in all protomers, which we predict corresponds to the 38-residue CTD (Fig. 2-11A). The density emerges from the NBD2 C-terminal site identified based on ClpB and extends to form a defined bridge connection to the adjacent protomer by contacting helix D11 in NBD2 (Fig. 2-11B). The interaction likely stabilizes the hexamer, supporting previous studies (Mackay et al. 2008) and the CTD position around the channel exit also rationalizes previously proposed functions in cochaperone binding

(Abbas-Terki et al. 2001), and thus could serve as a docking point for substrate hand-off to downstream chaperone systems.

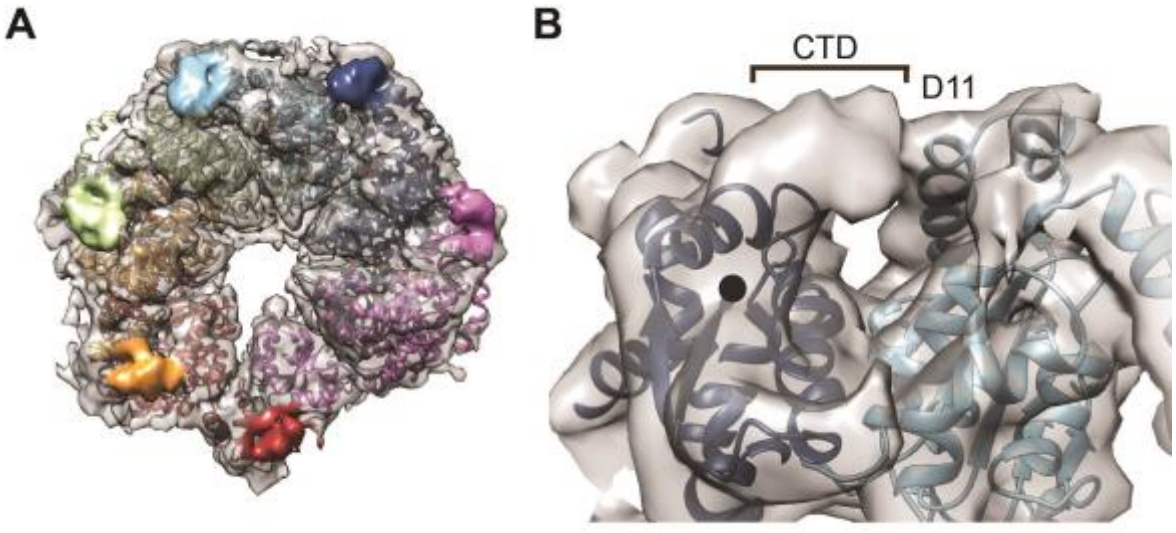

Figure 2-11. Density for CTD between protomers. (A) View of the NBD2 channel exit face of the hexamer with the density corresponding to the CTDs colored by protomer. (B) Enlarged view of the P5-CTD density extending from the NBD2 C-terminus (circle) and interacting with P4-NBD2, adjacent helix D11. The cryo-EM figures were created by Adam Yokom (Southworth lab, University of Michigan).

Based on the fit of the MD L1-L2 helices for P3-P6, the MD is rotated 47° rotation compared to the crystal structure and directly contacts NBD1 of the adjacent protomer (Fig. 2-12A). L1 and L2 are positioned alongside the clockwise neighbor, and together with helix C3, form a 60 Å-long strap across the small and large AAA+ subdomains (Fig. 2-12B). The interaction is with the opposite protomer that makes up the canonical AAA+ interface, such that each NBD1 is supported by the MD of one neighbor and the large AAA+ subdomain of the other neighbor. Density in this region is well defined for helix L1, which contacts helix C1, the C1-C2 connecting loop and part of helix B3 in the neighboring protomer. The interaction appears to involve conserved residues R419, E427, and D434, which have been previously identified to be critical for function (Wendler et al. 2007; Dulle, Stein, and True 2014; Oguchi et al. 2012). We

identify that these residues are positioned to interact with E190, R353 and R366, respectively, in the adjacent NBD1, potentially making stabilizing salt-bridge interactions (Fig. 2-12C).

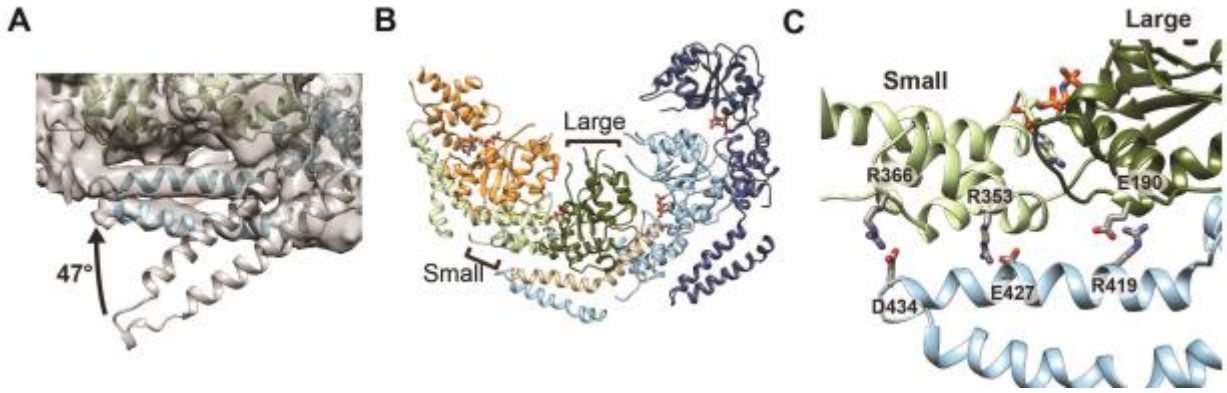

Figure 2-12. MD makes contact with neighboring NBD1. (A) Comparison between the MD L1-L2 orientation based on the docked ClpB structure (S. Lee et al. 2003) (grey) and Hsp104 model showing 47° rotation around C3-L1 connecting residues (409-410) to fit the density. (B) View of the NBD1-MD interactions for P2-P5, showing helices C3-L1 (brown) bridging across the large (dark green) and small (light green) subdomains of the adjacent protomer.(C) Views showing model with proposed salt bridge interactions between MD-L1 and adjacent NBD1 that bridge the large and small AAA+ subdomains across nucleotide-binding pocket. The cryo-EM figures were created by Adam Yokom (Southworth lab, University of Michigan).

2.7 Spiral staircase of pore loops defines the substrate path

Each NBD contains flexible loop regions that harbor the conserved Tyr residues (Tyr 257 for NBD1 and Tyr 662 in NBD2) that bind polypeptide substrates and are required for disaggregation (Weibezahn et al. 2004; Lum et al. 2004; Tessarz, Mogk, and Bukau 2008; Schlieker et al. 2004). These pore loops, however, are not resolved in the ClpB structure (S. Lee et al. 2003) and how polypeptides could be actively transferred from protomer to protomer and across the two AAA+ domains has been unclear. By flexible fitting we were able to model pore loop residues for NBD1 (excluding residues 253-258) and NBD2 (excluding residues 660-666) within large lobes of density identified in the channel (Fig. 2-13A). The NBD1 and NBD2 pore loops are separated by 35-40 Å, depending on the protomer, and project toward the channel axis

in a staggered, counter clockwise arrangement looking down the N-terminal channel entrance (Fig. 2-13B).

Seen from inside the channel, the NBD1 and NBD2 pore loops form a two-turn spiral staircase (Fig. 2-13B). The P1-NBD1 pore loop is nearest to the NTD channel cleft and each subsequent loop is 15-20 Å away, moving further into the channel towards the P6-NBD2 (Fig. 2-13C). The distances between the pore loops vary, with greater separation near the hexamer seam, particularly between P5 and P6, which are separated by 20 Å, reflecting conformational differences in the protomers. Notably, we observe additional lobes of density located beneath the NBD1 pore loops, corresponding to residues 288-298, which could serve as additional substrate binding surfaces via electrostatic interactions. Indeed, this corresponding region in ClpA has been shown to interact directly with substrate (Hinnerwisch et al. 2005). The position of NBD1 loops are approximately 10 Å away from the respective NTDs for each protomer, thus substrates could be transferred to the NBD at multiple sites around the channel. Remarkably, the heteromeric NBD1-NBD2 interaction at the hexamer seam positions the respective pore loops 17 Å apart, similar to the other distances, revealing a contiguous substrate transfer pathway between the AAA+ domains.

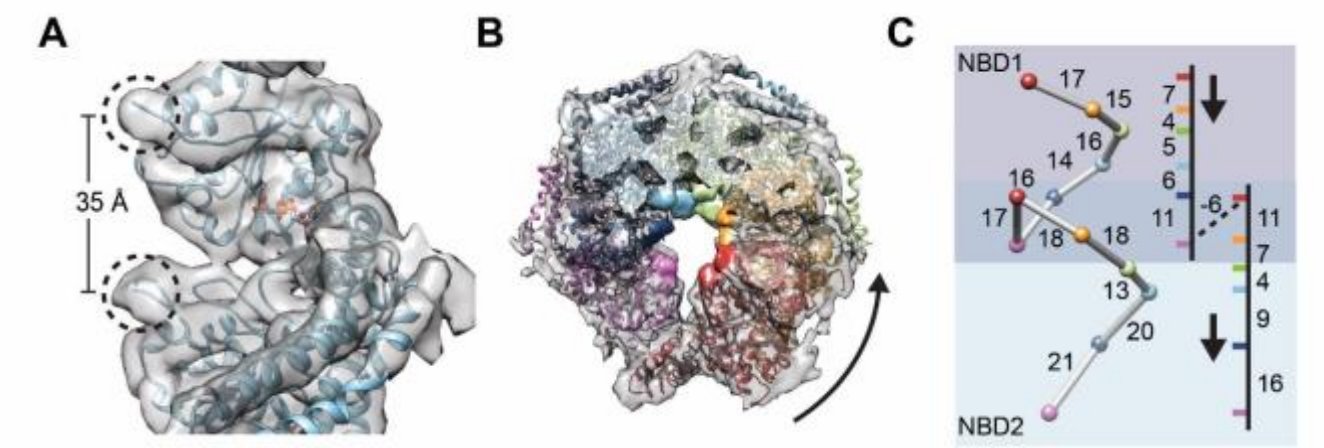

Figure 2-13. Two-turn spiral arrangement of the substrate-binding Tyr pore loops around the channel. (A) Density corresponding to the Tyr pore loops (circled) for NBD1 and NBD2 is shown for P4. (B) View down the channel from the NBD1 face with the pore loop densities colored according to protomer. Arrow indicates counter-clockwise shift between adjacent protomers moving down the channel. (C) Distances between the pore loops and corresponding movement down the channel axis are shown in Å. The cryo-EM figures were created by Adam Yokom (Southworth lab, University of Michigan).

2.8 Discussion

Achieving a definitive structure of the active Hsp104 hexamer has been a bottleneck to understanding how these conserved AAA+ complexes function as disaggregase machines. Previous cryo-EM structures were critical in revealing the overall hexameric three-tier architecture (S. Lee, Choi, and Tsai 2007; Wendler et al. 2007, 2009; S. Lee et al. 2010) but were limited in resolution, likely due to available cryo-EM technology, heterogeneity, and imposed symmetry. By utilizing the latest cryo-EM technical advances and acquiring a substantial single particle dataset for exhaustive classification and alignment, we have achieved a structure of Hsp104 that reveals, for the first time, that the hexamer adopts an asymmetric, near-helical architecture that connects the AAA+ domains around the channel. This unprecedented spiral arrangement provides a structural mechanism that explains how cooperative interactions between the protomers and across the AAA+ domains by Hsp104 might drive processive polypeptide translocation (Sweeny et al. 2015; Hattendorf and Lindquist 2002; DeSantis et al. 2012).

The left-handed helical organization establishes a substrate-binding path that appears optimally organized for transfer from protomer to protomer counter clockwise around the channel thereby achieving directional polypeptide movement from the NTD entrance to the NBD2 exit. The NBD1-NBD2 interaction aligns the pore loops, facilitating substrate transfer across the AAA+ domains, and enabling two or more cycles of interaction per protomer. This mechanism is likely necessary for substrates such as structured amyloids that are dependent on high protomer cooperativity and action from both AAA+ domains (DeSantis et al. 2012). Polypeptide threading could occur more stochastically or involve a subset of protomers, such as for disordered, unstructured aggregates, as proposed in previous studies (Doyle, Hoskins, and Wickner 2012; DeSantis et al. 2012). Nonetheless, the staircase arrangement of binding surfaces explains how Hsp104 can cooperatively utilize both AAA+ domains for more powerful unfolding. This is a remarkable extension of unidirectional threading models based on the asymmetric architecture of ClpX (Mogk, Kummer, and Bukau 2015; Glynn et al. 2009), which exhibits a staggered arrangement of pore loops around its single AAA+ ring. While the translocation step size is unknown for Hsp104, it is expected to be less than 30 Å based on measurements of ClpB (T. Li et al. 2015), ClpX (Aubin-Tam et al. 2011; Maillard et al. 2011) and ClpA (Olivares et al. 2014). The 15-20 Å distance between pore loops we identify is in agreement, indicating polypeptide translocation occurs by short, stepwise transfer events. Given the homology, we expect related ClpB and other type II Hsp100 family members could adopt a similar spiral architecture as Hsp104. Indeed, the ClpA (Guo et al. 2002) and ClpB (S. Lee et al. 2003) protomers each form unique right-handed spirals in the crystal. However, both display mechanistic differences: ClpA functions in conjunction with a bound ClpP protease (Alexopoulos, Guarné, and Ortega 2012), while ClpB is proposed to operate via non-processive

translocation events (DeSantis et al. 2012; T. Li et al. 2015), thus these complexes may adopt different hexamer arrangements in solution.

The asymmetric seam and protomer offset presents a unique architecture that is likely functionally significant. The P1 NTD and NBD1 substrate binding surfaces are at the topmost axial position and accessible due to the 50 Å-wide cleft formed by separation of P1 and P6 NTDs (Fig. 2-10). Thus, initial substrate engagement could involve preferential interactions with this protomer, followed by sequential downstream transfer to P2-P6. Furthermore, the cleft at the hexamer seam opens directly to the P1-NTD and MD, thereby presenting an optimal site for Hsp70 to interact and transfer substrates to the channel. The interface at the hexamer seam may also play critical roles in the functional plasticity of Hsp104 (Sweeny et al. 2015), facilitating recognition and engagement of different aggregate structures. Finally, given known nucleotide-dependent dynamics of the hexamer (Werbeck, Schlee, and Reinstein 2008), a compelling mechanism is that reorganization of the protomer offset is triggered by substrate binding, Hsp70 interaction or ATP hydrolysis to facilitate translocation.

A number of different MD arrangements have been proposed based on previous low-resolution models (S. Lee et al. 2003; S. Lee, Choi, and Tsai 2007; Wendler et al. 2007; Carroni et al. 2014; S. Lee et al. 2010). Our structure reveals the clearest view to date of the MD conformation in the ATP state and identifies bridging interactions between L1 and L2 and the small and large subdomains of the adjacent protomer, potentially stabilizing the nucleotide pocket for hydrolysis. Identification of potential salt bridge interactions involving R419, E427, and D434 (Fig. 2-12C) supports fluorescence resonance energy transfer experiments with ClpB that identify contact between L1 and the adjacent NBD1 (Oguchi et al. 2012), and mutagenesis studies showing Hsp104-R419M is functionally deficient (Wendler et al. 2007). DnaK/Hsp70

binds the opposite end of the MD coil-coil at helices L2 and L3 to deliver substrates and promote disaggregation (Rosenzweig et al. 2013; J. Lee et al. 2013; Haslberger et al. 2007). The MD L1-L2 interactions may serve as control elements for allosteric activation by DnaK/Hsp70 during substrate delivery (Seyffer et al. 2012; Oguchi et al. 2012). Indeed, mutations in L1 eliminate collaboration with Hsp70 (Desantis et al. 2014) and enable disaggregation to occur independently of Hsp70 and Hsp40 (Jackrel et al. 2014).

In addition to our results here, a number of recent cryo-EM structures of AAA+ complexes, including, in particular, the Pex1-Pex6 (Blok et al. 2015) and NSF (Zhao et al. 2015) double AAA+ ring complexes, have identified asymmetric states. Together this work is beginning to reveal that AAA+ proteins in general operate via large asymmetries in the protomer organization and hydrolysis mechanisms (Glynn et al. 2009). The Hsp104 structure we have determined here is the first AAA+ complex, to our knowledge, identified to adopt a two-turn spiral involving interaction between the different AAA+ (NBD1-NBD2) domains. Both Pex1-Pex6 and NSF complexes exhibit a planar, symmetric NBD1 ring that is flexibly connected to an asymmetric NBD2 ring. In Hsp104, the orientation between the two AAA+ domains within a protomer is relatively consistent around the ring except for the hexamer seam. At this position, conformational differences between P6 and P1, including a 20° rotation of NBD2 relative to NBD1, enable the NBD1-NBD2 interaction that maintains a closed hexamer ring despite the substantial, 100° rotation around the channel axis (compared to ~50° for the other protomers) (Fig. 2-7A). In addition we identified density corresponding to a bound nucleotide for 9 out of 12 ATP binding sites, while two sites show partial occupancy and one site is empty. This finding is consistent with previous estimates for nucleotide occupancy of 8-12 nucleotides for ClpB hexamers (Carroni et al. 2014; Lin and Lucius 2016), and supports an asymmetric hydrolysis

mechanism. Intriguingly, the NBD1s overall have reduced nucleotide occupancy compared to the NBD2s, which are completely bound. Similarly, kinetic studies determined that the NBD1 has a reduced ATP affinity but much higher catalytic activity compared to the NBD2 (Hattendorf and Lindquist 2002), supporting distinct functions during disaggregation. Nonetheless, with this overall high nucleotide occupancy together with the spiral architecture, the power of the two AAA+ domains appears to be uniquely coupled for Hsp104 compared to other AAA+ complexes and is perhaps reflective of the mechanical force required for disaggregation. Additional studies will be critical in elucidating conformational changes associated with ATP hydrolysis-dependent translocation events to understand the mechanical changes that drive disaggregation.

2.9 Materials and Methods

Protein Purification, ATPase and Luciferase Reactivation Assay. Wild type Hsp104 was purified as described (Jackrel et al. 2014). Hexameric Hsp104 (0.042 μM) was incubated with ATP (1 mM) at 25°C before monitoring the release of inorganic phosphate over 5 minutes using a malachite green kit (Innova). ATPase turnover was measured at a maximum rate of ~11min, which corresponded to a functional, ATPase-active complex. Disaggregase function was measured by a luciferase reactivation assay as previously described (DeSantis et al. 2012). Aggregated luciferase (50nM) was incubated with Hsp104 (0.167μM hexamer) in the presence of equimolar Hsc70 and Hdj2 (Enzo Life Sciences) plus ATP (5.1 mM) and an ATP regeneration system (1 mM creatine phosphate, 0.25μM creatine kinase) for 90 min at 25°C.

Cryo Sample Preparation and Data Collection. WT Hsp104 (8.5 mg/mL) was incubated with AMP-PNP (5 mM) for 20 minutes at 25°C. Samples were diluted to 0.7 mg/ml in 40 mM HEPES pH=7.5, 40 mM NaCl, 10 mM $MgCl_2$, 1 mM DTT, 5mM AMP-PNP and 3.5 μl was applied to plasma cleaned C-Flat 2/2 holey carbon grids (Protochips). Vitrification was

performed using a Vitrobot (FEI Company) and samples were blotted for 1.5-2 seconds prior to plunge freezing in liquid ethane. Of note, during initial attempts at imaging Hsp104 routinely dissociated into monomers and substantial optimization of buffer conditions, sample concentration and freezing conditions was required to achieve proper ice thickness and a homogeneous spread of hexameric particles. Furthermore, the presence of DDM detergent was tested to increase the angular distribution but resulted in dissociation of the hexamer at a variety of concentrations.

Samples were imaged using a Titan Krios TEM (FEI Inc.) operated at 300 kV. Images were recorded on a Gatan K2 Summit direct electron detector operated in counted mode at 50,000X nominal magnification corresponding to a calibrated to 1.00 Å/pixel. Dose fractionated imaging was performed by semi-automated collection methods using UCSF Image 4 (X. Li et al. 2015) with a defocus range of 1.5-3 um. Total exposure time was 8 seconds with 0.2 second frames with a cumulative dose of ~45 e^- per $Å^2$ for 40 frames. Motion corrected frames were summed with the first two frames excluded, and the FFT was visually inspected for sufficient Thon rings prior to additional processing (X. Li et al. 2013).

Image Processing and 3D Refinement. All micrographs were CTF corrected using CTFFIND4 (Rohou and Grigorieff 2015) and poorly corrected micrographs were removed following visual inspection of the FFT and CTF estimation. An initial single particle dataset was achieved by manual particle picking using e2boxer (EMAN2) (Tang et al. 2007), which yielded ~50,000 particles from 1731 micrographs. Well-populated reference-free 2D class averages, determined with Relion (Scheres 2012), were used for templated automated particle picking with the Template Picker in Appion (Lander et al. 2009) to achieve a ~200,000 single particles dataset from 1930 micrographs. The total dataset of ~250,000 particles was initially sorted following 2D

classification by removing particles images from poorly resolved class averages, resulting in a total dataset of ~190,000 particles. All subsequent 3D processing was performed using Relion (Scheres 2012) with no symmetry imposed based on the asymmetric arrangement identified in the 2D class averages (Fig. 2-1D). A previously determined cryo-EM 3D reconstruction of ATP–Hsp104 (EMDB: 1600) (Wendler et al. 2009), low pass filtered to 50Å, served as an initial model for 3D classification and refinement. The 8 models generated from 3D classification appeared homogenous, therefore, the full dataset was used for initial gold-standard 3D refinement. The resulting 3D model refined to an estimated resolution of 7.5 Å. Z-score parameters based on this refinement, defined in Relion, were written for the data set and the dataset was trimmed to the highest Z-score for 160,000 particles. Additional 3D refinement was performed with this trimmed data set and resulted in a final model with an estimated resolution of 6.54 Å using the FSC = 0.143 FSC criterion (Fig. 2-2C). Additional trimming based on the Z-score showed no improvement and extensive 3D classification and refinement of individual classes as well as local refinement using 3D masking was tested and did not yield improvements in the map. Thus, the resolution is likely limited by flexibility of multiple regions in the complex and moderate preferred orientation. For the final sharpened map, the "Post-processing" procedure was used to generate a soft mask for the two half maps prior to FSC estimation, which was determined to be 5.64 Å (Fig. 2-2C). Automated B-factor sharpening was carried on the combined map with an estimated -188 B-factor. The local resolution was estimated using ResMap on the unsharpened map (Kucukelbir, Sigworth, and Tagare 2014).

Modeling. This final sharpened map was used for all rigid body docking and flexible fitting of atomic structures. Rigid body fitting was performed with UCSF Chimera (Pettersen et al. 2004). Initial comparisons were performed by fitting individual protomers with the protomers in *T.*

thermophilus ClpB crystal structure (PBD_ID=1qvr), but resulted in a low cross correlation value and clear conformational differences were apparent. Individual subdomains (NTD, NBD1 large, NBD1 small, MD (residues 409-467), NBD2 large, NBD2 small) from the crystal structure were then docked as rigid bodies and resulted in an improved fit, however a number of AAA+ domain helices did not align with the density. Therefore, to more accurately interrupt the map, a homology model of Hsp104 (residues 6-857) was determined from the ClpB structure (residues 4-850) using SWISS_MODEL(Biasini et al. 2014) followed by rigid body docking the subdomains. Flexible fitting of the protomer sub volumes and the entire hexamer map was then performed using phenix.real_space_refine (Afonine et al. 2012) using backbone carbons of our homology model. The real space refinement was implemented at 6σ, resolution 6Å and the cross correlation improved from 0.72 to 0.9 for the complete map after refinement. To visualize whether density is present in the nucleotide pockets difference maps were generated by subtracting a simulated density map of the Hsp104 homology model without AMPPNP from the final refined map and shown at 5σ (Fig. 2-6). Based on the difference map, clear density was observed at 9 sites and partial density at two sites, therefore AMPPNP was included in the model at these sites and docked based on the ClpB structure. Modeling the P2-P4 NTDs was facilitated by localization of the well-defined NTD-NBD1 connecting density as well as regions that could be attributed to the larger A1 and A6 helices that make up the hydrophobic substrate-binding cleft (Rosenzweig et al. 2015). Manual modeling of the tyrosine loop regions was performed in COOT (Emsley et al. 2010). Loop regions within the NBD1 domain (248-260,287-300) were modeled by backbone positioning within the density; residues 251-259, 292-297 could not be modeled in the density. Of note, a major shift was required to model the NBD2 tyrosine loop (656-669), which showed a distinct curve away from the flanking helices. Similarly, the most

central portion of the loop lacked density and was not modeled (659-666). All images were generated using UCSF Chimera (Pettersen et al. 2004).

2.10 References

Abbas-Terki, T., O. Donzé, P. A. Briand, and D. Picard. 2001. "Hsp104 Interacts with Hsp90 Cochaperones in Respiring Yeast." *Molecular and Cellular Biology* 21 (22): 7569–75. doi:10.1128/MCB.21.22.7569-7575.2001.

Afonine, Pavel V., Ralf W. Grosse-Kunstleve, Nathaniel Echols, Jeffrey J. Headd, Nigel W. Moriarty, Marat Mustyakimov, Thomas C. Terwilliger, Alexandre Urzhumtsev, Peter H. Zwart, and Paul D. Adams. 2012. "Towards Automated Crystallographic Structure Refinement with Phenix.Refine." *Acta Crystallographica. Section D, Biological Crystallography* 68 (Pt 4): 352–67. doi:10.1107/S0907444912001308.

Aguado, Alejandra, José Angel Fernández-Higuero, Yovana Cabrera, Fernando Moro, and Arturo Muga. 2015. "ClpB Dynamics Is Driven by Its ATPase Cycle and Regulated by the DnaK System and Substrate Proteins." *The Biochemical Journal* 466 (3): 561–70. doi:10.1042/BJ20141390.

Alexopoulos, John A., Alba Guarné, and Joaquin Ortega. 2012. "ClpP: A Structurally Dynamic Protease Regulated by AAA+ Proteins." *Journal of Structural Biology* 179 (2): 202–10. doi:10.1016/j.jsb.2012.05.003.

Aubin-Tam, Marie-Eve, Adrian O. Olivares, Robert T. Sauer, Tania A. Baker, and Matthew J. Lang. 2011. "Single-Molecule Protein Unfolding and Translocation by an ATP-Fueled Proteolytic Machine." *Cell* 145 (2): 257–67. doi:10.1016/j.cell.2011.03.036.

Biasini, Marco, Stefan Bienert, Andrew Waterhouse, Konstantin Arnold, Gabriel Studer, Tobias Schmidt, Florian Kiefer, et al. 2014. "SWISS-MODEL: Modelling Protein Tertiary and Quaternary Structure Using Evolutionary Information." *Nucleic Acids Research* 42 (Web Server issue): W252-258. doi:10.1093/nar/gku340.

Blok, Neil B., Dongyan Tan, Ray Yu-Ruei Wang, Pawel A. Penczek, David Baker, Frank DiMaio, Tom A. Rapoport, and Thomas Walz. 2015. "Unique Double-Ring Structure of the Peroxisomal Pex1/Pex6 ATPase Complex Revealed by Cryo-Electron Microscopy." *Proceedings of the National Academy of Sciences of the United States of America* 112 (30): E4017-4025. doi:10.1073/pnas.1500257112.

Bösl, Benjamin, Valerie Grimminger, and Stefan Walter. 2005. "Substrate Binding to the Molecular Chaperone Hsp104 and Its Regulation by Nucleotides." *The Journal of Biological Chemistry* 280 (46): 38170–76. doi:10.1074/jbc.M506149200.

Carroni, Marta, Eva Kummer, Yuki Oguchi, Petra Wendler, Daniel K. Clare, Irmgard Sinning, Jürgen Kopp, Axel Mogk, Bernd Bukau, and Helen R. Saibil. 2014. "Head-to-Tail Interactions of the Coiled-Coil Domains Regulate ClpB Activity and Cooperation with Hsp70 in Protein Disaggregation." *ELife* 3 (April): e02481.

Chernoff, Y. O., S. L. Lindquist, B. Ono, S. G. Inge-Vechtomov, and S. W. Liebman. 1995. "Role of the Chaperone Protein Hsp104 in Propagation of the Yeast Prion-like Factor [Psi+]." *Science (New York, N.Y.)* 268 (5212): 880–84.

Cushman-Nick, Mimi, Nancy M. Bonini, and James Shorter. 2013. "Hsp104 Suppresses Polyglutamine-Induced Degeneration Post Onset in a Drosophila MJD/SCA3 Model." *PLoS Genetics* 9 (9): e1003781. doi:10.1371/journal.pgen.1003781.

DeSantis, Morgan E., Eunice H. Leung, Elizabeth A. Sweeny, Meredith E. Jackrel, Mimi Cushman-Nick, Alexandra Neuhaus-Follini, Shilpa Vashist, Matthew A. Sochor, M. Noelle Knight, and James Shorter. 2012. "Operational Plasticity Enables Hsp104 to Disaggregate Diverse Amyloid and Nonamyloid Clients." *Cell* 151 (4): 778–93. doi:10.1016/j.cell.2012.09.038.

Desantis, Morgan E., Elizabeth A. Sweeny, David Snead, Eunice H. Leung, Michelle S. Go, Kushol Gupta, Petra Wendler, and James Shorter. 2014. "Conserved Distal Loop Residues in the Hsp104 and ClpB Middle Domain Contact Nucleotide-Binding Domain 2 and Enable Hsp70-Dependent Protein Disaggregation." *The Journal of Biological Chemistry* 289 (2): 848–67. doi:10.1074/jbc.M113.520759.

Doyle, Shannon M., Joel R. Hoskins, and Sue Wickner. 2012. "DnaK Chaperone-Dependent Disaggregation by Caseinolytic Peptidase B (ClpB) Mutants Reveals Functional Overlap in the N-Terminal Domain and Nucleotide-Binding Domain-1 Pore Tyrosine." *The Journal of Biological Chemistry* 287 (34): 28470–79. doi:10.1074/jbc.M112.383091.

Dulle, Jennifer E., Kevin C. Stein, and Heather L. True. 2014. "Regulation of the Hsp104 Middle Domain Activity Is Critical for Yeast Prion Propagation." *PloS One* 9 (1): e87521. doi:10.1371/journal.pone.0087521.

Emsley, P., B. Lohkamp, W. G. Scott, and K. Cowtan. 2010. "Features and Development of Coot." *Acta Crystallographica. Section D, Biological Crystallography* 66 (Pt 4): 486–501. doi:10.1107/S0907444910007493.

Glover, J. R., and S. Lindquist. 1998. "Hsp104, Hsp70, and Hsp40: A Novel Chaperone System That Rescues Previously Aggregated Proteins." *Cell* 94 (1): 73–82.

Glynn, Steven E., Andreas Martin, Andrew R. Nager, Tania A. Baker, and Robert T. Sauer. 2009. "Structures of Asymmetric ClpX Hexamers Reveal Nucleotide-Dependent Motions in a AAA+ Protein-Unfolding Machine." *Cell* 139 (4): 744–56. doi:10.1016/j.cell.2009.09.034.

Guo, Fusheng, Michael R. Maurizi, Lothar Esser, and Di Xia. 2002. "Crystal Structure of ClpA, an Hsp100 Chaperone and Regulator of ClpAP Protease." *The Journal of Biological Chemistry* 277 (48): 46743–52. doi:10.1074/jbc.M207796200.

Haslberger, Tobias, Jimena Weibezahn, Regina Zahn, Sukyeong Lee, Francis T. F. Tsai, Bernd Bukau, and Axel Mogk. 2007. "M Domains Couple the ClpB Threading Motor with the DnaK Chaperone Activity." *Molecular Cell* 25 (2): 247–60. doi:10.1016/j.molcel.2006.11.008.

Hattendorf, Douglas A., and Susan L. Lindquist. 2002. "Cooperative Kinetics of Both Hsp104 ATPase Domains and Interdomain Communication Revealed by AAA Sensor-1 Mutants." *The EMBO Journal* 21 (1–2): 12–21. doi:10.1093/emboj/21.1.12.

Hinnerwisch, Jörg, Wayne A. Fenton, Krystyna J. Furtak, George W. Farr, and Arthur L. Horwich. 2005. "Loops in the Central Channel of ClpA Chaperone Mediate Protein Binding, Unfolding, and Translocation." *Cell* 121 (7): 1029–41. doi:10.1016/j.cell.2005.04.012.

Jackrel, Meredith E., Morgan E. DeSantis, Bryan A. Martinez, Laura M. Castellano, Rachel M. Stewart, Kim A. Caldwell, Guy A. Caldwell, and James Shorter. 2014. "Potentiated Hsp104 Variants Antagonize Diverse Proteotoxic Misfolding Events." *Cell* 156 (1–2): 170–82. doi:10.1016/j.cell.2013.11.047.

Jackrel, Meredith E., and James Shorter. 2014. “Reversing Deleterious Protein Aggregation with Re-Engineered Protein Disaggregases.” *Cell Cycle (Georgetown, Tex.)* 13 (9): 1379–83. doi:10.4161/cc.28709.

Kedzierska, Sabina, Vladimir Akoev, Micheal E. Barnett, and Michal Zolkiewski. 2003. “Structure and Function of the Middle Domain of ClpB from Escherichia Coli.” *Biochemistry* 42 (48): 14242–48. doi:10.1021/bi035573d.

Kucukelbir, Alp, Fred J. Sigworth, and Hemant D. Tagare. 2014. “Quantifying the Local Resolution of Cryo-EM Density Maps.” *Nature Methods* 11 (1): 63–65. doi:10.1038/nmeth.2727.

Lander, Gabriel C., Scott M. Stagg, Neil R. Voss, Anchi Cheng, Denis Fellmann, James Pulokas, Craig Yoshioka, et al. 2009. “Appion: An Integrated, Database-Driven Pipeline to Facilitate EM Image Processing.” *Journal of Structural Biology* 166 (1): 95–102.

Lee, Jungsoon, Ji-Hyun Kim, Amadeo B. Biter, Bernhard Sielaff, Sukyeong Lee, and Francis T. F. Tsai. 2013. “Heat Shock Protein (Hsp) 70 Is an Activator of the Hsp104 Motor.” *Proceedings of the National Academy of Sciences of the United States of America* 110 (21): 8513–18. doi:10.1073/pnas.1217988110.

Lee, Sukyeong, Jae-Mun Choi, and Francis T. F. Tsai. 2007. “Visualizing the ATPase Cycle in a Protein Disaggregating Machine: Structural Basis for Substrate Binding by ClpB.” *Molecular Cell* 25 (2): 261–71. doi:10.1016/j.molcel.2007.01.002.

Lee, Sukyeong, Bernhard Sielaff, Jungsoon Lee, and Francis T. F. Tsai. 2010. “CryoEM Structure of Hsp104 and Its Mechanistic Implication for Protein Disaggregation.” *Proceedings of the National Academy of Sciences of the United States of America* 107 (18): 8135–40. doi:10.1073/pnas.1003572107.

Lee, Sukyeong, Mathew E. Sowa, Yo-hei Watanabe, Paul B. Sigler, Wah Chiu, Masasuke Yoshida, and Francis T. F. Tsai. 2003. “The Structure of ClpB: A Molecular Chaperone That Rescues Proteins from an Aggregated State.” *Cell* 115 (2): 229–40.

Li, Tao, Clarissa L. Weaver, Jiabei Lin, Elizabeth C. Duran, Justin M. Miller, and Aaron L. Lucius. 2015. “Escherichia Coli ClpB Is a Non-Processive Polypeptide Translocase.” *The Biochemical Journal* 470 (1): 39–52. doi:10.1042/BJ20141457.

Li, Xueming, Paul Mooney, Shawn Zheng, Christopher R. Booth, Michael B. Braunfeld, Sander Gubbens, David A. Agard, and Yifan Cheng. 2013. “Electron Counting and Beam-Induced Motion Correction Enable near-Atomic-Resolution Single-Particle Cryo-EM.” *Nature Methods* 10 (6): 584–90. doi:10.1038/nmeth.2472.

Li, Xueming, Shawn Zheng, David A. Agard, and Yifan Cheng. 2015. “Asynchronous Data Acquisition and On-the-Fly Analysis of Dose Fractionated CryoEM Images by UCSFImage.” *Journal of Structural Biology* 192 (2): 174–78. doi:10.1016/j.jsb.2015.09.003.

Lin, JiaBei, and Aaron L. Lucius. 2016. “Examination of ClpB Quaternary Structure and Linkage to Nucleotide Binding.” *Biochemistry* 55 (12): 1758–71. doi:10.1021/acs.biochem.6b00122.

Lo Bianco, Christophe, James Shorter, Etienne Régulier, Hilal Lashuel, Takeshi Iwatsubo, Susan Lindquist, and Patrick Aebischer. 2008. “Hsp104 Antagonizes Alpha-Synuclein Aggregation and Reduces Dopaminergic Degeneration in a Rat Model of Parkinson Disease.” *The Journal of Clinical Investigation* 118 (9): 3087–97. doi:10.1172/JCI35781.

Lum, Ronnie, Johnny M. Tkach, Elizabeth Vierling, and John R. Glover. 2004. “Evidence for an Unfolding/Threading Mechanism for Protein Disaggregation by Saccharomyces

Cerevisiae Hsp104." *The Journal of Biological Chemistry* 279 (28): 29139–46. doi:10.1074/jbc.M403777200.
Mackay, Ryder G., Christopher W. Helsen, Johnny M. Tkach, and John R. Glover. 2008. "The C-Terminal Extension of Saccharomyces Cerevisiae Hsp104 Plays a Role in Oligomer Assembly." *Biochemistry* 47 (7): 1918–27. doi:10.1021/bi701714s.
Maillard, Rodrigo A., Gheorghe Chistol, Maya Sen, Maurizio Righini, Jiongyi Tan, Christian M. Kaiser, Courtney Hodges, Andreas Martin, and Carlos Bustamante. 2011. "ClpX(P) Generates Mechanical Force to Unfold and Translocate Its Protein Substrates." *Cell* 145 (3): 459–69. doi:10.1016/j.cell.2011.04.010.
Mogk, Axel, Eva Kummer, and Bernd Bukau. 2015. "Cooperation of Hsp70 and Hsp100 Chaperone Machines in Protein Disaggregation." *Frontiers in Molecular Biosciences* 2: 22. doi:10.3389/fmolb.2015.00022.
Moriyama, H., H. K. Edskes, and R. B. Wickner. 2000. "[URE3] Prion Propagation in Saccharomyces Cerevisiae: Requirement for Chaperone Hsp104 and Curing by Overexpressed Chaperone Ydj1p." *Molecular and Cellular Biology* 20 (23): 8916–22.
Motohashi, K., Y. Watanabe, M. Yohda, and M. Yoshida. 1999. "Heat-Inactivated Proteins Are Rescued by the DnaK.J-GrpE Set and ClpB Chaperones." *Proceedings of the National Academy of Sciences of the United States of America* 96 (13): 7184–89.
Oguchi, Yuki, Eva Kummer, Fabian Seyffer, Mykhaylo Berynskyy, Benjamin Anstett, Regina Zahn, Rebecca C. Wade, Axel Mogk, and Bernd Bukau. 2012. "A Tightly Regulated Molecular Toggle Controls AAA+ Disaggregase." *Nature Structural & Molecular Biology* 19 (12): 1338–46. doi:10.1038/nsmb.2441.
Olivares, Adrian O., Andrew R. Nager, Ohad Iosefson, Robert T. Sauer, and Tania A. Baker. 2014. "Mechanochemical Basis of Protein Degradation by a Double-Ring AAA+ Machine." *Nature Structural & Molecular Biology* 21 (10): 871–75. doi:10.1038/nsmb.2885.
Parsell, D. A., A. S. Kowal, and S. Lindquist. 1994. "Saccharomyces Cerevisiae Hsp104 Protein. Purification and Characterization of ATP-Induced Structural Changes." *The Journal of Biological Chemistry* 269 (6): 4480–87.
Parsell, D. A., A. S. Kowal, M. A. Singer, and S. Lindquist. 1994. "Protein Disaggregation Mediated by Heat-Shock Protein Hsp104." *Nature* 372 (6505): 475–78. doi:10.1038/372475a0.
Pettersen, Eric F., Thomas D. Goddard, Conrad C. Huang, Gregory S. Couch, Daniel M. Greenblatt, Elaine C. Meng, and Thomas E. Ferrin. 2004. "UCSF Chimera--a Visualization System for Exploratory Research and Analysis." *Journal of Computational Chemistry* 25 (13): 1605–12. doi:10.1002/jcc.20084.
Rohou, Alexis, and Nikolaus Grigorieff. 2015. "CTFFIND4: Fast and Accurate Defocus Estimation from Electron Micrographs." *Journal of Structural Biology* 192 (2): 216–21. doi:10.1016/j.jsb.2015.08.008.
Rosenzweig, Rina, Patrick Farber, Algirdas Velyvis, Enrico Rennella, Michael P. Latham, and Lewis E. Kay. 2015. "ClpB N-Terminal Domain Plays a Regulatory Role in Protein Disaggregation." *Proceedings of the National Academy of Sciences of the United States of America* 112 (50): E6872-6881. doi:10.1073/pnas.1512783112.
Rosenzweig, Rina, Shoeib Moradi, Arash Zarrine-Afsar, John R. Glover, and Lewis E. Kay. 2013. "Unraveling the Mechanism of Protein Disaggregation through a ClpB-DnaK

Interaction." *Science (New York, N.Y.)* 339 (6123): 1080–83. doi:10.1126/science.1233066.
Sanchez, Y., and S. L. Lindquist. 1990. "HSP104 Required for Induced Thermotolerance." *Science (New York, N.Y.)* 248 (4959): 1112–15.
Scheres, Sjors H. W. 2012. "RELION: Implementation of a Bayesian Approach to Cryo-EM Structure Determination." *Journal of Structural Biology* 180 (3): 519–30. doi:10.1016/j.jsb.2012.09.006.
Schlieker, Christian, Jimena Weibezahn, Holger Patzelt, Peter Tessarz, Christine Strub, Kornelius Zeth, Annette Erbse, et al. 2004. "Substrate Recognition by the AAA+ Chaperone ClpB." *Nature Structural & Molecular Biology* 11 (7): 607–15. doi:10.1038/nsmb787.
Seyffer, Fabian, Eva Kummer, Yuki Oguchi, Juliane Winkler, Mohit Kumar, Regina Zahn, Victor Sourjik, Bernd Bukau, and Axel Mogk. 2012. "Hsp70 Proteins Bind Hsp100 Regulatory M Domains to Activate AAA+ Disaggregase at Aggregate Surfaces." *Nature Structural & Molecular Biology* 19 (12): 1347–55. doi:10.1038/nsmb.2442.
Shorter, James, and Susan Lindquist. 2004. "Hsp104 Catalyzes Formation and Elimination of Self-Replicating Sup35 Prion Conformers." *Science (New York, N.Y.)* 304 (5678): 1793–97. doi:10.1126/science.1098007.
Sweeny, Elizabeth A., Meredith E. Jackrel, Michelle S. Go, Matthew A. Sochor, Beatrice M. Razzo, Morgan E. DeSantis, Kushol Gupta, and James Shorter. 2015. "The Hsp104 N-Terminal Domain Enables Disaggregase Plasticity and Potentiation." *Molecular Cell* 57 (5): 836–49. doi:10.1016/j.molcel.2014.12.021.
Tang, Guang, Liwei Peng, Philip R. Baldwin, Deepinder S. Mann, Wen Jiang, Ian Rees, and Steven J. Ludtke. 2007. "EMAN2: An Extensible Image Processing Suite for Electron Microscopy." *Journal of Structural Biology* 157 (1): 38–46. doi:10.1016/j.jsb.2006.05.009.
Tessarz, Peter, Axel Mogk, and Bernd Bukau. 2008. "Substrate Threading through the Central Pore of the Hsp104 Chaperone as a Common Mechanism for Protein Disaggregation and Prion Propagation." *Molecular Microbiology* 68 (1): 87–97. doi:10.1111/j.1365-2958.2008.06135.x.
Weibezahn, Jimena, Peter Tessarz, Christian Schlieker, Regina Zahn, Zeljka Maglica, Sukyeong Lee, Hanswalter Zentgraf, et al. 2004. "Thermotolerance Requires Refolding of Aggregated Proteins by Substrate Translocation through the Central Pore of ClpB." *Cell* 119 (5): 653–65. doi:10.1016/j.cell.2004.11.027.
Wendler, Petra, James Shorter, Celia Plisson, Anil G. Cashikar, Susan Lindquist, and Helen R. Saibil. 2007. "Atypical AAA+ Subunit Packing Creates an Expanded Cavity for Disaggregation by the Protein-Remodeling Factor Hsp104." *Cell* 131 (7): 1366–77. doi:10.1016/j.cell.2007.10.047.
Wendler, Petra, James Shorter, David Snead, Celia Plisson, Daniel K. Clare, Susan Lindquist, and Helen R. Saibil. 2009. "Motor Mechanism for Protein Threading through Hsp104." *Molecular Cell* 34 (1): 81–92. doi:10.1016/j.molcel.2009.02.026.
Werbeck, Nicolas D., Sandra Schlee, and Jochen Reinstein. 2008. "Coupling and Dynamics of Subunits in the Hexameric AAA+ Chaperone ClpB." *Journal of Molecular Biology* 378 (1): 178–90. doi:10.1016/j.jmb.2008.02.026.

Zhao, Minglei, Shenping Wu, Qiangjun Zhou, Sandro Vivona, Daniel J. Cipriano, Yifan Cheng, and Axel T. Brunger. 2015. “Mechanistic Insights into the Recycling Machine of the SNARE Complex.” *Nature* 518 (7537): 61–67. doi:10.1038/nature14148.

CHAPTER 3

RATCHET-LIKE POLYPEPTIDE TRANSLOCATION MECHANISM OF THE AAA+ DISAGGREGASE HSP104

This chapter is published: SN Gates*, AL Yokom*, JiaBei Lin, ME Jackrel, AN Rizo, NM Kendsersky, CE Buell, EA Sweeny, KL Mack, E Chuang, MP Torrente, M Su, J Shorter, and DR Southworth. Ratchet-like polypeptide translocation mechanism of the AAA+ disaggregase Hsp104. *Science* **357**, 273-279 (2017).
*These authors contributed equally to this work[1]

3.1 Abstract

Hsp100 polypeptide translocases are conserved AAA+ machines that maintain proteostasis by unfolding aberrant and toxic proteins for refolding or proteolytic degradation. The Hsp104 disaggregase from *S. cerevisiae* solubilizes stress-induced amorphous aggregates and amyloid. The structural basis for substrate recognition and translocation is unknown. Using a model substrate (casein), we report cryo-EM structures at near-atomic resolution of Hsp104 in different translocation states. Substrate interactions are mediated by conserved, pore-loop tyrosines that contact an 80 Å-long unfolded polypeptide along the axial channel. Two protomers undergo a ratchet-like conformational change that advances pore-loop-substrate interactions by two-amino acids. These changes are coupled to activation of specific ATPase sites and, when transmitted

[1] My contribution to this chapter was complex formation, SEC, cryo-EM sample preparation, data collection and processing, 3D classification between open and closed states and structural analysis. Adam Yokom (Southworth lab), the co-first author, also contributed significantly to data collection, processing and atomic modeling. Alex Rizo (Southworh lab) collected cryo-EM data. Members of the Jim Shorter lab (University of Pennsylvania), including J Lin, ME Jackrel, AN Rizo, NM Kendsersky, CE Buell, EA Sweeny, KL Mack, E Chuang, MP Torrente, purified WT and mutant Hsp104 variants and performed FP experiments.

around the hexamer, reveal a processive rotary translocation mechanism and a remarkable structural plasticity of Hsp104-catalyzed disaggregation.

3.2 Introduction

Hsp100 disaggregases are highly conserved stress responders that unfold and solubilize protein aggregates (Olivares, Baker, and Sauer 2016; Sweeny and Shorter 2016). They are AAA+ (ATPases Associated with diverse cellular Activities) proteins that form hexameric rings, which couple ATP hydrolysis to polypeptide translocation through a central channel (Olivares, Baker, and Sauer 2016; Sweeny and Shorter 2016). *S. cerevisiae* Hsp104 is powered by two distinct AAA+ domains per protomer and collaborates with the Hsp70 system to disaggregate and refold amorphous aggregates and amyloids such as Sup35 prions, thereby promoting stress tolerance and prion propagation (Sweeny and Shorter 2016).

Cooperative ATP hydrolysis by nucleotide-binding domains (NBD1 and NBD2) of Hsp104 requires conserved Walker A and B motifs, 'sensor' residues, and an Arg finger from the adjacent protomer (Sweeny and Shorter 2016; Erzberger and Berger 2006). The coiled-coil middle domain (MD) of Hsp104 mediates Hsp70 interactions and allosteric functions during hydrolysis and disaggregation (Jackrel et al. 2014; Oguchi et al. 2012; J. Lee et al. 2013). Conserved substrate-binding "pore loops" in the NBDs line the axial channel and contain essential Tyr residues that mechanically couple hydrolysis to translocation (Lum et al. 2004; Tessarz, Mogk, and Bukau 2008). A recent structure of Hsp104 bound to the nonhydrolysable ATP analog, AMPPNP, identifies an "open", spiral conformation with a ~30 Å-wide channel and an unusual heteromeric NBD1-NBD2 interaction that forms a flexible seam (Yokom et al. 2016). High-resolution structures of the active hexamer have remained elusive and it is unknown how hydrolysis and conformational changes power disaggregation.

Here, we establish how Hsp104 binds and mechanically translocates substrates. Using the slowly hydrolysable ATP analog, ATPγS (Doyle et al. 2007) and the substrate casein we determined Hsp104 structures to ~4.0 Å by cryo-EM. We identify pore-loop-substrate contacts and a rotary translocation mechanism involving a ratchet-like change that advances interactions along the substrate polypeptide by two amino acids. NBD1-ATP hydrolysis and substrate binding triggers a massive open to closed conformational change in the hexamer, thereby coupling substrate engagement and release to processive disaggregation.

3.3 Forming a Stable Substrate-Bound Hsp104 Complex for Cryo-EM

Casein is a model amorphous substrate for Hsp104 that is actively translocated (Jackrel et al. 2014; Tessarz, Mogk, and Bukau 2008), therefore we used FITC-casein (Sigma) to form a stable substrate-bound Hsp104 complex. To determine the best nucleotide condition to capture the substrate-bound state of Hsp104, binding was assessed via fluorescence polarization (FP). High-affinity interactions (K_d ~ 20nM) between Hsp104 and casein were identified in the presence of ATPγS but not ATP, AMPPNP, or ADP (Fig. 3-1A). This is a bit surprising, considering Hsp104 can actively process casein in the presence of ATP (Jackrel et al. 2014), but it seems that the slowed rate of hydrolysis (Doyle et al. 2007) with ATPγS allowed casein to be trapped in a translocating step, whereas it is processed too quickly with ATP. These results were also confirmed using Size Exclusion Chromatography (SEC), showing that with ATPγS there is a significant shift in elution and an overlap of the 280nm Absorbance and 495nm Absorbance, which indicates the FITC-casein is co-eluting with Hsp104 (Fig. 3-1B). Fractions of Hsp104:casein complex were collected following SEC for cryo-EM analysis.

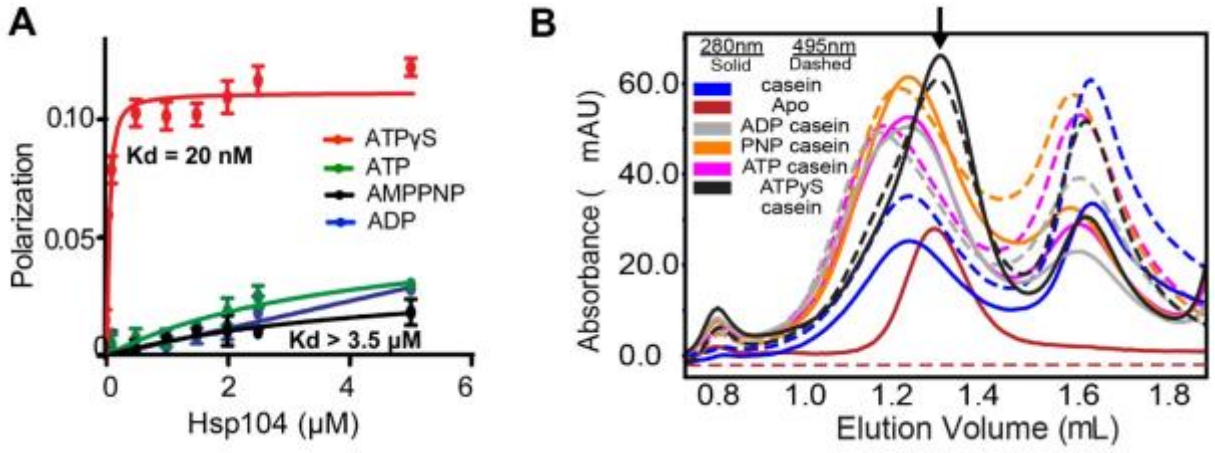

Figure 3-1. Substrate-bound Hsp104:casein closed complex. (A) FITC-casein binding analysis, measured by fluorescence polarization in the presence of: ATPγS (red), ATP (green), AMPPNP (black), and ADP (blue) (values = mean ±SD, n=3). (B) Hsp104 and casein incubated with the indicated nucleotides, showing a shift in peak elution and alignment of the absorbance curves for protein, 280 (solid), and FITC, 495 (dash) occurs specifically in the presence of ATPγS. Fraction collected for cryo-EM characterization of Hsp104:casein is indicated (arrow). FP data and figure generated by Shorter lab (University of Pennsylvania).

Initial cryo-EM analysis involved obtaining the best ice and particle spread for the highest-resolution data. Significant effort was put into screening cryo-EM grid preparation conditions, including changing blot times and concentrations, which led to nicely spread particles in ice (Fig. 3-2A). The single particles remained as intact hexamers, therefore a large dataset was collected and particles were auto-picked to get a large enough particle count to determine a high-resolution structure of the complex (Fig. 3-2B).

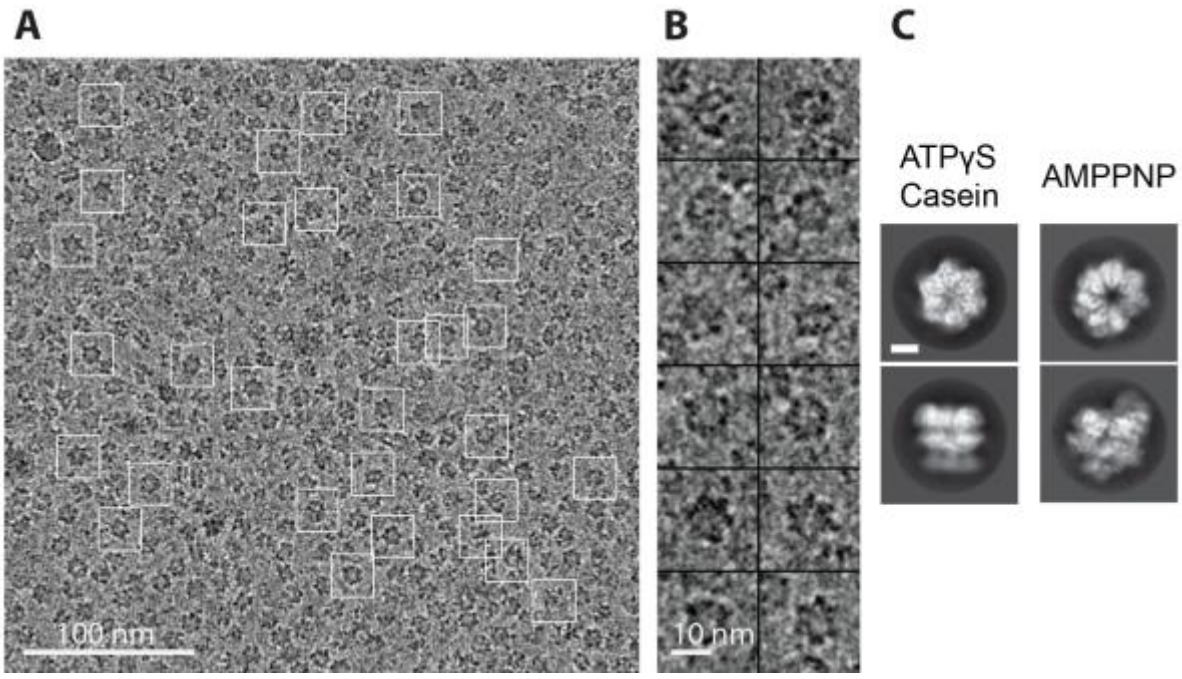

Figure 3-2. Forming a Stable Substrate-Bound Hsp104 Complex for Cryo-EM. (A) Cryo-EM micrograph of Hsp104:casein particles spread in thin layer of vitreous ice. (B) Selected single particles of Hsp104:casein complex. (C) Representative top and side-view 2D class averages comparing Hsp104-ATPγS:casein closed state and Hsp104:AMPPNP open state (scale bar equals 50 Å).

3.4 Initial 2D and 3D analysis of substrate-bound Hsp104.

About 500,000 particles of purified Hsp104:casein-ATPγS complex were subjected to two-dimensional (2D) reference-free classification, revealing a large rearrangement from the Hsp104:AMPPNP and Hsp104:ADP open state discussed previously (Fig. 3-2C). Top down views of the 2D averages of the hexamer show a very constricted channel, with some averages showing either a missing protomer or a small cleft (Fig. 3-3A). Side views of 2D averages show the three tiers of the hexamer in a planar-like conformation (Fig. 3-3A). These averages have secondary structure density, indicating the potential of a high-resolution 3D reconstruction. Bad particles that were picked by the auto-picker, such as ice contamination or not-fully formed hexamers, were removed from the dataset from the 2D averages, which resulted in a dataset of 460,000 particles. An initial 3D structure of the entire particle dataset refined to ~3.9 Å

resolution (Fig. 3-3B). However, upon examination of this electron density map, a two-protomer site was identified to be flexible and very low resolution, indicating there may be more than one conformational state in the data (Fig. 3-3C).

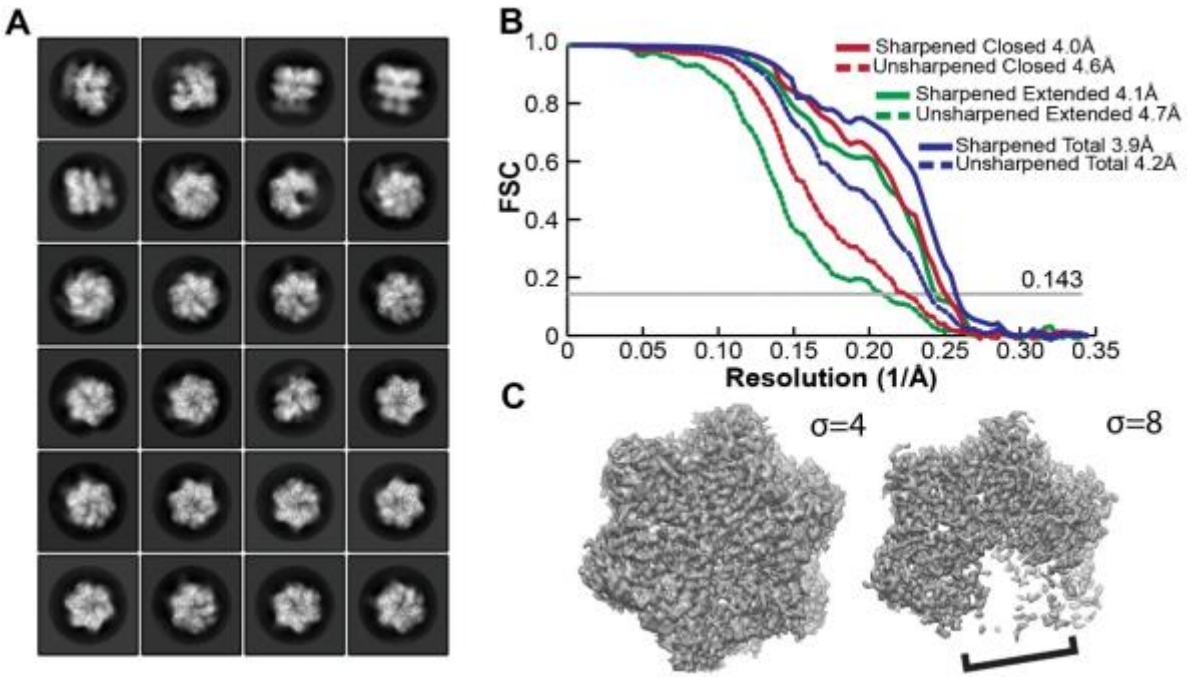

Figure 3-3 Analysis and cryo-EM processing of the Hsp104:casein complex. (A) Representative reference-free 2D class averages of the purified Hsp104:casein complex incubated with ATPγS. (B) Gold standard FSC curves of the masked and unmasked processed final reconstructions for the total dataset and the closed- and extended-conformation subclasses, determined using Relion *post_processing*(*33*). (C) Top views of the Hsp104:casein 3D reconstruction using the total dataset (following sorting by 2D classification), shown at 4σ and 8σ, showing the loss of density for the lower-resolution mobile two-protomer site (bracket).

Extensive 3D classification resolved these protomers and revealed two hexamer conformations, denoted: “closed” and “extended” (Fig. 3-4). Refinement of the closed state yielded a 4.0 Å-resolution map with well-resolved protomers and axial channel (Fig. 3-3B). The AAA+ subdomains show side-chain features, enabling an atomic model to be built and refined using a homology model from the bacterial orthologue ClpB (S. Lee et al. 2003) (Fig. 3-5A) The AAA+ domains (protomers denoted P1-P6) form a near-symmetric closed double-ring (Fig. 3-5B). Protomers P2-P5 are identical (RMSD = 2 Å) while the two mobile protomers, P1 and P6, each

adopt different conformations (Fig. 3-5C). The outside hexamer diameter is ~115 Å (compared to 125 Å for the open state), and density for the AAA+ domains surround a ~10 Å-wide axial channel. Remarkably, the channel is partially occluded by a continuous, 80 Å strand of density that, based on the molecular model, is an unfolded portion of the substrate, casein (Fig. 3-5D).

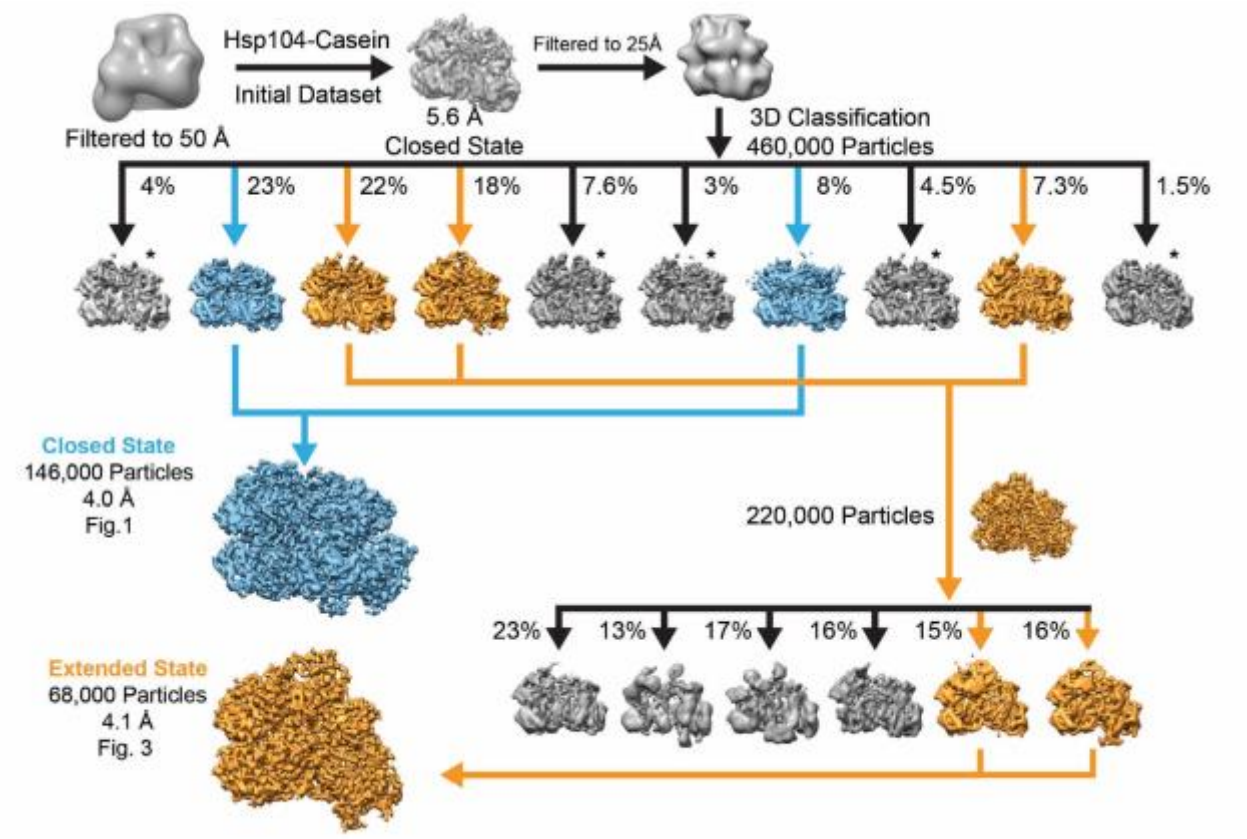

Figure 3-4. 3D classification scheme for the Hsp104:casein dataset. Indicated classes were used for closed (blue), extended (orange) and MD class (grey) refinements, with a 3D sub-classification of the extended-state single particles to achieve a better resolved P6-P1 interface.

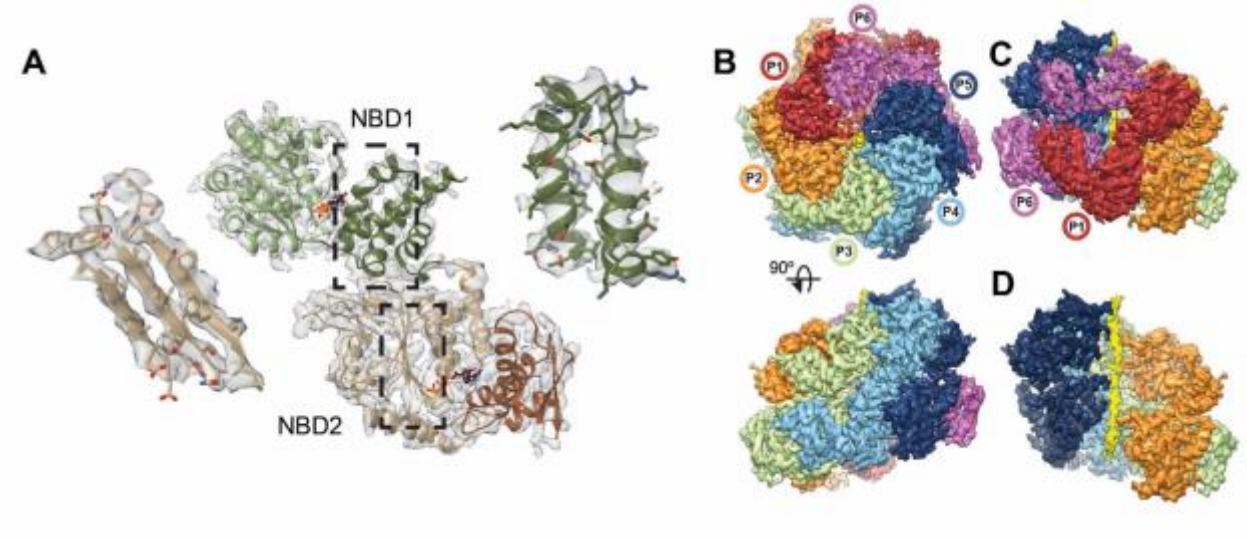

Figure 3-5. High-resolution of AAA+ domains and substrate. (A) Atomic model and segmented map of the AAA+ small (NBD1, green) and large subdomains (NBD2, brown). (B) Final reconstruction of Hsp104:casein segmented by protomers (P1-P6) and substrate (yellow). (C) Side view of the mobile protomer face (P1 and P6). (D) Channel view showing substrate polypeptide density (yellow).

3.5 Tyr Pore-Loop Contacts Along Substrate

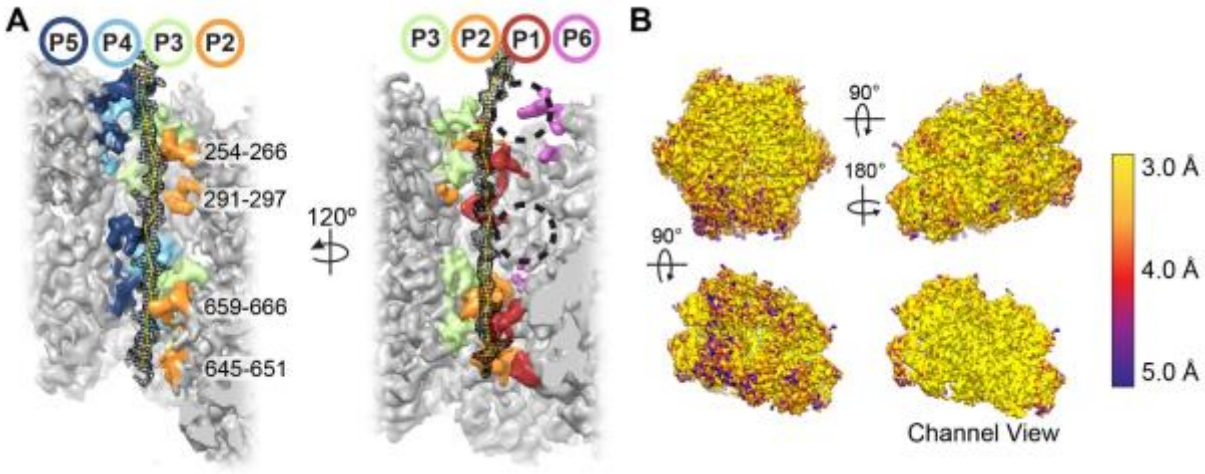

Fig. 3-6. **Structural basis for substrate binding in the axial channel.** (A) Channel view of the map showing the extended poly-Ala strand modeled as the substrate (mesh) and pore loops with residues indicated. The P6 pore-loop regions not contacting substrate are indicated (circles) (B) Resolution shown across the final 3D map for the reconstruction of the closed state, determined using Resmap (Kucukelbir, Sigworth, and Tagare 2014).

In the closed state, pore-loop strands from both AAA+ domains become ordered compared to

Hsp104-AMPPNP (Yokom et al. 2016) and other structures (S. Lee et al. 2003; Carroni et al.

2014), and contact substrate in a right-handed spiral arrangement (Fig. 3-6A). These regions are among the most highly resolved (< 4.0 Å, Fig. 3-6B), indicating bona fide interactions critical for translocation. The casein sequence could not be determined from the density, therefore a strand of 26 Ala residues was modeled. Hsp104 translocates unfolded polypeptides in the presence of ATPγS (Tessarz, Mogk, and Bukau 2008), therefore, the pore loop-substrate interactions likely adopt a fixed register during translocation. Alternatively, a specific region of casein may be uniformly trapped in the channel. Substrate contacts are made by five protomers (P1-P5), while protomer P6 breaks the helical arrangement and makes no direct contact (Fig. 3-6A, 3-7A). Substrate density is not observed outside the channel, thus non-translocated portions of casein are likely disordered.

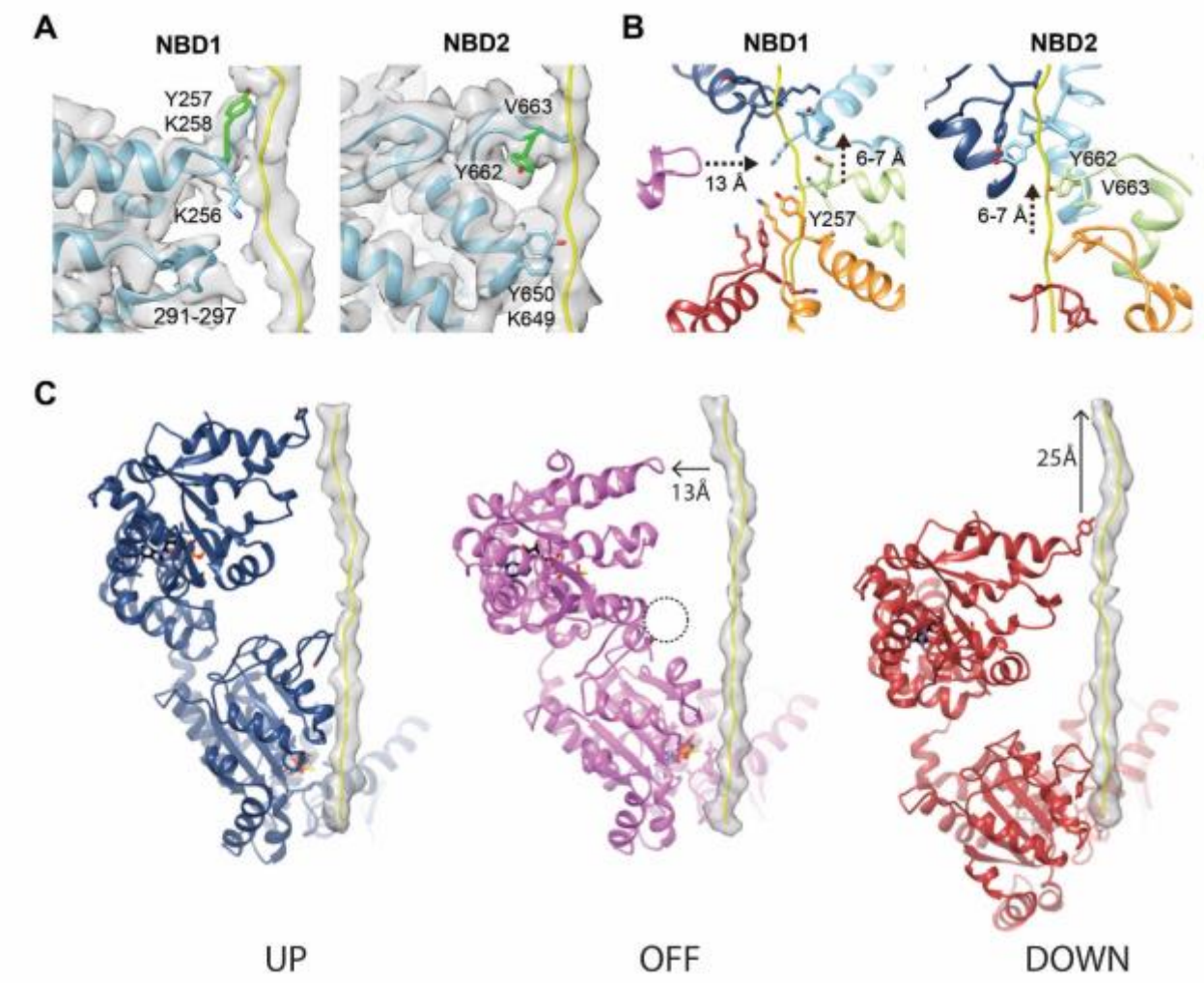

Figure 3-7. Tyrosine pore loops form a spiral of contacts around substrate. (A) Model and cryo-EM density showing P4 pore loop-substrate interactions mediated by Y257 (green) in the NBD1 and Y662 (green) and V663 in the NBD2 as well as lower pore loops that include residues K649 and Y650. (B) Spiral arrangement of the NBD1 and NBD2 canonical pore loops for P1-P5 contacting substrate and the disconnected position of the P6-NBD1 pore loop.

Conserved pore-loop tyrosines 257 and 662 in protomers P1-P5 directly contact substrate, potentially via the aromatic rings, which are positioned ~4-5 Å away from the backbone (Fig. 3-7A). Together with conserved V663 in NBD2, these residues contribute the majority of substrate interactions in the channel (Fig. 3-7A). The lower loops (291-297 for NBD1 and 645-651 for NBD2) are also ordered and adjacent to the substrate, and K649 and Y650 for P2 and P4 appear to make contact (Fig. 3-6A, 3-7A).

The pore loops are separated by ~6-7 Å along the channel, making contact with approximately every second amino acid of the substrate (Fig. 3-7B). K256 and K258 in NBD1, which flank Y257, project towards neighboring loops, possibly stabilizing the spiral arrangement. Protomers P1 and P5 comprise the lowest (Down) and highest (Up) contact sites with the substrate and are separated by ~26 Å along the channel axis. Protomer P6 is between these sites, but disconnected from the substrate; its NBD1 pore loop is 13 Å away while its NBD2 pore loop was less resolved and unable to be modeled (Fig. 3-7C, dotted circle). Overall, this structure reveals that substrate interactions are mediated almost entirely by the conserved Tyr residues, establishing their direct role in coordinating substrate during translocation (Olivares, Baker, and Sauer 2016; Sweeny and Shorter 2016).

3.6 Ratchet-Like States of Protomers

In addition to the closed state, our 3D classification analysis identified an 'extended' conformation of Hsp104:casein (Fig. 3-4). Further classification and refinement resulted in a 4.1 Å resolution map from which an atomic model was determined (Fig. 3-8C). The structure reveals a substrate-bound hexamer with a different arrangement of the mobile protomers P1 and P6, which show distinct flexibility in the NBD1 and NBD2, respectively (Fig. 3-8A,B). Protomers P2-P5 are identical to the closed state (RMSD = ~0.8 Å) and density for the polypeptide substrate is slightly extended at the top of the channel, but overall similar and localizes to the same region (Fig. 3-8A).

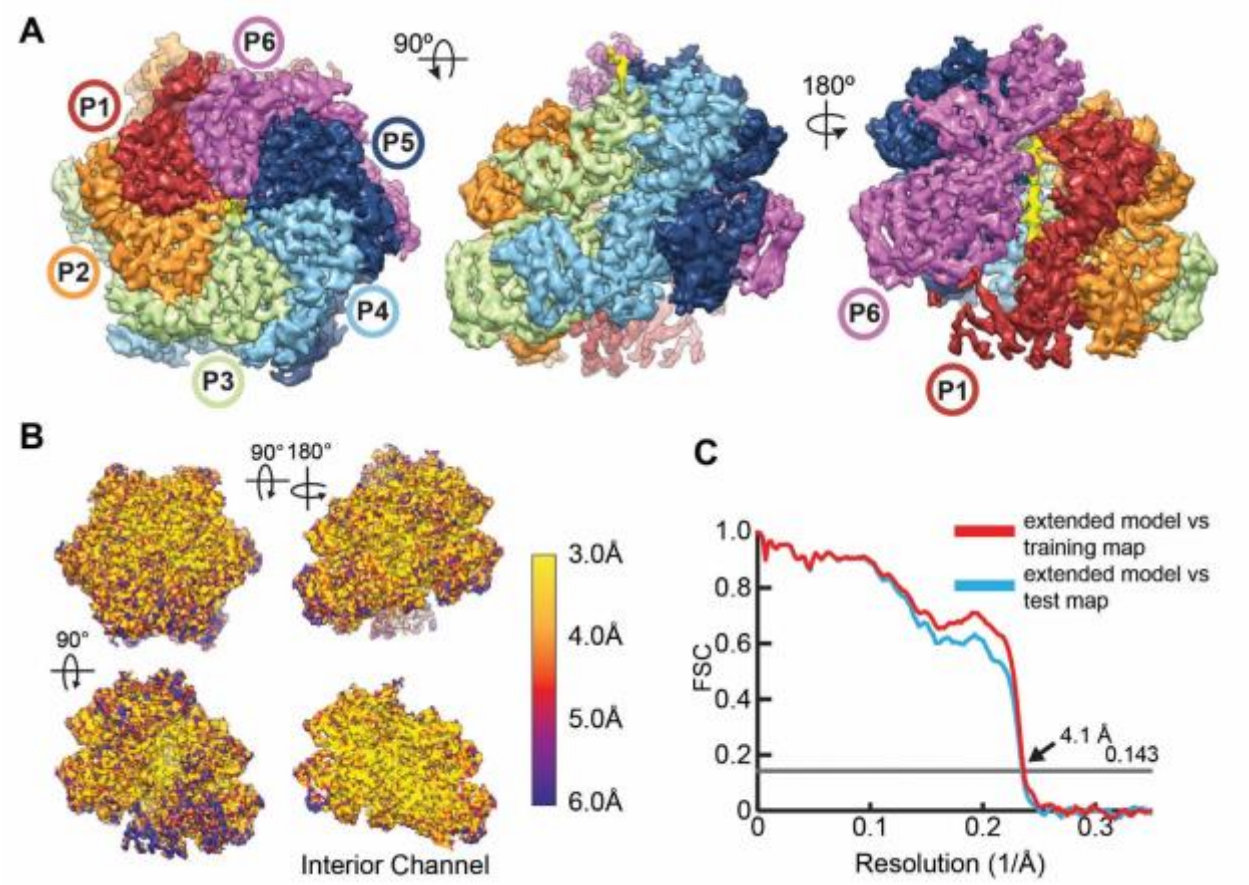

Figure 3-8. High-resolution extended state shows different mobile protomer conformation. (A) Cryo-EM reconstruction of Hsp104:casein identifying substrate (yellow) and an extended conformation of protomers P1 and P6. (B) Resolution across the final map determined by Resmap (Kucukelbir, Sigworth, and Tagare 2014) analysis. (C) FSC curve of the final model comparing the training (red) and test (blue) models used during refinement and model building with Rosetta (Song et al. 2013).

The closed-extended state conformational differences for P1 and P6 are substantial (RMSD = 13.7 Å and 11.5 Å, respectively) and involve rotations of P1-NBD1 and P6-NBD2 (Fig. 3-9A). P6 rotates towards the channel axis and the pore loops become well-ordered and directly contact substrate. The P6 pore-loop tyrosines, Y257 and Y662, directly contact substrate similarly as the other protomers (Fig. 3-9B). Conversely, P1-NBD2 rotates counterclockwise, releasing its interaction with P6 to contact P2-NBD2 but maintains contact with the substrate (Fig. 3-9A, 3-10A).

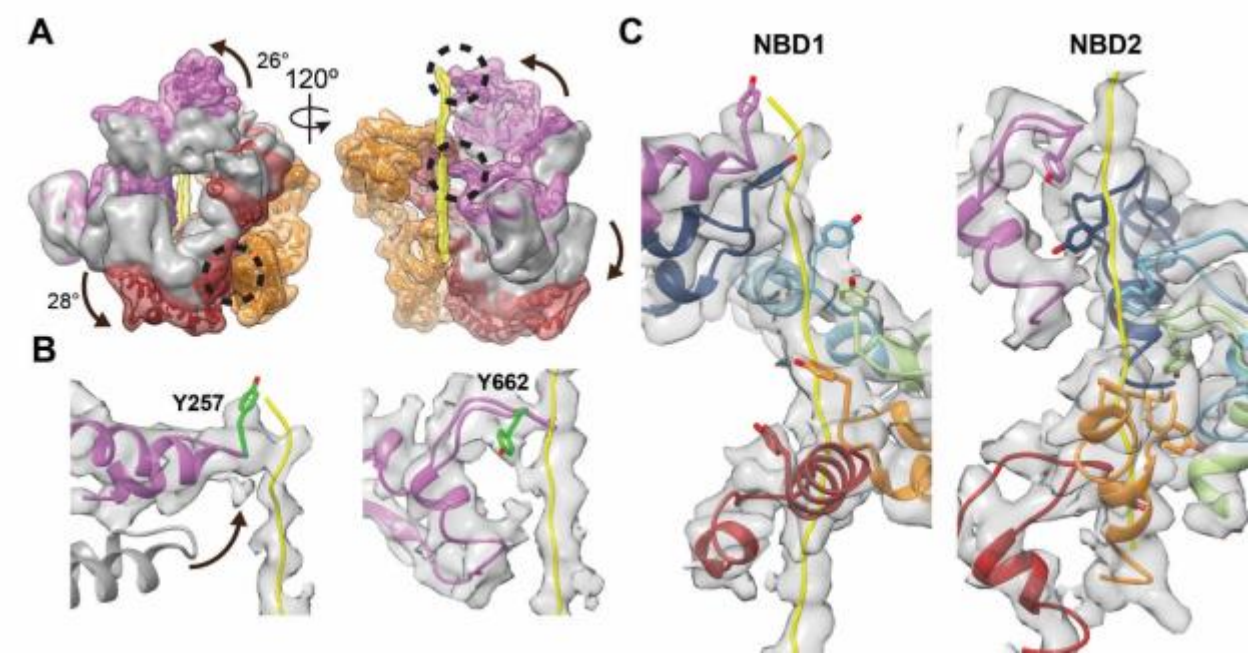

Figure 3-9. Hsp104:casein extended-state conformation advances substrate contacts. (A) Filtered map of P1 (red), and P6 (magenta) overlaid with the corresponding closed-state protomers (grey) following alignment to P4 in the hexamer. NBD conformational changes (arrows) resulting in extended-state interactions (black circles) with substrate (yellow) and the P2-NBD2 (orange) are shown. (B) Model and map of the P6 NBD1 and NBD2 pore loops showing change in the pore loop position (arrow) compared to the closed state (grey) for NBD1 and substrate contact by Y257 and Y662 (green). (C) Model and map of the NBD1 and NBD2 P1-P6 spiral of pore loop-substrate interactions.

Remarkably, P6-Y257 becomes positioned at the topmost contact site along the polypeptide, advancing interactions by 2 amino acids (~7 Å) compared P5-Y257 (Fig. 3-9C, 3-10B). These changes bring P6 pore loops in register to form a two-turn right-handed spiral of contacts (Fig. 3-9C). Each pore loop rotates ~60° and rises ~6-7 Å, enabling evenly spaced Tyr-substrate interactions across a 74 Å-length of the channel (Fig. 3-10B). Together, the extended and closed states reveal a ratchet-like conformational change of the hexamer that yields a two-amino acid translocation step. While other conformations may exist that were not resolved, the extended and closed states predominate the dataset (Fig. 3-4), therefore, these changes are likely critical for orchestrating substrate binding and release steps during translocation.

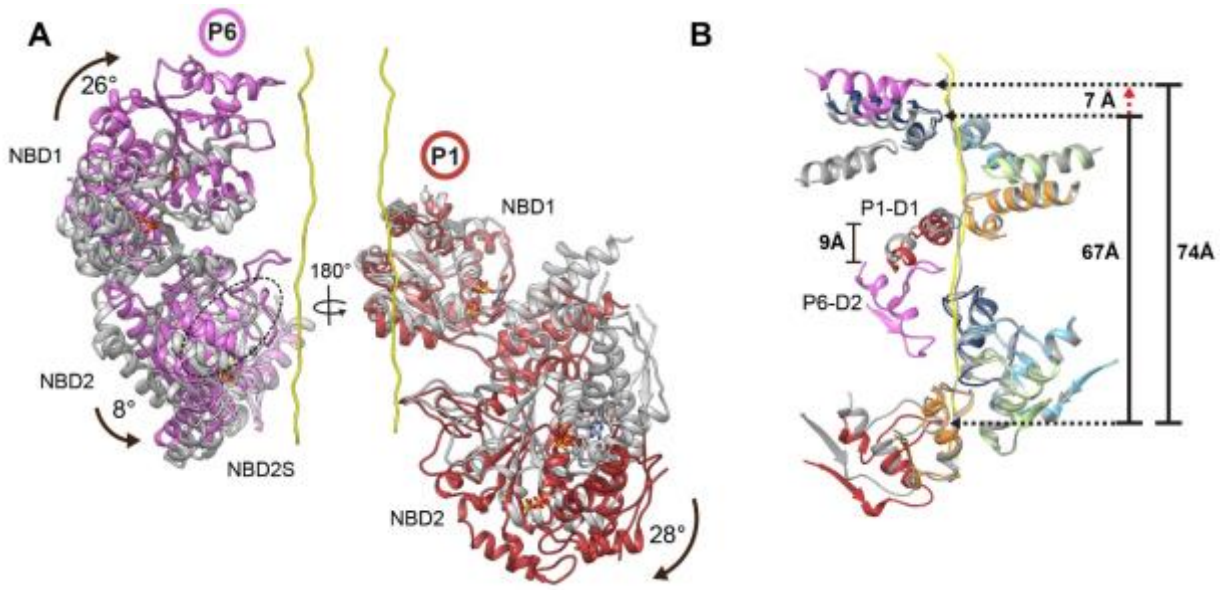

Figure 3-10. Conformational differences and pore loop-substrate contacts in the closed and extended states. (A) Overlay of the P6 and P1 protomers in the closed (grey) and extended (magenta and red, respectively) states following alignment of the hexamers identifying specific NBD1 and NBD2 rotations. (B) Overlay of the of the pore loops and polypeptide substrate in the closed (grey) and extended (colored by protomer) states showing complete substrate engagement and a 7 Å translocation step along the polypeptide that occurs in the extended state.

3.7 Coordinated Nucleotide Pockets

NBD1 and NBD2 nucleotide pockets were examined to determine how nucleotide state is coupled to substrate interactions. P3-P5 nucleotide pockets are identical with well-resolved density and a bound ATPγS (Fig. 3-11A). In NBD1, R334 from the clockwise neighboring promoter contacts the γ-phosphate, establishing this residue as the Arg finger (Wendler et al. 2007). R333 is adjacent the α/β-phosphates, acting potentially as a sensor residue considering that the NBD1 does not contain a cis sensor 2 motif (Erzberger and Berger 2006). In the NBD2 pocket, the Arg finger, R765, interacts with the γ-phosphate while the sensor 2, R826 in the cis protomer, is positioned adjacent the α/β-phosphates (Fig. 3-11A). Thus, for P3-P5, which make well-defined contacts with the substrate in both states, NBD1 and NBD2 are primed for ATP hydrolysis.

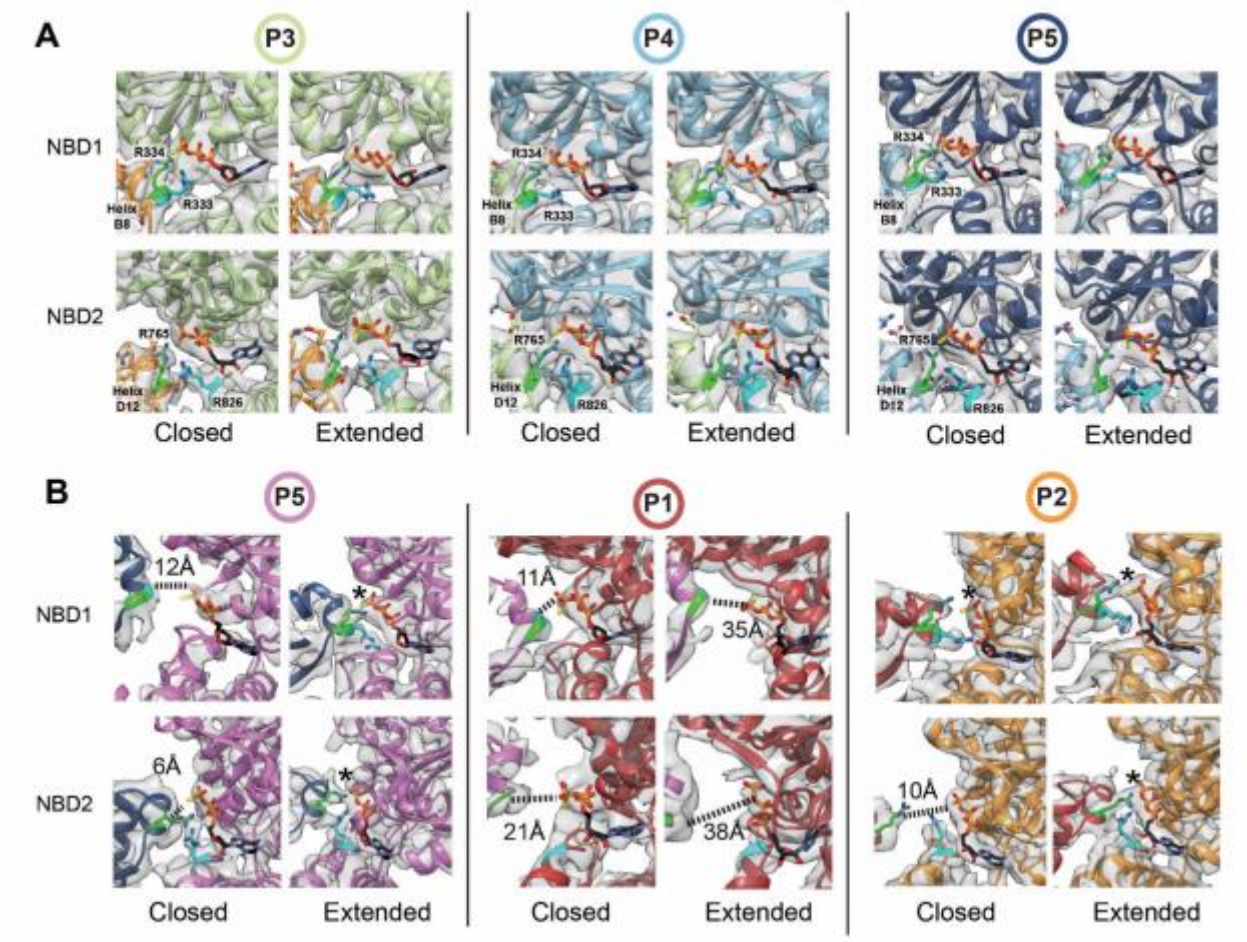

Figure 3-11. Arrangement of the nucleotide pockets in the closed and extended states. (A) Cryo-EM density and model for the NBD1 and NBD2 nucleotide pockets of P3-P5, in the closed and extended states, showing an active configuration. The Arg finger residues (green), R334 (NBD1) and R765 (NBD2), from the adjacent protomer (helix B8 and helix D12, respectively) and the putative NBD1 sensor 2, R333 (cyan) and the NBD2 sensor 2, R826 (cyan) are shown. (B) Map and model of the P6, P1 and P2 nucleotide pockets. Arg-fingers, NBD1-R334 and NBD2-R765, are shown (green) with γ-phosphate contact indicated (*) for the active sites and distances shown for the inactive sites. Sensor 2 residues NBD1-R333 and the NBD2-R826 are shown (cyan).

Conversely, the mobile promoter (P6, P1, and P2) NBDs, are in different active and inactive configurations, based on the position of Arg fingers and nucleotide density. For the P6 protomer, both NBDs appear inactive in the closed state (Fig. 3-11B) with P5-R334 ~12 Å away and P5-R765 ~6 Å from the respective NBD1 and NBD2 γ-phosphate in P6. In contrast, both P5-

R334 and P5-R765 in the extended state are identified to contact the respective γ-phosphates directly, indicating these sites are in an active configuration. Notably, the closed-extended conformational change results in both nucleotide-pocket activation and substrate contact by P6 (Fig. 3-9A).

P1 contacts substrate at the lowest position in the hexamer and appears inactive in both states (Fig. 3-11B). In the closed state, P6-R334 is ~11 Å away and P6-R765 is ~21 Å from the respective γ-phosphate in P1. These Arg residues are further separated from the nucleotide pockets in the extended state, with R333, R334, and R765 more than 30 Å away (Fig. 3-11B). For P2, NBD1 is in an active configuration in both states. However, P2-NBD2 switches from inactive in the closed state to active in the extended state due to the P1-NBD2 conformational change that brings R765 adjacent the γ-phosphate (Fig. 3-11B). Finally, based on difference maps, density for nucleotide is present in all sites, but appears reduced at certain sites: NBD1 in P6 and P1 for the closed state, and the NBD2 in P1 for both states, indicating partial occupancy or a post-hydrolysis state.

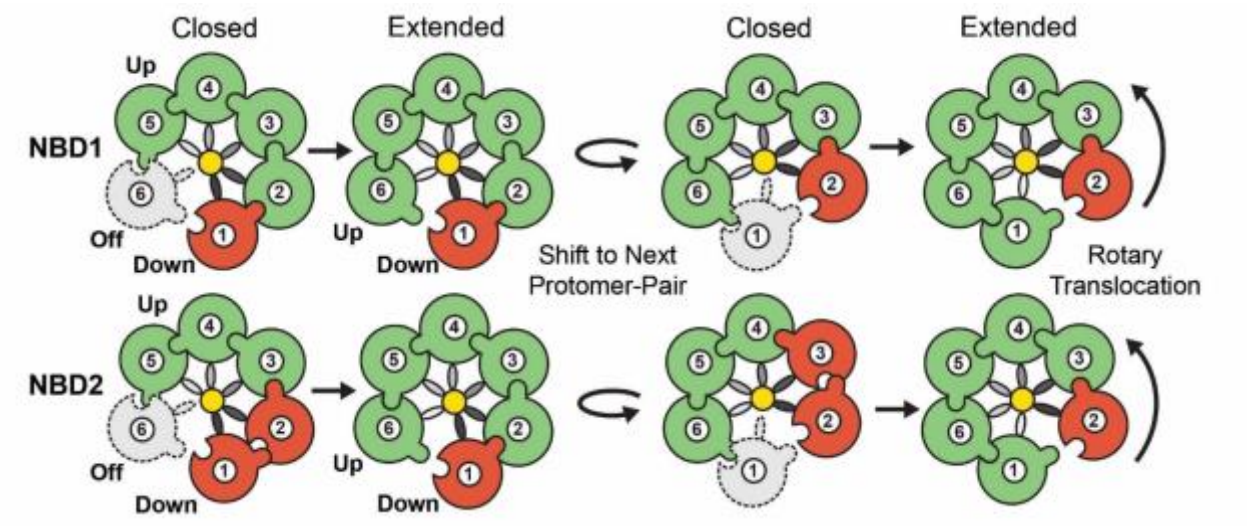

Fig. 3-12. Extended-state activation of the nucleotide pockets is coupled to translocation. Rotary translocation model showing closed-to-extended states resulting in active (green), inactive (red) and unbound/inactive (grey dash) states of the NBDs. Pore loop spiral (grey

gradient) is shown contacting substrate (yellow). Arg-finger contact and NBD activation is depicted by the interlocking contact.

The NBD states along with substrate interactions are depicted in a schematic to explain how active site rearrangements and the closed-extended conformational changes drive substrate translocation (Fig. 3-12). In the closed state, substrate is bound by five protomers with four NBD1 sites and three NBD2 sites in an active (ATP) configuration. By contrast, in the extended state, substrate is bound by six protomers with five NBD1 sites and five NBD2 sites in an active state. Importantly, the 'off' protomer (P6) that is unbound to substrate in the closed state becomes active in the extended state and binds substrate at the next position. The protomer counterclockwise from this position is in the lowest 'down' position (P1) and remains inactive in both states, but undergoes a rotation in the extended state that activates NBD2 of the neighboring protomer.

These results suggest a rotary-type translocation mechanism whereby four protomers remain bound to substrate in a similar configuration with the NBDs primed for hydrolysis, while two protomers at the transition site between the lowest and highest position undergo conformational changes that alter substrate interactions. Given the right-handed spiral of pore loops, position of the 'up' and 'down' protomers, and NBD1-NBD2 direction of translocation, peptide movement could occur through a counterclockwise cycling of these closed and extended states. Based on this model the inactive protomer in the 'down' position could release substrate and re-engage in the 'up' position, thereby advancing translocation by a two-amino acid step. Transmitting these changes counterclockwise would enable the hexamer to advance processively along the polypeptide during translocation. Some variability in the step size, potentially to accommodate bulky residues, could be achieved by conformational changes in the extended-state protomer in the 'up' position that shift its pore-loop contact. These results parallel the right-

handed substrate interactions and rotary-driven hydrolysis models for DNA/RNA helicases, including AAA+ (E1, DnaA and MCM) (Erzberger and Berger 2006; Enemark and Joshua-Tor 2006; Abid Ali et al. 2016) and RecA (Rho) (Thomsen and Berger 2009) families. Thus, this ratcheting mechanism may be conserved among many ATP-driven translocases.

3.8 Allosteric Control by the MD

The Hsp104-AMPPNP (Yokom et al. 2016) structure revealed an open spiral conformation that is substantially different from the closed, substrate-bound states characterized here. Furthermore, a MD-NBD1 interaction was identified that suggested an allosteric control mechanism. To further explore the MD and the role of nucleotide in the Hsp104 conformational cycle we determined the cryo-EM structure of Hsp104 incubated with ADP to 5.6 Å resolution (Fig. 3-13B). The reconstruction reveals an identical AAA+ arrangement compared to Hsp104-AMPPNP (RMSD = 2.5 Å) involving a left-handed spiral architecture defined by a ~10 Å rise per protomer and a heteromeric AAA+ interaction between P6-NBD1 and P1-NBD2.

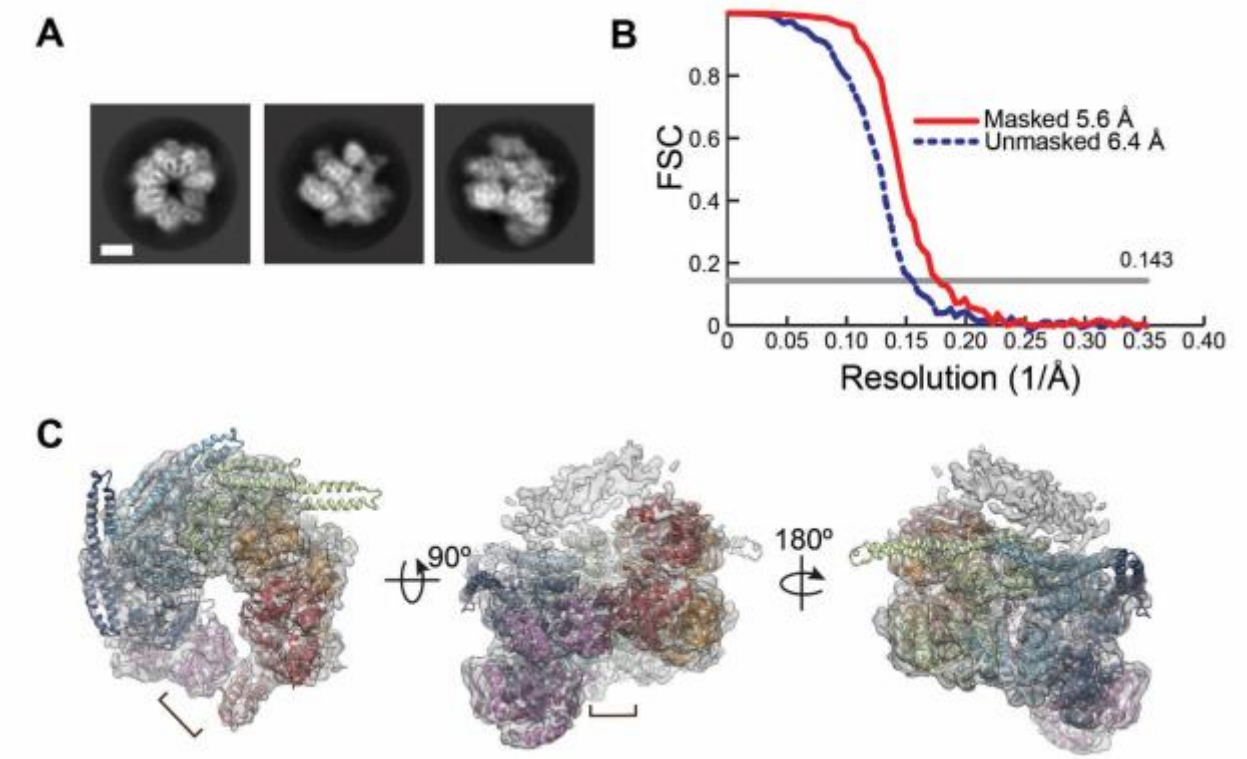

Figure 3-13. 2D and 3D analysis of Hsp104:ADP model. (A) Representative 2D class averages of Hsp104:ADP. (scale bar = 50 Å). (B) Gold standard FSC curve for the un-masked and masked reconstructions of the final model estimated from the FSC=0.143 criterion to be 6.4 Å and 5.6 Å, respectively. (C) Top down view and side views of Hsp104:ADP fit with atomic model, colored by protomer, with asymmetric seam indicated.

The MD is resolved for three protomers (P3-P5) and identified to be in a crisscross equatorial arrangement stabilized by contacts between the first (L1) and third (L3) helices (Fig. 3-14B). This arrangement is similar to previous structures (S. Lee et al. 2003; Carroni et al. 2014; Heuck et al. 2016) but strikingly different to the Hsp104-AMPPNP structure, in which the same MD helix L1 region makes contact across NBD1 of the clockwise protomer (Fig. 3-14A). Comparison of these ATP- and ADP-state MD conformations reveals a substantial, ~30° rotation around position 409 at the NBD1-MD junction (Fig. 3-14C). While hexamers exclusively-bound to ATP or ADP are likely rare *in vivo*, these data reveal that the MD adopts two nucleotide-specific conformations that reflect pre- and post-hydrolysis states.

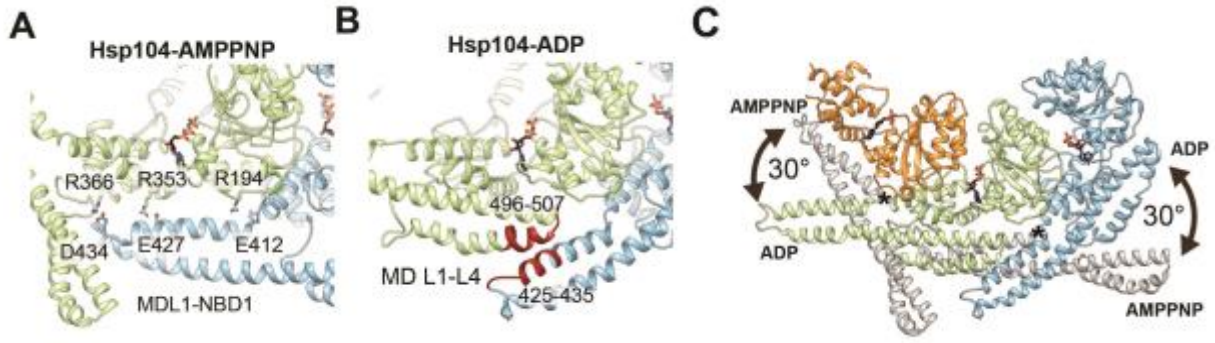

Figure 3-14 Large rotation of MD coiled-coil with hydrolysis.. (A) MD L1-NBD1 interaction identified in the Hsp104-AMPPNP structure (Yokom et al. 2016), showing putative salt-bridge contacts analyzed by mutagenesis. (B) MD-MD (L1-L3) interaction interface identified in the Hsp104-ADP reconstruction (red). Overlay of MD and NBD1 for Hsp104:AMPPNP (grey) and Hsp104:ADP (colored by protomer) reconstructions aligned to their AAA+ domains showing MD conformational changes.

Sites that comprise the MD-MD interactions in Hsp104-ADP are critical for function (Jackrel et al. 2014; Oguchi et al. 2012; Carroni et al. 2014; Wendler et al. 2007). However, the AMPPNP-specific MD L1-NBD1 interaction has not been characterized. Therefore, single

charge-reversal mutations were introduced to disrupt three putative L1-NBD1 salt bridges (Yokom et al. 2016): E412-R194, E427-R353, and D434-R366 (Fig. 3-14A). These mutants exhibit robust ATPase activity (Fig. 3-15B). However, they are unable to reactivate denatured firefly luciferase aggregates *in vitro* (Fig. 3-15A) or confer thermotolerance *in vivo* (Fig. 3-15C), supporting a functional role for the L1-NBD1 interaction.

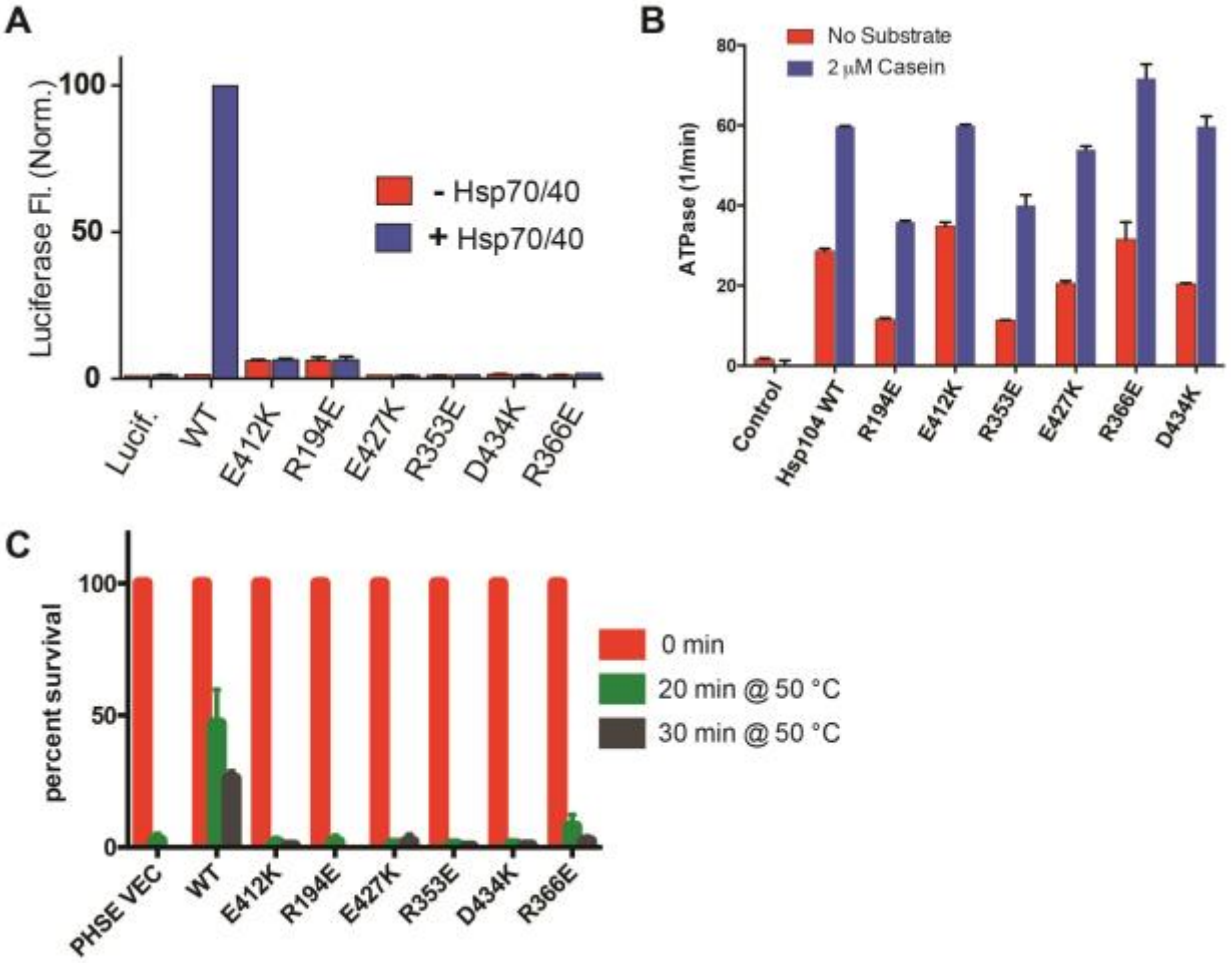

Figure 3-15. Mutations of MD-NBD1 salt bridges. (A) Luciferase reactivation measured by fluorescence following incubation with Hsp104 wildtype or indicated mutants in the absence (red) or presence (blue) of Hsp70/40 system. Values are normalized to wt+Hsp70/40 and represent the mean ±SD (n=4). (B) ATPase activity of wildtype Hsp104 and L1-NBD1 variants identified in the Hsp104-AMPPNP structure in the absence (red) and presence (blue) of casein (2 μM). Values represent mean±SD (n=2).(C) Δ*hsp104* yeast cells harboring empty pHSEgc vector or the indicated pHSEgc-Hsp104 variant (WT, E412K, R194E, E427K, R535E, D434K, or R366E) were grown to mid-log phase in SD-his. Prior to the 50°C heat treatment, matched cultures were preincubated at 37°C for 30 min. Following treatment at 50°C for 0 min (red bars), 20 min (green bars), or 30 min (black bars) cells were transferred to ice and plated on SD-his.

After 2 days at 30°C, survival (%) was quantified. Values represent mean±SD (n=3). Luciferase reactivation assay, ATPase assay, and thermotolerance experiments generated by the Shorter lab (University of Pennsylvania).

To determine MD conformations in the casein-bound complex, additional 3D sub-classification analysis and refinement was performed on the Hsp104 closed-state data without applying a mask (Fig. 3-4). Three classes with distinct MD arrangements were identified: MD Class 1, Class 2 and Class 3, which refined to 6.7-6.9 Å (Fig. 3-16A). For these maps, the AAA+ core and substrate density are identical to the closed-state structure. In the MD Class1, density corresponding to the MD coiled-coil is identified for 4 protomers (P1, P2, P5 and P6), revealing an ADP-state, crisscross arrangement around the P6-P1 mobile-protomer face (Fig. 3-16A). Notably, the NTDs for all protomers are also resolved in this class, revealing that they interact together in an alternating, triangular arrangement with the polypeptide strand oriented asymmetrically in the channel, towards the P3 and P5 NTDs (Fig. 3-16B,C).

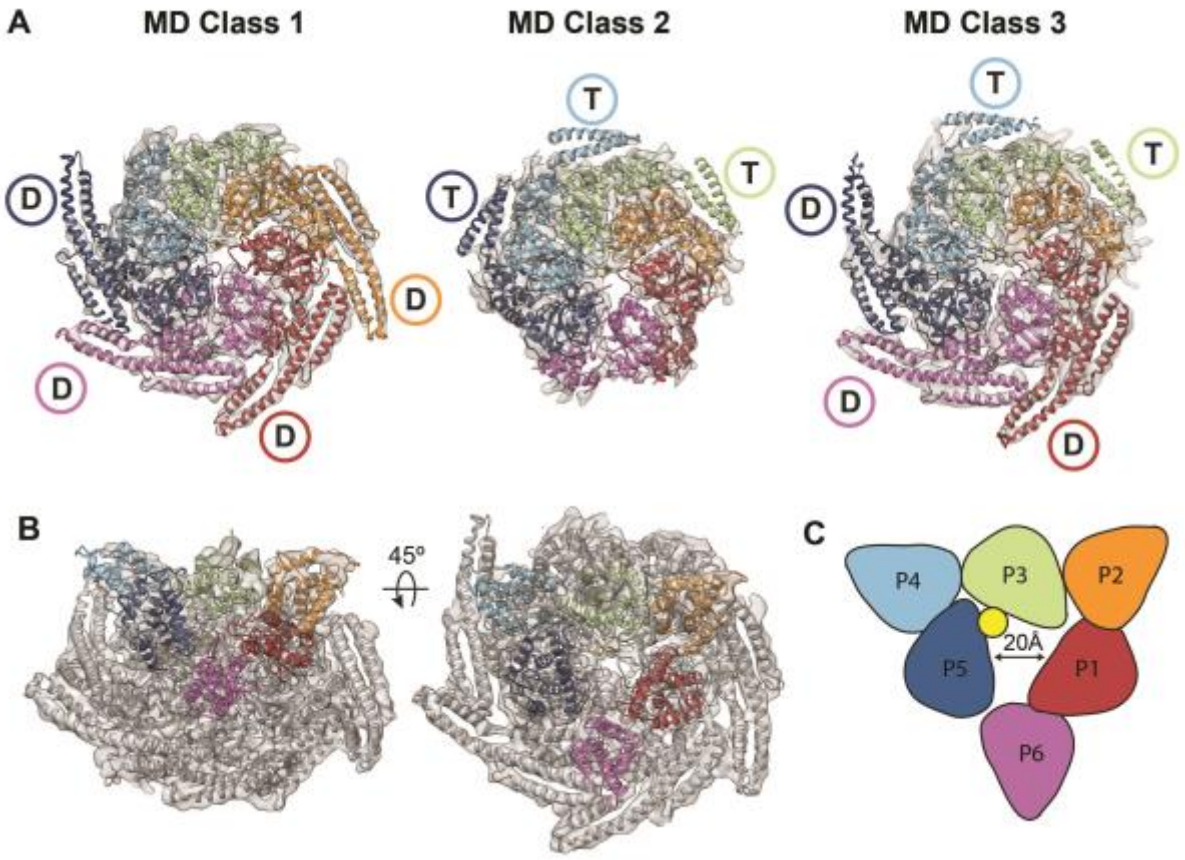

Figure 3-16. MD and NTD Classification of closed, casein bound data. Final reconstructions and models of Hsp104:casein following MD classification analysis identifying the ADP-state (D) or ATP-state (T) conformation. (B) Map and model of MD Class 1 showing the NTD-NBD1 region, NTDs colored corresponding to protomer (C) Schematic based on the model showing alternating orientation of the NTDs and triangular arrangement of the channel entrance with substrate (yellow) positioned off-center, adjacent P3 and P5.

For MD Class 2, density corresponding to MD helices L1 and L2 is identified for protomers P3-P5 revealing L1 is positioned across the clockwise protomer, indicating an ATP-state conformation. (Fig. 3-16A). For Class 3 both MD conformations are identified: P1, P5, and P6 adopt the ADP-state, while P3 and P4 are in the ATP-state (Fig. 3-16A). This classification captures specific MD conformations that are in remarkable agreement with our analysis of the nucleotide pockets (Fig. 3-11). Thus, in an actively translocating hexamer, MD conformational changes likely propagate around the hexamer in accordance with nucleotide state. The MD could function to lock the ATP state for protomers that are in contact with substrate (P2-P5) and

transition to a release, ADP-state towards the mobile face, thereby allosterically tuning the closed and extended conformational changes that advance substrate.

3.9 NBD1-Driven Rearrangement Engages Substrate

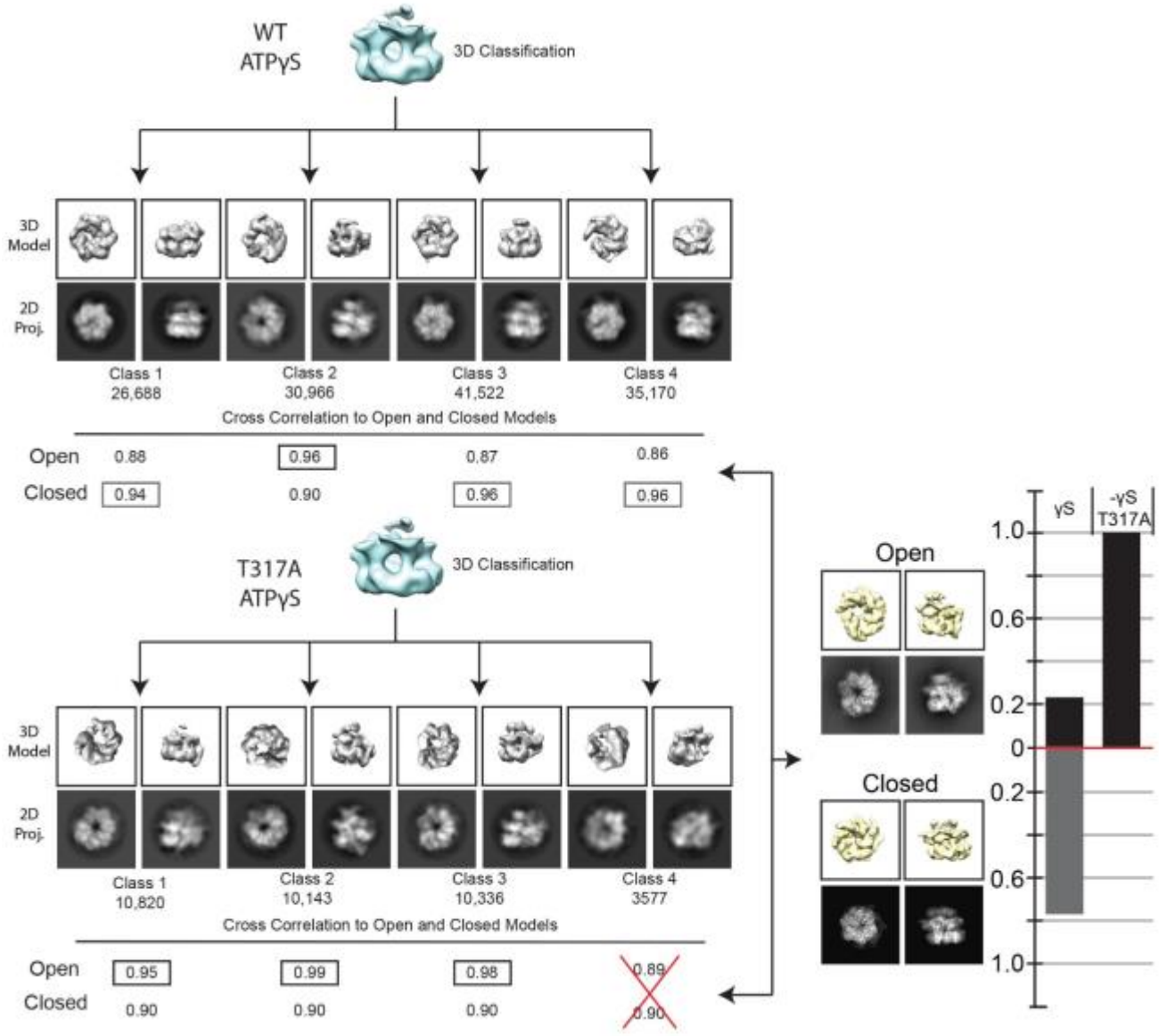

Figure 3-17. 3D Classification protocol for sorting closed and open particles. 3D classification scheme of wildtype and T317A mutant Hsp104 incubated with ATPγS and cross-correlation analysis to determine the classes that match the open or closed states (cross-correlation ≥ 0.93 indicates a match). Note that the top views of the 2D projections for each class clearly depict the open and closed conformation and agree with the cross-correlation analysis. Classes with cross-correlation values < 0.93 for both the open and closed model comparisons were considered poorly defined and excluded from further analysis (red X). Resulting bar graph is shown of wildtype Hsp104-ATPγS and T317A Hsp104-ATPγS showing the fraction of

particles that match the open or closed conformations, determined from the above cross correlation analysis.

To determine how the open and closed states may function together, cryo-EM datasets of wildtype and mutant Hsp104 incubated with different nucleotides were analyzed by 2D and 3D classification methods (Fig. 3-17). As expected, AMPPNP and ADP datasets classify with 100% of the data matching the open conformation. With ATP incubations, alone and with substrate, Hsp104 primarily adopts the open conformation (>80%), however a notable fraction (10-20%) are in the closed state (Fig. 3-18). A 3D reconstruction of the Hsp104-ATP was determined to 6.7 Å and is identical to the AMPPNP and ADP-bound structures (cross-correlation = 0.98) (Fig. 3-19). Thus, during active hydrolysis the open state is favored, however both conformations exist in equilibrium. With ATPγS, nearly 80% of hexamers are in the closed state (Fig. 3-18), which increases to 100% with casein, demonstrating that ATPγS and substrate together trigger complete conversion to the closed state.

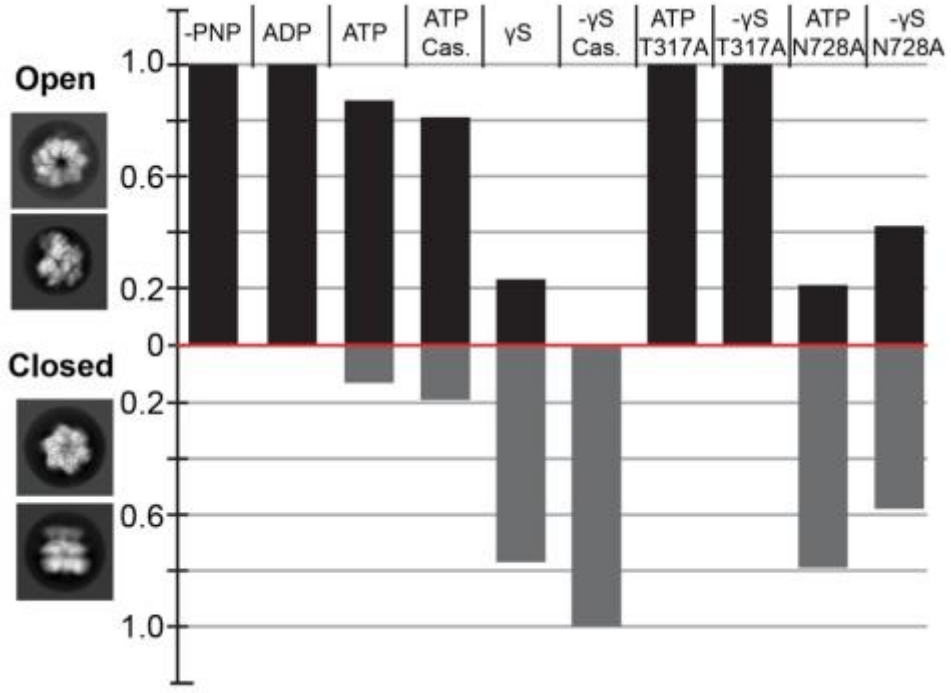

Figure 3-18. Nucleotide-state and NBD function in the open-closed conformations and model for the disaggregation cycle. The fraction of open and closed conformations, determined

by 3D classification analysis, is shown for wildtype Hsp104 and sensor 1 ATPase mutants (T317A in NBD1 and N728A in NBD2) following incubation with indicated nucleotides and substrate.

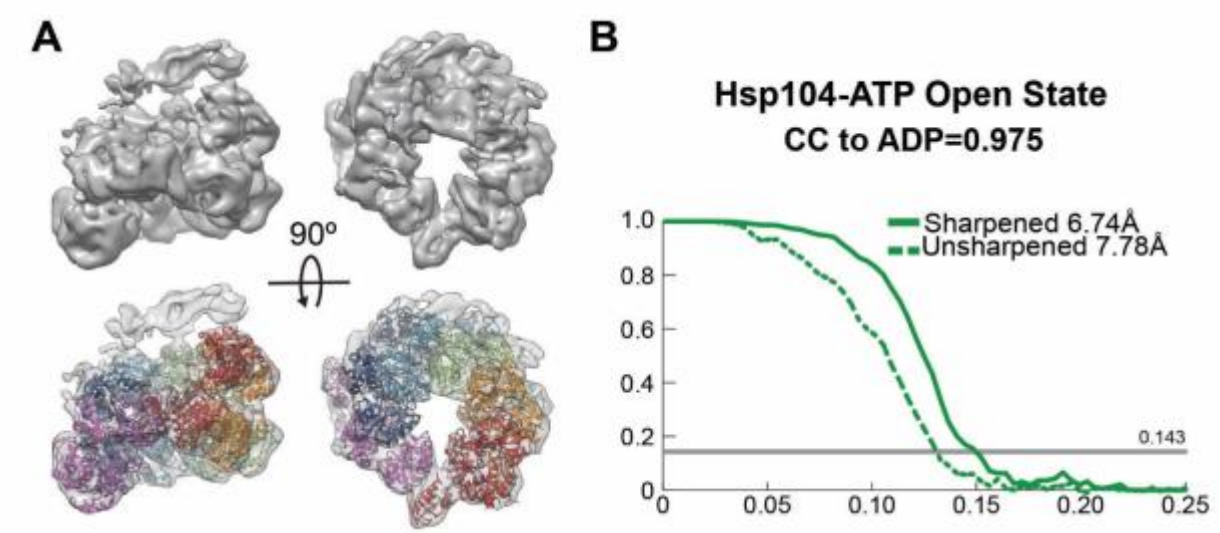

Figure 3-19. Hsp104:ATP adopts the same open conformation as AMPPNP and ADP. (A) Top down view and side view of Hsp104:ATP electron density fit with the Hsp104:AMPPNP atomic model, colored by protomer. (B) Gold standard (Scheres 2012) FSC curve of the final masked and unmasked 3D refinement of Hsp104:ADP, to 6.7 Å and 7.8 Å respectively.

The sensor 1 ATPase mutants(*18*), T317A in NBD1 and N728A in NBD2, were investigated to determine the role of NBD1 and NBD2 function (Fig. 3-18). In contrast to wildtype, T317A incubated with ATP or ATPγS classifies with 100% matching the open state, indicating that a hydrolysis-active NBD1 promotes the closed conformation. Conversely, ~80% and 60% of N728A hexamers match the closed state in the presence of ATP and ATPγS, respectively.

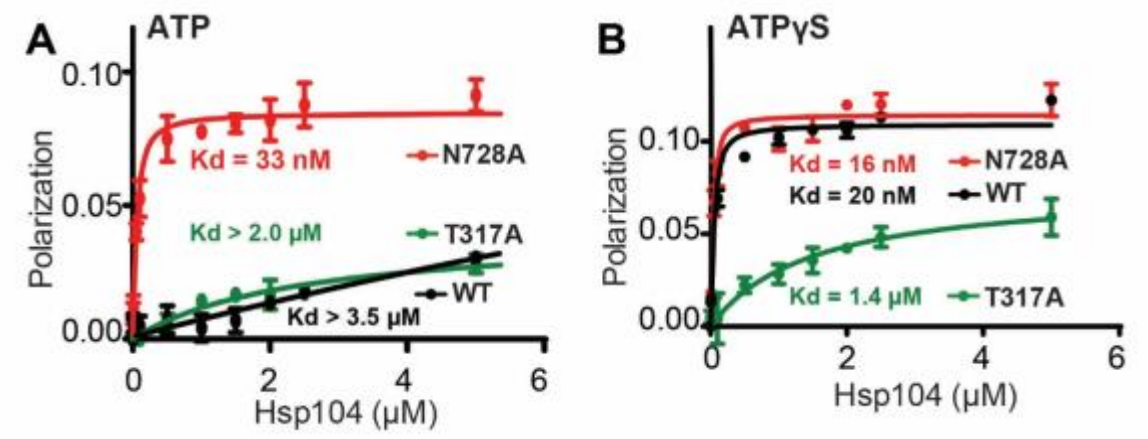

Fig. 3-20. Mutant casein binding experiments. (A,B) FITC-casein (60 nM) binding to Hsp104 wildtype (black) and mutants: T317A (green) and N728A (red) in the presence of (2 mM) (A) ATP or (B) ATPγS. Values represent mean ±SD (n=3). FP data and figure generated by the Shorter lab (University of Pennsylvania).

In casein-binding experiments, N728A binds with high affinity (K_d ~33nM), while wildtype and T317A show weak binding (K_d > 2µM) (Fig. 3-20A) in the presence of ATP. With ATPγS, both wildtype and N728A bind with a high affinity (K_d ~16-20nM), whereas T317A has a reduced affinity, in comparison (K_d ~1.4µM) (Fig. 3-20B). Thus, Hsp104 exists in open-closed conformational equilibrium that is differentially controlled by NBDs. Hydrolysis by NBD1 promotes the closed state, while hydrolysis by NBD2 favors the open state. Substrate binding and the open-closed conformational change are coupled and likely driven by NBD1 function, whereas NBD2 may be important for substrate release steps.

3.10 Discussion

Massive conformational changes are required to transition between the open and closed states (Fig. 3-21). In the open state, protomer P1 is in the topmost position and the hexamer adopts a left-handed spiral with P6 ~50 Å below, along the axial channel. Upon conversion to the closed state, P6 shifts by ~65 Å, and rotates towards the channel by ~60° (Fig. 3-22), resulting in a right-handed spiral and a channel that has narrowed by ~10 Å. Considering that substrate

interactions and hydrolysis by NBD1 are critical for the closed state (Fig. 3-18,3-20), we propose that this large conformational change drives substrate binding and release steps of the cycle (3-21). When the conformational change is modeled with substrate, nearly 30 residues can be translocated into the channel. Additionally, similar open 'lock-washer' conformations are populated by other translocases (Lyubimov et al. 2012; Skordalakes and Berger 2003; Śledź et al. 2013; Zhao et al. 2015), which may represent a conserved 'off-state'.

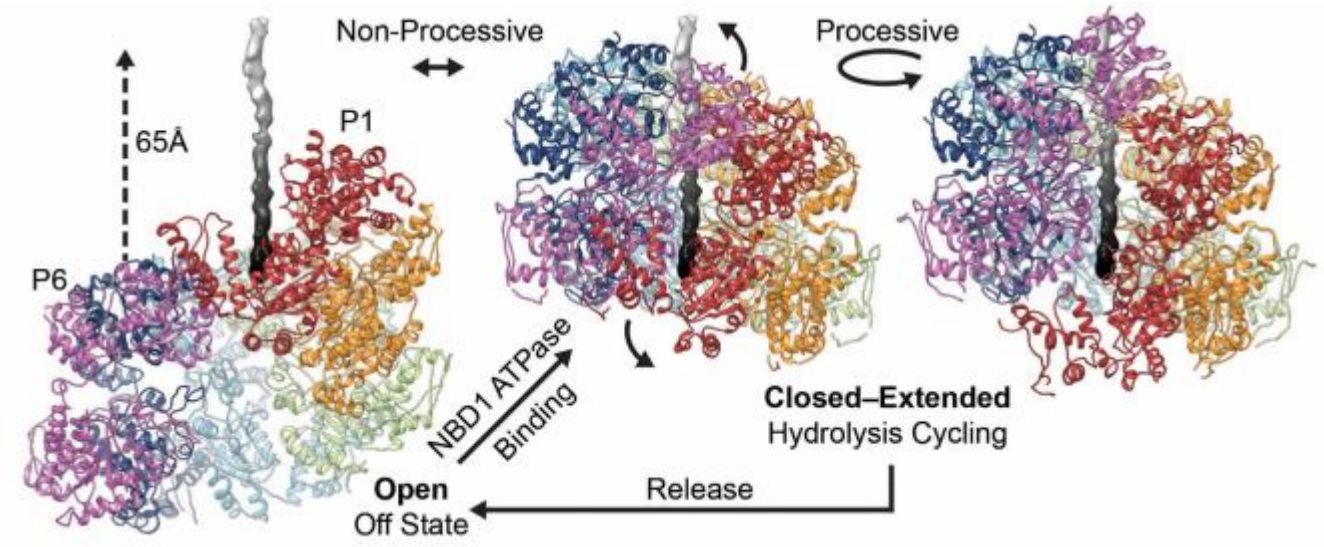

Fig. 3-21. Hsp104 translocation mechanism involves processive and non-processive modes. Proposed models for non-processive and processive modes of translocation involving open to closed conformational change upon substrate engagement/release and ratchet-like open-to-extended protomer changes that occur around the hexamer during cycles of ATP hydrolysis.

Disaggregation involves nonprocessive and processive mechanisms (DeSantis et al. 2012; T. Li et al. 2015). Cycling between the open and closed states may enable nonprocessive bind/release "pulling" events. Alternatively, the two different substrate-bound states suggest a processive mechanism whereby two protomers undergo ratchet-like conformational changes that enable substrate binding and release steps to occur while the hexamer remains engaged. This rotary-like mechanism could drive disaggregation when coupled to stepwise cycles of ATP hydrolysis around the ring. Such a cooperative mechanism could enable dissolution of more stable aggregates or amyloids (DeSantis et al. 2012). While this mechanism contrasts with

'stochastic' models proposed for ClpX (Olivares, Baker, and Sauer 2016), Hsp104 may exhibit different conformational cycles tuned to different substrates (DeSantis et al. 2012). Remarkably, both extended and closed states reveal a precise 6-7 Å separation of the pore loop-substrate contacts. A two-amino acid step involving conformational changes at the spiral interface would continually maintain this register during translocation. This pore-loop spacing is observed in related AAA+ rings (Wehmer and Sakata 2016; Glynn et al. 2009; Matyskiela, Lander, and Martin 2013), and likely represents a conserved feature of translocases. While additional states are likely involved, our structures reveal the remarkable structural plasticity of Hsp104, which enables adaptable mechanisms of protein disaggregation (Sweeny and Shorter 2016; DeSantis et al. 2012).

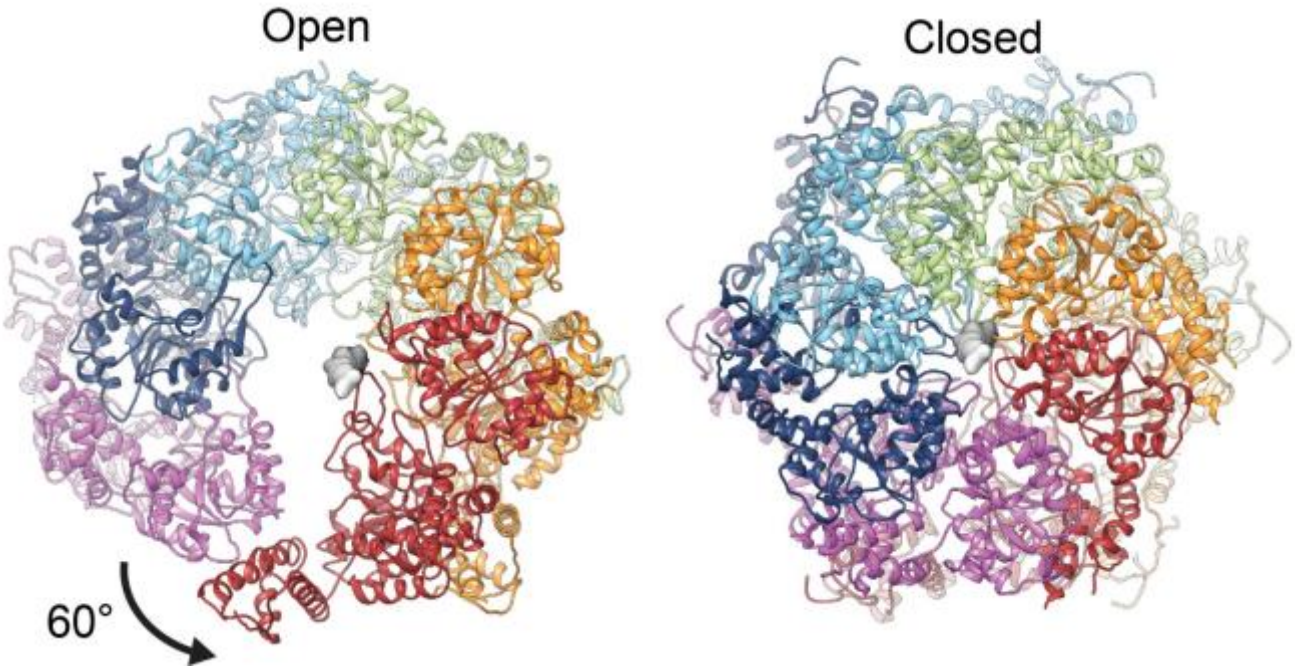

Figure 3-22. Comparison of the channel in the open and closed state. Top views of open and closed states, colored by protomers, showing the hexamer undergoes a ~60° rotation.

3.11 Materials and Methods

Purification, Fluorescence Polarization, and Size Exclusion Chromatography.

All Hsp104 variants were generated using QuikChange site-directed mutagenesis (Agilent) and confirmed by DNA sequencing. Hsp104, Hsp104^{T317A}, Hsp104^{N728A}, Hsp104^{E412K}, Hsp104^{R194E}, Hsp104^{E427K}, Hsp104^{R353E}, Hsp104^{D434K}, and Hsp104^{R366E} were purified as described (Jackrel et al. 2014; Torrente, Castellano, and Shorter 2014). Hsc70 and Hdj2 were from Enzo Life Sciences. For fluorescence polarization studies, Hsp104^{WT}, Hsp104^{T317A}, or Hsp104^{N728A} were exchanged into 40 mM Hepes-KOH pH 7.4, 20 mM $MgCl_2$, 150 mM KCl, 10% Glycerol (v/v), 2 mM 2-Mercaptoethanol. To assess FITC-casein binding, FITC-casein (60 nM) was incubated with increasing concentrations (0-5μM hexameric) of Hsp104, Hsp104^{T317A}, or Hsp104^{N728A} with 2 mM of the indicated nucleotide for 10 min at 25°C. For the ATP condition, an ATP regeneration system (5mM creatine phosphate and 0.125μM creatine kinase) was also included to maintain the ATP concentration. Fluorescence polarization was measured (excitation 470 nm, emission 520 nm) using a Tecan Infinite M1000 plate reader. The binding isotherms were analyzed using MicroMath Scientist 3.0. Parameters: IndVars=Xt; DepVars=P; Params: Bmax, K, Mtot; Xbar=Xf / (K + Xf); Xt=Xf+Xbar*Mtot; P=Bmax *Xbar; 0<Xf<Xt (P represents the fluorescence polarization values, Xt represents total $[Hsp104]_6$, Xf represents free $[Hsp104]_6$, Xbar represents degree of binding, and Mtot represents total [casein]).

Size exclusion chromatography (SEC) analysis and purification was performed by incubating wildtype Hsp104 (20 μM) with nucleotide (ATP, ATPγS, AMPPNP or ADP at 5 mM) in the presence or absence of FITC-casein (#C0528, Sigma) in buffer containing: 20 mM Hepes (pH=7.5), 50 mM KCl, 10 mM $MgCl_2$, 1 mM DTT. Samples were subsequently separated using a Superose 6 PC 3.2/30 column (GE Healthcare) in a running buffer containing: 40 mM

Hepes (pH=7.5), 40 mM KCl, 10 mM $MgCl_2$, 1 mM DTT. Fractions were analyzed by SDS-PAGE to confirm the presence of Hsp104 and casein. Of note, SEC analysis of FITC-casein alone (Fig. 3-1B) identified a monomer peak, eluting at ~1.7 mL, and a broad oligomer peak, eluting at ~1.2 mL, which is distinguishable from the ATPγS-Hsp104 and ATPγS-Hsp104:casein peaks, which elute at ~1.3 mL. The casein oligomer is attributed to its known polymerization capability (Redwan et al. 2015) and appears to be solubilized by Hsp104 considering it is significantly diminished in the presence of Hsp104 (Fig, 3-1B). For samples subjected to cryo-EM analysis, excess nucleotide (1mM) was added following fractionation to ensure binding during grid preparations.

	Total	Closed	Extended	MD Class 1	MD Class 2	MD Class 3	ADP
Data Collection							
Microscope	Titan Krios						
Direct Detector	Gatan K2 Summit						
Voltage	300 kV						
Magnification	50,000x						
Pixel Size	1.00Å						
Dose Rate	4.8 electrons/pixel/sec						
Total Dose	10 per sec						
# of Frames	48 electrons						
Defocus Range	1.5-3.5 µm						
Movies Taken	2764						2422
Data Processing							
Single Particles	454,924	146,463	68,459	31,969	37,361	14,494	124,933
Symmetry	C1	C1	C1	C1	C1	C1	C1
Resolution (Unmasked)	4.19 Å	4.57 Å	4.74 Å	7.31 Å	7.53 Å	7.76 Å	6.40 Å
Resolution (Masked)	3.94 Å	4.00 Å	4.13 Å	6.73 Å	6.73 Å	6.91 Å	5.64 Å
Applied B-Factor	-200	-176	-136	-381	-446	-183	-192
Model Composition							
Residues		3485	3502	4895			3906
Nucleotides		12	12	12			12
Model Scores							
Ramachandran Outliers		0.90%	1.41%	1.75%			1.65%
Ramachandran Favored		95.21%	94.02%	92.51%			92.67%
Molprobity Score		1.81	1.92	1.88			1.84
Clashscore		8.88	9.90	7.53			6.82
Poor Rotamers		0.71%	0.67%	0.14%			0.27%
Favored Rotamers		98.59%	98.39%	98.97%			99.25%
EMBD ID		8697	8746	8745			8744
PBD ID		5VJH	5VYA	5VY9			5VY8

Table 1. Data collection, processing and model parameters for all reconstructions and atomic models.

*Cryo-EM Data Collection and 3D Reconstructions***.** Protein samples were diluted to ~700µg/mL and applied to glow-discharged C-Flat holey carbon grids (CF-2/1-4C-T, Protochips) following SEC fractionation or incubation with various nucleotides (when casein was not present). Samples were plunge-frozen using a vitrobot (FEI Company) and imaged as indicated (Table 1), on a Titan Krios TEM operated at 300 keV (FEI Company). Images were recorded on a K2 Summit detector (Gatan Inc.) operated in counted mode at 50,000X nominal magnification corresponding to a calibrated 1.00 Å/pixel. Dose fractionated imaging was performed by semi-automated collection methods using UCSF Image 4 (X. Li et al. 2015). Six second exposures were collected at 100 msec/frame, with a total electron dose of 48 e- per micrograph in 60 frames (Table 1). Whole-frame drift correction was performed via Unblur (Grant and Grigorieff 2015), removing the first 2 frames of the data due to the large degree of drift. Dose weighting was applied to frames above a 30-electron total dose.

Micrographs were CTF corrected using CTFFIND4 (Rohou and Grigorieff 2015) in Relion (Scheres 2012) and single particles were automatically selected using Appion template picker within the Leginon pipeline (Lander et al. 2009). Templates were determined from the previously published Hsp104:AMPPNP data (Yokom et al. 2016). Initial 2D classification was performed to assess data quality and remove contamination and incomplete hexamer particles; this amounted to < 5% of the data for the Hsp104-ATPγS:casein dataset. All 3D classification and refinement steps were performed with Relion (Scheres 2012). For the Hsp104-ATPγS:casein data, the refinement scheme and resulting data are depicted (Fig. 3-4 and Table 1). An initial 3D refinement was performed using the Hsp104-AMPPNP structure (Yokom et al. 2016), low pass

filtered to 50 Å, as an initial model. The resulting reconstruction was used as the model for refinement using the total dataset, (~460,000 single particles from 3,000 micrographs) (Fig. 3-4). Although this structure refined to an estimated 3.9 Å (Fig. 3-3B), two protomer sites were identified to be poorly resolved. Therefore, a 10-class 3D classification was performed resulting in the identification of the 'closed' and 'extended' conformations. Extensive combinations of these classes were tested by 3D refinement in order to obtain the highest resolution models. A mask around the AAA+ core, determined with Relion, was imposed during refinement to exclude the flexible NTDs and MDs and improve the resolution. Combining classes 2 and 7 yielded the highest resolution map of the closed conformation (4.0Å) (Fig. 3-3B, 3-4). Additional sub-classifications of the 'closed-state' data (combining classes: 1,2, 5-8, and 10, or classes: 1, 5, 6, 8, 10) were performed, but did not yield improvements to the final map, and no additional conformations were identified. The final map of the extended state, at 4.1 Å resolution, was achieved by combining classes 3, 4 and 9 and performing a sub-classification with 6-classes, followed by refinement of two of the resulting classes (Fig. 3-4 and Table 1). Refinement of the total extended state particles (classes 3,4 and 9) yielded a nearly identical structure at 4.0 Å resolution however the additional classification and refinement showed improved density for the NBD2 small domain of P1 and the NBD1 of P6.

For the Hsp104-ADP reconstruction (Table 1), ~190,000 particles were automatically picked, as above, and 2D classification was performed to remove any contamination and poorly-resolved particles, resulting in a total of ~125,000 particles. The reconstruction was determined as previously described (Yokom et al. 2016), using the Hsp104-AMPPNP map, low pass filtered to 50 Å, as the initial model. 3D classification indicated the data were homogeneous with no

additional MD states therefore all the single particles were used in the refinement, resulting in a final model that represents the predominant ADP-bound Hsp104 conformation (Fig. 3-13).

To resolve the MD conformations in the Hsp104:casein complex, all closed-state data (~231,000 particles) were re-classified into 16 classes and a closed-state map (low-pass filtered to 50 Å) with the MDs and NTDs removed served as the starting model. The 3D classes were grouped by superposition and visual comparison of the MD conformations and then combined for refinement, resulting in three final models (MD Class 1-3) (Fig. 3-16A and Table 1). This approach was performed with the extended-state data; however, the MDs were unable to be clearly resolved for the mobile protomers and thus not refined further. For all final maps, the "Post-processing" procedure was used to generate a soft mask for the two half maps prior to FSC estimation and automated B-factor sharpening was performed with the combined maps (Table 1). The local resolution was estimated using ResMap (Kucukelbir, Sigworth, and Tagare 2014) for the unsharpened closed and extended-state maps (Fig. 3-6B, 3-8B).

Atomic Modeling. Initial rigid body fitting of a SWISS-MODEL (Biasini et al. 2014) homology model based on ClpB (pbd=1qvr) served as the starting structure for model building using the closed-state map. Sub Domains (NBD1 Large/Small and NBD2 Large/Small) were segmented and rigid body fit using UCSF Chimera's *Fit in Map* function. P4 was selected for initial modeling as it showed the best resolution among protomers. Missing pore loop residues in P4 of the closed model were built de novo using COOT (Emsley et al. 2010) and Phenix (Afonine et al. 2012). Rosetta Comparative Modeling procedures (described below) were then used for refinement to achieve the complete hexamer model (DiMaio et al. 2015; Song et al. 2013).

Template models were selected through HHsearch against full-length *S. cerevisiae* Hsp104 sequence. This sequence was threaded onto the initial model, fit by rigid body methods,

and the four top-scoring matches were selected using the *partial_thread* tool within Rosetta (pbd=1qvr, 5d4w, 5kne, 1rxg). These templates were set to *template_weight=0.0* within the template mover of Rosetta CM, while our initial model was set to *template_weight=1.0*. Modeling and refinement of P4 was performed as a P3-P4 dimer within a segmented map in order to accurately build the CTD, which was not available in published structures and forms part of the protomer interface. 1000 trajectories were sampled for this P3-P4 dimer and the top 20 models, based on rosetta energy score, were inspected for convergence. An additional template was used to ensure the convergence of the NBD2 pore loop (pdb=4fcv) (Biter et al. 2012), which was added to improve further trajectories of the loop region 639-686. The converged P4 model was rigid body fit into P2,P3, and P5 without change in the NBD1-NBD2 orientation, however both P1 and P6 are in substantially different conformations compared to the P4 model and modeled independently. This was achieved by rigid body-fitting the NBD1 and NBD2 domains using UCSF Chimera and then running trajectories in Rosetta CM for the P1-P6 protomer dimer with an additional 1000 models generated to obtain an accurate final model for P1 and P6. The extended-state model was determined by docking P2-P5 from the closed state and independently modeling P1 and P6, as above.

The final protomer models were combined into the full hexamer map with ATPyS molecules docked in all 12 NBD pockets. Additional density in the channel was attributed to an unfolded polypeptide from the FITC-casein substrate. The sequence could not be resolved, therefore a poly-Alanine chain (26 and 28 residues for the closed and extended states, respectively) was modeled. The N-terminus was arbitrarily oriented towards NBD2; Hsp104 may translocate either orientation of the substrate in the NBD1-to-NBD2 direction (Doyle et al. 2007; Hattendorf and Lindquist 2002; Sweeny et al. 2015). To ensure the protomer interfaces were

correctly modeled, 400 trajectories were sampled on the full hexamer complex. The 20 best models, which had the lowest energy and best electron density fit, were taken for manual inspection. Models converged well in all areas and the top model was chosen for local relax to ensure proper sidechain rotamer modeling. The final closed and extended models were relaxed into training maps derived from half of the respective data and checked for overfitting by comparing the FSC against the training or test maps. All images and movies were generated using UCSF Chimera (Pettersen et al. 2004).

Dataset		Class 1	Class 2	Class 3	Class 4	Total
AMPPNP	Particles	42562	43654	26405	48405	161026
	Open CC	**0.98**	**0.96**	0.88	0.92	100%
	Closed CC	0.90	0.91	0.90	0.90	0%
ADP	Particles	22101	38645	19539	44649	124934
	Open CC	**0.96**	**0.98**	0.89	**0.99**	100%
	Closed CC	0.91	0.92	0.92	0.87	0%
ATP	Particles	17737	37881	10344	13195	79157
	Open CC	**0.99**	**0.99**	0.85	**0.97**	87%
	Closed CC	0.90	0.89	**0.95**	0.93	13%
ATP Casein	Particles	13966	27109	18803	17627	77505
	Open CC	0.88	**0.97**	**0.95**	**0.98**	82%
	Closed CC	**0.93**	0.89	0.90	0.90	18%
ATPγS	Particles	26688	30966	41522	35170	134346
	Open CC	0.88	**0.96**	0.87	0.86	23%
	Closed CC	**0.94**	0.90	**0.96**	**0.96**	77%
ATPγS Casein	Particles	148006	136162	115782	54986	454936
	Open CC	0.86	0.84	0.85	0.87	0%
	Closed CC	**0.97**	**0.99**	**0.97**	**0.98**	100%
ATP T317A	Particles	5952	9890	8392	7826	32060
	Open CC	**0.96**	**0.99**	0.85	**0.99**	100%
	Closed CC	0.91	0.90	0.87	0.90	0%
ATPγS T317A	Particles	10820	10143	10336	3577	34876
	Open CC	**0.95**	**0.99**	**0.98**	0.89	100%
	Closed CC	0.90	0.90	0.91	0.90	0%
ATP N728A	Particles	11977	19951	7906	16123	55957
	Open CC	**0.94**	0.88	0.91	0.87	21%
	Closed CC	0.89	**0.95**	**0.96**	**0.93**	79%
ATPγS N728A	Particles	10624	5872	9105	21211	46812
	Open CC	**0.98**	0.88	**0.93**	0.86	42%
	Closed CC	0.91	**0.93**	0.91	**0.98**	58%

Table 2. Cross-correlation analysis and particle distributions for the open and closed hexamer states following 3D classification.

Open/Closed Conformational Analysis. A specific 3D classification and analysis scheme was performed to determine the fraction of open and closed hexamer populations in the presence of

different nucleotides and casein for Hsp104 wildtype, T317A and N728A (Fig. 3-17 and Table 2). 3D classification was performed for each of the datasets with Relion (Scheres 2012) using the MD Class 1 closed-state reconstruction low pass filtered to 30 Å as an initial model. Data were split into 4 classes in order to properly separate the open and closed states and account for poorly-resolved data that did not classify to either state. Both the open and closed-state reconstructions were tested as initial models but only the closed-state allowed convergence to either conformation in initial test datasets. The resulting maps were fit into the closed- and open-state reconstructions, low pass filtered to 15 Å, using the *Fit in Map* function in Chimera (Pettersen et al. 2004) to determine the cross-correlation (CC). Maps with a CC value ≥ 0.93 were designated as a match to that state. Maps that compared with a CC value < 0.93 to both the open and closed states were overall poorly resolved, thus the data were not included in subsequent analysis. Notably, top-view projections of the open and closed states show clear distinguishing features (Fig 3-17), including clear differences in the channel diameter, therefore 2D classification was performed on all data sets as well to verify proper classification.

ATPase Assay. Hsp104 (0.25μM monomer) WT or mutant was equilibrated in Luciferase Refolding Buffer (LRB: 25 mM HEPES-KOH, pH 7.4, 150 mM KAOc, 10 mM MgAOc, 10 mM DTT) for 15 min on ice and then incubated for 5 min at 25°C in the presence of ATP (1 mM) plus or minus casein (2μM). ATPase activity was assessed by the release of inorganic phosphate, which was determined using a malachite green phosphate detection kit (Innova) (Fig. 3-15B)

Luciferase Reactivation Assay. To generate aggregated luciferase, firefly luciferase (50 μM) in LRB plus 8 M urea was incubated at 30°C for 30 min. The sample was then rapidly diluted 100-fold into LRB. Aliquots were snap frozen in liquid N_2 and stored at −80°C until use. Aggregated luciferase (50 nM) was incubated with Hsp104 (1 μM monomer), Hsc70 (0.167 μM) and Hdj2

(0.167 μM) plus ATP (5 mM) and an ATP regeneration system (10 mM creatine phosphate, 0.25μM creatine kinase) for 90 min at 25°C. At the end of the reaction, luciferase activity was assessed with a luciferase assay system (Promega). Recovered luminescence was monitored using a Tecan Infinite M1000 plate reader (Fig. 3-15A).

Induced Thermotolerance Assay. W303aΔ*hsp104* (MATa, can1–100, his3–11,15, leu2–3,112, trp1–1, ura3–1, ade2–1, hsp104:kanMX4) yeast cells were transformed with a centromeric plasmid, pHSEgc, encoding Hsp104 or indicated variant under the control of the HSP104 promoter. The empty pHSEgc vector served as a negative control. Transformed yeast were grown at 30°C in S-Dextrose-His (SD-His) media to an optical density of OD_{600}=0.6. Cells were incubated at 37°C for 30 min to induce the expression of Hsp104 or the indicated variant and then transferred to 50°C for 0, 20 min or 30 min heat shock. Cells were then transferred to ice for 2 min. To evaluate viability, cells were then diluted 1,000-fold in ice-cold SD-His and plated on SD-His. Colonies were counted using an aCOLyte automated colony counter (Synbiosis) after growth at 30°C for 2 days (Fig. 3-15C). Immunoblot analysis showed that each Hsp104 variant was expressed at a similar level under equivalent conditions.

3.12 References

Abid Ali, Ferdos, Ludovic Renault, Julian Gannon, Hailey L. Gahlon, Abhay Kotecha, Jin Chuan Zhou, David Rueda, and Alessandro Costa. 2016. "Cryo-EM Structures of the Eukaryotic Replicative Helicase Bound to a Translocation Substrate." *Nature Communications* 7 (February): 10708. doi:10.1038/ncomms10708.

Afonine, Pavel V., Ralf W. Grosse-Kunstleve, Nathaniel Echols, Jeffrey J. Headd, Nigel W. Moriarty, Marat Mustyakimov, Thomas C. Terwilliger, Alexandre Urzhumtsev, Peter H. Zwart, and Paul D. Adams. 2012. "Towards Automated Crystallographic Structure Refinement with Phenix.Refine." *Acta Crystallographica. Section D, Biological Crystallography* 68 (Pt 4): 352–67. doi:10.1107/S0907444912001308.

Biasini, Marco, Stefan Bienert, Andrew Waterhouse, Konstantin Arnold, Gabriel Studer, Tobias Schmidt, Florian Kiefer, et al. 2014. "SWISS-MODEL: Modelling Protein Tertiary and Quaternary Structure Using Evolutionary Information." *Nucleic Acids Research* 42 (Web Server issue): W252-258. doi:10.1093/nar/gku340.

Biter, Amadeo B., Sukyeong Lee, Nuri Sung, and Francis T. F. Tsai. 2012. "Structural Basis for Intersubunit Signaling in a Protein Disaggregating Machine." *Proceedings of the National Academy of Sciences of the United States of America* 109 (31): 12515–20. doi:10.1073/pnas.1207040109.

Carroni, Marta, Eva Kummer, Yuki Oguchi, Petra Wendler, Daniel K. Clare, Irmgard Sinning, Jürgen Kopp, Axel Mogk, Bernd Bukau, and Helen R. Saibil. 2014. "Head-to-Tail Interactions of the Coiled-Coil Domains Regulate ClpB Activity and Cooperation with Hsp70 in Protein Disaggregation." *ELife* 3 (April): e02481.

DeSantis, Morgan E., Eunice H. Leung, Elizabeth A. Sweeny, Meredith E. Jackrel, Mimi Cushman-Nick, Alexandra Neuhaus-Follini, Shilpa Vashist, Matthew A. Sochor, M. Noelle Knight, and James Shorter. 2012. "Operational Plasticity Enables Hsp104 to Disaggregate Diverse Amyloid and Nonamyloid Clients." *Cell* 151 (4): 778–93. doi:10.1016/j.cell.2012.09.038.

DiMaio, Frank, Yifan Song, Xueming Li, Matthias J. Brunner, Chunfu Xu, Vincent Conticello, Edward Egelman, Thomas Marlovits, Yifan Cheng, and David Baker. 2015. "Atomic-Accuracy Models from 4.5-Å Cryo-Electron Microscopy Data with Density-Guided Iterative Local Refinement." *Nature Methods* 12 (4): 361–65. doi:10.1038/nmeth.3286.

Doyle, Shannon M., James Shorter, Michal Zolkiewski, Joel R. Hoskins, Susan Lindquist, and Sue Wickner. 2007. "Asymmetric Deceleration of ClpB or Hsp104 ATPase Activity Unleashes Protein-Remodeling Activity." *Nature Structural & Molecular Biology* 14 (2): 114–22. doi:10.1038/nsmb1198.

Emsley, P., B. Lohkamp, W. G. Scott, and K. Cowtan. 2010. "Features and Development of Coot." *Acta Crystallographica. Section D, Biological Crystallography* 66 (Pt 4): 486–501. doi:10.1107/S0907444910007493.

Enemark, Eric J., and Leemor Joshua-Tor. 2006. "Mechanism of DNA Translocation in a Replicative Hexameric Helicase." *Nature* 442 (7100): 270–75. doi:10.1038/nature04943.

Erzberger, Jan P., and James M. Berger. 2006. "Evolutionary Relationships and Structural Mechanisms of AAA+ Proteins." *Annual Review of Biophysics and Biomolecular Structure* 35: 93–114. doi:10.1146/annurev.biophys.35.040405.101933.

Glynn, Steven E., Andreas Martin, Andrew R. Nager, Tania A. Baker, and Robert T. Sauer. 2009. "Structures of Asymmetric ClpX Hexamers Reveal Nucleotide-Dependent Motions in a AAA+ Protein-Unfolding Machine." *Cell* 139 (4): 744–56. doi:10.1016/j.cell.2009.09.034.

Grant, Timothy, and Nikolaus Grigorieff. 2015. "Measuring the Optimal Exposure for Single Particle Cryo-EM Using a 2.6 Å Reconstruction of Rotavirus VP6." *ELife* 4 (May): e06980. doi:10.7554/eLife.06980.

Hattendorf, Douglas A., and Susan L. Lindquist. 2002. "Cooperative Kinetics of Both Hsp104 ATPase Domains and Interdomain Communication Revealed by AAA Sensor-1 Mutants." *The EMBO Journal* 21 (1–2): 12–21. doi:10.1093/emboj/21.1.12.

Heuck, Alexander, Sonja Schitter-Sollner, Marcin Józef Suskiewicz, Robert Kurzbauer, Juliane Kley, Alexander Schleiffer, Pascaline Rombaut, Franz Herzog, and Tim Clausen. 2016. "Structural Basis for the Disaggregase Activity and Regulation of Hsp104." *ELife* 5 (November). doi:10.7554/eLife.21516.

Jackrel, Meredith E., Morgan E. DeSantis, Bryan A. Martinez, Laura M. Castellano, Rachel M. Stewart, Kim A. Caldwell, Guy A. Caldwell, and James Shorter. 2014. "Potentiated

Hsp104 Variants Antagonize Diverse Proteotoxic Misfolding Events." *Cell* 156 (1–2): 170–82. doi:10.1016/j.cell.2013.11.047.
Kucukelbir, Alp, Fred J. Sigworth, and Hemant D. Tagare. 2014. "Quantifying the Local Resolution of Cryo-EM Density Maps." *Nature Methods* 11 (1): 63–65. doi:10.1038/nmeth.2727.
Lander, Gabriel C., Scott M. Stagg, Neil R. Voss, Anchi Cheng, Denis Fellmann, James Pulokas, Craig Yoshioka, et al. 2009. "Appion: An Integrated, Database-Driven Pipeline to Facilitate EM Image Processing." *Journal of Structural Biology* 166 (1): 95–102.
Lee, Jungsoon, Ji-Hyun Kim, Amadeo B. Biter, Bernhard Sielaff, Sukyeong Lee, and Francis T. F. Tsai. 2013. "Heat Shock Protein (Hsp) 70 Is an Activator of the Hsp104 Motor." *Proceedings of the National Academy of Sciences of the United States of America* 110 (21): 8513–18. doi:10.1073/pnas.1217988110.
Lee, Sukyeong, Mathew E. Sowa, Yo-hei Watanabe, Paul B. Sigler, Wah Chiu, Masasuke Yoshida, and Francis T. F. Tsai. 2003. "The Structure of ClpB: A Molecular Chaperone That Rescues Proteins from an Aggregated State." *Cell* 115 (2): 229–40.
Li, Tao, Clarissa L. Weaver, Jiabei Lin, Elizabeth C. Duran, Justin M. Miller, and Aaron L. Lucius. 2015. "Escherichia Coli ClpB Is a Non-Processive Polypeptide Translocase." *The Biochemical Journal* 470 (1): 39–52. doi:10.1042/BJ20141457.
Li, Xueming, Shawn Zheng, David A. Agard, and Yifan Cheng. 2015. "Asynchronous Data Acquisition and On-the-Fly Analysis of Dose Fractionated CryoEM Images by UCSFImage." *Journal of Structural Biology* 192 (2): 174–78. doi:10.1016/j.jsb.2015.09.003.
Lum, Ronnie, Johnny M. Tkach, Elizabeth Vierling, and John R. Glover. 2004. "Evidence for an Unfolding/Threading Mechanism for Protein Disaggregation by Saccharomyces Cerevisiae Hsp104." *The Journal of Biological Chemistry* 279 (28): 29139–46. doi:10.1074/jbc.M403777200.
Lyubimov, Artem Y., Alessandro Costa, Franziska Bleichert, Michael R. Botchan, and James M. Berger. 2012. "ATP-Dependent Conformational Dynamics Underlie the Functional Asymmetry of the Replicative Helicase from a Minimalist Eukaryote." *Proceedings of the National Academy of Sciences of the United States of America* 109 (30): 11999–4. doi:10.1073/pnas.1209406109.
Matyskiela, Mary E., Gabriel C. Lander, and Andreas Martin. 2013. "Conformational Switching of the 26S Proteasome Enables Substrate Degradation." *Nature Structural & Molecular Biology* 20 (7): 781–88. doi:10.1038/nsmb.2616.
Oguchi, Yuki, Eva Kummer, Fabian Seyffer, Mykhaylo Berynskyy, Benjamin Anstett, Regina Zahn, Rebecca C. Wade, Axel Mogk, and Bernd Bukau. 2012. "A Tightly Regulated Molecular Toggle Controls AAA+ Disaggregase." *Nature Structural & Molecular Biology* 19 (12): 1338–46. doi:10.1038/nsmb.2441.
Olivares, Adrian O., Tania A. Baker, and Robert T. Sauer. 2016. "Mechanistic Insights into Bacterial AAA+ Proteases and Protein-Remodelling Machines." *Nature Reviews. Microbiology* 14 (1): 33–44. doi:10.1038/nrmicro.2015.4.
Pettersen, Eric F., Thomas D. Goddard, Conrad C. Huang, Gregory S. Couch, Daniel M. Greenblatt, Elaine C. Meng, and Thomas E. Ferrin. 2004. "UCSF Chimera--a Visualization System for Exploratory Research and Analysis." *Journal of Computational Chemistry* 25 (13): 1605–12. doi:10.1002/jcc.20084.

Redwan, Elrashdy M., Bin Xue, Hussein A. Almehdar, and Vladimir N. Uversky. 2015. "Disorder in Milk Proteins: Caseins, Intrinsically Disordered Colloids." *Current Protein & Peptide Science* 16 (3): 228–42.

Rohou, Alexis, and Nikolaus Grigorieff. 2015. "CTFFIND4: Fast and Accurate Defocus Estimation from Electron Micrographs." *Journal of Structural Biology* 192 (2): 216–21. doi:10.1016/j.jsb.2015.08.008.

Scheres, Sjors H. W. 2012. "RELION: Implementation of a Bayesian Approach to Cryo-EM Structure Determination." *Journal of Structural Biology* 180 (3): 519–30. doi:10.1016/j.jsb.2012.09.006.

Skordalakes, Emmanuel, and James M. Berger. 2003. "Structure of the Rho Transcription Terminator: Mechanism of MRNA Recognition and Helicase Loading." *Cell* 114 (1): 135–46.

Śledź, Paweł, Pia Unverdorben, Florian Beck, Günter Pfeifer, Andreas Schweitzer, Friedrich Förster, and Wolfgang Baumeister. 2013. "Structure of the 26S Proteasome with ATP-ΓS Bound Provides Insights into the Mechanism of Nucleotide-Dependent Substrate Translocation." *Proceedings of the National Academy of Sciences of the United States of America* 110 (18): 7264–69. doi:10.1073/pnas.1305782110.

Song, Yifan, Frank DiMaio, Ray Yu-Ruei Wang, David Kim, Chris Miles, Tj Brunette, James Thompson, and David Baker. 2013. "High-Resolution Comparative Modeling with RosettaCM." *Structure (London, England: 1993)* 21 (10): 1735–42. doi:10.1016/j.str.2013.08.005.

Sweeny, Elizabeth A., Meredith E. Jackrel, Michelle S. Go, Matthew A. Sochor, Beatrice M. Razzo, Morgan E. DeSantis, Kushol Gupta, and James Shorter. 2015. "The Hsp104 N-Terminal Domain Enables Disaggregase Plasticity and Potentiation." *Molecular Cell* 57 (5): 836–49. doi:10.1016/j.molcel.2014.12.021.

Sweeny, Elizabeth A., and James Shorter. 2016. "Mechanistic and Structural Insights into the Prion-Disaggregase Activity of Hsp104." *Journal of Molecular Biology* 428 (9 Pt B): 1870–85. doi:10.1016/j.jmb.2015.11.016.

Tessarz, Peter, Axel Mogk, and Bernd Bukau. 2008. "Substrate Threading through the Central Pore of the Hsp104 Chaperone as a Common Mechanism for Protein Disaggregation and Prion Propagation." *Molecular Microbiology* 68 (1): 87–97. doi:10.1111/j.1365-2958.2008.06135.x.

Thomsen, Nathan D., and James M. Berger. 2009. "Running in Reverse: The Structural Basis for Translocation Polarity in Hexameric Helicases." *Cell* 139 (3): 523–34. doi:10.1016/j.cell.2009.08.043.

Torrente, Mariana P., Laura M. Castellano, and James Shorter. 2014. "Suramin Inhibits Hsp104 ATPase and Disaggregase Activity." *PloS One* 9 (10): e110115. doi:10.1371/journal.pone.0110115.

Wehmer, Marc, and Eri Sakata. 2016. "Recent Advances in the Structural Biology of the 26S Proteasome." *The International Journal of Biochemistry & Cell Biology* 79 (October): 437–42. doi:10.1016/j.biocel.2016.08.008.

Wendler, Petra, James Shorter, Celia Plisson, Anil G. Cashikar, Susan Lindquist, and Helen R. Saibil. 2007. "Atypical AAA+ Subunit Packing Creates an Expanded Cavity for Disaggregation by the Protein-Remodeling Factor Hsp104." *Cell* 131 (7): 1366–77. doi:10.1016/j.cell.2007.10.047.

Yokom, Adam L., Stephanie N. Gates, Meredith E. Jackrel, Korrie L. Mack, Min Su, James Shorter, and Daniel R. Southworth. 2016. “Spiral Architecture of the Hsp104 Disaggregase Reveals the Basis for Polypeptide Translocation.” *Nature Structural & Molecular Biology* 23 (9): 830–37. doi:10.1038/nsmb.3277.

Zhao, Minglei, Shenping Wu, Qiangjun Zhou, Sandro Vivona, Daniel J. Cipriano, Yifan Cheng, and Axel T. Brunger. 2015. “Mechanistic Insights into the Recycling Machine of the SNARE Complex.” *Nature* 518 (7537): 61–67. doi:10.1038/nature14148.

CHAPTER 4

THE PROTEIN TARGETING FACTOR GET3 MOONLIGHTS AS ATP-INDEPENDENT CHAPERONE UNDER OXIDATIVE STRESS CONDITIONS

This chapter is published:
Voth W, Schick M, Gates S, Li S, Vilardi F, Gostimskaya I, Southworth DR, Schwappach B, and Jakob U. THE PROTEIN TARGETING FACTOR GET3 FUNCTIONS AS AN ATP-INDEPENDENT CHAPERONE UNDER OXIDATIVE STRESS CONDITIONS. *Molecular cell*. 2014;56(1):116-127. [1]

4.1 Abstract

Exposure of cells to reactive oxygen species (ROS) causes a rapid and significant drop in intracellular ATP-levels. This energy depletion negatively affects ATP-dependent chaperone systems, making ROS-mediated protein unfolding and aggregation a potentially very challenging problem. Here we show that Get3, a protein involved in ATP-dependent targeting of tail-anchored (TA) proteins under non-stress conditions, turns into an effective ATP-*in*dependent chaperone under oxidative stress conditions. Activation of Get3's chaperone function, which is a fully reversible process, involves disulfide bond formation, metal release and its conversion into distinct, higher oligomeric structures. Mutational studies demonstrate that the chaperone activity of Get3 is functionally distinct from and likely mutually exclusive with its targeting function, and responsible for the oxidative stress sensitive phenotype that has long been noted for yeast cells lacking functional Get3. These results provide convincing evidence that Get3

[1] My contributions to this chapter were the SEC-MALS and EM analysis. Contributions by members of the Jakob lab (University of Michigan) and Schwappach lab (Max-Planck Institute), and Sheng Li (UCSD) are indicated in the figure legends.

moonlights as a redox regulated chaperone, effectively protecting eukaryotic cells against oxidative protein damage.

4.2 Introduction

The cytosolic ATPase Get3 in yeast (mammalian TRC40) is a central player of the *G*uided *E*ntry of *T*ail-anchored proteins (GET) pathway, which is responsible for the posttranslational integration of tail-anchored (TA) proteins into the membrane of the endoplasmic reticulum (Favaloro et al. 2008; Schuldiner et al. 2008; Stefanovic and Hegde 2007). In this role, Get3 shuttles between a cytosolic multi-protein complex that receives the TA precursor proteins from the ribosome, and a Get1/Get2 receptor complex at the ER membrane, where the TA-protein precursors are released and integrated into the lipid bilayer (Mariappan et al. 2010, 2011; Stefer et al. 2011). This cycle is associated with significant conformational changes in Get3, induced by substrate binding and ATP hydrolysis. Importantly, while mutations in components of the GET system are lethal in higher eukaryotes (Mukhopadhyay et al. 2006), yeast cells survive their absence (Metz et al. 2006; Shen et al. 2003). Nevertheless, deletion of the *GET3* gene in yeast leads to several, seemingly unrelated phenotypes, including hygromycin sensitivity, copper and H_2O_2 sensitivity, heat sensitivity and the inability to grow on iron-limiting media (Schuldiner et al. 2008; Shen et al. 2003). It still remains to be elucidated whether these different phenotypes are all due to the reduced integration of specific TA proteins into the ER membrane, or are caused by the absence of a potentially second role of Get3 in maintaining metal homeostasis and/or mediating oxidative stress resistance.

Get3 is a zinc-binding protein with four highly conserved cysteines, two of which (C285/C288) are essential for complementing the growth defect of a *get3* deletion strain under various stress conditions (Metz et al. 2006). Arranged in a C-X-C $-X_{43}$-C-X-X-C motif, this

cysteine arrangement is highly reminiscent of the oxidation sensitive zinc-binding motif found in Hsp33, a redox-regulated ATP-*in*dependent chaperone in bacteria. Once activated by disulfide bond formation and zinc release, Hsp33 prevents oxidative stress mediated protein aggregation, thereby increasing bacterial oxidative stress resistance (Jakob et al. 1999). Like oxidized Hsp33, aerobically purified Get3 was recently found to also function as ATP-*in*dependent general chaperone *in vitro*, highly effective in protecting unfolding proteins against aggregation (Powis et al. 2013). *In vivo* studies agreed with these results by demonstrating that Get3 co-localizes with unfolding proteins and chaperones in distinct foci during ATP-depleting stress conditions in yeast (Powis et al. 2013).

The intriguing similarities between Get3 and the structurally unrelated Hsp33 prompted our investigations into the regulation of Get3's ATP-*in*dependent chaperone function. We discovered that incubation of Get3 with the hydroxyl-radical producing combination of H_2O_2 and Cu^{2+} rapidly and reversibly switches the protein from an ATPase-driven TA-binding protein into a general, ATP-independent chaperone. Triggered by disulfide bond formation and zinc release, Get3 undergoes massive conformational rearrangements, which result in the formation of highly active Get3 tetramers and higher oligomers, capable of binding unfolding proteins and preventing their non-specific aggregation. *In vitro* and *in vivo* studies using established TA-binding or ATPase deficient Get3 variants confirmed our discovery that Get3 has two distinct functions, and moonlights as general chaperone under ATP-depleted oxidative stress conditions.

4.3 Get3 – A redox-regulated chaperone in eukaryotes

Get3's copper sensitive phenotype, its ability to chaperone soluble proteins *in vitro*, the similarity between Get3's cysteine motif with that found in the redox-regulated chaperone Hsp33, and the presence of disulfide-linked Get3 dimers in Get3 crystals (Suloway et al. 2009) raised the intriguing possibility that Get3 might serve as redox-controlled ATP-independent chaperone that protects proteins against oxidative stress-induced protein aggregation. ATP-*in*dependent chaperone function is particularly crucial under these stress conditions, since exposure of cells to ROS is known to cause a severe and rapid decrease in cellular ATP-levels, incapacitating ATP-dependent chaperones (Winter et al. 2005).

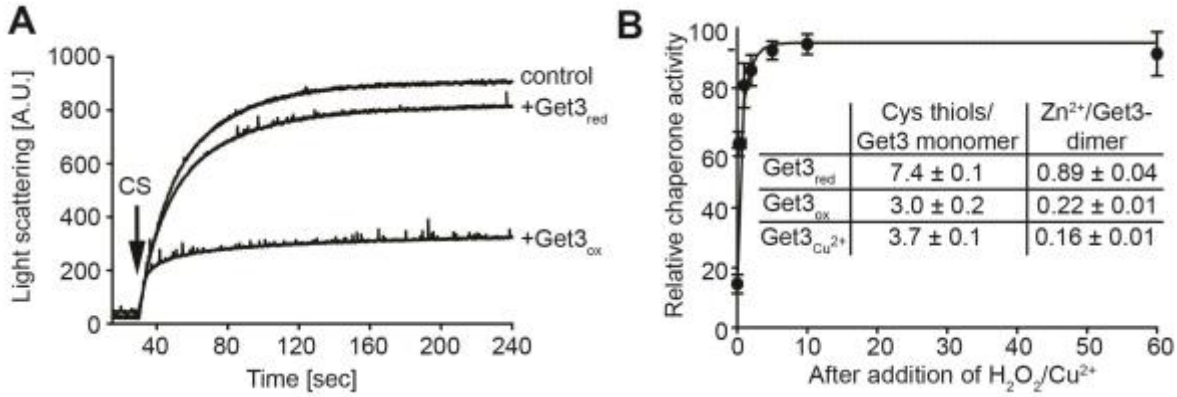

Figure 4-1. ROS-mediated activation of Get3 as ATP-independent chaperone
(A) Effect of an 8-fold molar excess of $Get3_{red}$ or $Get3_{ox}$ on the light scattering of chemically denatured Citrate Synthase (CS) (75 nM). Light scattering of CS in the absence of added chaperones is shown as control. (B) The chaperone function of 0.3 µM $Get3_{red}$ before and at defined time points after incubation in 2 mM H_2O_2/50 µM Cu^{2+} at 37°C was determined by analyzing the influence of Get3 on the aggregation of 0.075 µM chemically denatured CS. The light scattering signal of CS in the absence of added chaperones was set to 0% chaperone activity, whereas the light scattering signal in the presence of fully oxidized Get3 was set to 100%. **Insert:** The number of cysteine thiols in reduced and oxidized Get3 was determined under denaturing conditions using Ellman's assay. The precise amount of zinc associated with reduced and oxidized Get3 was determined by ICP analysis. The following experiments and figures were performed and created by Voth W (Jakob Laboratory, University of Michigan).

To test if Get3's general chaperone activity is indeed redox-regulated, we purified Get3 under reducing conditions ($Get3_{red}$), and tested its ability to prevent the aggregation of chemically unfolding citrate synthase (CS). An eight-fold molar excess of $Get3_{red}$ over CS had only a

minor effect on the aggregation behavior of CS (Figure 4-1A). However, incubation of $Get3_{red}$ with the hydroxyl-radical producing mixture of hydrogen peroxide (H_2O_2) and Cu^{2+} ($Get3_{ox}$) led to the very rapid activation of Get3's chaperone function ($T_{1/2} < 1$ min) (Fig. 4-1B, black circles) and an almost complete inhibition of CS aggregation at an 8:1 molar ratio of Get_{ox} to CS (Fig. 4-1A). Very similar results were obtained when we tested the influence of $Get3_{red}$ and $Get3_{ox}$ on chemically or thermally unfolding luciferase (Fig. 4-2). These results suggest that incubation with hydroxyl-producing oxidants converts Get3 into a general molecular chaperone for unfolding soluble proteins.

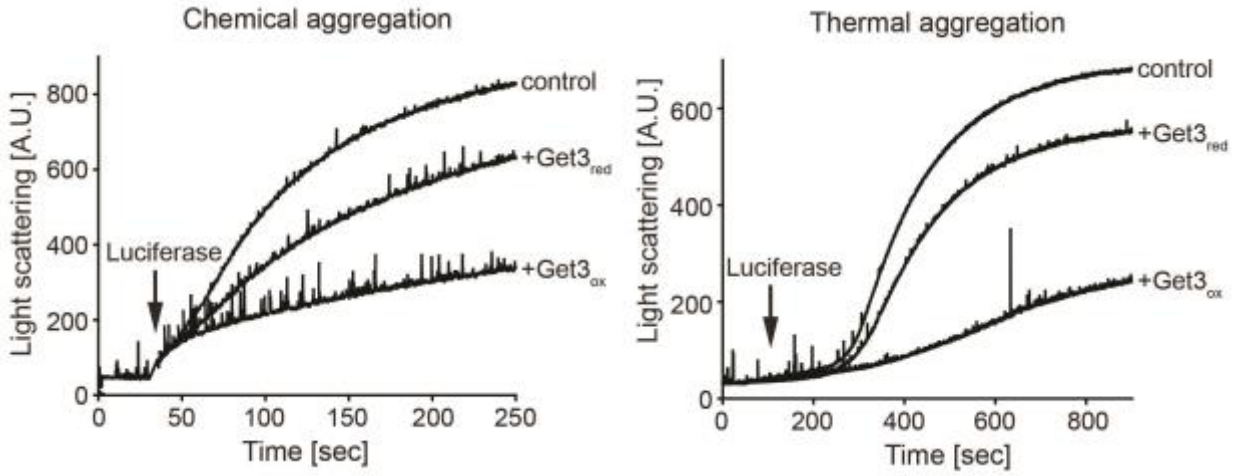

Figure 4-2. Get3 functions as chaperone when oxidized. Effect of $Get3_{red}$ or $Get3_{ox}$ on the light scattering of chemically denatured luciferase (Get3:luciferase ratio 8:1) or thermally unfolding luciferase at 43°C (Get3:luciferase ratio 1:1). Light scattering of luciferase in the absence of added chaperones is shown (control). The following experiments and figures were performed and created by Voth W (Jakob Laboratory, University of Michigan).

Incubation of Get3 with 50 μM Cu^{2+} in the absence of H_2O_2 also activated the chaperone function of Get3 but displayed biphasic kinetics with an extremely fast initial activation followed by a slower activation phase (Figure 4-3A, triangles). At 200 μM copper, however, full activation was achieved within the mixing time of the experiment (Fig. 4-3B). Removal of Cu^{2+} using the strong chelator tetrakis(2pyridylmethyl) ethylene-diamine (TPEN)

immediately before testing the chaperone function of Get3 revealed no difference in the chaperone activity of Get3 (Fig. 4-3B, insert), indicating that the activation of Get3's chaperone function is not triggered by copper binding but is likely due to oxidative modification of Get3. Consistent with this conclusion we found that presence of 2 mM H_2O_2, a kinetically slow oxidant also converted Get3 into a chaperone but with slower activation kinetics ($T_{1/2}$ ~ 5 min) (Fig. 4-3A, squares).

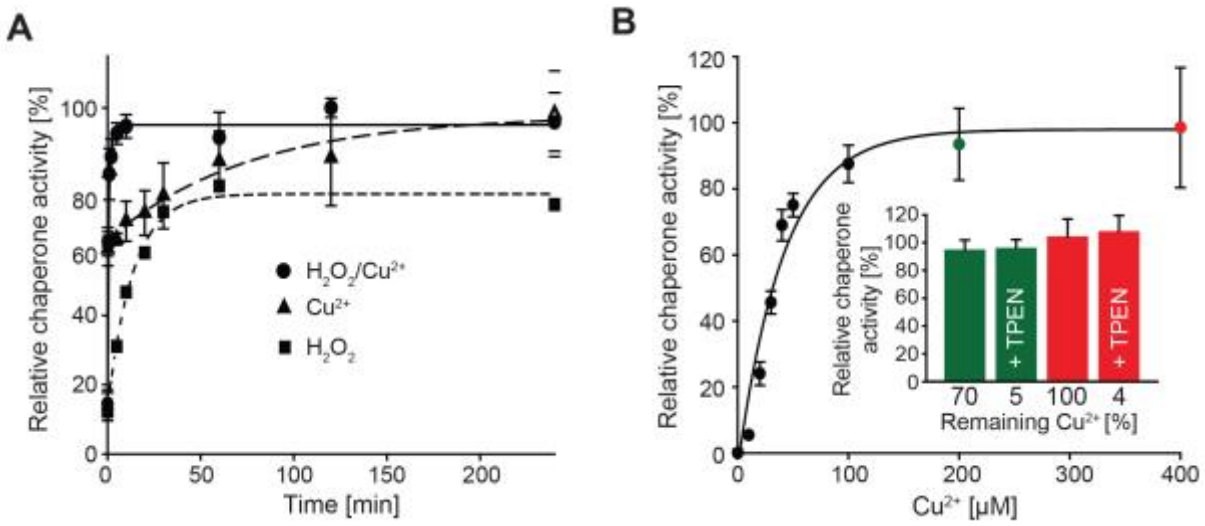

Figure 4-3.Get3 chaperone activity with Cu^{2+}. (A) The chaperone function of 0.3 µM $Get3_{red}$ before and at defined time points after incubation in either 2 mM H_2O_2/50 µM Cu^{2+} (circles), 50 µm Cu^{2+} (triangles) or 2 mM H_2O_2 (squares) at 37°C was determined by analyzing the influence of Get3 on the aggregation of 0.075 µM chemically denatured CS. The light scattering signal of CS in the absence of added chaperones was set to 0% chaperone activity, whereas the light scattering signal in the presence of fully oxidized Get3 was set to 100%. (B) The chaperone function of 0.3 µM $Get3_{red}$ before and 4 min after addition of various concentrations of copper at 37°C was analyzed as described. Insert: $Get3_{red}$ that was incubated in either 200 µm $CuCl_2$ (green bars) or 400 µM $CuCl_2$ (red bars) for 5 min was either incubated with a 100-fold excess of the copper chelator TPEN for 10 min or left untreated. The samples were then loaded onto gel filtration columns equilibrated with metal-free buffer and tested for their remaining copper content by ICP analysis. The same samples were tested for their chaperone activity as described above. At least 3-6 replicates were performed and the standard error is shown. The following experiments and figures were performed and created by Voth W (Jakob Laboratory, University of Michigan).

To test how oxidation affects the ATPase activity of Get3, we directly compared the ability of oxidized and reduced Get3 to hydrolyze ATP. As shown in Figure 4-4A, chaperone-

active $Get3_{ox}$ showed less than 20% ATPase activity compared to $Get3_{red}$, suggesting that oxidation leads to conformational changes that affect ATP hydrolysis. These results are fully consistent with previous findings revealing that Get3's chaperone function is not affected by ATP, and that *in vivo* co-localization of Get3 with protein aggregates occurs under ATP-depleting stress conditions (Powis et al. 2013). Analysis of the chaperone function of the ATPase-deficient Get3 D57E mutant variant revealed that this mutant protein is fully chaperone-active when oxidized further agreeing with our conclusions (Fig. 4-4B). These results indicate that ATP-hydrolysis is neither required for the oxidative activation of Get3 nor for its general chaperone function. From these data we concluded that Get3 converts into a potent ATP-independent chaperone when exposed to oxidative stress conditions *in vitro*.

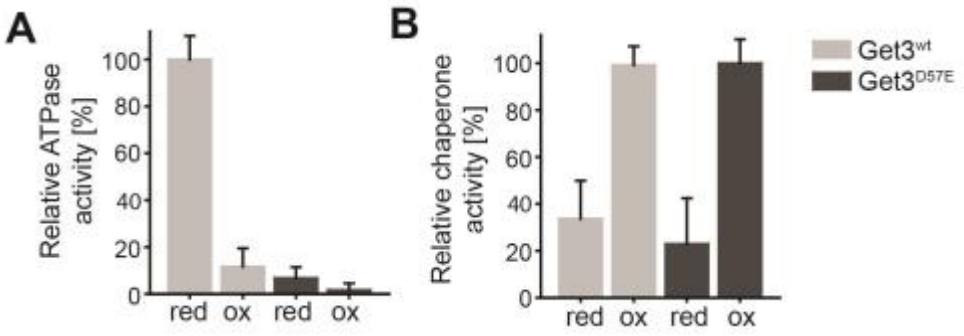

Figure 4-4. ATPase activity of $Get3_{ox}$ and $Get3_{red}$. (A) Relative ATPase activity and (B) chaperone activity of reduced and oxidized wild-type Get3 and the ATPase deficient Get3 D57E mutant. A four-fold excess of Get3 to CS was used for the chaperone assays. At least 3-6 replicates were performed and the standard error is shown. The following experiments and figures were performed and created by Voth W (Jakob Laboratory, University of Michigan).

4.4 Mechanism of Get3's activation process

Whereas mixtures of hydroxyl radicals and copper produce highly reactive hydroxyl radicals that rapidly react with cysteine thiols, Cu^{2+} is known to catalyze the auto-oxidation of cysteine thiols displaying biphasic oxidation kinetics (Kachur, Koch, and Biaglow 1999). To investigate whether incubation of Get3 with H_2O_2/Cu^{2+} or Cu^{2+} alone leads indeed to the

oxidation of Get3's cysteines, we compared the thiol oxidation status of $Get3_{red}$ with that of the two fully chaperone-active species, Get3 treated with 2 mM H_2O_2 / 50 µM Cu^{2+} for 10 min ($Get3_{ox}$) or Get3 treated with 50 µM Cu^{2+} for 240 min ($Get3_{Cu2+}$), upon their denaturation in 6 M guanidinium-HCl (Fig. 4-1B, insert). The reaction revealed about seven cysteines for $Get3_{red}$, representing the four absolutely conserved cysteines as well as three non-conserved cysteines. In contrast, we detected only about three cysteines in both chaperone-active species. These results suggest the formation of two disulfide bonds in $Get3_{ox}$, whose formation either precedes or parallels the activation of Get3 as an ATP-independent chaperone.

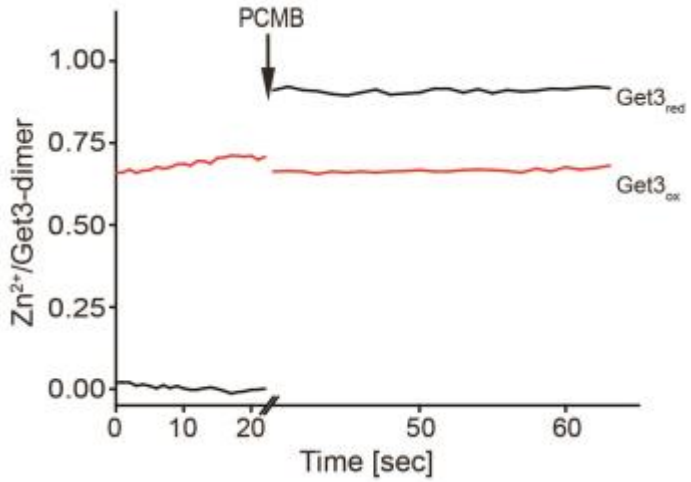

Figure 4-5. Oxidation of Get3 causes zinc release. Reduced and oxidized Get3 (2 µM) were incubated in the presence of 100 µM 4-(2-pyridylazo)resorcinol (PAR), which forms bright red complexes with metals such as zinc (K_d for Zn-PAR_2 = 7.7 x 10^{-11} M) or copper (K_d for Cu-PAR_2 = 2.6 x 10^{-15} M). PAR is unable to compete for zinc binding with high affinity sites, like cysteine-coordinating zinc centers. Addition of parachloromercuribenzoic acid (PAR/PCMB) leads to thiol-mercaptide bond formation which releases cysteine-coordinated metal that now interacts with PAR. Signal from surface-attached metal was subtracted from the baseline. The following experiments and figures were performed and created by Voth W (Jakob Laboratory, University of Michigan).

Since the cysteine thiols of the C-X-Y-C motif contribute to dimer formation via zinc coordination (Mateja et al. 2009), we next tested whether the observed oxidation of Get3 causes zinc release. We therefore performed metal analysis using inductively coupled plasma mass

spectrometry (ICP) of both oxidized and reduced species. Indeed, ICP analysis revealed the presence of about 0.9 zinc equivalents per Get3 dimer in the reduced form (Fig. 4-1B, insert), and only about 0.2 equivalents of zinc in the oxidized species. According to the 4-(2-pyridylazo)resorcinol/parachloromercuribenzoic acid (PAR/PCMB) assay, which allows discrimination between high-affinity cysteine-coordinated and low-affinity surface metal binding (Ilbert et al. 2007), only reduced Get3 had metals bound via cysteine thiols (Fig. 4-5). From these experiments we concluded that Get3's activation as ATP-independent chaperone involves thiol oxidation and concomitant release of the cysteine-coordinated zinc.

4.5 Activation of Get3's chaperone function is a fully reversible process *in vitro*

Reversibility is a major aspect of every posttranslational regulation event. To test whether oxidative activation of Get3's chaperone function and, correspondingly, the inactivation of Get3's ATPase activity are reversible processes, we incubated $Get3_{ox}$ with DTT and Zn to reduce any reversible thiol modifications and reconstitute the zinc site. We found that treatment with DTT rapidly re-reduced the cysteines, with six cysteines detectable after 5 min of DTT treatment and all seven cysteines accessible within 30 min of incubation. However, even after 6-hour treatment with DTT and zinc, the chaperone activity of Get3 was not significantly different from untreated $Get3_{ox}$ incubated over the same amount of time (Fig. 4-6).

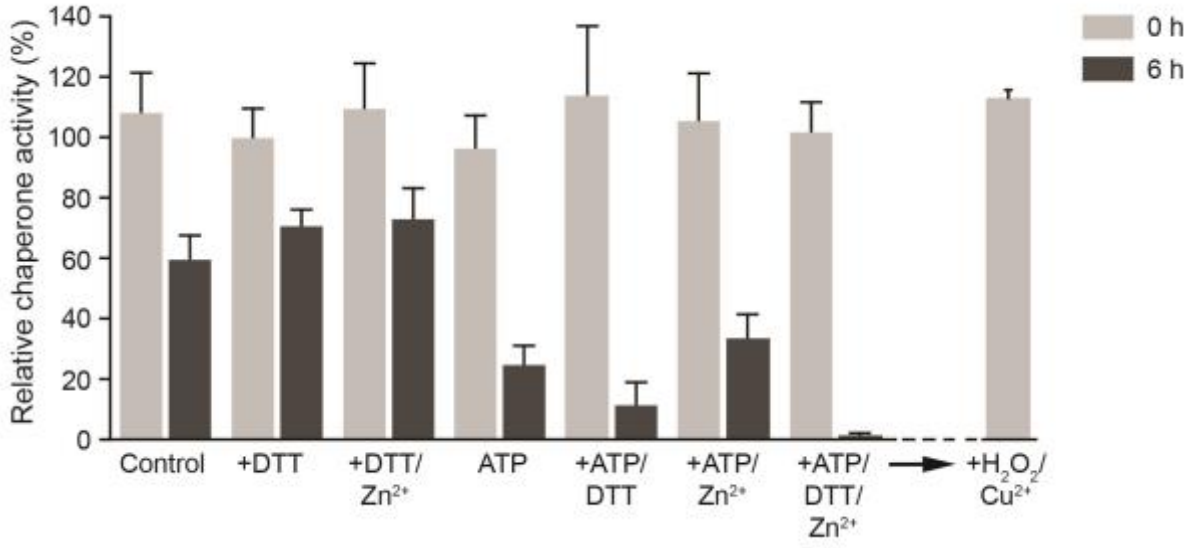

Figure 4-6. Activation of Get3's chaperone function is a fully reversible process. Chaperone-active wild-type $Get3_{ox}$ (0.3 µM) was incubated in the presence of either 5 mM DTT / 5 µM zinc ($Get3_{ox□DTT/Zn}$) or 2 mM MgATP, 5 mM DTT / 5 µM zinc ($Get3_{ox□red}$) for 6 h at 30°C. The reductants were removed and the various Get3 preparations were tested for their ability to prevent aggregation of chemically denatured CS as outlined in Figure legend 4-1. To investigate whether Get3 can undergo multiple rounds of oxidation and reduction processes, we incubated the chaperone-inactive $Get3_{ox\ □red}$ with 2 mM H_2O_2 and 50 µM Cu^{2+} for 10 min and tested its chaperone function as described. The following experiments and figures were performed and created by Voth W (Jakob Laboratory, University of Michigan).

These results were highly reminiscent of oxidized Hsp33, whose inactivation was found to be very slow despite the very rapid reduction of its disulfide bonds (Hoffmann et al. 2004). We therefore reasoned that like Hsp33, Get3 might undergo conformational rearrangements, whose re-organization upon cysteine reduction and zinc-coordination might become rate-limiting in the inactivation process. Indeed, comparison of the secondary structure of $Get3_{red}$ and $Get3_{ox}$ by far-UV-CD revealed extensive conformational changes upon oxidation, consistent with a substantial loss in α-helices and the accumulation of random-coil structure (Fig. 4-7A, compare black and red traces). Binding studies with bis(4-anilino-5-napththalenesulfonic acid) (bis-ANS), a fluorescent sensor molecule of hydrophobic surfaces revealed that this partial unfolding of $Get3_{ox}$ was accompanied by the exposure of hydrophobic

surfaces, a hallmark of active chaperones (Fig. 4-7A, insert).

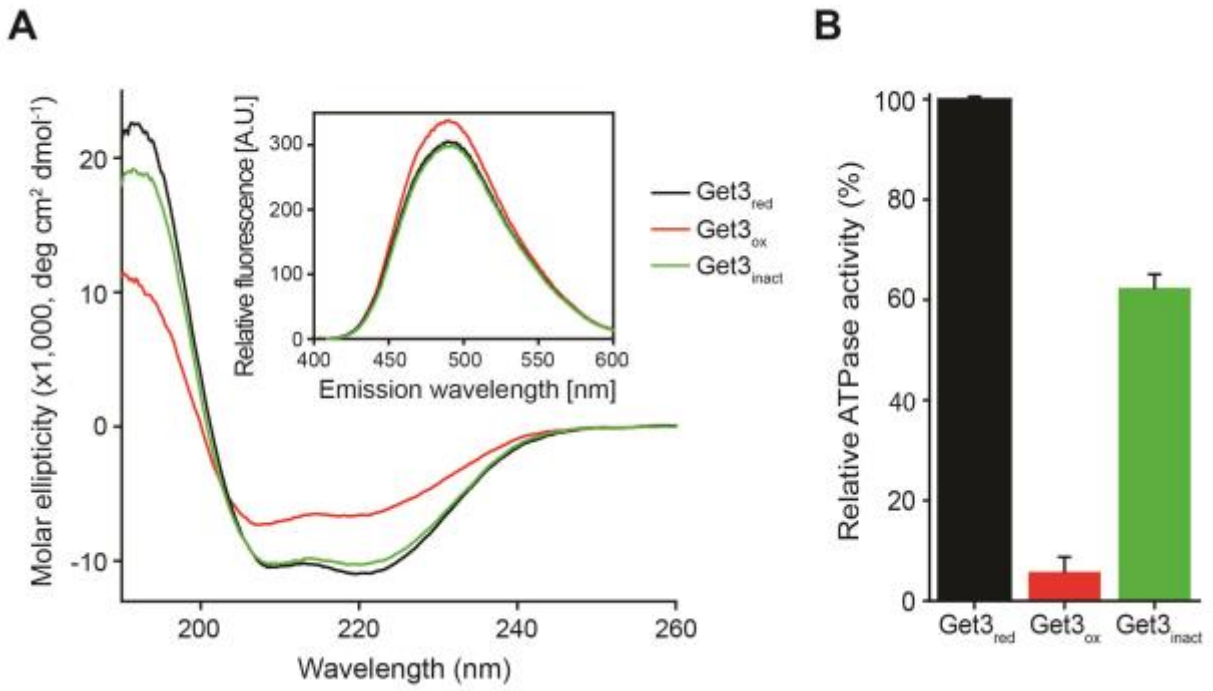

Figure 4-7. Far-UV Circular Dichroism and ATPase activity of Get3ox. (A) Analysis of secondary structure and surface hydrophobicity (**insert**) of $Get3_{red}$ (black trace), $Get3_{ox}$ (red trace) and $Get3_{ox}$ □$_{red}$ (green trace) using far-UV circular dichroism and bis-ANS fluorescence spectroscopy (insert), respectively. **(B)** ATPase activity of $Get3_{ox}$ and $Get3_{ox}$ □$_{red}$ relative to untreated $Get3_{red}$. The following experiments and figures were performed and created by Voth W (Jakob Laboratory, University of Michigan).

Since the ATP-binding site in Get3 is located in close proximity to two of the four highly conserved cysteines (C242/C244), we reasoned that Mg-ATP binding should stabilize the reduced form and hence accelerate refolding. Indeed, as shown in Figure 4-6, in the presence of DTT, Zn^{2+} and MgATP, $Get3_{ox}$ was completely inactivated within the time frame of the experiment ($Get3_{ox}$□$_{red}$), and could be activated again upon incubation with Cu_{2+}/H_2O_2. These results suggest that presence of MgATP plays a critical role for the inactivation of Get3's chaperone function. This makes physiological sense since restoration of cellular ATP levels serves to indicate a cell's return to pre-stress conditions. Analysis of the secondary structure revealed almost complete reversal of the structural rearrangements and decrease in surface

hydrophobicity in Get3 upon incubation with DTT, Zn^{2+} and MgATP (Fig.'s 4-7A, compare red and green traces), paralleled by a substantial reactivation of Get3's ATPase activity (Fig.4-7B). These results demonstrate that the oxidative activation of Get3 as an ATP-independent chaperone is a reversible process, enabling Get3 to potentially undergo multiple rounds of oxidative activation as a molecular chaperone.

4.6 The minimal unit of chaperone-active Get3 is the oxidized tetramer

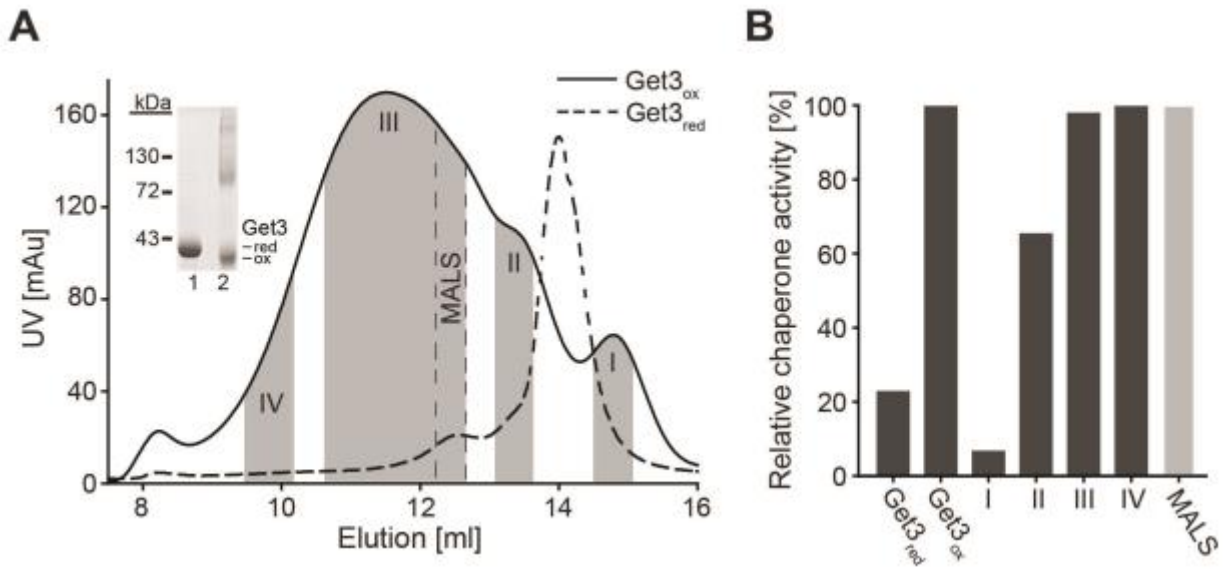

Figure 4-8. Chaperone-active $Get3_{ox}$ forms distinct oligomeric species. (A) $Get3_{red}$ and $Get3_{ox}$ were analyzed on size exclusion chromatography. Peak fractions (indicated by gray bars) containing various oligomeric states of $Get3_{ox}$ were collected (fractions I-IV) and (B) subsequently analyzed for their chaperone activity as described in figure legend 1. Insert: Analysis of $Get3_{red}$ and $Get3_{ox}$ on non-reducing SDS-PAGE. The following experiments and figures were performed and created by Voth W (Jakob Laboratory, University of Michigan).

Analysis of reduced and oxidized Get3 on non-reducing SDS-PAGE revealed the expected monomeric migration behavior of $Get3_{red}$ and a slightly faster migrating $Get3_{ox}$ monomer, indicative of *intra*molecular disulfide bonds (Figure 4-8A, insert). In addition, however, we also noted the presence of some dimers and higher oligomers in our $Get3_{ox}$ preparation. To determine if oligomerization correlates with the chaperone function of $Get3_{ox}$,

we separated oxidized Get3 on size exclusion chromatography, collected individual peak fractions (Fig. 4-8A, shaded areas I-IV), and determined their respective chaperone activity (Fig. 4-8B). Whereas the specific chaperone activity of $Get3_{ox}$ was negligible in fractions harboring species that eluted in a similar volume as the reduced Get3 dimer, it was high in fractions that contained higher oligomeric Get3-species.

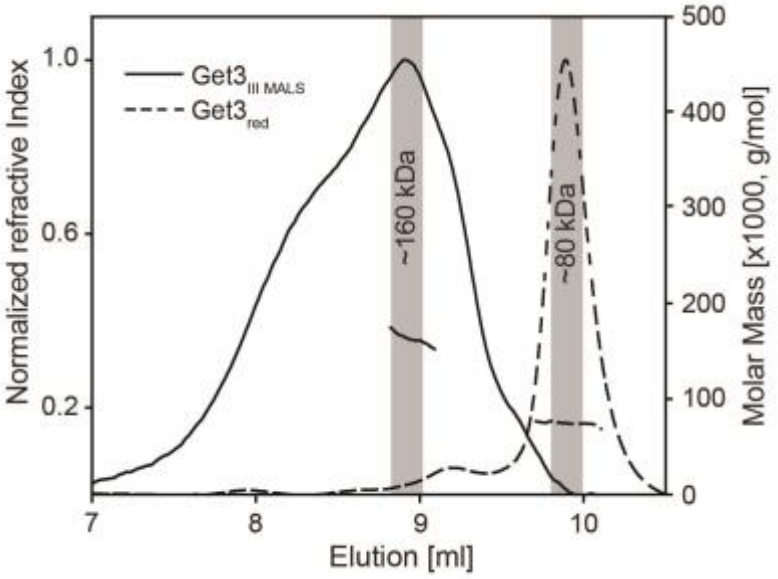

Figure 4-9. SEC-MALS reveals Get3ox is a tetramer. $Get3_{red}$ and the $Get3_{ox}$ sub-fraction of fraction III indicated in Fig. 4-8A were analyzed by SEC-MALS and calculated to be approximately 160 and 80 kDa, respectively. The following experiments and figures were performed and created by Voth W (Jakob Laboratory, University of Michigan).

To better characterize the stoichiometry of the minimal oligomeric unit of $Get3_{ox}$ that confers chaperone function, we further separated fraction III, and re-chromatographed each of the sub-fractions using a second size exclusion column connected to a static light scattering instrument for molecular weight determination (SEC-MALS). The fraction corresponding to the smallest chaperone-active $Get3_{ox}$ complex (indicated as "MALS" in Fig. 4-8A) eluted as a broad single peak at ~9.0 ml in the SEC-MALS (Fig. 4-9). The average molecular weight was determined to be about 160 kDa, indicating a tetramer complex. Notably, we also observed a

large shoulder and an increasing molecular weight across the peak, indicating larger oligomers are present as well. By comparison, $Get3_{red}$ eluted at ~ 10 ml with a calculated molecular weight of 80 kDa, confirming that it is a dimer under these conditions (Fig. 4-9).

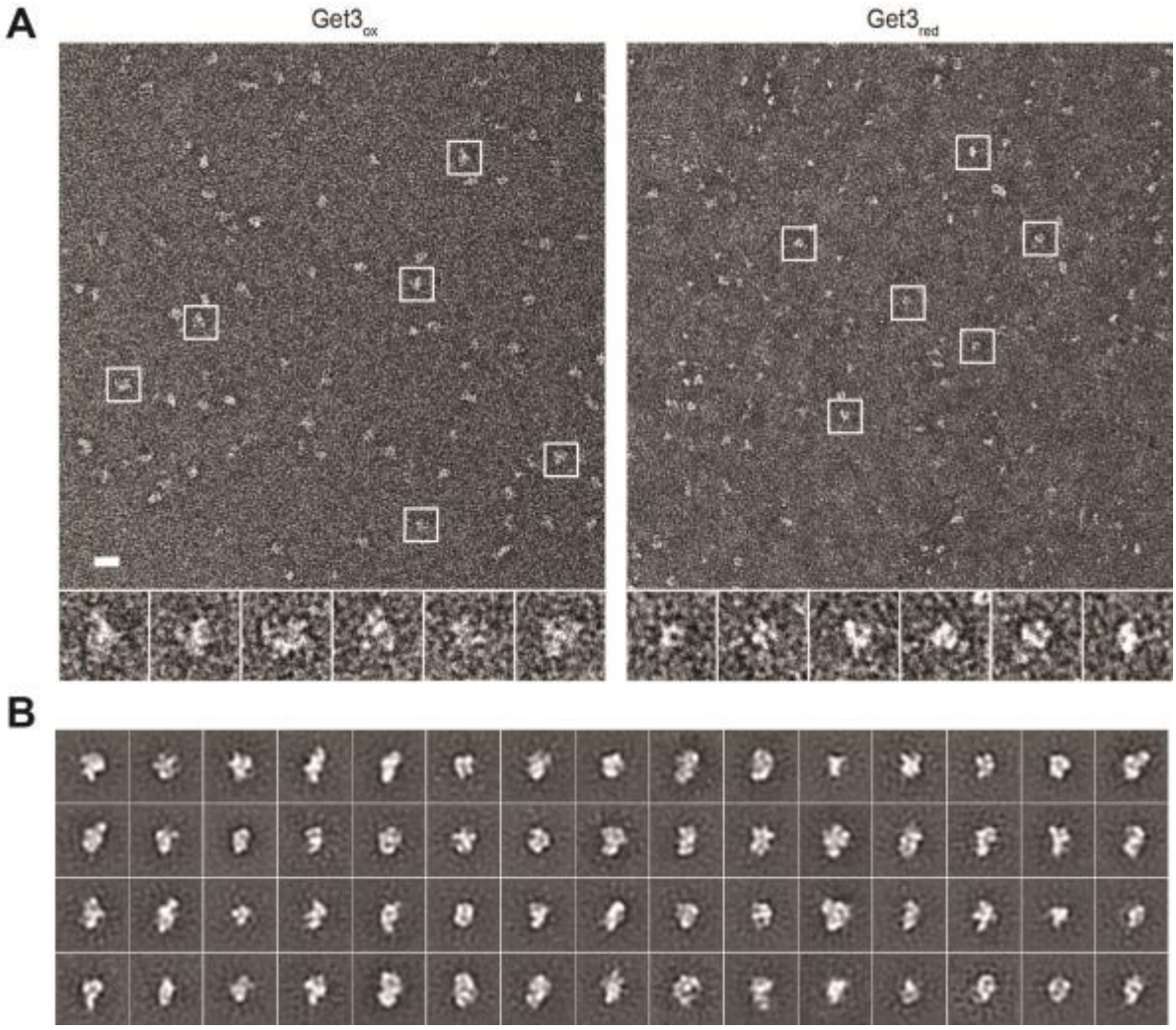

Figure 4-10. Negative-stain EM particles and 2D class averages of Get3ox.
(A) Representative micrograph images and selected particles of $Get3_{ox}$ (left panel) and $Get3_{red}$ (right panel) are shown. Scale bar equals 200 Å and the box size is 260 Å. (B) Representative reference-free class averages of $Get3_{ox}$, generated using SPIDER (Frank et al., 1996).

To further characterize the architecture of the oxidized Get3 oligomeric states, we conducted negative-stain electron microscopy (EM) on peak fractions following SEC-MALS. In micrograph images and single particles, $Get3_{ox}$ appeared larger and in a different

arrangement compared to images of the $Get3_{red}$ dimer (Fig. 4-10A). Single particle data sets were then collected and analyzed by generating 2D reference-free projection averages. For $Get3_{ox}$, the 2D averages showed a globular arrangement with two defined lobes that form a 'W' shape in some views (Fig. 4-10B, 4-11A). Larger, elongated complexes were also observed in the overall set of 2D averages, indicating the presence of multiple oligomeric states, however the smaller, compact form clearly predominated (Fig. 4-10B). The arrangement was different than the crystallographic tetramer of the archaeal homologue, which forms an elongated 'dumbbell' shape (Suloway et al., 2012). Reference-free classification of the $Get3_{red}$ dimer was also performed and clearly showed a small 'U' shaped arrangement that matched well with 2D projections and corresponding 3D views of the crystal structure (Hu et al. 2009) (Fig. 4-11B). Based on comparisons of these 2D projection images it is clear that $Get3_{ox}$ is larger then $Get3_{red}$, and contains two lobes that are consistent with two dimers of Get3 connected in a tetrameric complex.

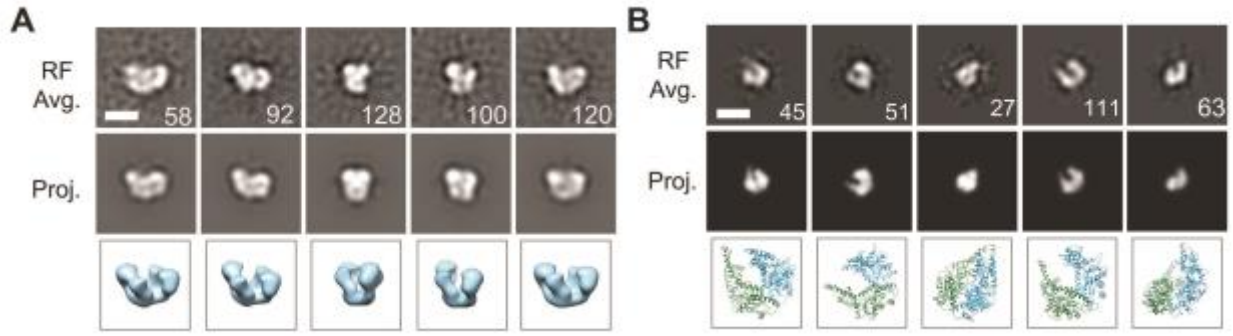

Figure 4-11. 2D and 3D negative stain EM analysis of $Get3_{ox}$ and $Get3_{red}$. Negative-stain EM 2D reference-free class averages of (A) $Get3_{ox}$ and (B) $Get3_{red}$, collected following SEC-MALS (gray bars in Fig 4-9), determined using SPIDER (Frank et al. 1996). Matching projections and corresponding images of the (A) $Get3_{ox}$ 3D model and (B) $Get3_{red}$ dimer crystal structure (PDB: 3H84) are shown (Hu et al. 2009). The number of single particles is shown for each average and the scale bars equal 100 Å.

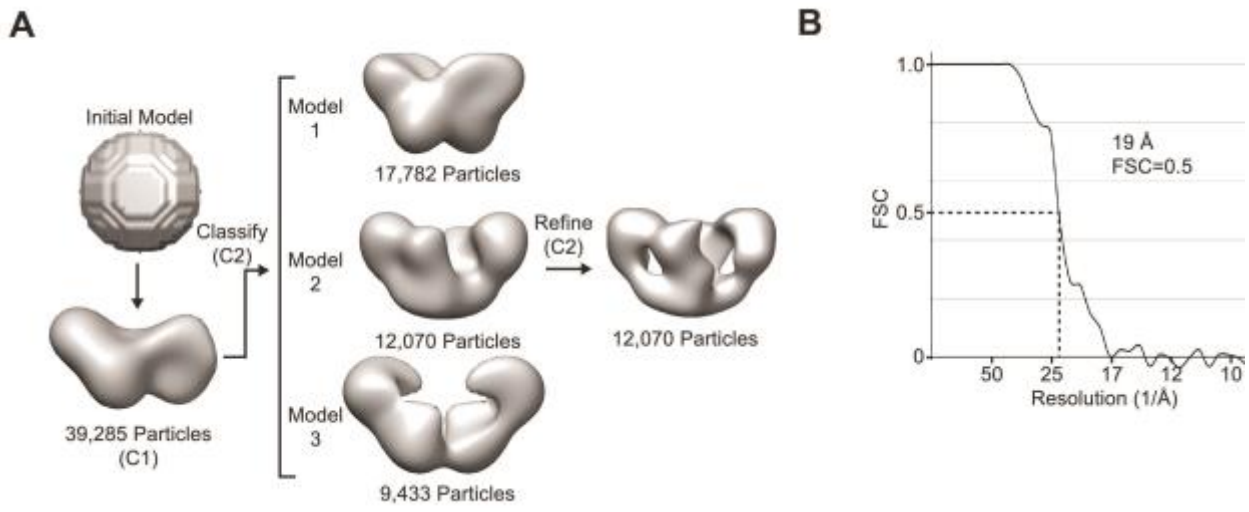

Figure 4-12. Get3ox 3D reconstruction scheme. (A) 3D reconstruction method and **(B)** gold-standard Fourier Shell Correlation (FSC) curve of the final refinement showing a 19Å resolution at an FSC=0.5 criterion, performed using RELION (Scheres 2012).

To further characterize the architecture of the $Get3_{ox}$ tetramer, we determined a 3D reconstruction using RELION (Scheres 2012). Initial rounds of refinement were performed using a sphere as an initial model with no imposed symmetry (Fig. 4-12A). The final model, calculated to be 19 Å by the Fourier shell correlation procedure (Fig. 4-12B), was achieved following additional rounds of refinement with 2-fold symmetry imposed. The reconstruction reveals a 70 by 120-Å complex with two oval-shaped domains that are connected along one side, resulting in a 40-Å cleft between the domains (Fig. 4-13). Importantly, the reference-free averages agree with the 2D projections of the model, supporting this tetramer arrangement (Figure 4-11A).

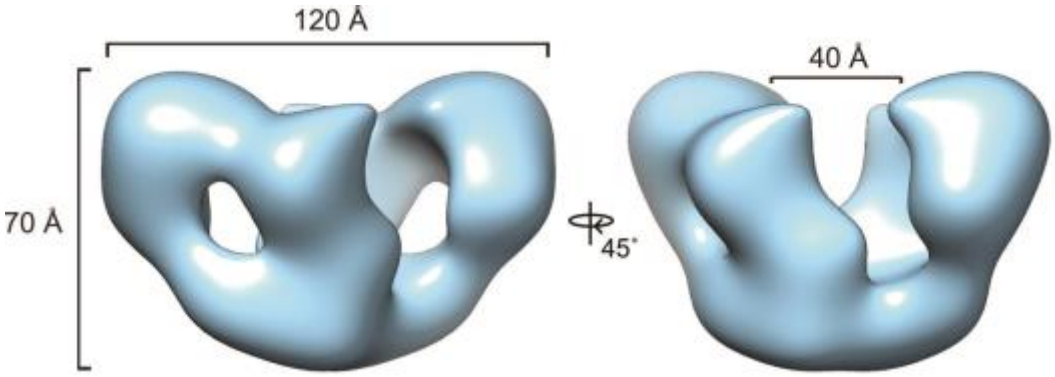

Figure 4-13. Final 3D model of the Get3$_{ox}$ tetramer complex, filtered to 19 Å.

The crystal structures of the dimer and tetramer forms of Get3 were docked into the EM map and found to be incompatible, however the dimensions of each oval domain in the 3D model are consistent with the size and shape of the dimer (Fig. 4-14). Overall the SEC-MALS and EM structural work identifies that the minimal chaperone-active form of Get3$_{ox}$ is a distinct tetramer complex that is likely in a different conformation and arrangement than previously characterized structures of the reduced form.

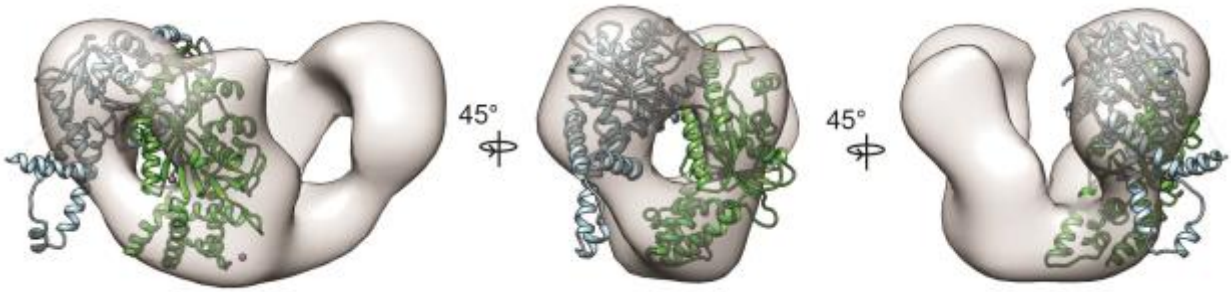

Figure 4-14. 3D model of Get3ox tetramer with dimer crystal structure docked in.

4.7 Oxidative activation of Get3 causes massive structural rearrangements

To obtain more detailed insights into the structural changes that Get3 undergoes during its oxidative activation process, we decided to conduct kinetic H/D exchange experiments in combination with mass spectrometry (Englander 2006). Proteins of interest are incubated in deuterated buffer to allow amide protons to exchange with deuterium. After defined time points,

the exchange is quenched by a sudden shift to pH 2.5. Then, the protein is digested with pepsin in the presence of 1 M Gdn-HCl, and the resulting peptides are analyzed by MS/MS. We first analyzed reduced $Get3_{red}$ and tested its proteolytic sensitivity towards pepsin, assessing the protein coverage. We found that a 30 sec treatment with pepsin was sufficient to digest $Get3_{red}$ into numerous, often overlapping fragments that covered ~99.8% of the entire Get3.

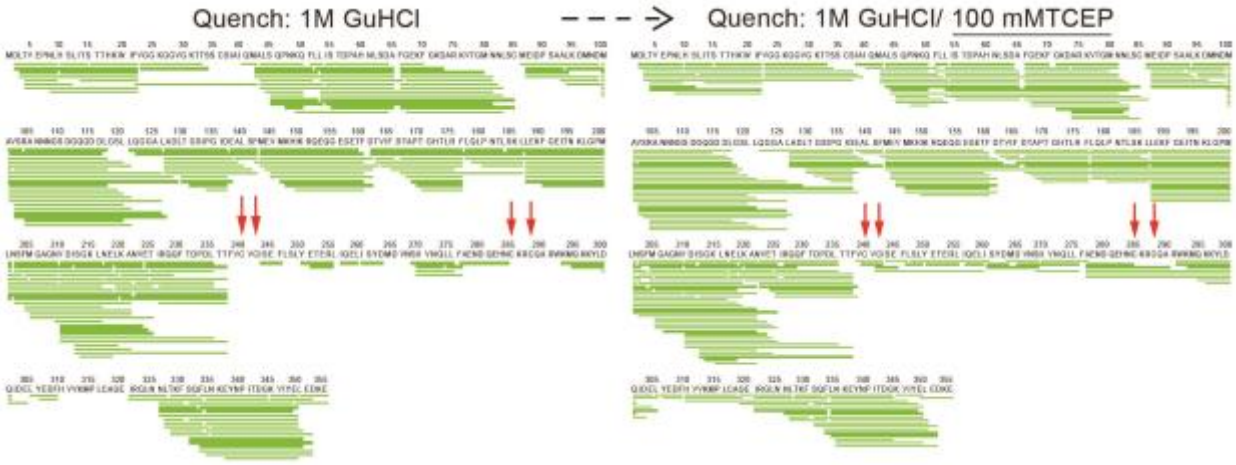

Figure 4-15. Oxidative stress mediated disulfide bond formation and conformational rearrangements of Get3. Pepsin digest of $Get3_{ox}$ in the absence of reducing agents revealed significant differences in the patterns of proteolytic cleavage surrounding the two pairs of conserved cysteines (red arrows). However, quenching in the presence of 100 mM TCEP, a thiol reductant, reconstituted the cleavage pattern of $Get3_{red}$. The following data was provided by Li S (University of California) and analyzed by Voth W (Jakob Laboratory, University of Michigan).

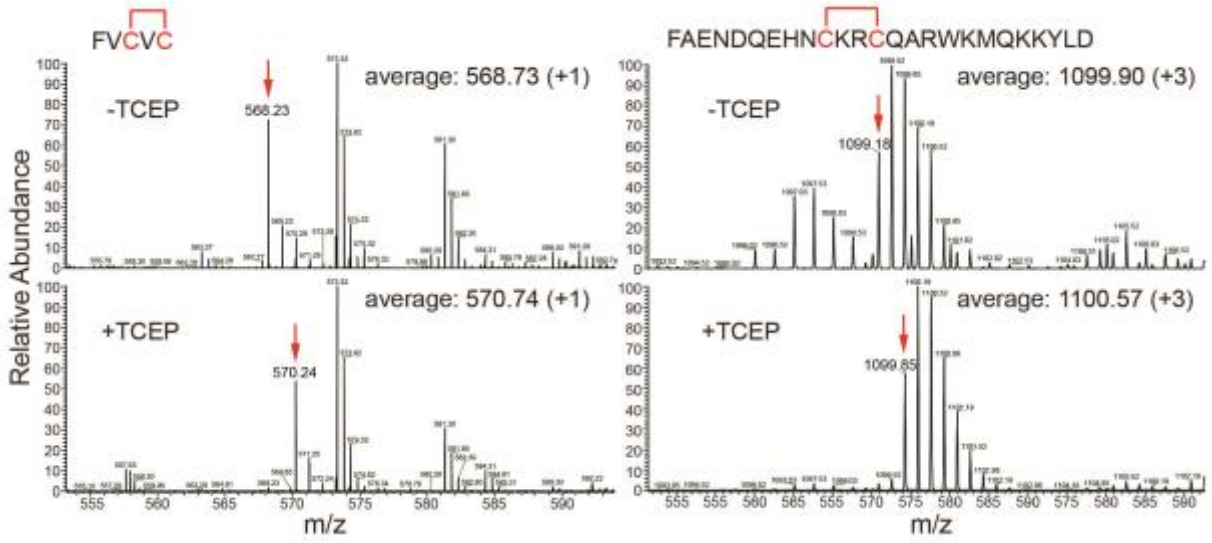

Figure 4-16. Get3 peptides MS spectra. MS spectra for Get3 peptides containing the CXC- and CXXC-motif with and without TCEP reveal disulfide bond formation within the peptide chain. The calculated mass of the first monoisotopic peaks (red arrow) in both peptides shows a mass increase of ~ 2 Da upon addition of the reducing agent TCEP, consistent with the reduction of one disulfide bond. The following data was provided by Li S (University of California) and analyzed by Voth W (Jakob Laboratory, University of Michigan).

When we compared the digestion pattern of oxidized, disulfide-bonded $Get3_{ox}$ in the absence and presence of the strong thiol reductant 100 mM Tris(2-carboxyethyl)phosphine hydrochloride (TCEP), however, we observed some striking differences; a near-absence of proteolytic cleavage in the regions surrounding both pairs of conserved cysteines as well as the non-conserved Cys317 (Fig. 4-15, left panel). These results suggest that thiol oxidation prevents pepsin from accessing its target sites consistent with our conclusion that the conserved cysteines are involved in disulfide bonds. Manual inspection of the MS spectra allowed us to identify two additional peptides, which harbor the conserved cysteine pairs in their oxidized, disulfide-bonded state, indicating that the four conserved cysteines engage in intramolecular disulfide bonds, connecting the next-neighbor cysteines (Fig. 4-16).

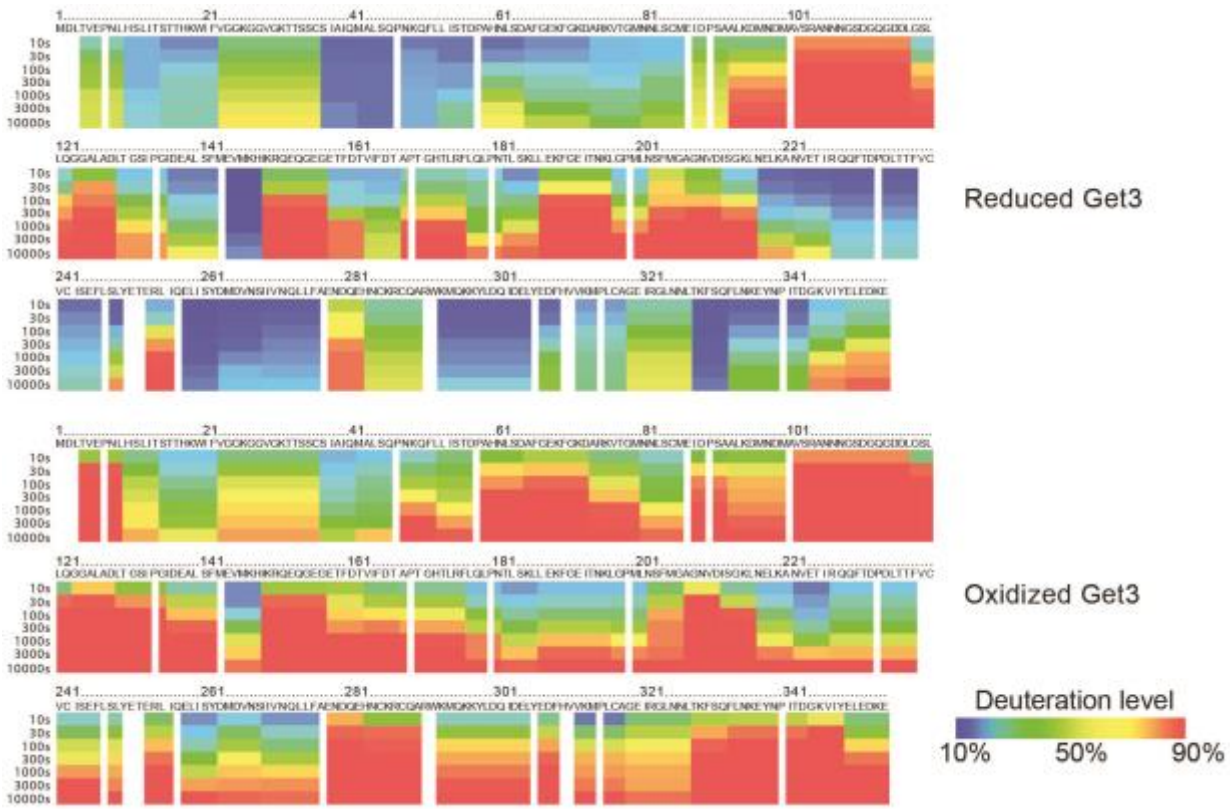

Figure 4-17. Deuteration levels of Get3$_{ox}$ and Get3$_{red}$ peptides. Deuterium incorporation into peptides of Get3$_{red}$ and Get3$_{ox}$ after quenching and pepsin digest in the presence of 100 mM TCEP. The deuteration level was calculated as described in the experimental procedures. The following data was provided by Li S (University of California) and analyzed by Voth W (Jakob Laboratory, University of Michigan).

Since pepsin digestion of TCEP-reduced Get3$_{ox}$ was indistinguishable from the digestion pattern of Get3$_{red}$ that was never oxidized, we conducted all subsequent pH quench and pepsin digests in the presence of 100 mM TCEP. By using this method, which has been previously established to avoid differences in pepsin coverage when comparing oxidized and reduced proteins (Zhang et al. 2010), we were able to directly compare the mass differences in the individual Get3 peptides over time. As shown in Figure 4-17 and Figure 4-18, analysis of the H/D exchange rates in Get3$_{red}$ and Get3$_{ox}$ peptides revealed astounding differences. Nearly every region in Get3$_{ox}$ showed a faster exchange rate with deuterium than the corresponding region in Get3$_{red}$ as indicated by the red shading (Figure 4-18A), and shown for select peptides

in Figure 4-18.

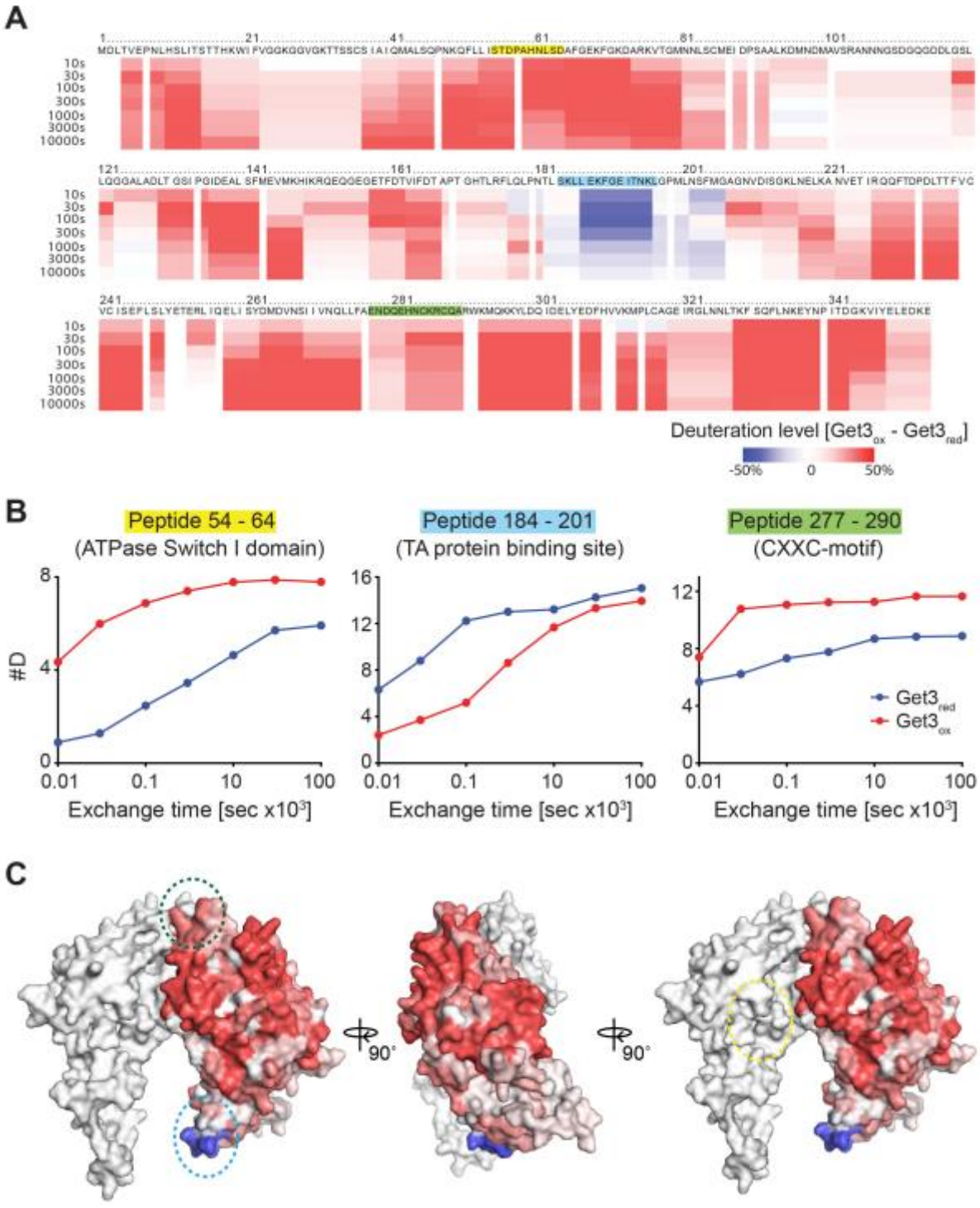

Figure 4-18. Get3 undergoes massive conformational rearrangements upon oxidation. (A) Incorporation of deuterium after select times into $Get3_{ox}$ *versus* $Get3_{red}$. Quenching and pepsin digest was performed in the presence of 100 mM TCEP. The deuteration level was calculated as described in the experimental procedures. (B) Direct comparison of the deuterium incorporation

over time into select Get3 peptides prepared from either $Get3_{red}$ (blue trace) or $Get3_{ox}$ (red trace). (C) Surface representation of the data shown in (A) using the $Get3_{red}$ dimer crystal structure (PDB: 3H84). Location of peptides shown in (B) is indicated using the same color code. The following data was provided by Li S (University of California) and analyzed by Voth W (Jakob Laboratory, University of Michigan).

These results are fully consistent with our CD data and indicative of an oxidation-induced partial unfolding of Get3's structure and/or increase in dynamic properties of the protein. They are reminiscent of other recently identified stress-specific chaperones, including Hsp33 and HdeA, whose activation appears to be triggered by significant protein unfolding (Reichmann et al. 2012; Tapley et al. 2009). Astonishingly, the only region in $Get3_{ox}$ that showed a slower exchange with deuterium than the corresponding region in $Get3_{red}$ involved residues 184-201 of the alpha-helical subdomain in Get3 (Fig. 4-18B middle panel; Fig. 4-18C indicated by blue circle), which is proposed to form the composite hydrophobic binding site for TA-proteins (Mateja et al. 2009). Mutagenesis in this region revealed several Get3 variants that had lost their capacity to co-immunoprecipitate the TA-protein Sec61beta but retained high levels of ATPase activity indicative of a folded protein (Mateja et al. 2009). These results revealed that oxidative activation of Get3 leads to major conformational rearrangements, which cause the exposure of binding sites for unfolding proteins while potentially masking the binding sites for TA-proteins.

4.8 Dissecting the two Get3 functions *in vivo*

Our structural analysis suggested that the binding of Get3 to TA-proteins under non-stress conditions and the interaction of Get3 with unfolding proteins under stress conditions might represent two independent and hence separable protein functions. We therefore decided to purify and test one of the mutant proteins (Get3 I193D), which has been previously shown to no longer bind TA-proteins (Mateja et al. 2009). We reasoned that if our hypothesis was correct, this mutant protein would still work as a redox-active chaperone and would complement specifically

those *get3* phenotypes that require the redox-regulated chaperone function but not the TA-protein targeting function of Get3.

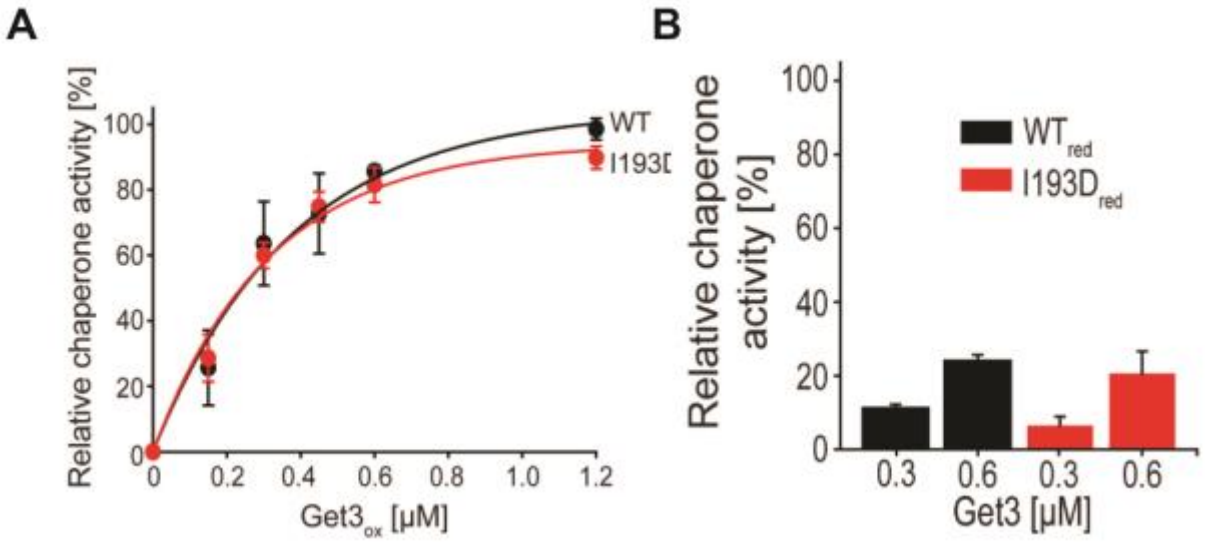

Figure 4-19. Get3I193D has chaperone activity independent of TA protein targeting. (A) Both wild-type Get3 and the TA-binding deficient mutant Get3I193D were prepared in their oxidized form and tested for their influence on the aggregation behavior of chemically denatured CS (see figure legend 1 for details). (B) Both wild-type Get3 and the tail-anchored binding deficient mutant Get3I193D were prepared in their reduced form and tested for their influence on the aggregation behavior of chemically denatured CS (see figure legend 4-1 for details). The following experiments and figures were performed and created by Voth W (Jakob Laboratory, University of Michigan).

Purification of the Get3 I193D variant was indistinguishable from that of wild type Get3, excluding major structural alterations in the protein. Furthermore, analysis of its ability to prevent protein aggregation *in vitro* revealed wild-type like redox-regulated chaperone function with little chaperone activity in the reduced form (Fig. 4-19B) and high chaperone function in the oxidized form (Fig. 4-19A). When we tested the Get3 I193D mutant variant for its capacity to rescue the oxidative stress phenotype of a *get3* strain, we found that the mutant protein rescued the growth defect of the deletion strain to the same extent as the wild-type protein, indicating that it is likely the chaperone function of Get3 I193D that is essential to cells under these stress conditions (Fig. 4-20A). The phenotype was also partially complemented by expression of the

ATPase-deficient Get3D57E, consistent with the observation that the chaperone function of Get3 is independent of ATP hydrolysis (Fig. 4-20A).

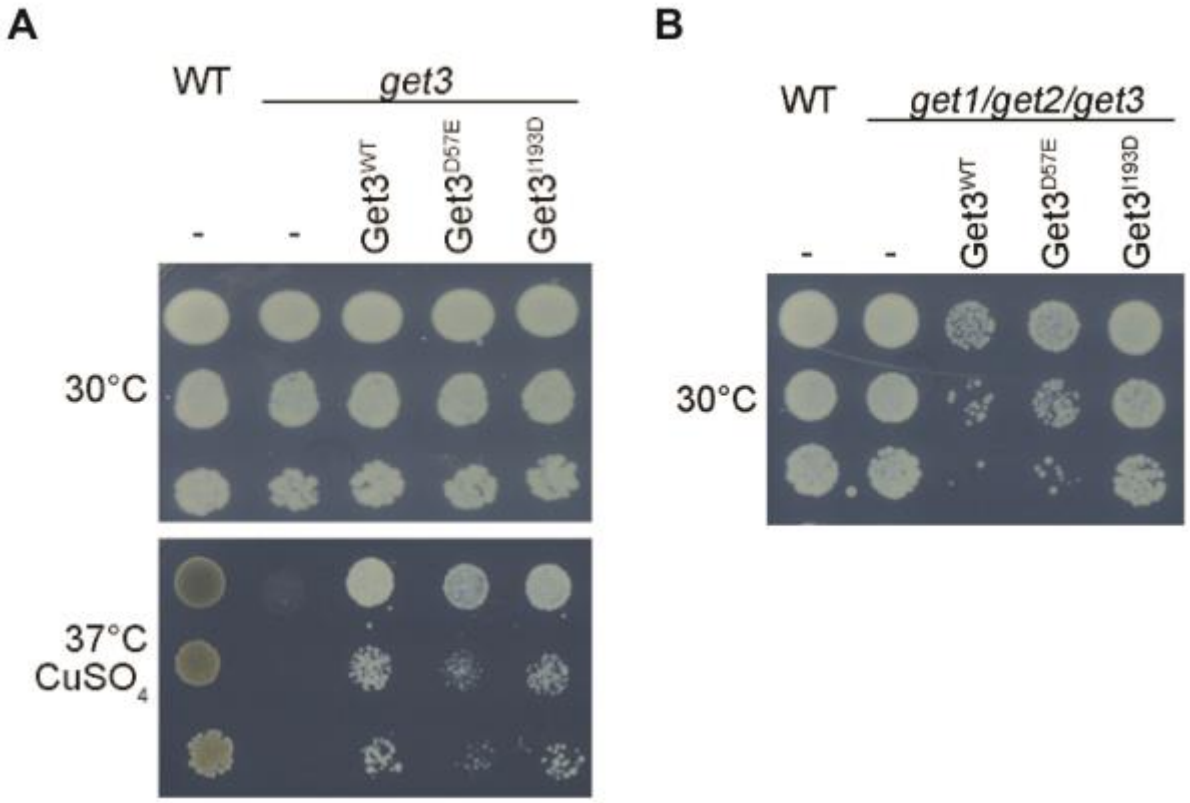

Figure 4-20. Cell viability assays of WT and mutant Get3. (A) *get3* cells were transformed with an empty construct or with constructs containing the coding sequence of wild-type or mutant variants of Get3. Serial dilutions were then spotted on control plates or plates containing 1 mM of $CuSO_4$ at 37°C. WT (BY4741) cells served as control. (B) Serial dilutions of *get1/get2/get3* cells, transformed with constructs containing the coding sequence of Get3 variants, were spotted and grown at 30°C. The following data was provided by Vilardi F (Schwappach Laboratory, Universitätsmedizin Göttingen) and analyzed by Voth W (Jakob Laboratory, University of Michigan).

To further segregate the *in vivo* chaperone function from any residual activity in TA-protein targeting, we then assayed the mutant proteins for a potential dominant negative effect, which has been observed for Get3-expressing strains in the absence of the Get1/Get2 receptor complex. In this strain background, overexpression of wild-type Get3 is toxic (Fig. 4-20B), thought to be due to Get3's unproductive sequestration of TA protein precursors, which

effectively prevents their membrane targeting by other GET-independent mechanisms (Schuldiner et al. 2008). Expression of the ATPase-deficient Get3 D57E mutant protein was similarly toxic, presumably because Get3 D57E is still able to bind and sequester TA-proteins (Powis et al. 2013). In contrast, we found no dominant negative effect for the Get3 I193D mutant variant (Fig. 4-20B), whose expression levels were very similar to the levels of soluble wild-type Get3 and Get3 D57E (Fig. 4-21B).

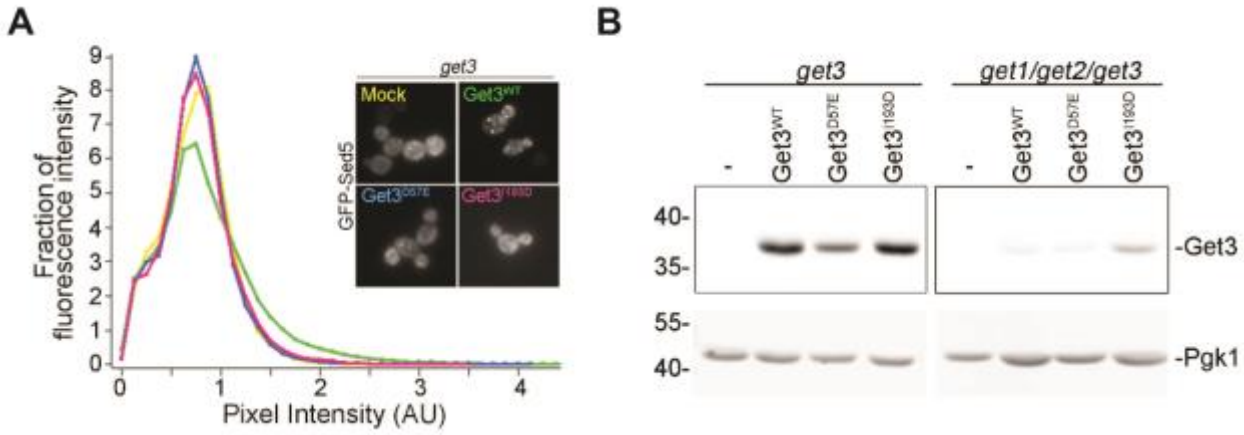

Figure 4-21. Localization of Sed5, TA-binding protein. (A) *get3* cells expressing GFP-tagged Sed5 were transformed with an empty construct or with constructs containing the coding sequence of Get3 variants. Subcellular localization of GFP-Sed5 was recorded by fluorescence microscopy (insert). At least 40 cells per strain were analyzed to determine the distribution of fluorescence across bins of different pixel fluorescence intensity. (B) *get3* and *get1/get2/get3* cells were transformed with constructs containing the coding sequence of wt or mutant Get3 variants. Protein lysates were analyzed by immunoblot using a Get3 specific serum. Pgk1 was used as loading control. The following data was provided by Vilardi F (Schwappach Laboratory, Universitätsmedizin Göttingen) and analyzed by Voth W (Jakob Laboratory, University of Michigan).

These results are fully consistent with the conclusion that the Get3 I193D mutant variant is no longer capable of binding TA-proteins. We further corroborated this finding by directly testing our Get3 I193D mutant protein in a well-established *in vivo* TA-targeting assay (Jonikas et al. 2009). In this assay, we followed the fate of a known TA-protein tagged with GFP (i.e., GFP-Sed5) in a *get3* deletion strain, that either expresses no Get3 (mock), wild-type Get3, the

ATPase-deficient Get3 D57E variant or the Get3 I193D mutant (Fig. 4-21A, insert). While the strain expressing wild-type Get3 showed the expected formation of multiple puncta against a dark cytosol, indicative of the correct targeting of GFP-Sed5 to the ER and subsequent trafficking to the Golgi, *get3* cells expressing either no Get3 or any of the two mutants revealed a much higher cytosolic background and only very few puncta (Fig. 4-21A, insert). These results are highly reminiscent of other reported conditions in which GFP-Sed5 was mistargeted and moved to deposition sites for aggregated proteins (Battle et al. 2010; Kohl et al. 2011; Vilardi et al. 2014). Quantitative analysis further confirmed that GFP-Sed5 (mis)targeting observed in cells expressing either Get3 D57E or I193D was comparable to the strain lacking Get3 altogether (Fig. 4-21A). These results were in excellent agreement with the structural analysis of Mateja et al. as they demonstrated that a Get3 protein with an altered hydrophobic groove is incapable of TA protein targeting or sequestration (Mateja et al. 2009). Moreover, our results provide strong evidence that TA protein targeting activity can be segregated from its redox-dependent chaperone activity, which appears to be responsible for the cellular fitness of yeast cells under copper-induced oxidative stress conditions.

4.9 Get3 co-localizes with unfolding proteins during oxidative stress *in vivo*

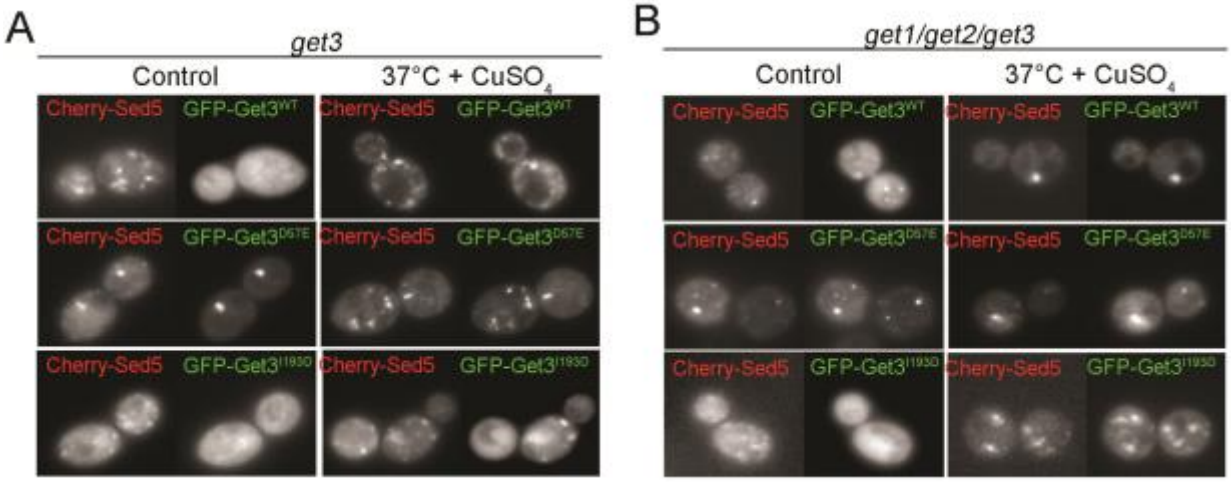

Figure 4-22. Get3 accumulates at deposition sites of mistargeted Sed5 under stress conditions. (A) *get3* or (B) *get1/get2/get3* deletion cells expressing mCherry-tagged Sed5 in combination with GFP-tagged Get3 (wt or mutants) were grown under control conditions (30°C) or in presence of 1 mM $CuSO_4$ at 37°C for 4 hours. Subcellular distribution of mCherry-Sed5 and GFP-Get3 was recorded by fluorescence microscopy. The following data was provided by Vilardi F (Schwappach Laboratory, Universitätsmedizin Göttingen) and analyzed by Voth W (Jakob Laboratory, University of Michigan).

Co-localization studies using GFP-Get3 and Cherry-Sed5 revealed that under non-stress conditions, Get3 is diffusely distributed in the cytosol while the TA-protein is localized to its previously observed distinct ER/Golgi foci (Fig. 4-22A, control panel). Upon exposure of yeast cells to copper stress, however, Get3-GFP localizes to foci, which only partially overlap with the foci formed by Cherry-Sed5 (Fig. 4-22A, right panel), and are reminiscent of previously observed co-deposition sites of Get3, aggregated proteins, and other chaperones (Powis et al. 2013). Intriguingly, we found a very similar oxidative stress-mediated redistribution of the TA-binding deficient Get3 I193D mutant, supporting the notion that the recruitment of Get3 to stress foci occurs through the oxidative activation of its ATP-independent chaperone function and not through TA-protein binding (Fig. 4-22A, lower panel).

Analysis of Get3-GFP localization in the receptor-deficient *get1get2* deletion strain further confirmed these conclusions. In this strain background, wild-type Get3 is not freely diffusible but co-localizes with TA-proteins in distinct foci even under non-stress conditions (Fig. 4-22B). This is presumably because TA-protein can no longer be released from Get3 and inserted into the membrane, which explains the previously shown dominant negative effect of wild-type Get3 expression in a strain that lacks the receptor complex (Schuldiner et al. 2008). As expected, the Get3 I193D mutant variant did not co-localize with Cherry-Sed5 in the strain lacking the ER receptor proteins (Fig. 4-22B). However, once challenged with copper stress, we observed the re-localization the Get3 I193-GFP mutant variant into distinct stress foci. These results demonstrate that Get3 exerts a TA-binding-independent function under oxidative stress conditions *in vivo*, thereby playing an important role in protecting yeast cells during stress conditions that lead to protein unfolding and ATP-depletion.

4.10 Substrate binds Get3 tetramer in hydrophobic pocket

To determine how the Get3 tetramer associates with substrates, we used SEC-MALS to form a stable substrate-bound complex using model substrate, luciferase. To form complex, we thermally unfold luciferase in the presence of the oxidized tetramer and then run it on the SEC-MALS. The complex had light scattering MW of ~220kDa, which corresponds to a 4:1 Get3:luciferase ratio (Figure 4-23B). We also ran the complex over an analytical size exclusion column, and collected the fractions for EM analysis (Fig. 4-23A).

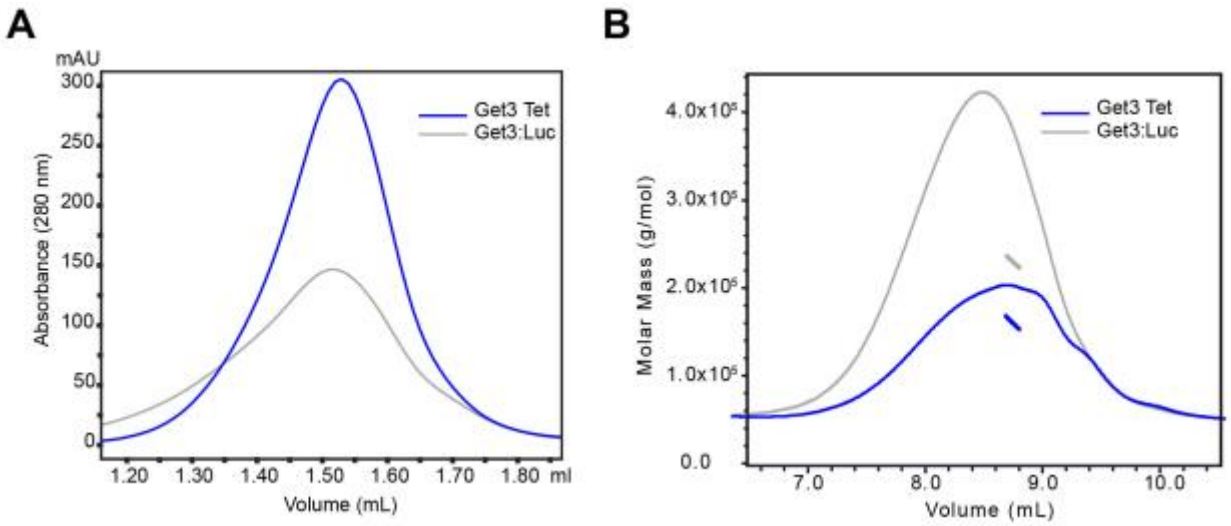

Figure 4-23. SEC-MALS reveals 4:1 stoichiometry of Get3:luciferase. (A) Analytical SEC of Get3 tetramer (blue) and Get3:luciferase (grey) complex demonstrate a shift in elution upon complex formation. (B) SEC-MALS of Get3 tetramer (blue) and Get3:luciferase (grey) complex, with Get3 tetramer with a molecular weight reading of ~160kDa, and Get3:luciferase complex with ~220kDa molecular weight.

In the Get3:luciferase dataset we saw many 2D class averages that have similar, 'W' characteristics reminiscent of the tetramer alone (Fig. 4-24B). Other 2D averages in the dataset have notable extra density, appearing between the two tetramer lobes (Fig. 4-24C). This seems like it would align the substrate right in the hydrophobic pocket of the tetramer, between the two dimers. This data is consistent with the HD/MS data, which reveals that more hydrophobic residues become accessible in the oxidized tetramer compared to the dimer. This allows the oxidized tetramer to function as a more general chaperone, with less specificity than the TA-binding function.

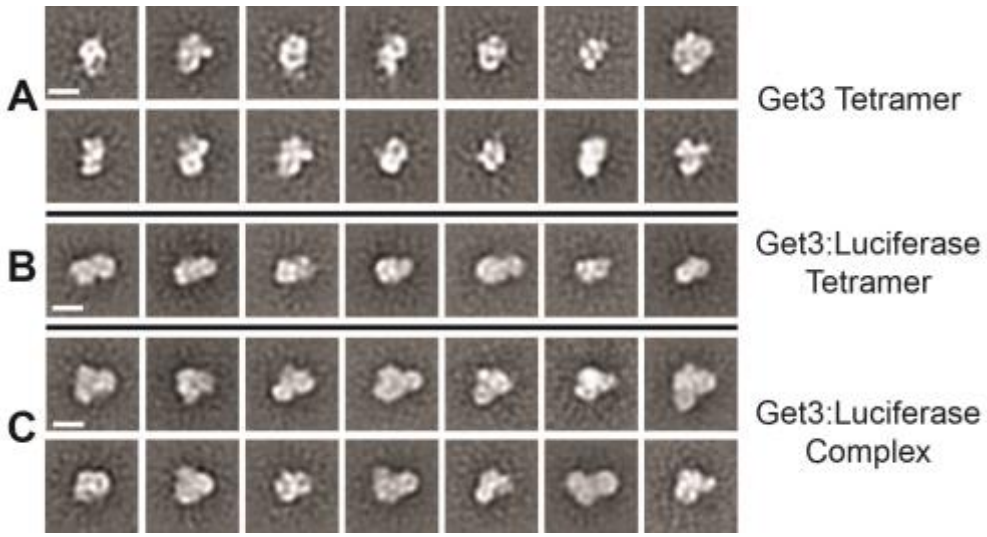

Figure 4-24. Negative Stain EM of Get3:luciferase complex shows extra density in hydrophobic pocket. (A) 2D averages of Get3 tetramer alone. (B) 2D averages from Get3:luciferase dataset that appears to be the tetramer alone. (C) 2D averages from Get3:luciferase dataset showing extra density for the luciferase. Scale bar= 100A.

4.11 Discussion

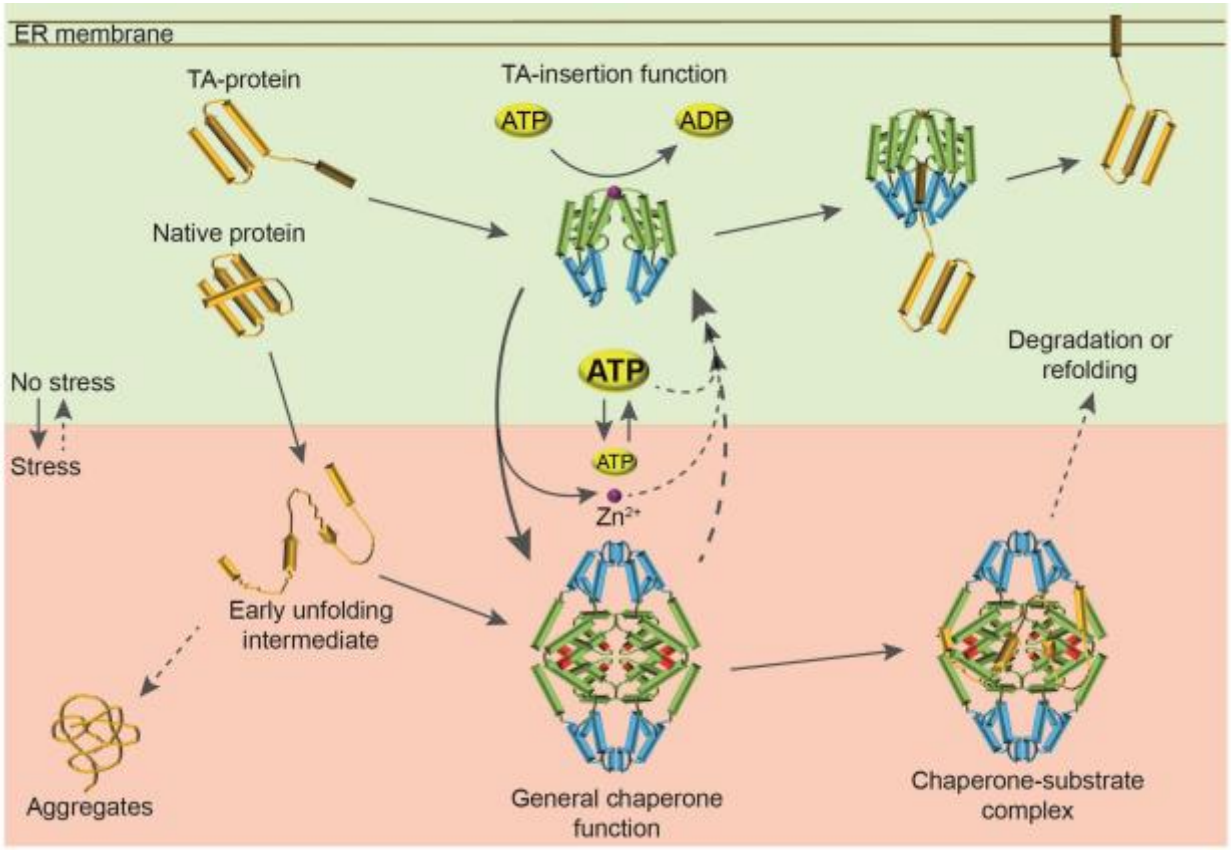

Figure 4-25. Get3 – Moonlighting as ATP-independent chaperone under oxidative stress conditions. Under non-stress conditions, Get3 is reduced and functions as cytosolic component of the GET complex, which supports insertion of TA-proteins into the ER membrane. The structure of reduced Get3 has been solved and shown to be a symmetrical homo-dimer, stabilized by the coordination of zinc (red sphere). Binding of TA-clients to Get3 (proposed TA binding site shown in blue), and subsequent release on the membrane is regulated by ATP-binding and hydrolysis (shown in green), and involves several other cytosolic and membrane proteins, which are not shown for simplicity. Upon exposure to ATP-depleting oxidative stress conditions, Get3's cysteines are oxidized and zinc is released. Oxidation causes major conformational rearrangements, which appear to bury the proposed TA-binding site on Get3 and turn Get3 into ATP-independent, highly chaperone-active tetramers. Oxidized Get3 now binds unfolding proteins and prevents their irreversible aggregation. Upon return to non-stress condition and restoration of normal cellular ATP levels, Get3 returns into its initial dimer structure and presumably releases its substrate for refolding or degradation. The following figure was by Voth W (Jakob Laboratory, University of Michigan).

In this study we demonstrate a second function of Get3 as oxidative stress-activated, ATP-independent chaperone (Fig. 4-25). By using a TA-protein targeting deficient yet fully chaperone-active variant of Get3, we discovered that the two Get3 functions can indeed be

segregated *in vivo*, and that the copper sensitivity observed in a *get3* strain is caused by the loss of the Get3 chaperone and not by impaired TA-protein targeting. Furthermore, our observation that both Get3 and the Get3 variant deficient in TA-protein targeting specifically accumulate in foci upon an oxidative challenge supports the idea that $Get3_{ox}$ serves as an integrated member of the cellular chaperone network, active at sites where unfolding and aggregation-prone proteins are sequestered.

Get3 undergoes a large conformational change upon oxidation, and the most important features of this structural change is the burying of the parts of the alpha-helical subdomain responsible for TA-protein binding and the formation of a disulfide-bonded higher oligomer, minimally a tetramer. Structural modeling revealed that none of the known structures, including the tetramer formed by the archaeal Get3 homologue, match the particles that we identified by EM. Since Get3 proteins employed for crystallization were routinely purified and crystallized under reducing, zinc coordinating conditions, it is not surprising that the existing structures cannot be matched with oxidized Get3 particles. The 2D averages of the luciferase complex indeed show that the hydrophobic cleft of the oxidized tetramer is the substrate-binding interface, important for the general chaperone function opposed to the TA-protein binding.

Importantly, the structural and functional changes observed for Get3 upon oxidation are fully reversible. Upon ATP-depletion, *in vivo* Get3 co-localizes with chaperones of the Hsp70 family and Hsp104 at deposition sites for aggregated proteins (Powis et al. 2013). Of note, the same pool of Get3 protein can be chased out of this localization upon restoration of energy levels. Thus, it is conceivable that Get3 takes an active role in returning to cellular homeostasis by resuming its role in protein targeting after it has contributed to countering proteotoxic challenge. Similar to Hsp33, reduction of oxidized Get3 was fast whereas

inactivation of the chaperone function was very slow. Mg-ATP accelerated the conversion to the more structured, chaperone-inactive reduced form, implying that the availability of ATP rather than the end of the oxidative challenge may serve as the physiological cue involved in switching the Get3 chaperone off and returning the protein to the TA-protein targeting function.

4.12 Materials and Methods

Plasmids construction - For p416Met25-Get3^{I193D}, the coding sequence of Get3^{I193D} was amplified by PCR from pLAC33-Get3^{I193D} (Mateja et al. 2009) using the primers 5'-TATGATACTAGTATGGATTTAACCGTGGAA-3' and 5'-ATCATACTCGAGCTATTCCTTATCTTCTAA-3' containing SpeI and XhoI restriction sites, respectively. For p416Met25-GFP-Get3^{I193D}, a SpeI/BamHI fragment was originated from p416Met25-Get3^{I193D} and ligated to p416Met25-GFP-Get3^{WT} previously digested with the same restriction endonucleases. Cells were grown in Hartwell's Complete (HC) medium and experiments were performed at mid-log phase. Copper sensitivity was determined on HC agar plates in the absence or presence of 1 mM $CuSO_4$ after 2-3 days at the indicated temperatures.

Get3 Purification - Get3 wild-type and the D57E mutant were expressed in *E. coli* Rosetta2(DE3)/pLysS (Novagen) from a pQE80 derivative as a fusion of two Z domains (IgG-binding domain of protein A) to Get3 (Metz et al. 2006) containing a tobacco etch virus (TEV) protease cleavage site between an N-terminal 6×His tag in front of the Z domain and the polylinker. Get3^{I193D} was expressed from a pet280 vector (kind gift of Robert Keenan) containing a TEV protease cleavage site between the N-terminal 6×His tag and a polylinker. After cells reached an A_{600} of ~0.6, protein expression was induced with 0.4 mM IPTG and cells were cultivated for another 4 h at 30 °C. The cells were pelleted and resuspended in extraction

buffer (50 mM Tris, 50 mM NaCl, 2 mM MgAc, 1 mM imidazole, optional 2 mM DTT, pH 7.5), supplemented with one tablet of protease inhibitor (Roche) and 1 mM PMSF (Sigma Aldrich). Cells were lysed using a commercial French press (3 x 1300 psi). The cleared lysate was purified by a nickel-NTA column (QIAGEN). For further purification an anion-exchange chromatography column (Q-sepharose HP, GE Healthcare) was used. The purified protein was simultaneously cleaved with 6×His-tagged TEV protease and dialyzed for 20 h at 4°C against cleavage buffer (50 mM Tris, 50 mM NaCl, pH 7.5) containing 0.5 mM DTT and 0.5 mM EDTA. Uncleaved Get3 and the 6×His-tagged TEV protease was removed by subtractive Ni-NTA purification. The efficiency of cleavage was quantified by SDS-PAGE and was >90%. Get3 concentrations were determined spectroscopically using a Jasco spectrophotometer V-550.

Get3 reduction, oxidation and re-reduction - Wild-type Get3 and the mutant variants were purified as described in the Supplemental Material section. To prepare $Get3_{red}$, ~100 µM Get3 in storage buffer (50 mM Tris, 50 mM NaCl, 5 mM MgAc, pH 7.5) was incubated with 5 mM dithiothreitol (DTT) for 1 h at 30°C. DTT was removed using a Zeba spin column (Thermo Scientific) or Micro Spin 30 (Bio-Rad) column equilibrated with 40 mM HEPES-KOH (pH 7.5). For oxidation, $Get3_{red}$ was incubated with either 2 mM H_2O_2/50 µM $CuCl_2$ ($Get3_{ox}$), various concentrations of $CuCl_2$, or 2 mM H_2O_2 for the indicated time points at 37°C. Oxidants were removed as described. To remove copper, the protein was incubated with 5 mM TPEN (10 min at 30°C) before loading it onto the spin column. To re-reduce $Get3_{ox}$, 5 µM $Get3_{ox}$ was incubated with 5 mM DTT/5 µM $ZnCl_2$ for up to 6 h at 37°C in the absence or presence of 2 mM MgATP. The reductants were removed as described.

Chaperone and ATPase activity - To analyze chaperone activity, the influence of Get3 on the

aggregation of chemically denatured citrate synthase (CS) was tested (Buchner, Grallert, and Jakob 1998). 12 μM CS was denatured in 40 mM HEPES, 6 M guanidine hydrochloride (Gdn-HCl), pH 7.5 overnight at RT. To initiate protein aggregation, chemically denatured CS was diluted to a final concentration of 0.075 μM into 40 mM HEPES, pH 7.5 at 30°C under continuous stirring. The maximum in light scattering signal was reached after 4 min of CS incubation and was set to 0% chaperone activity. To determine the effect of Get3 on CS aggregation, Get3 was diluted into the buffer and light scattering was monitored after addition of chemically denatured CS using a Hitachi F4500 fluorescence spectrophotometer equipped with a temperature-controlled cuvette holder and stirrer. Excitation and emission wavelengths were set to 360 nm. To monitor the activation and inactivation kinetics of Get3, the protein was incubated with the respective oxidants or reductants as described. At defined time points, aliquots were taken and Get3 was diluted to a final concentration of 0.3 μM into assay buffer. Chaperone activity measurements were monitored as described.

The ATPase activity of 2-4 mM Get3 was monitored using a NADH-coupled ATPase assay in a 96-well BMG FLUOstar Omega microplate reader (Kiianitsa, Solinger, and Heyer 2003).

Redox state and metal analysis - To determine the number of cysteine thiols in Get3, the proteins were denatured in 6 M Gdn-HCl, 40 mM KPi buffer, pH 7.5 followed by an Ellman's assay (Riddles, Blakeley, and Zerner 1983). To determine the amount of zinc bound to reduced and oxidized Get3, the cysteine-coordinated zinc was determined using the PAR/PCMB assay (Jakob, Eser, and Bardwell 2000). For ICP analysis, samples were purified twice using Micro Spin 30 columns, equilibrated with metal-free 50 mM Tris, 50 mM NaCl, pH 7.5 buffer.

Monitoring structural changes in Get3 - To determine changes in the secondary structure, far-

UV CD spectra of Get3 (5 μM) in 20 mM KH_2PO_4, pH 7.5 were recorded (Jasco-J810) at 25°C. Changes in surface hydrophobicity were monitored in a Hitachi F4500 fluorescence spectrophotometer using 5 μM Get3 and 15 μM bis-ANS in 40 mM Hepes, pH 7.5.

Analytical gel filtration, SEC-MALS - $Get3_{red}$ and $Get3_{ox}$ was applied onto a Superdex 200 column (GE Healthcare), equilibrated with 40 mM HEPES, 140 mM NaCl, pH 7.5. Individual fractions of the gel filtration run were collected, pooled and tested for chaperone activity as described. The average Mw of was determined by separation using a WTC-050S5 SEC column (Wyatt Technology Corporation) with an Akta micro (GE Healthcare) and analysis using a DAWN HELEOS II MALS detector and Optilab rEX differential refractive index detector using ASTRA VI software (Wyatt Technology Corporation). The Mw was calculated from Raleigh ratio based on the static light scattering and corresponding protein concentration of a selected peak.

EM Sample imaging and analysis - For negative-stain EM, fractions were diluted and stained with 0.75% uranyl formate (pH 5.5-6.0) on thin carbon-layered 400 mesh copper grids (Pelco) (Ohi et al. 2004) and micrographs were taken at 52,000x magnification with 2.16 Å per pixel using a 4k x 4k CCD camera (Gatan). Samples were imaged under low dose conditions using a G2 Spirit TEM (FEI) operated at 120 keV. Micrographs were taken at 52,000x magnification with 2.16 Å per pixel using a 4k x 4k CCD camera (Gatan). Single particles were selected using E2boxer in EMAN2 (Tang et al. 2007) and totaled 39,285 for $Get3_{ox}$ and 7,731 for $Get3_{red}$. Reference free 2D classification and analysis of Get3 was performed using SPIDER (Radermacher et al. 1987) and generated 400 classes for $Get3_{ox}$ and 100 classes for $Get3_{red}$. 3D refinement was performed using RELION (Scheres 2012) by first running a 3D classification on the entire data set, binned two-fold, with two classes, using a sphere as an initial model and no

imposed symmetry. The model that appeared symmetric and agreed best with the reference-free averages was used in additional refinement with un-binned data, using '3D Refine' with two-fold symmetry. Additional symmetries were tested, however only the two-fold remained consistent with the asymmetric model and the 2D averages. The final model, at 19 Å resolution by the gold-standard FSC, was achieved after 9 rounds of refinement (Fig. 4-12A).

Hydrogen/Deuterium exchange experiments combined with mass spectrometry - Prior to performing deuteration studies, enzymatic digestion conditions of Get3 were optimized as previously described (Marsh et al. 2013).

A greater than 99.8% peptide coverage maps of Get3 was obtained using quench buffer containing 1 M Gdn-HCl, and 100 mM TCEP. The H/D exchange experiments were initiated by diluting 45 µl of reduced $Get3_{red}$ (~36 µM) or $Get3_{ox}$ (~32 µM) with 135 µl of D_2O buffer (8.3 mM Tris, 50 mM NaCl, in D_2O, pD_{READ} 7.2) at 0°C. At 10, 30, 100, 300, 1000, 3000, and 10000 sec, 24 µl of the reaction were removed and quenched by adding 36 µl of optimized quench buffer (1.0 M Gdn-HCl, 100 mM TCP, 0.8 % formic acid, 16.6 % v/v glycerol) at 0°C. The quenched samples were incubated on ice for 5 min, and then frozen at -80°C. In addition, non-deuterated control samples (incubated in non-deuterated D_2O buffer) and equilibrium-deuterated back exchange control samples (incubated in D_2O buffer containing 0.5% formic acid overnight at 25°C) were prepared.

The deuteration level for each peptide was calculated according to equation 1:

Deuteration (%) = C(P)-C(N)) / (C(F)-C(N)) x C(N) x MaxD x 100

where C(P), C(N) and C(F) are the centroid values of partially deuterated peptide, non-deuterated peptide, and fully deuterated peptide at each time point. MaxD is the maximum

deuterium incorporation for each peptide. It is calculated as the number of amino acids in the peptide minus 2 minus any proline that is present beyond position 2 of the peptide.

Live Cell Fluorescence microscopy - Images of yeast cells were acquired on a Delta Vision RT (Applied Precision) microscope using a 100×/0.35-1.5 Uplan Apo objective and specific band pass filter sets for GFP or mCherry. The images were acquired using a Coolsnap HQ (Photometrics) camera. Image processing was performed using ImageJ (http://rsbweb.nih.gov/ij/). Pixel fluorescence intensity of at least 40 cells per sample was quantified as described in (Jonikas et al., 2009; Vilardi et al., 2014) using Knime software (www.knime.org/knime).

Analysis of plasmid-induced Get3 expression levels –1 ml of mid-log phase yeast culture was pelleted by low speed centrifugation, resuspended in 0.1 M NaOH and incubated for ten minutes at room temperature. Cells were recovered by centrifugation and dissolved in 1X SDS loading buffer. 10 µl of lysate per lane were separated by SDS-PAGE and analyzed by immunoblot using a mouse monoclonal antibody against Pgk1 (Molecular Probes) or a guinea pig serum against Get3 (Metz et al. 2006).

4.13 References

Battle, Alexis, Martin C. Jonikas, Peter Walter, Jonathan S. Weissman, and Daphne Koller. 2010. "Automated Identification of Pathways from Quantitative Genetic Interaction Data." *Molecular Systems Biology* 6 (June): 379. doi:10.1038/msb.2010.27.

Buchner, J., H. Grallert, and U. Jakob. 1998. "Analysis of Chaperone Function Using Citrate Synthase as Nonnative Substrate Protein." *Methods in Enzymology* 290: 323–38.

Englander, S. Walter. 2006. "Hydrogen Exchange and Mass Spectrometry: A Historical Perspective." *Journal of the American Society for Mass Spectrometry* 17 (11): 1481–89. doi:10.1016/j.jasms.2006.06.006.

Favaloro, Vincenzo, Milan Spasic, Blanche Schwappach, and Bernhard Dobberstein. 2008. "Distinct Targeting Pathways for the Membrane Insertion of Tail-Anchored (TA) Proteins." *Journal of Cell Science* 121 (11): 1832–40. doi:10.1242/jcs.020321.

Frank, J., M. Radermacher, P. Penczek, J. Zhu, Y. Li, M. Ladjadj, and A. Leith. 1996. "SPIDER

and WEB: Processing and Visualization of Images in 3D Electron Microscopy and Related Fields." *Journal of Structural Biology* 116 (1): 190–99. doi:10.1006/jsbi.1996.0030.

Hoffmann, Jörg H., Katrin Linke, Paul C. F. Graf, Hauke Lilie, and Ursula Jakob. 2004. "Identification of a Redox-Regulated Chaperone Network." *The EMBO Journal* 23 (1): 160–68. doi:10.1038/sj.emboj.7600016.

Hu, Junbin, Jingzhi Li, Xinguo Qian, Vlad Denic, and Bingdong Sha. 2009. "The Crystal Structures of Yeast Get3 Suggest a Mechanism for Tail-Anchored Protein Membrane Insertion." *PloS One* 4 (11): e8061. doi:10.1371/journal.pone.0008061.

Ilbert, Marianne, Janina Horst, Sebastian Ahrens, Jeannette Winter, Paul C. F. Graf, Hauke Lilie, and Ursula Jakob. 2007. "The Redox-Switch Domain of Hsp33 Functions as Dual Stress Sensor." *Nature Structural & Molecular Biology* 14 (6): 556–63. doi:10.1038/nsmb1244.

Jakob, U., M. Eser, and J. C. Bardwell. 2000. "Redox Switch of Hsp33 Has a Novel Zinc-Binding Motif." *The Journal of Biological Chemistry* 275 (49): 38302–10. doi:10.1074/jbc.M005957200.

Jakob, U., W. Muse, M. Eser, and J. C. Bardwell. 1999. "Chaperone Activity with a Redox Switch." *Cell* 96 (3): 341–52.

Jonikas, Martin C., Sean R. Collins, Vladimir Denic, Eugene Oh, Erin M. Quan, Volker Schmid, Jimena Weibezahn, et al. 2009. "Comprehensive Characterization of Genes Required for Protein Folding in the Endoplasmic Reticulum." *Science (New York, N.Y.)* 323 (5922): 1693–97. doi:10.1126/science.1167983.

Kachur, A. V., C. J. Koch, and J. E. Biaglow. 1999. "Mechanism of Copper-Catalyzed Autoxidation of Cysteine." *Free Radical Research* 31 (1): 23–34.

Kiianitsa, Konstantin, Jachen A. Solinger, and Wolf-Dietrich Heyer. 2003. "NADH-Coupled Microplate Photometric Assay for Kinetic Studies of ATP-Hydrolyzing Enzymes with Low and High Specific Activities." *Analytical Biochemistry* 321 (2): 266–71.

Kohl, Christian, Peter Tessarz, Karina von der Malsburg, Regina Zahn, Bernd Bukau, and Axel Mogk. 2011. "Cooperative and Independent Activities of Sgt2 and Get5 in the Targeting of Tail-Anchored Proteins." *Biological Chemistry* 392 (7): 601–8. doi:10.1515/BC.2011.066.

Mariappan, Malaiyalam, Xingzhe Li, Sandra Stefanovic, Ajay Sharma, Agnieszka Mateja, Robert J. Keenan, and Ramanujan S. Hegde. 2010. "A Ribosome-Associating Factor Chaperones Tail-Anchored Membrane Proteins." *Nature* 466 (7310): 1120–24. doi:10.1038/nature09296.

Mariappan, Malaiyalam, Agnieszka Mateja, Malgorzata Dobosz, Elia Bove, Ramanujan S. Hegde, and Robert J. Keenan. 2011. "The Mechanism of Membrane-Associated Steps in Tail-Anchored Protein Insertion." *Nature* 477 (7362): 61–66. doi:10.1038/nature10362.

Marsh, James J., Henry S. Guan, Sheng Li, Peter G. Chiles, Danny Tran, and Timothy A. Morris. 2013. "Structural Insights into Fibrinogen Dynamics Using Amide Hydrogen/Deuterium Exchange Mass Spectrometry." *Biochemistry* 52 (32): 5491–5502. doi:10.1021/bi4007995.

Mateja, Agnieszka, Anna Szlachcic, Maureen E. Downing, Malgorzata Dobosz, Malaiyalam Mariappan, Ramanujan S. Hegde, and Robert J. Keenan. 2009. "The Structural Basis of Tail-Anchored Membrane Protein Recognition by Get3." *Nature* 461 (7262): 361–66. doi:10.1038/nature08319.

Metz, Jutta, Andrea Wächter, Bastian Schmidt, Janusz M. Bujnicki, and Blanche Schwappach.

2006. “The Yeast Arr4p ATPase Binds the Chloride Transporter Gef1p When Copper Is Available in the Cytosol.” *The Journal of Biological Chemistry* 281 (1): 410–17. doi:10.1074/jbc.M507481200.

Mukhopadhyay, Rita, Ye-Shih Ho, Pamela J. Swiatek, Barry P. Rosen, and Hiranmoy Bhattacharjee. 2006. “Targeted Disruption of the Mouse Asna1 Gene Results in Embryonic Lethality.” *FEBS Letters* 580 (16): 3889–94. doi:10.1016/j.febslet.2006.06.017.

Ohi, Melanie, Ying Li, Yifan Cheng, and Thomas Walz. 2004. “Negative Staining and Image Classification - Powerful Tools in Modern Electron Microscopy.” *Biological Procedures Online* 6: 23–34. doi:10.1251/bpo70.

Powis, Katie, Bianca Schrul, Heather Tienson, Irina Gostimskaya, Michal Breker, Stephen High, Maya Schuldiner, Ursula Jakob, and Blanche Schwappach. 2013. “Get3 Is a Holdase Chaperone and Moves to Deposition Sites for Aggregated Proteins When Membrane Targeting Is Blocked.” *Journal of Cell Science* 126 (Pt 2): 473–83. doi:10.1242/jcs.112151.

Radermacher, M., T. Wagenknecht, A. Verschoor, and J. Frank. 1987. “Three-Dimensional Reconstruction from a Single-Exposure, Random Conical Tilt Series Applied to the 50S Ribosomal Subunit of Escherichia Coli.” *Journal of Microscopy* 146 (Pt 2): 113–36.

Reichmann, Dana, Ying Xu, Claudia M. Cremers, Marianne Ilbert, Roni Mittelman, Michael C. Fitzgerald, and Ursula Jakob. 2012. “Order out of Disorder: Working Cycle of an Intrinsically Unfolded Chaperone.” *Cell* 148 (5): 947–57. doi:10.1016/j.cell.2012.01.045.

Riddles, P. W., R. L. Blakeley, and B. Zerner. 1983. “Reassessment of Ellman’s Reagent.” *Methods in Enzymology* 91: 49–60.

Scheres, Sjors H. W. 2012. “RELION: Implementation of a Bayesian Approach to Cryo-EM Structure Determination.” *Journal of Structural Biology* 180 (3): 519–30. doi:10.1016/j.jsb.2012.09.006.

Schuldiner, Maya, Jutta Metz, Volker Schmid, Vladimir Denic, Magdalena Rakwalska, Hans Dieter Schmitt, Blanche Schwappach, and Jonathan S. Weissman. 2008. “The GET Complex Mediates Insertion of Tail-Anchored Proteins into the ER Membrane.” *Cell* 134 (4): 634–45. doi:10.1016/j.cell.2008.06.025.

Shen, Jian, Ching-Mei Hsu, Bae-Kwang Kang, Barry P. Rosen, and Hiranmoy Bhattacharjee. 2003. “The Saccharomyces Cerevisiae Arr4p Is Involved in Metal and Heat Tolerance.” *Biometals: An International Journal on the Role of Metal Ions in Biology, Biochemistry, and Medicine* 16 (3): 369–78.

Stefanovic, Sandra, and Ramanujan S. Hegde. 2007. “Identification of a Targeting Factor for Posttranslational Membrane Protein Insertion into the ER.” *Cell* 128 (6): 1147–59. doi:10.1016/j.cell.2007.01.036.

Stefer, Susanne, Simon Reitz, Fei Wang, Klemens Wild, Yin-Yuin Pang, Daniel Schwarz, Jörg Bomke, et al. 2011. “Structural Basis for Tail-Anchored Membrane Protein Biogenesis by the Get3-Receptor Complex.” *Science (New York, N.Y.)* 333 (6043): 758–62. doi:10.1126/science.1207125.

Suloway, Christian J. M., Justin W. Chartron, Ma’ayan Zaslaver, and William M. Clemons. 2009. “Model for Eukaryotic Tail-Anchored Protein Binding Based on the Structure of Get3.” *Proceedings of the National Academy of Sciences of the United States of America* 106 (35): 14849–54. doi:10.1073/pnas.0907522106.

Suloway, Christian J. M., Michael E. Rome, and William M. Clemons. 2012. “Tail-Anchor

Targeting by a Get3 Tetramer: The Structure of an Archaeal Homologue." *The EMBO Journal* 31 (3): 707–19. doi:10.1038/emboj.2011.433.

Tang, Guang, Liwei Peng, Philip R. Baldwin, Deepinder S. Mann, Wen Jiang, Ian Rees, and Steven J. Ludtke. 2007. "EMAN2: An Extensible Image Processing Suite for Electron Microscopy." *Journal of Structural Biology* 157 (1): 38–46. doi:10.1016/j.jsb.2006.05.009.

Tapley, Timothy L., Jan L. Körner, Madhuri T. Barge, Julia Hupfeld, Joseph A. Schauerte, Ari Gafni, Ursula Jakob, and James C. A. Bardwell. 2009. "Structural Plasticity of an Acid-Activated Chaperone Allows Promiscuous Substrate Binding." *Proceedings of the National Academy of Sciences of the United States of America* 106 (14): 5557–62. doi:10.1073/pnas.0811811106.

Vilardi, Fabio, Milena Stephan, Anne Clancy, Andreas Janshoff, and Blanche Schwappach. 2014. "WRB and CAML Are Necessary and Sufficient to Mediate Tail-Anchored Protein Targeting to the ER Membrane." *PloS One* 9 (1): e85033. doi:10.1371/journal.pone.0085033.

Winter, Jeannette, Katrin Linke, Anna Jatzek, and Ursula Jakob. 2005. "Severe Oxidative Stress Causes Inactivation of DnaK and Activation of the Redox-Regulated Chaperone Hsp33." *Molecular Cell* 17 (3): 381–92. doi:10.1016/j.molcel.2004.12.027.

Zhang, Hui-Min, Shaun M. McLoughlin, Stephen D. Frausto, Hengli Tang, Mark R. Emmett, and Alan G. Marshall. 2010. "Simultaneous Reduction and Digestion of Proteins with Disulfide Bonds for Hydrogen/Deuterium Exchange Monitored by Mass Spectrometry." *Analytical Chemistry* 82 (4): 1450–54. doi:10.1021/ac902550n.

CHAPTER 5

HSP90 CO-CHAPERONE, FKBP51, REGULATES TAU STABILIZATION

5.1 Abstract

Hsp90 is an important chaperone protein involved in folding client proteins implicated in many cellular processes. Hsp90 is an ATPase homodimer that undergoes large conformational changes during its hydrolysis cycle, enabling client binding. One of Hsp90's key client proteins is tau, which is found in axonal neurons. When tau is hyperphosphorylated it can aggregate and form neurofibrillary tangles (NFTs), hallmarks of neurodegenerative diseases. Hsp90 binds to tau directly, stabilizing it and protecting it from proteasomal degradation. FKBP51, a TPR-domain containing co-chaperone with a peptidyl prolyl isomerase (PPIase) domain, regulates Hsp90 stabilization of tau. Deeper mechanistic and structural information of this interaction is therefore necessary to develop effective inhibitors of this interaction for potential neurodegenerative disease therapeutics. In this study, we explored the Hsp90:FKBP51 complex, finding that FKBP51 only binds Hsp90 in its closed, ATP-bound state. Electron microscopy studies of this complex highlight the TPR-domain interaction, localizing the PPIase domain near the Hsp90 client binding domain.

5.2 Introduction

Hsp90 is central to many cellular signaling pathways due to its role in promoting folding of kinases and transcription factors (Gronemeyer, Gustafsson, and Laudet 2004). Hsp90 is a homodimer that undergoes large conformational changes during ATP hydrolysis to facilitate

proper client protein binding (Southworth and Agard 2008). Hsp90 contains three major domains: the N-terminal nucleotide binding domain (NTD), the middle domain (MD) that is important for binding client proteins and contains the catalytic arginine for hydrolysis, and the C-terminal dimerization domain (CTD), which also contains the MEEVD motif for binding tetratricopeptide repeat (TPR) domain co-chaperones (Pearl and Prodromou 2006; Taipale, Jarosz, and Lindquist 2010; Young, Obermann, and Hartl 1998). Extensive structural studies have revealed that during hydrolysis, Hsp90 can cycle between three major states: an apo, open 'V' conformation, an ATP-bound, closed conformation, and a compact ADP conformation (Shiau et al. 2006; Bron et al. 2008; Krukenberg et al. 2008; Ali et al. 2006; Southworth and Agard 2008). Co-chaperones, such as p23 and FKBP51, regulate the hydrolysis and client binding cycle by modulating hydrolysis rate and conformational state, which can provide specificity for clients (Csermely et al. 1993; Kirschke et al. 2014; Lavery et al. 2014; Zuehlke and Johnson 2010).

Due to the many important cellular processes Hsp90 regulates, such as cell growth and differentiation, it is upregulated in cancers and neurodegenerative diseases (Workman 2004; Lindberg et al. 2015; Moulick et al. 2011). Hsp90 has been viewed as a potential drug target due to its direct interaction with many oncogenic proteins (Workman 2004; Workman et al. 2007; Moulick et al. 2011; Lindberg et al. 2015; Yi and Regan 2008). Inhibition of Hsp90 function in cancer cells has been shown to upregulate the Ubiquitin Proteasome System (UPS) promoting degradation of oncogenic proteins and rescuing cells from malignancy (Jinwal et al. 2010; Blair et al. 2013). However, Hsp90 inhibitors have proven to be fairly toxic due to low specificity for disease cells (Roe et al. 1999; Sidera and Patsavoudi 2014; Jhaveri et al. 2012; Trendowski

2015). One way to address this issue would be to target co-chaperone regulated interactions that are implicated in specific diseases.

Tau is an important client protein of Hsp90 due to its role in neurodegenerative diseases. Found in neuronal axons, tau promotes microtubule (MT) polymerization and stability. Phosphorylation of tau leads to oligomerization and formation of tau filaments and neurofibrillary tangles (NFTs), which are the hallmarks of neurodegenerative tauopathies like Alzheimer's disease (AD) and frontotemporal dementia with Parinsonism (FTDP-17) (Grundke-Iqbal et al. 1986). Hsp90 binds tau directly, increasing tau stability and preventing UPS degradation (Karagöz et al. 2014). A co-chaperone that regulates the Hsp90 and tau interaction is FKBP51, an immunophilin that contains an N-terminal peptidyl-prolyl isomerase (PPIase) domain and C-terminal TPR domain (Allan and Ratajczak 2011). FKBP51 expression increases with age and in AD, therefore its role in regulating Hsp90:tau binding is implicated in protecting neurotoxic tau from proteosomal degradation (Blair et al. 2013). Understanding this interaction is important to develop drugs with more specificity than general Hsp90 inhibitors.

In this study we establish that Hsp90 binds to FKBP51 specifically in a closed, ATP-bound state, an interaction that is enhanced by p23. Negative stain and cryo-EM of the Hsp90:FKBP51 complex demonstrate that the PPIase domain of FKBP51 positions near the Hsp90 client binding MD to position it for direct client regulation. These findings are important for establishing the best way to target the Hsp90:FBP51 interaction for potential therapeutic treatment of tauopathies.

5.3 Hsp90 conformational states are prominent by Size Exclusion Chromatography

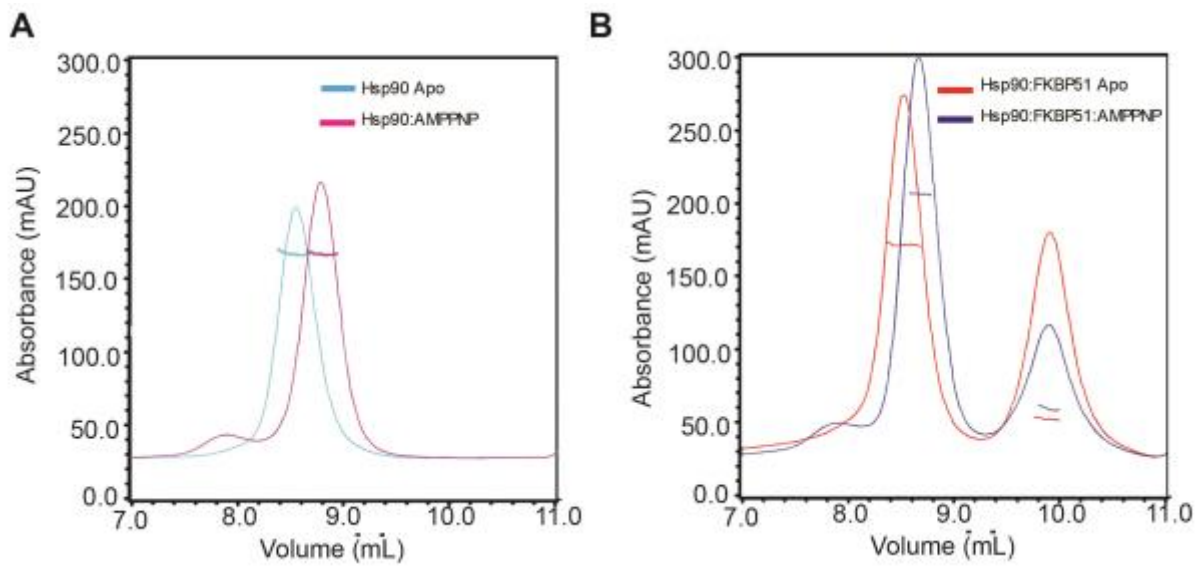

Figure 5-1. SEC-MALS of Hsp90 establishes elution shift from Open to Closed state. (A) SEC-MALS of Hsp90 apo (cyan) and incubated with nucleotide, salt and heat (pink), both with MWs indicated at ~170 kDa. (B) SEC-MALS of Hsp90:FKBP51 apo (red) and incubated with nucleotide, salt and heat (blue). Hsp90:FKBP51 apo has MW of ~170 kDa, and Hsp90:FKBP51:AMPPNP has MW of ~210 kDa.

Size Exclusion Chromatography in tandem with Multi-Angle Light Scattering (SEC-MALS) was used to determine the nucleotide state necessary for Hsp90 to bind FKBP51. First we established a protocol to force Hsp90 into a closed, ATP-bound conformation. To do so, we incubated Hsp90 with AMPPNP, a non-hydrolysable ATP analog, high salt (500 mM $(NH_4)_2SO_4$, and heated to 37°C. By SEC-MALS we can see a significant shift in elution volume from the apo, open state to the ATP-bound, closed state (Fig. 5-1A). This elution shift demonstrates that the addition of nucleotide, salt and heat changes the hydrodynamic radius while the molecular weight remains the same. This shows that we can use SEC-MALS to determine when Hsp90 undergoes the large conformational change from the extended 'V' open state to a much more compact closed state.

This same experiment was done with the addition of FKBP51, and we see that Hsp90:FKBP51 the apo has an indicated MW of ~170 kDa, but the Hsp90:FKBP51:AMPPNP has a shift to the right to the closed, ATP-bound complex with an indicated MW of ~210 kDa (Fig. 5-1B). We also see a loss in the FKBP51 excess peak, indicating that it is binding Hsp90 and shifting into that peak. The molecular weight of this complex indicates 2:1 stoichiometry for Hsp90:FKPB51, meaning it binds in an asymmetric manner. To characterize this complex we collected peak fractions of the Hsp90:AMPPNP Hsp90:FKBP51:AMPPNP complex for glutaraldehyde crosslinking and negative stain EM analysis.

5.4 Negative Stain Electron Microscopy analysis of Hsp90:FKBP51:AMPPNP

Looking at the particles of Hsp90:AMPPNP and Hsp90:FKBP51:AMPPNP, it is already evident that the Hsp90 particles are in a consistent compact, closed state (Fig. 5-2A,B). The single particles were subjected to reference free 2D averaging and aligned to each other using SPIDER 2D refine (Frank et al., 1996). The Hsp90:AMPPNP averages show the characteristic domain architecture of closed Hsp90 particles, with the two NTD lobes forming the top of the tight 'V', with the CTD at the dimerization point of the 'V' (Fig. 502C). In comparison, the Hsp90:FKBP51:AMPPNP averages show extra density for FKBP51 (arrows) near the CTD of the closed Hsp90 particle (Fig. 5-2C). Given the expected size of FKBP51 protein, this arrangement agrees with the 2:1 Hsp90:FKBP51 stoichiometry indicated by SEC-MALS, and presents an asymmetric architecture.

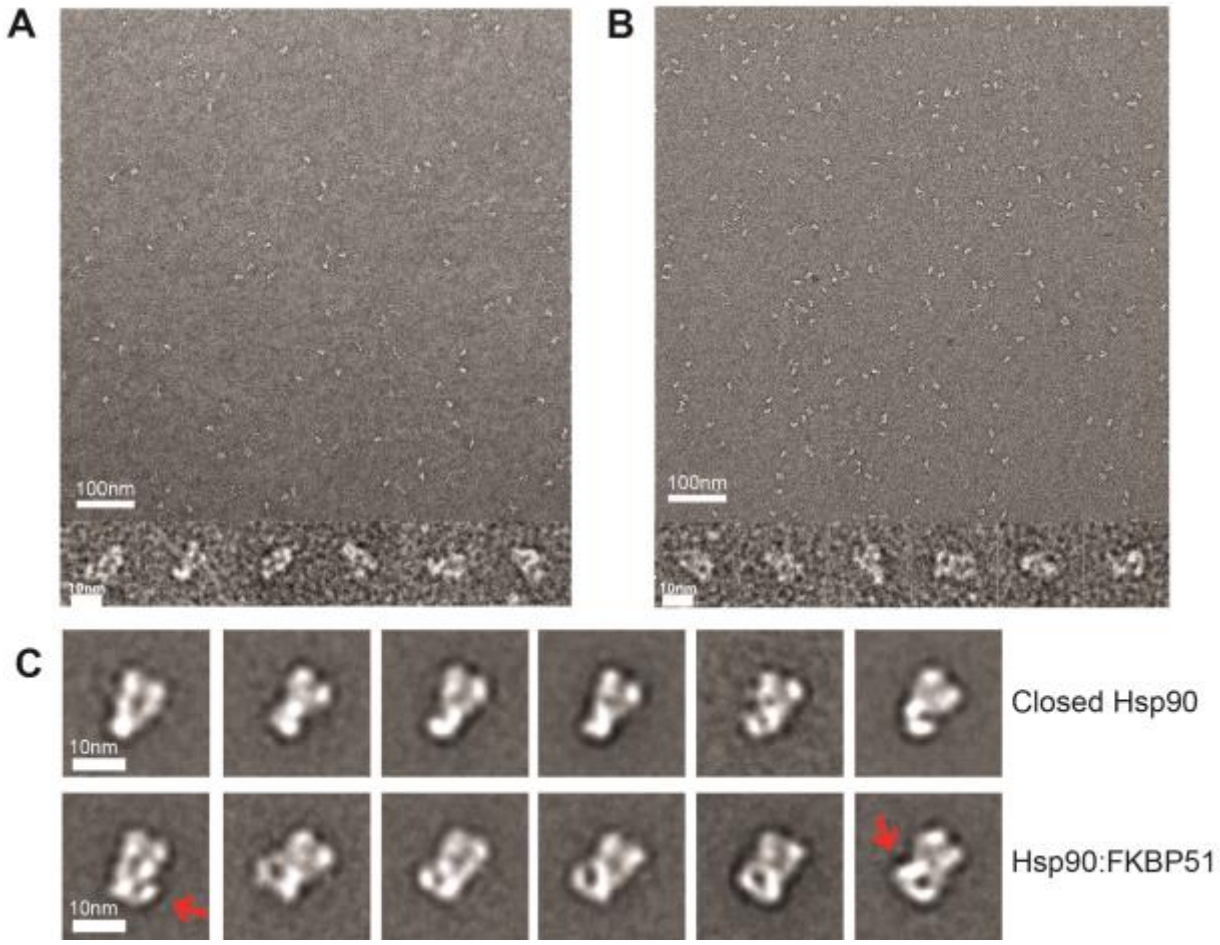

Figure 5-2. Negative stain electron microscopy (EM) evaluation of Hsp90:AMPPNP and Hsp90:FKBP51:AMPPNP. Representative micrograph and single particles of (A) Hsp90:AMPPNP and (B) Hsp90:FKBP51:AMPPNP. (C) Reference free 2D averages of Hsp90:AMPPNP and Hsp90:FKBP51:AMPPNP. Arrow (red) indicate extra density for FKBP51.

Following 2D analysis, we performed a 3D classification of the entire particle set, split into 3 classes. The Hsp90 closed state crystal structure (2CG9) was low passed to 15A and used as the initial model. One of the classes lacked the FKBP51 extra density, whereas the other two appeared very similar, with the FKBP51 density appearing near the CTD (Fig. 5-3). The Hsp90 closed crystal structure and FKBP51 crystal structure (1KT0) were both docked into the 3D models to determine the best fit, with the best class shown (Fig. 5-3). Although the 3D model is very low resolution (~27A), both crystral structures fit into the model reasonably well. The α-helical TPR domains of FKBP51 are arranged near the MEEVD binding site of the C-terminal

domain of Hsp90, with the PPIase domains positioned near the middle domain of Hsp90. Because FKBP51 binds Hsp90 specifically in the closed, ATP-bound state, this structural model would suggest that the PPIase domain needs to be positioned near the client binding site of Hsp90 to assist with client protein folding.

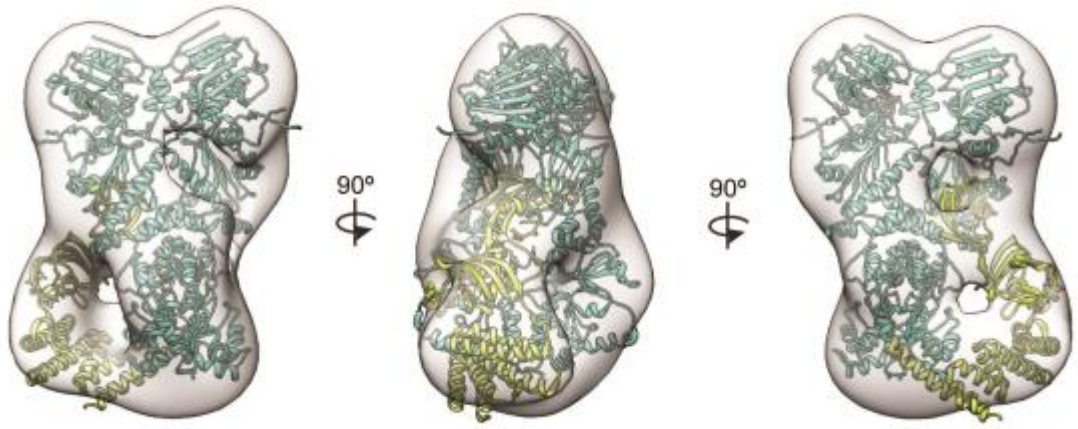

Figure 5-3. Negative Stain 3D EM model of Hsp90:FKBP51:AMPPNP docked with Hsp90 (blue, 2CG9) and FKBP51 (yellow, 1KT0).

5.5 Cryo-EM of Hsp90:FKBP51:AMPPNP

To achieve a higher-resolution structure of Hsp90:FKBP51:AMPPNP, the complex was purified by SEC at a higher concentration for vitrification. Although crosslinking was necessary for negative stain EM, due to the low concentration of proteins on the grid (~150 nM), we hoped that the higher concentrations used for cryo-EM (~5uM) would be enough for the complex to remain stable. A lot of effort was put into optimizing concentration and freezing conditions to get a nice spread of particles in ice, with an important improvement being the use of DDM detergent that was essential for getting good particle orientations. The ice thickness was also critical for getting a good ice spread (Fig. 5-4).

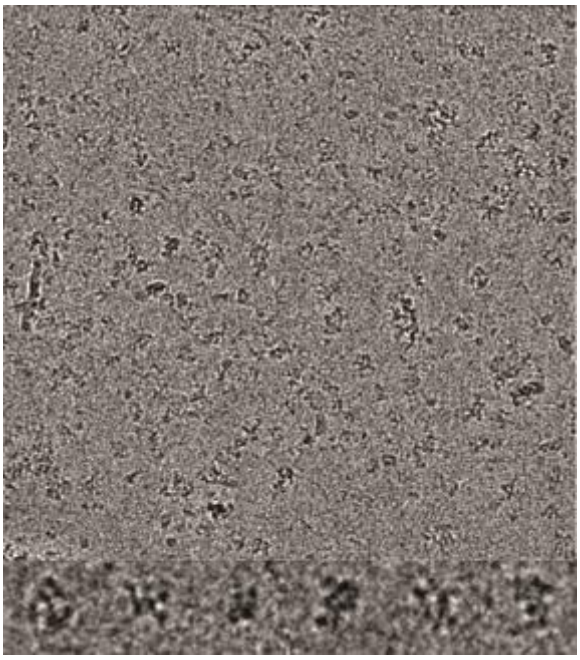

Figure. 5-4. Representative cryo-EM micrograph and single particles of Hsp90:FKBP51:AMPPNP

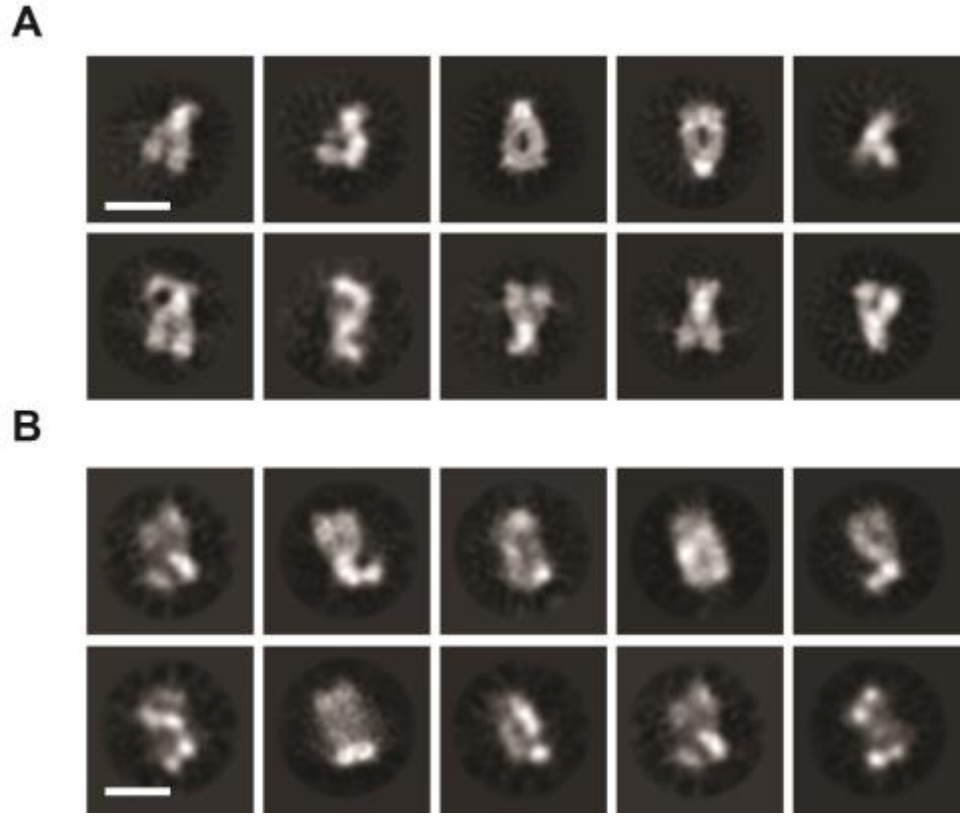

Figure 5-5. Cryo-EM 2D reference-free class averages. Hsp90:FKBP51:AMPPNP (A) and Hsp90:FKBP51:p23:AMPPNP (B) 2D averages were generated using RELION (Scheres, 2012). Scale bar=100 Å.

Reference free 2D averages of Hsp90:FKBP51:AMPPNP were generated using RELION (Scheres, 2012). Fortunately, class averages show characteristics of high resolution particles, and the architecture is consistent with the Hsp90 closed structure (Fig 5-5A). Unfortunately, the uncrosslinked complex seems to fall apart in cryo-EM, resulting in low occupancy in the dataset and many class averages are of the Hsp90 alone. The Hsp90:FKBP51 interaction is low affinity (~5uM), so it's likely still falling apart when it is diluted for cryo-EM conditions.

5.6 p23 Stabilizes the Hsp90:FKBP51 complex

In an effort to stabilize the complex we formed the complex with the addition of p23, another co-chaperone that stabilizes the closed, ATP-bound state of Hsp90 (Ali et al., 2006). P23 binds to Hsp90 at the NTD, trapping Hsp90 in the ATP state to slow hydrolysis. We formed the Hsp90:FKBP51:p23:AMPPNP complex with nucleotide, salt and heat as described previously and analyzed it by SEC-MALS. We see that the Hsp90:FKBP51:AMPPNP complex shifts to the left of the closed, Hsp90:AMPPNP complex, with an increase of MW from 170 to 200 kDa, respectively (Fig. 5-6A). With the addition of p23 there is an increase in the MW reading, from the 200 kDa of the Hsp90:FKBP51:AMPPNP complex, to 220 kDa for the Hsp90:FKBP51:p23:AMPPNP.

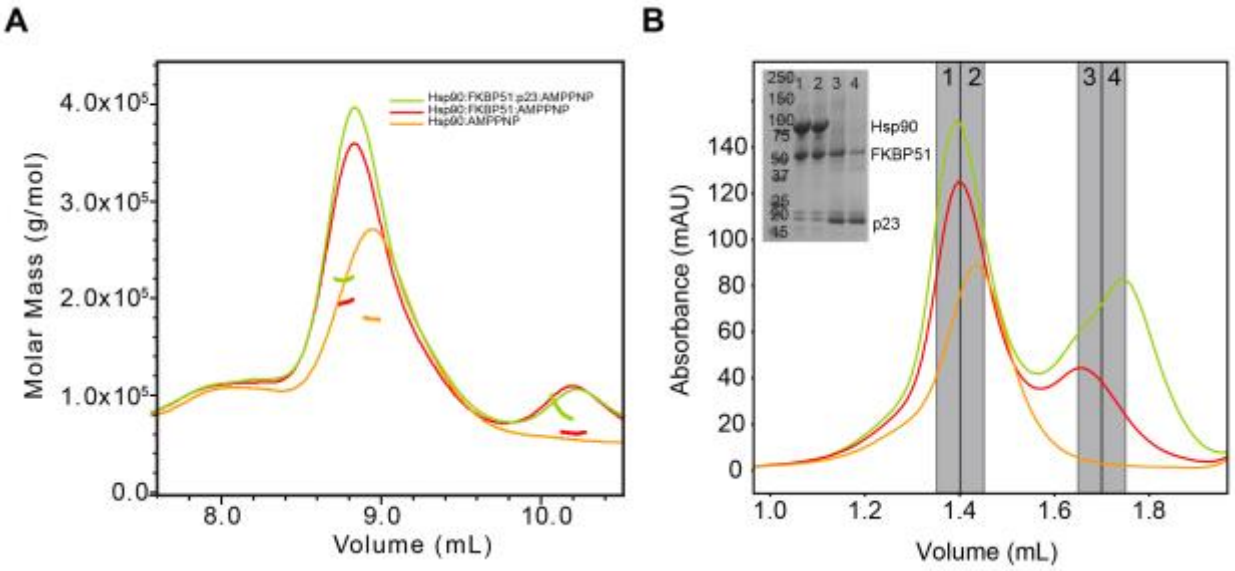

Figure 5-6. Hsp90:FKBP51:p23:AMPPNP can be purified by SEC. (A) SEC-MALS of Hsp90:AMPPNP (orange), Hsp90:FKBP51:AMPPNP (red), and Hsp90:FKBP51:p23:AMPPNP (green), with indicated MWs of ~170 kDa, ~200 kDa, and ~220 kDa, respectively. (B) Analytical SEC of Hsp90:AMPPNP (orange), Hsp90:FKBP51:AMPPNP (red), and Hsp90:FKBP51:p23:AMPPNP (green). Peak fractions are indicated (grey), which were analyzed by SDS-PAGE (insert).

The MW of the Hsp90:FKBP51:p23:AMPPNP is about the same as what we would expect for the Hsp90:FKBP51:AMPPNP complex, so it's unclear if p23 is remaining bound, or if it is just stabilizing the Hsp90:FKBP51:AMPPNP complex. Either way, we decided to analyze this complex by cryo-EM to determine if it increased occupancy of the Hsp90:FKBP51:AMPPNP complex. The complex was concentrated and then purified using analytical SEC (Fig. 5-5B), which shows an increase in absorbance of the complex peak upon addition of p23 (green). Peak fractions were analyzed by SDS-PAGE, showing bands for Hsp90, FKBP51 and p23. Fractions were collected for cryo-EM analysis. 2D averages of this dataset show a shift in occupancy of the FKBP51, with extra density noticeable in almost all averages (Fig. 5-5B). Notably, there does not seem to be extra density at the NTD for p23, with these averages looking very similar to the negative stain averages, indicating p23 is likely stabilizing the Hsp90:FKBP51:AMPPNP complex rather than remaining bound. Preliminary 3D analysis of

this ~100,00 particle dataset revealed models with similar resolution to the negative stain model. This complex is pretty small, making it challenging to get high enough signal to noise achieve a high-resolution model with so few particles, indicating a much larger dataset will be necessary to achieve high-resolution.

5.7 Discussion

In this study, we have established that FKBP51 specifically binds Hsp90 in an ATP bound, closed conformation. Our 3D negative stain EM model of the complex suggests that FKBP51 is binding to the CTD of Hsp90, positioning the PPIase domain of FKBP51 near the client site of Hsp90. This conformation is important for understanding how FKBP51 regulates client binding of Hsp90, and how it could help stabilize tau for microtubule binding, and prevent proteasomal degradation of hyperphosphorylated tau. The PPIase activity of FKBP51 is certainly important in helping to refold proteins when associated with Hsp90 (cite, expand). The p23 co-chaperone, known to lock Hsp90 in a closed state by binding at the NTD dimerization domain, regulates Hsp90 hydrolysis. We established by SEC and cryo-EM that p23 stabilizes the Hsp90:FKBP51:AMPPNP complex by stabilizing the ATP-bound Hsp90 dimer.

FKBP51 regulates Hsp90 tau-binding in neurodegenerative diseases, such as Alzheimer's disease. Getting a higher resolution structure of the Hsp90:FKBP51:AMPPNP complex will be important to establish the direct interaction sites between FKBP51 and Hsp90. Although it is known that they interact between the TPR and MEEVD motif in the CTD of Hsp90, according to our 3D EM structure it seems that there could be a secondary binding interaction between the PPIase domain and the client binding MD of Hsp90. Finding a way to alter the interaction between the PPIase domain and client proteins, such as tau, could be an alternative way to develop Hsp90 inhibitors specific to AD. There is great potential for a high-resolution structure,

considering the definition seen in 2D averages of the current cryo-EM data. A much larger dataset, and potentially with the help of phase plate technology to boost contrast, could benefit the project greatly.

5.8 Materials and methods

Protein purification

Hsp90α was expressed in *E. coli* BL21 DE3 from a pET151 (Invitrogen) derivative, containing an N-terminal 6x His-tag, V5 epitope and Tobacco Etch Virus (TEV) protease cleavage site. After cells reached an A600 of ~0.8-1 in TB, grown at 37 °C, protein expression was induced with 1 mM IPTG and cells were grown overnight at 16 °C. Cells were pelleted and resuspended in Lysis buffer (20 mM Tris pH 8.0, 500 mM KCl, 6 mM β-ME, 10 mM imidazole pH 8.0, 10% glycerol), ~ 20mL per L growth, supplemented with one tablet of protease inhibitor (Roche). Cells were lysed by Avestin EmulsiFlex homogenizer. The lysate was purified by nickel affinity using Nickel sepharose 6 Fast Flow beads (GE Healthcare). The elution was further purifided over an anion-exchange chromatography column (5 mL HiTrap QFF, GE Healthcare). The purified protein was dialyzed overnight and cleaved with 6xHis-tagged TEV protease overnight at 4 °C in Dialysis buffer (20 mM Tris pH 8.0, 50 M KCl, 6 mM β-ME, 10% glycerol) at a 1:10 molar ratio TEV:Hsp90. Purified protein was syringe filtered (Macherey-Nagel Chromafil 0.20 μm) and concentrated down to ~5mL before Size Exclusion Chromatography on the Superdex 200 16/60 (GE Healthcare) in s200 buffer (20 mM HEPES pH 7.5, 250 mM KCl, 6 mM β-ME). Peak fractions were pooled and dialyzed into Storage Buffer (20 mM HEPES pH 7.5, 50 mM KCl, 6 mM β-ME, 10% glycerol) overnight at 4 °C. Protein was concentrated and aliquoted for storage. Hsp90 concentration was determined spectroscopically using NanoDrop 2000 (Thermo Fisher).

FKBP51 was expressed in *E. coli* BL21 DE3 from a pET151 (Invitrogen) derivative, containing an N-terminal 6x His-tag, V5 epitope and TEV protease cleavage site. Purification protocol is the same as Hsp90.

Tau was expressed in *E. coli* BL21 DE3 from a pET28 (Invitrogen) derivative, containing an N-terminal 6x His-tag, V5 epitope and TEV protease cleavage site. Purification protocol is the same as Hsp90, except for the use of a Cation exchange column (HiTrap QFF, GE Healthcare) instead of the anion exchange used for Hsp90.

P23 was expressed in *E. coli* BL21 DE3 from a pET151 (Invitrogen) derivative, containing an N-terminal 6x His-tag, V5 epitope and TEV protease cleavage site. Purification protocol is the same as Hsp90, except the His tag was not removed.[1]

Closed Hsp90 Complex Formation, SEC-MALS and analytical SEC purification

To form a stable, closed Hsp90 complex, Hsp90 is incubated at 20 μM with 2 mM AMPPNP, 5 mM $MgCl_2$, 500 mM $(NH_4)_2SO_4$ with 5X Binding Buffer (250 mM Na_2PO_4, pH 7.4) for 30 mins at 20°C (RT), then 45 minutes at 37°C. To form complex with FKBP51, p23, or tau, the closed complex is formed in the same way, with addition of an equimolar ratio of Hsp90:FKBP51:p23:tau. For SEC-MALS, the average MW of protein complexes was determined by separation using a WTC-050S5 SEC column (Wyatt Technology Corporation) with an Akta micro (GE Healthcare) and analysis using a DAWN HELEOS II MALS detector and Optilab rEX differential refractive index detector using ASTRA VI software (Wyatt Technology Corporation). The MW was calculated from Raleigh ratio based on the static light scattering and corresponding protein concentration of a selected peak.

[1] P23 purification completed by Dan Southworth

For analytical Size Exclusion Chromatography, protein complexes were run over an analytical Size Exclusion Column, Superose 6pc 3.2/30 (GE Healthcare) with Running Buffer: 20 mM Hepes pH=7.5, 100 mM Kl, 10 mM MgCl2, 6 mM β-ME. Peak fractions were spiked with 1 mM AMPPNP. To purify complexes for crosslinking and negative stain electron microscopy, complexes were formed at 50 μM, purified over the Superose 6 pc 3.2/30 (GE Healthcare), and spiked with 1 mM AMPPNP. To purify higher concentration complexes for cryo-EM samples, 300 μL of 50 μM Hsp90:FKBP51:p23, 2 mM AMPPNP, 5 mM MgCl2, and 500 mM $(NH_4)_2SO_4$ is incubated for 30 mins at 20 °C (RT), then 45 minutes at 37 °C. Once formed, 10% glycerol is added and concentrated down to 100 μL, then injected onto the Superose6 pc 3.2/30 (GE Healthcare).

Glutaraldehyde crosslinking and negative stain analysis

Crosslinking was done by diluting protein complexes from SEC fractions in Dilution Buffer (20 mM Hepes, pH=7.5, 100 mM KCl, 10 mM $MgCl_2$, 6 mM β-ME) to 1 μM with 0.05% glutaraldehyde. Samples were incubated at RT for 15 minutes, then quenched with 500mM Tris, pH=8 for 15 minutes at RT. Crosslinking is evaluated by SDS-PAGE. For negative-stain EM, complexes were diluted to ~150 nM and stained with 0.75% uranyl formate (pH 5.5-6.0) on thin carbon-layered 400 mesh copper grids (Pelco) (Ohi et al., 2004) and micrographs were imaged under low dose conditions using a G2 Spirit TEM (FEI) operated at 120 keV. Micrographs were taken at 52,000x magnification with 2.16 Å per pixel using a 4k x 4k CCD camera (Gatan). Single particles were selected using E2boxer in EMAN2 (Tang et al., 2007) and totaled 8,234 for Hsp90 closed and 15,612 for Hsp90:FKBP51. Reference free 2D classification and analysis was performed using SPIDER (Radermacher et al., 1987) and generated 100 classes for Hsp90:AMPPNP and 200 classes for Hsp90:FKBP51:AMPPNP. 3D classification was

performed using RELION (Scheres, 2012) by first running a 3D classification on the entire data set, binned two-fold, with three classes, using the Hsp90:p23 crystal structure (2CG9), low pass filtered to 15Å, as an initial model with no imposed symmetry. Each resulting model was examined for presence of FKBP51 density and compared to the 2D reference free averages of the complex.

Cryo-EM Sample Preparation

Purified complexes were diluted in 20 mM Hepes pH=7.5, 100 mM Kl, 10 mM MgCl2, 6 mM BME, 85 μM DDM and 3.5 μl was applied to plasma cleaned C-Flat 2/2 holey carbon grids (Protochips). Vitrification was performed using a Vitrobot (FEI Company) and samples were blotted for 2 seconds prior to plunge freezing in liquid ethane. Notably, the presence of DDM detergent was critical for good ice spread across the grids. Samples were imaged using a Titan Krios TEM (FEI Inc.) operated at 300 kV. Images were recorded on a Gatan K2 Summit direct electron detector operated in counted mode at 50,000X nominal magnification corresponding to a calibrated to 1.00 Å/pixel. Dose fractionated imaging was performed by semi-automated collection methods using UCSF Image 4 (Li et al. 2015, 4) with a defocus range of 1.5-3 μm. Total exposure time was 6 seconds with 0.2 second frames with a cumulative dose of ~45 e^- per $Å^2$ for 40 frames. Motion corrected frames were summed, and the FFT was visually inspected for sufficient Thon rings prior to additional processing (Li et al. 2013). All micrographs were CTF corrected using CTFFIND4 (Rohou and Grigorieff 2015) and poorly corrected micrographs were removed following visual inspection of the FFT and CTF estimation. Well-populated reference-free 2D class averages, determined with RELION (Scheres 2012), were used for templated automated particle picking with the Template Picker in Appion (Lander et al. 2009) to achieve a ~37,000 single particles dataset from 2150 micrographs for Hsp90:FKBP51:AMPPNP, and 1400

micrographs for 180,000 particles of Hsp90:FKBP51:p23:AMPPNP. The total dataset of particles was initially sorted following 2D classification by removing particles images from poorly resolved class averages, resulting in a total dataset of ~30,000 particles for Hsp90:FKBP51:AMPPNP, and ~100,00 for Hsp90:FKBP51:p23AMPPNP.

5.9 References

Ali, Maruf M. U., S. Mark Roe, Cara K. Vaughan, Phillipe Meyer, Barry Panaretou, Peter W. Piper, Chrisostomos Prodromou, and Laurence H. Pearl. 2006. "Crystal Structure of an Hsp90-Nucleotide-P23/Sba1 Closed Chaperone Complex." *Nature* 440 (7087): 1013–17. doi:10.1038/nature04716.

Allan, Rudi Kenneth, and Thomas Ratajczak. 2011. "Versatile TPR Domains Accommodate Different Modes of Target Protein Recognition and Function." *Cell Stress & Chaperones* 16 (4): 353–67. doi:10.1007/s12192-010-0248-0.

Blair, Laura J., Bryce A. Nordhues, Shannon E. Hill, K. Matthew Scaglione, John C. O'Leary, Sarah N. Fontaine, Leonid Breydo, et al. 2013. "Accelerated Neurodegeneration through Chaperone-Mediated Oligomerization of Tau." *The Journal of Clinical Investigation* 123 (10): 4158–69. doi:10.1172/JCI69003.

Bron, Patrick, Emmanuel Giudice, Jean-Paul Rolland, Rubén M. Buey, Pascale Barbier, J. Fernando Díaz, Vincent Peyrot, Daniel Thomas, and Cyrille Garnier. 2008. "Apo-Hsp90 Coexists in Two Open Conformational States in Solution." *Biology of the Cell* 100 (7): 413–25. doi:10.1042/BC20070149.

Csermely, P., J. Kajtár, M. Hollósi, G. Jalsovszky, S. Holly, C. R. Kahn, P. Gergely, C. Söti, K. Mihály, and J. Somogyi. 1993. "ATP Induces a Conformational Change of the 90-KDa Heat Shock Protein (Hsp90)." *The Journal of Biological Chemistry* 268 (3): 1901–7.

Gronemeyer, Hinrich, Jan-Ake Gustafsson, and Vincent Laudet. 2004. "Principles for Modulation of the Nuclear Receptor Superfamily." *Nature Reviews. Drug Discovery* 3 (11): 950–64. doi:10.1038/nrd1551.

Grundke-Iqbal, I., K. Iqbal, M. Quinlan, Y. C. Tung, M. S. Zaidi, and H. M. Wisniewski. 1986. "Microtubule-Associated Protein Tau. A Component of Alzheimer Paired Helical Filaments." *The Journal of Biological Chemistry* 261 (13): 6084–89.

Jhaveri, Komal, Tony Taldone, Shanu Modi, and Gabriela Chiosis. 2012. "Advances in the Clinical Development of Heat Shock Protein 90 (Hsp90) Inhibitors in Cancers." *Biochimica Et Biophysica Acta* 1823 (3): 742–55. doi:10.1016/j.bbamcr.2011.10.008.

Jinwal, Umesh K., John Koren, Sergiy I. Borysov, Andreas B. Schmid, Jose F. Abisambra, Laura J. Blair, Amelia G. Johnson, et al. 2010. "The Hsp90 Cochaperone, FKBP51, Increases Tau Stability and Polymerizes Microtubules." *The Journal of Neuroscience: The Official Journal of the Society for Neuroscience* 30 (2): 591–99. doi:10.1523/JNEUROSCI.4815-09.2010.

Karagöz, G. Elif, Afonso M. S. Duarte, Elias Akoury, Hans Ippel, Jacek Biernat, Tania Morán Luengo, Martina Radli, et al. 2014. "Hsp90-Tau Complex Reveals Molecular Basis for Specificity in Chaperone Action." *Cell* 156 (5): 963–74. doi:10.1016/j.cell.2014.01.037.

Kirschke, Elaine, Devrishi Goswami, Daniel Southworth, Patrick R. Griffin, and David A. Agard. 2014. "Glucocorticoid Receptor Function Regulated by Coordinated Action of the Hsp90 and Hsp70 Chaperone Cycles." *Cell* 157 (7): 1685–97. doi:10.1016/j.cell.2014.04.038.

Krukenberg, K.A., F. Förster, L.M. Rice, A. Sali, and D.A. Agard. 2008. "A Novel Conformation of E. Coli Hsp90 in Solution: Insights into the Conformational Dynamics of Hsp90." *Structure (London, England : 1993)* 16 (5): 755–65. doi:10.1016/j.str.2008.01.021.

Lander, Gabriel C., Scott M. Stagg, Neil R. Voss, Anchi Cheng, Denis Fellmann, James Pulokas, Craig Yoshioka, et al. 2009. "Appion: An Integrated, Database-Driven Pipeline to Facilitate EM Image Processing." *Journal of Structural Biology* 166 (1): 95–102.

Lavery, Laura A., James R. Partridge, Theresa A. Ramelot, Daniel Elnatan, Michael A. Kennedy, and David A. Agard. 2014. "Structural Asymmetry in the Closed State of Mitochondrial Hsp90 (TRAP1) Supports a Two-Step ATP Hydrolysis Mechanism." *Molecular Cell* 53 (2): 330–43. doi:10.1016/j.molcel.2013.12.023.

Li, Xueming, Paul Mooney, Shawn Zheng, Christopher R. Booth, Michael B. Braunfeld, Sander Gubbens, David A. Agard, and Yifan Cheng. 2013. "Electron Counting and Beam-Induced Motion Correction Enable near-Atomic-Resolution Single-Particle Cryo-EM." *Nature Methods* 10 (6): 584–90. doi:10.1038/nmeth.2472.

Li, Xueming, Shawn Zheng, David A. Agard, and Yifan Cheng. 2015. "Asynchronous Data Acquisition and On-the-Fly Analysis of Dose Fractionated CryoEM Images by UCSFImage." *Journal of Structural Biology* 192 (2): 174–78. doi:10.1016/j.jsb.2015.09.003.

Lindberg, Iris, James Shorter, R. Luke Wiseman, Fabrizio Chiti, Chad A. Dickey, and Pamela J. McLean. 2015. "Chaperones in Neurodegeneration." *The Journal of Neuroscience: The Official Journal of the Society for Neuroscience* 35 (41): 13853–59. doi:10.1523/JNEUROSCI.2600-15.2015.

Moulick, Kamalika, James H. Ahn, Hongliang Zong, Anna Rodina, Leandro Cerchietti, Erica M. Gomes DaGama, Eloisi Caldas-Lopes, et al. 2011. "Affinity-Based Proteomics Reveal Cancer-Specific Networks Coordinated by Hsp90." *Nature Chemical Biology* 7 (11): 818–26. doi:10.1038/nchembio.670.

Pearl, Laurence H., and Chrisostomos Prodromou. 2006. "Structure and Mechanism of the Hsp90 Molecular Chaperone Machinery." *Annual Review of Biochemistry* 75: 271–94. doi:10.1146/annurev.biochem.75.103004.142738.

Roe, S. M., C. Prodromou, R. O'Brien, J. E. Ladbury, P. W. Piper, and L. H. Pearl. 1999. "Structural Basis for Inhibition of the Hsp90 Molecular Chaperone by the Antitumor Antibiotics Radicicol and Geldanamycin." *Journal of Medicinal Chemistry* 42 (2): 260–66. doi:10.1021/jm980403y.

Rohou, Alexis, and Nikolaus Grigorieff. 2015. "CTFFIND4: Fast and Accurate Defocus Estimation from Electron Micrographs." *Journal of Structural Biology* 192 (2): 216–21. doi:10.1016/j.jsb.2015.08.008.

Scheres, Sjors H. W. 2012. "RELION: Implementation of a Bayesian Approach to Cryo-EM Structure Determination." *Journal of Structural Biology* 180 (3): 519–30. doi:10.1016/j.jsb.2012.09.006.

Shiau, Andrew K., Seth F. Harris, Daniel R. Southworth, and David A. Agard. 2006. "Structural Analysis of E. Coli Hsp90 Reveals Dramatic Nucleotide-Dependent Conformational Rearrangements." *Cell* 127 (2): 329–40. doi:10.1016/j.cell.2006.09.027.

Sidera, Katerina, and Evangelia Patsavoudi. 2014. "HSP90 Inhibitors: Current Development and Potential in Cancer Therapy." *Recent Patents on Anti-Cancer Drug Discovery* 9 (1): 1–20.

Southworth, Daniel R., and David A. Agard. 2008. "Species-Dependent Ensembles of Conserved Conformational States Define the Hsp90 Chaperone ATPase Cycle." *Molecular Cell* 32 (5): 631–40. doi:10.1016/j.molcel.2008.10.024.

Taipale, Mikko, Daniel F. Jarosz, and Susan Lindquist. 2010. "HSP90 at the Hub of Protein Homeostasis: Emerging Mechanistic Insights." *Nature Reviews. Molecular Cell Biology* 11 (7): 515–28. doi:10.1038/nrm2918.

Trendowski, Matthew. 2015. "PU-H71: An Improvement on Nature's Solutions to Oncogenic Hsp90 Addiction." *Pharmacological Research* 99 (September): 202–16. doi:10.1016/j.phrs.2015.06.007.

Workman, Paul. 2004. "Combinatorial Attack on Multistep Oncogenesis by Inhibiting the Hsp90 Molecular Chaperone." *Cancer Letters* 206 (2): 149–57. doi:10.1016/j.canlet.2003.08.032.

Workman, Paul, Francis Burrows, Len Neckers, and Neal Rosen. 2007. "Drugging the Cancer Chaperone HSP90: Combinatorial Therapeutic Exploitation of Oncogene Addiction and Tumor Stress." *Annals of the New York Academy of Sciences* 1113 (October): 202–16. doi:10.1196/annals.1391.012.

Yi, Fang, and Lynne Regan. 2008. "A Novel Class of Small Molecule Inhibitors of Hsp90." *ACS Chemical Biology* 3 (10): 645–54. doi:10.1021/cb800162x.

Young, J. C., W. M. Obermann, and F. U. Hartl. 1998. "Specific Binding of Tetratricopeptide Repeat Proteins to the C-Terminal 12-KDa Domain of Hsp90." *The Journal of Biological Chemistry* 273 (29): 18007–10.

Zuehlke, Abbey, and Jill L. Johnson. 2010. "Hsp90 and Co-Chaperones Twist the Functions of Diverse Client Proteins." *Biopolymers* 93 (3): 211–17. doi:10.1002/bip.21292.

CHAPTER 6

DISCUSSION AND FUTURE DIRECTIONS

In this thesis, three different classes of chaperones were explored: disaggregases (Hsp104), holdases (Get3), and foldases (FKBP51). Cryo-EM was the main technique used to study these chaperones, and resulting structures were informative about the functional mechanisms of these complex molecular machines.

6.1 Hsp104 Disaggregase

In our study of the Hsp104 yeast disaggregase structure we solved high resolution structures of three different conformational states: open, closed and extended. We hypothesize that Hsp104 cycles between these states with substrate binding, processive ratcheting of the polypeptide, and substrate release. This mechanism is highly dependent upon ATP hydrolysis for the power to undergo a 65Å shift from the open to closed state, and then sequentially ratchet mobile protomers between closed and extended states in a hand-over-hand translocation mechanism (Yokom et al. 2016). In the open state, we established an asymmetric spiral hexamer arrangement that generates a unique hetero-AAA+ interaction between the P1-NBD2 and P6-NBD1. This arrangement allows for the critical substrate binding tyrosine loops to align in a two-turn left-handed spiral staircase down the central channel. Due to the large cleft and arrangement of the substrate recognition NTDs, we hypothesize that the open conformation is an important off state and primed for substrate binding.

Our analysis of the AMPPNP- and ADP-bound states established that the MD undergoes nucleotide-specific conformational changes. In the ATP-state, several functionally relevant salt-

bridges stabilize an interprotomer MD-NBD1 interaction, which could have an allosteric effect on hydrolysis due to the interaction with the nucleotide pocket. In the ADP-state, the MD's form an MD-MD criss-cross interaction. Interestingly, the potentiated Hsp104 variants characterized in the Shorter lab (Jackrel et al. 2014) are mutations along the MD-MD interaction site. These potentiated variants can function independent of Hsp70, which is intriguing since Hsp70 binds Hsp104 at the MD-MD interaction site, therefore they have implications for the role of Hsp70 in disaggregation. Overall, these two nucleotide-specific conformations of the MD are important for regulating the disaggregase ability of Hsp104.

With the addition of casein, a model substrate, Hsp104 undergoes a significant rearrangement to the closed and extended states. The substrate-bound states are more constricted and planar than the open, substrate-free conformation. In the closed state, five of the protomers have substrate engagement of the tyrosine loops, with a mobile interface that has the sixth protomer, P6 disengaged. The extended state has an identical arrangement of P2-P4, but the mobile protomers extend up (P6) and down (P1) the substrate, with P6 substrate engagement. This generates a two-turn right handed spiral staircase of tyrosine loop substrate contacts, with a 6-7Å, or 2 amino acid, rise between loops. Analysis of nucleotide pockets reveals that active hydrolysis correlates with substrate engagement, more specifically with P6 going from an inactive off state in the closed conformation to the active on state in the extended conformation. Altogether these results suggest a rotary-like translocation mechanism that cycles between the closed and extended states with ATP hydrolysis and binding and release of the substrate.

Incredibly, both the open and closed states appear similar to other AAA+ complexes including VAT, Pex1-Pex6, NSF and Vps4. VAT, Pex1-Pex and NSF are double ring AAA+ hexamers that adopt an open asymmetric, left-handed spiral architecture (Huang et al. 2016;

Blok et al. 2015; M. Zhao et al. 2015) similar to the open Hsp104 structure. Both VAT and Vps4 have also been observed in a substrate bound state, revealing a right-handed spiral of pore loops similar to the closed, substrate bound state of Hsp104 (Ripstein et al. 2017; Monroe et al. 2017). In single ring AAA+ hexamers, like ClpX (Glynn et al. 2009) and the proteasome (Schweitzer et al. 2016), the tyrosine loops have been observed in a right-handed spiral arrangement. Altogether, it seems that the open and closed spiral tyrosine loop arrangements are conserved across AAA+ species and systems.

Interestingly, of the recently published substrate-bound AAA+ structures, no other lab to date has captured a state similar to the extended state with all six protomers engaging substrate. This could indicate that the extended state is unique to Hsp104, due to its high level of processivity, although it is possible that the other AAA+ proteins can adopt the extended state but it has not been seen in the current substrate-bound datasets due to data quality or quantity. We performed very extensive 3D classification to solve a high-resolution structure of the extended state, therefore if the extended state was a minority of particles in other datasets it could have been overlooked. Perhaps the efficiency and processivity of a AAA+ relates to the presence and frequency of the extended state in the translocation mechanism, and therefore further analysis of AAA+ structures will be required to resolve this concept. Overall, our structures contribute a high-resolution view of the translocation mechanism of a AAA+ machine, which appears highly conserved among AAA+ proteins.

6.2 Hsp104 Future Directions

Although the open, closed and extended Hsp104 structures give insight into the AAA+ translocation mechanism, there is still much to be done to better understand how this mechanism works. Hsp70 is critical for Hsp104 function in yeast, and so a future goal is to solve a structure

of Hsp70 bound to the Hsp104-substrate complex (Mogk, Kummer, and Bukau 2015). This structure would indicate the stoichiometry of Hsp70 bound to Hsp104, as well as localize the interactions of Hsp70 with the MD relative to the substrate and mobile protomer interface. It would be pertinent to determine if Hsp70 is binding Hsp104 in the open, substrate free state, which would establish whether or not Hsp70 is indeed binding to the MD of P1 in the large open cleft as we initially proposed (Yokom et al. 2016). These structures would provide insight into the substrate recognition and recruitment of Hsp70, and potentially explain how the potentiated mutants (Jackrel et al. 2014) are affecting Hsp70 interactions.

Another question to be addressed in this project is how conserved the established translocation mechanism of Hsp104 is in the bacterial homolog, ClpB. ClpB contains 45% sequence identity with Hsp104, and is structurally very similar (Doyle and Wickner 2009). ClpB is thought to be non-processive, compared to the highly processive nature of Hsp104 (Li et al. 2015), therefore ClpB is unable to pull apart amyloids as efficiently as Hsp104. To properly compare ClpB to Hsp104 structure and function, it is necessary to determine the substrate bound, ATP and ADP-states of ClpB. If ClpB adopts the same open, closed and extended states observed in Hsp104 it would confirm our translocation mechanism is conserved within the Hsp100 family and possibly other AAA+ machines. If so, the question remains why these proteins have such differing functions. If VAT or Vps4, like ClpB, do not have the extended state, it could potentially indicate that the extended state is specific to Hsp104 and may point towards Hsp104's incredibly processive disaggregase mechanism. Other AAA+ proteins could be investigated, such as ClpA, which is a two-ring AAA+ similar to Hsp104 that lacks the MD. The goal is to establish how conserved this rotary mechanism is, and how it relates to function.

Another important future direction of this project is to explore more substrates of Hsp104 to determine if different substrates alter the disaggregase mechanism. Sup35, a yeast prion Hsp104 is known to disassemble (X. Zhao et al. 2017), is a good target to determine the plasticity of Hsp104 with a more complex, beta-sheet substrate. Another substrate of interest is RepA. RepA is a plasmid P1 initiator protein, stimulated by chaperones such as ClpA and DnaJ/DnaK/GrpE to bind DNA (Wickner et al. 1994), therefore a prime binding target for Hsp104. The Shorter lab has studied GFP-tagged forms of RepA of varying lengths, which would be useful to form a substrate-bound complex in which the stable GFP tag traps the RepA in a sequence-specific manner in the central channel. Using a RepA-GFP construct would elucidate the direct contacts between the substrate and tyrosine loops, therefore using varying lengths and sequences would demonstrate how these contacts vary with changes in the substrate sequence.

The functional relevance of the open state has been puzzling, therefore there is further work to be done to determine how Hsp104 engages substrate, or if the open state is merely an off state. A series of biochemical and kinetic experiments could be used to address this question. The Sauer lab has done extensive studies of ClpX by covalently linking hexamers, with different mixtures of mutated protomers (Martin, Baker, and Sauer 2005). A similar approach could be used, with two neighboring protomers having Fluorescence Resonance Energy Transfer (FRET) pairs arranged so that FRET would only occur when they assume the P6-NBD1-P1:NBD2 hetero-AAA+ interaction. A series of mutations around the hexamer could demonstrate how altering hydrolysis and substrate binding affects the open to closed conformation equilibrium. Optical tweezers could also be used to determine the rate of translocation, with dwell phases, and

determine how the potentiated mutants (Jackrel et al. 2014) alter the open to closed conformational plasticity, and therefore the non-processive to processive function of Hsp104.

6.3 Get3 is a redox holdase

In our study of yeast Get3, we identified that under oxidizing conditions, the Tail Anchor (TA) insertion protein factor can undergo large conformational reorganization from the reduced, ATP-dependent dimer, to an oxidized, ATP-independent tetramer. We hypothesize that Get3 can moonlight as a holdase chaperone capable of protecting cytosolic proteins from aggregation upon oxidative stress. This function is important for cell regulation because oxidation depletes ATP, therefore reducing function of ATP-dependent chaperones that are necessary for stress responses.

The first observation of Get3 as a holdase revealed that in cells with oxidative stress, Get3 localizes in stress foci in the cytosol rather than at the membrane for TA-binding protein insertion. Following this observation, we fully characterized this oxidized Get3 by recombinantly purifying it for further biochemical analysis. We demonstrated that $Get3_{ox}$ no longer has ATPase activity like the $Get3_{red}$. $Get3_{ox}$ can reactivate substrates, such as luciferase, similar to general chaperones, compared to $Get3_{red}$ which cannot. The transformation between the oxidized and reduced forms is fully reversible, and upon re-reduction, Get3 regains its ATPase activity and TA-protein insertion function.

The structural change between $Get3_{red}$ and $Get3_{ox}$ was determined using Size Exclusion Chromatography in tandem with Multi Angle Light Scattering (SEC-MALS), revealing a transition from a reduced dimer to an oxidized tetramer. Other oligomers were observed in these experiments, but by negative stain EM analysis it was shown that they all collapse into a tetramer, which appears to be the functional oligomer. The 3D structure of the tetramer was solved using negative stain EM, revealing a dimer of dimers in a ‘W’ conformation. The tetramer

structure appears to have a hydrophobic cleft between the two dimers, and negative stain EM of the tetramer bound to luciferase contained extra density in this cleft, indicating it as the substrate binding site. The structural rearrangement from the reduced dimer to the oxidized tetramer were confirmed using Hydrogen Deuterium Exchange Mass Spectrometry (HD/MS), indicating that the TA-binding sites become buried in the tetramer, exposing hydrophobic residues for its general chaperone function. Oxidation of Get3 involves formation of two disulfide bonds in the conserved cysteines at the dimerization contact, and release of the coordinated zinc at this site. The large conformational changes and disulfide bond formation are reminiscent of other redox holdase chaperones, such as Hsp33. These findings have demonstrated the incredible ATP-independent holdase function of Get3 under oxidizing conditions, which is important for protecting cells from oxidative stress in ATP depleting conditions.

6.4 Get3 Future Directions

Identifying and characterizing the Get3 holdase chaperone is a great advancement of our knowledge of the yeast oxidative stress response. To further explore the Get3 holdase, it would be pertinent to determine what occurs following oxidative stress. Likely, Get3 hands substrates off to Hsp70 when proper folding conditions and ATP levels return, and so biochemical analysis of this critical chaperone step is necessary. One way we could address this is by doing FRET of Get3 and Hsp7-, oxidizing the samples and then returning them to reduced conditions to determine under which conditions they interact, and how this affects the folded state of substrate. Another way to study this interaction is by doing single molecule experiments to determine Hsp70 localization following oxidative stress.

Cryo-EM could be used to get a higher resolution structure of the Get3 tetramer and Get3:luciferase complex. Unfortunately, many issues have prevented a high-resolution

reconstruction of either complex to be determined by our labs. These samples are difficult cryo-EM targets due to the size, ~160kDa, which has a low signal-to-noise, making image alignment difficult. The recent advancement of phase plate technology could help address this issue. During data collection, low electron doses are used to minimize radiation damage of the sample, which leads to a low signal-to-noise ratio of particles. Phase contrast is low because particles weakly modify the phase of the electron wave (Frank 2006). The objective lens is defocused from low to high spatial frequencies to obtain defocus phase contrast, but low spatial frequencies have very low contrast (Frank 2006). Phase plates were developed in an effort to generate phase contrast without the need for defocusing (Glaeser 2013).

The Zernike phase plate (ZPP) (R. Danev and Nagayama 2001) has a thin amorphous carbon film with a small hole in the center. The electron beam needs to be centered to travel through the hole so that it can alter the electron wave phase. These phase plates have been limited in their success due to a short lifetime and the difficulty of maintaining a centered beam (Radostin Danev, Glaeser, and Nagayama 2009). Volta phase plates (VPP) were developed more recently (Radostin Danev et al. 2014), with a similar design but without the hole, therefore the phase shift is created by the interaction of the electron beam with the carbon film. VPPs have an increased lifespan from ZPP, being able to recover from radiation after a few days, and they do not require the centering of the beam. The VPP leads to signal loss because of the carbon film (Radostin Danev et al. 2014), and variations in the film could introduce astigmatism over time. Moving forward, a high intensity focused laser beam is being developed as another way to create the phase shift (Müller et al. 2010; Schwartz et al. 2017). As we see the continued improvement upon this technology, it will become more achievable to determine high-resolution structures of small protein complexes, like the Get3 tetramer, due to the increased phase contrast.

Another issue that has prevented progress on $Get3_{ox}$ cryo-EM has been overall particle and ice spread. Detergents are often used in cryo-EM to improve the ice spread, but for the Get3 sample the detergent caused the tetramer to fall apart. The concentration of Get3 particles in the grid holes was often low relative to the concentration loaded onto the grid, therefore the particle density was too low for image alignment. To address these issues we have worked on improving the biochemistry and purification steps prior to vitrification. Recent datasets have given promise, showing the potential for high resolution with a much larger dataset. Obtaining a higher resolution Get3 structure would allow us to determine the new interaction sites between the two dimers and better understand the hydrophobic cleft and how it interacts with substrates. If this is a relatively conserved holdase mechanism, we could potentially predict other redox holdases.

6.5 Hsp90:FKBP51 complex

In this study, we determined that FKBP51 binds to Hsp90 in its closed, ATP-bound state. With negative stain and cryo-EM we demonstrate that FKBP51 binds in a 2:1 stoichiometry, orienting the TPR domains near the 'MEEVD' motif of the Hsp90 CTD and the PPIase domain toward the MD client binding region. The addition of the p23 cochaperone stabilizes the Hsp90:FKBP51 complex by trapping Hsp90 in the closed ATP-state, increasing occupancy of the complex for cryo-EM. It appears that the FK1 PPIase of FKBP51 directly interacts with the client protein binding domain of Hsp90, therefore elucidating a critical interaction in this chaperone complex.

The Hsp90:FKBP51 complex is important for regulating cellular signaling and altering malignancy and neurodegeneration (Workman et al. 2007; Moulick et al. 2011; Lindberg et al. 2015; Rodina et al. 2016; Yi and Regan 2008). Upregulation of FKBP51, which occurs with age, has been implicated in AD and prostate cancer (Blair et al. 2013; Periyasamy et al. 2010). The

Hsp90:FKBP51 complex stabilizes neurotoxic tau, protecting it from proteasomal degradation (Jinwal et al. 2010; Blair et al. 2013), which leads to the formation of neurofibrillary tangles (NFTs) found in AD neurons (Grundke-Iqbal et al. 1986; Cao and Konsolaki 2011). The Hsp90:FKBP51 complex regulates receptor binding of the Androgen Receptor (AR), therefore increased expression of FKBP51 leads to prostate cancer (Periyasamy et al. 2010). It's been shown that p23 stabilizes the Hsp90:FKBP51 interaction that associates with the androgen receptor (AR) to increase the AR transcriptional response (Jinwal et al. 2010). It appears that p23 is an important regulator of FKBP51 binding Hsp90, which can affect tau stability or AR transcriptional response. Our structural analysis of the Hsp90:FKBP51 complex has provided insight into a good drug target site, the PPIase-MD interaction. Drugs that target this site would provide better specificity than previous Hsp90 inhibitors.

6.6 Hsp90 Future Directions

There is immense potential for high resolution structure determination of the Hsp90:FKBP51:AMPPNP complex using cryo-EM. In a paper published from the David Agard group (Verba et al. 2016), they solved a 3.9Å cryoEM structure of the Hsp90:Cdc37:Cdk4 kinase complex. To achieve such high-resolution, ~1 million particles were collected and subjected to extensive 3D classification. Analysis of the Hsp90:FKBP51:AMPPNP 2D class averages demonstrates similar high-resolution quality as seen in the Hsp90:Cdc37:Cdk4 kinase paper, indicating that the limitations seen in the 3D analysis are from small particle datasets, with low signal-to-noise due to the small size of the particles. Occupancy of the complex has been a challenge, and crosslinkers were initially used to address this issue. The addition of p23 significantly increased complex occupancy, therefore moving forward the size of the dataset

needs to be boosted significantly, using the same complex formation and freezing conditions as established in this study.

Following structural characterization of the Hsp90:FKBP51:AMPPNP complex, more extensive biochemical analysis of these interactions and their implications in disease should be performed. First, truncations and mutations of the FK1 domain in FKBP51 could be studied, specifically targeting the interactions determined from the Hsp90:FKBP51:AMPPNP structure. These mutations could be evaluated in a cell based assay to determine the effects on tau, GR and AR, and therefore the potential application for therapeutics. Looking specifically at prostate cancer cells, mutations that disrupt the Hsp90:FKBP51 complex could demonstrate how this chaperone complex affects malignancy. With important residues identified, a high throughput screen of small molecules could be performed targeting the Hsp90:FKBP51 interaction, using NMR to study the chemical shifts of important residues. Hopefully, with these efforts, specific inhibitors for AD, prostate cancer and other diseases could be developed. The specificity between disease states should be tested to hopefully reduce the toxicity observed with current Hsp90 inhibitors.

6.7 References

Bao, Yi Ping, Lynnette J. Cook, Dominic O'Donovan, Eiichiro Uyama, and David C. Rubinsztein. 2002. "Mammalian, Yeast, Bacterial, and Chemical Chaperones Reduce Aggregate Formation and Death in a Cell Model of Oculopharyngeal Muscular Dystrophy." *The Journal of Biological Chemistry* 277 (14): 12263–69. doi:10.1074/jbc.M109633200.

Blair, Laura J., Bryce A. Nordhues, Shannon E. Hill, K. Matthew Scaglione, John C. O'Leary, Sarah N. Fontaine, Leonid Breydo, et al. 2013. "Accelerated Neurodegeneration through Chaperone-Mediated Oligomerization of Tau." *The Journal of Clinical Investigation* 123 (10): 4158–69. doi:10.1172/JCI69003.

Blok, Neil B., Dongyan Tan, Ray Yu-Ruei Wang, Pawel A. Penczek, David Baker, Frank DiMaio, Tom A. Rapoport, and Thomas Walz. 2015. "Unique Double-Ring Structure of the Peroxisomal Pex1/Pex6 ATPase Complex Revealed by Cryo-Electron Microscopy." *Proceedings of the National Academy of Sciences of the United States of America* 112 (30): E4017-4025. doi:10.1073/pnas.1500257112.

Cao, Weihuan, and Mary Konsolaki. 2011. “FKBP Immunophilins and Alzheimer’s Disease: A Chaperoned Affair.” *Journal of Biosciences* 36 (3): 493–98.

Danev, R., and K. Nagayama. 2001. “Transmission Electron Microscopy with Zernike Phase Plate.” *Ultramicroscopy* 88 (4): 243–52.

Danev, Radostin, Bart Buijsse, Maryam Khoshouei, Jürgen M. Plitzko, and Wolfgang Baumeister. 2014. “Volta Potential Phase Plate for In-Focus Phase Contrast Transmission Electron Microscopy.” *Proceedings of the National Academy of Sciences of the United States of America* 111 (44): 15635–40. doi:10.1073/pnas.1418377111.

Danev, Radostin, Robert M. Glaeser, and Kuniaki Nagayama. 2009. “Practical Factors Affecting the Performance of a Thin-Film Phase Plate for Transmission Electron Microscopy.” *Ultramicroscopy* 109 (4): 312–25. doi:10.1016/j.ultramic.2008.12.006.

Doyle, Shannon M., and Sue Wickner. 2009. “Hsp104 and ClpB: Protein Disaggregating Machines.” *Trends in Biochemical Sciences* 34 (1): 40–48. doi:10.1016/j.tibs.2008.09.010.

Frank, Joachim. 2006. *Three-Dimensional Electron Microscopy of Macromolecular Assemblies: Visualization of Biological Molecules in Their Native State*. Oxford University Press.

Glaeser, Robert M. 2013. “Invited Review Article: Methods for Imaging Weak-Phase Objects in Electron Microscopy.” *The Review of Scientific Instruments* 84 (11): 111101. doi:10.1063/1.4830355.

Glynn, Steven E., Andreas Martin, Andrew R. Nager, Tania A. Baker, and Robert T. Sauer. 2009. “Structures of Asymmetric ClpX Hexamers Reveal Nucleotide-Dependent Motions in a AAA+ Protein-Unfolding Machine.” *Cell* 139 (4): 744–56. doi:10.1016/j.cell.2009.09.034.

Grundke-Iqbal, I., K. Iqbal, M. Quinlan, Y. C. Tung, M. S. Zaidi, and H. M. Wisniewski. 1986. “Microtubule-Associated Protein Tau. A Component of Alzheimer Paired Helical Filaments.” *The Journal of Biological Chemistry* 261 (13): 6084–89.

Huang, Rui, Zev A. Ripstein, Rafal Augustyniak, Michal Lazniewski, Krzysztof Ginalski, Lewis E. Kay, and John L. Rubinstein. 2016. “Unfolding the Mechanism of the AAA+ Unfoldase VAT by a Combined Cryo-EM, Solution NMR Study.” *Proceedings of the National Academy of Sciences of the United States of America* 113 (29): E4190–99. doi:10.1073/pnas.1603980113.

Jackrel, Meredith E., Morgan E. DeSantis, Bryan A. Martinez, Laura M. Castellano, Rachel M. Stewart, Kim A. Caldwell, Guy A. Caldwell, and James Shorter. 2014. “Potentiated Hsp104 Variants Antagonize Diverse Proteotoxic Misfolding Events.” *Cell* 156 (1–2): 170–82. doi:10.1016/j.cell.2013.11.047.

Jinwal, Umesh K., John Koren, Sergiy I. Borysov, Andreas B. Schmid, Jose F. Abisambra, Laura J. Blair, Amelia G. Johnson, et al. 2010. “The Hsp90 Cochaperone, FKBP51, Increases Tau Stability and Polymerizes Microtubules.” *The Journal of Neuroscience: The Official Journal of the Society for Neuroscience* 30 (2): 591–99. doi:10.1523/JNEUROSCI.4815-09.2010.

Lindberg, Iris, James Shorter, R. Luke Wiseman, Fabrizio Chiti, Chad A. Dickey, and Pamela J. McLean. 2015. “Chaperones in Neurodegeneration.” *The Journal of Neuroscience: The Official Journal of the Society for Neuroscience* 35 (41): 13853–59. doi:10.1523/JNEUROSCI.2600-15.2015.

Manilal, S., C. A. Sewry, Nguyen thi Man, F. Muntoni, and G. E. Morris. 1997. “Diagnosis of X-Linked Emery-Dreifuss Muscular Dystrophy by Protein Analysis of Leucocytes and Skin

with Monoclonal Antibodies." *Neuromuscular Disorders* 7 (1): 63–66. doi:10.1016/S0960-8966(96)00405-1.
Martin, Andreas, Tania A. Baker, and Robert T. Sauer. 2005. "Rebuilt AAA + Motors Reveal Operating Principles for ATP-Fuelled Machines." *Nature* 437 (7062): 1115–20. doi:10.1038/nature04031.
Mogk, Axel, Eva Kummer, and Bernd Bukau. 2015. "Cooperation of Hsp70 and Hsp100 Chaperone Machines in Protein Disaggregation." *Frontiers in Molecular Biosciences* 2: 22. doi:10.3389/fmolb.2015.00022.
Monroe, Nicole, Han Han, Peter S. Shen, Wesley I. Sundquist, and Christopher P. Hill. 2017. "Structural Basis of Protein Translocation by the Vps4-Vta1 AAA ATPase." *ELife* 6 (April). doi:10.7554/eLife.24487.
Moulick, Kamalika, James H. Ahn, Hongliang Zong, Anna Rodina, Leandro Cerchietti, Erica M. Gomes DaGama, Eloisi Caldas-Lopes, et al. 2011. "Affinity-Based Proteomics Reveal Cancer-Specific Networks Coordinated by Hsp90." *Nature Chemical Biology* 7 (11): 818–26. doi:10.1038/nchembio.670.
Müller, H., Jian Jin, R. Danev, J. Spence, H. Padmore, and R. M. Glaeser. 2010. "Design of an Electron Microscope Phase Plate Using a Focused Continuous-Wave Laser." *New Journal of Physics* 12 (July). doi:10.1088/1367-2630/12/7/073011.
Periyasamy, S., T. Hinds, L. Shemshedini, W. Shou, and E. R. Sanchez. 2010. "FKBP51 and Cyp40 Are Positive Regulators of Androgen-Dependent Prostate Cancer Cell Growth and the Targets of FK506 and Cyclosporin A." *Oncogene* 29 (11): 1691–1701. doi:10.1038/onc.2009.458.
Ripstein, Zev A, Rui Huang, Rafal Augustyniak, Lewis E Kay, and John L Rubinstein. 2017. "Structure of a AAA+ Unfoldase in the Process of Unfolding Substrate." *ELife* 6. Accessed July 24. doi:10.7554/eLife.25754.
Rodina, Anna, Tai Wang, Pengrong Yan, Erica DaGama Gomes, Mark P. S. Dunphy, Nagavarakishore Pillarsetty, John Koren, et al. 2016. "The Epichaperome Is an Integrated Chaperome Network That Facilitates Tumour Survival." *Nature* 538 (7625): 397–401. doi:10.1038/nature19807.
Schwartz, Osip, Jeremy J. Axelrod, Philipp Haslinger, Colin Ophus, Robert M. Glaeser, and Holger Müller. 2017. "Continuous 40 GW/Cm^2 Laser Intensity in a near-Concentric Optical Cavity." *Optics Express* 25 (13): 14453. doi:10.1364/OE.25.014453.
Schweitzer, Andreas, Antje Aufderheide, Till Rudack, Florian Beck, Günter Pfeifer, Jürgen M. Plitzko, Eri Sakata, Klaus Schulten, Friedrich Förster, and Wolfgang Baumeister. 2016. "Structure of the Human 26S Proteasome at a Resolution of 3.9 Å." *Proceedings of the National Academy of Sciences of the United States of America* 113 (28): 7816–21. doi:10.1073/pnas.1608050113.
Verba, Kliment A., Ray Yu-Ruei Wang, Akihiko Arakawa, Yanxin Liu, Mikako Shirouzu, Shigeyuki Yokoyama, and David A. Agard. 2016. "Atomic Structure of Hsp90-Cdc37-Cdk4 Reveals That Hsp90 Traps and Stabilizes an Unfolded Kinase." *Science (New York, N.Y.)* 352 (6293): 1542–47. doi:10.1126/science.aaf5023.
Wickner, S., S. Gottesman, D. Skowyra, J. Hoskins, K. McKenney, and M. R. Maurizi. 1994. "A Molecular Chaperone, ClpA, Functions like DnaK and DnaJ." *Proceedings of the National Academy of Sciences of the United States of America* 91 (25): 12218–22.
Workman, Paul, Francis Burrows, Len Neckers, and Neal Rosen. 2007. "Drugging the Cancer Chaperone HSP90: Combinatorial Therapeutic Exploitation of Oncogene Addiction and

Tumor Stress." *Annals of the New York Academy of Sciences* 1113 (October): 202–16. doi:10.1196/annals.1391.012.
Yi, Fang, and Lynne Regan. 2008. "A Novel Class of Small Molecule Inhibitors of Hsp90." *ACS Chemical Biology* 3 (10): 645–54. doi:10.1021/cb800162x.
Yokom, Adam L., Stephanie N. Gates, Meredith E. Jackrel, Korrie L. Mack, Min Su, James Shorter, and Daniel R. Southworth. 2016. "Spiral Architecture of the Hsp104 Disaggregase Reveals the Basis for Polypeptide Translocation." *Nature Structural & Molecular Biology* 23 (9): 830–37. doi:10.1038/nsmb.3277.
Zhao, Minglei, Shenping Wu, Qiangjun Zhou, Sandro Vivona, Daniel J. Cipriano, Yifan Cheng, and Axel T. Brunger. 2015. "Mechanistic Insights into the Recycling Machine of the SNARE Complex." *Nature* 518 (7537): 61–67. doi:10.1038/nature14148.
Zhao, Xiaohong, Ramon Rodriguez, Rebecca E. Silberman, Joseph M. Ahearn, Sheela Saidha, Kaelyn C. Cummins, Evan Eisenberg, and Lois E. Greene. 2017. "Heat Shock Protein 104 (Hsp104)-Mediated Curing of [PSI(+)] Yeast Prions Depends on Both [PSI(+)] Conformation and the Properties of the Hsp104 Homologs." *The Journal of Biological Chemistry* 292 (21): 8630–41. doi:10.1074/jbc.M116.770719.